MASARYK UNIVERSITY

FACULTY OF SCIENCE

PH.D. DISSERTATION

Interstellar Bubbles

Author:
Lenka Zychová

Supervisor:
RNDr. Soňa Ehlerová, Ph.D.

A thesis submitted in fulfillment of the requirements
for the degree of Doctor of Philosophy

in the

Department of Theoretical Physics and Astrophysics

Brno, 2017

Bibliographic Entry

Author:	Lenka Zychová Masaryk University Faculty of Science Department of Theoretical Physics and Astrophysics

Title of Dissertation:	Interstellar Bubbles
Degree Programme:	PřF D-FY4 Physics
Field of Study:	PřF TEFY Theoretical Physics and Astrophysics

Supervisor:	RNDr. Soňa Ehlerová, Ph.D. Academy of Sciences of Czech Republic Astronomical Institute

Academic Year:	2016/2017
Number of Pages:	147
Keywords:	interstellar bubbles, interstellar matter, neutral hydrogen, molecular gas, HII region

Bibliografický záznam

Autor:	Lenka Zychová Masarykova univerzita Přírodovědecká fakulta Ústav teoretické fyziky a astrofyziky

Název práce:	Bubliny v mezihvězdném prostředí
Studijní program:	PřF D-FY4 Fyzika
Studijní obor:	PřF TEFY Teoretická fyzika a astrofyzika
Školitel:	RNDr. Soňa Ehlerová, Ph.D. Akademie věd České republiky Astronomický ústav
Akademický rok:	2016/2017
Počet stran:	147
Klíčová slova:	mezihvězdné bubliny, mezihvězdná látka, neutrální vodík, molekulární plyn, HII region

MASARYK UNIVERSITY

Abstract

Faculty of Science
Department of Theoretical Physics and Astrophysics

Doctor of Philosophy

Interstellar Bubbles

Lenka Zychová

Massive O and B stars ionize and heat the surrounding interstellar medium, which expands and drives a shock into the ambient gas. The expanding hot plasma plows through the surrounding medium and collects the cold neutral gas, which is often observed between the ionization and the shock front. These phenomena are called interstellar bubbles.

Interstellar bubbles were first discovered and investigated in the infrared, but a systematic study in the distribution of the neutral hydrogen (HI) was lacking. Using a catalog of interstellar bubbles based on infrared observations, we searched for their counterparts in HI and CO (carbon monoxide) data. Out of 24 systems above a threshold angular size, we discovered HI counterparts for 20 systems, described their morphology, compared their neutral atomic and molecular content and determined their basic properties, such as size, distance, mass, density and expansion velocity. We used these parameters to estimate their energy input and age.

Although the molecular content of the interstellar bubbles may be distributed in a flat ring, in HI we resolve clear 3D structures. Some of the studied interstellar bubbles are clearly visible as bright envelopes in HI data, some are recognizable only as holes (showing an absence of HI emission). For the first time, we discovered several envelopes visible in absorption.

According to our results we suppose that the atomic matter is being collected and accumulated during the expansion, but probably does not effectively form H_2. According to energy input requirements we assume that most of the bubbles are created by stellar feedback of B type stars.

We separately studied the interstellar environment in the vicinity of N115, N116 and N117 bubbles. We discovered two new bubbles visible mainly in HI emission and identified two independent systems of bubbles, lying at different distances. Both systems include two large bubbles (20 – 30 pc in radius) and one small bubble ($\sim$ 4 pc in radius) lying at the point where larger bubbles interact. The two pairs of large bubbles are probably colliding, resulting in star formation in the place of the collision. We propose that such collisions are an important mechanism and can increase the probability of further star formation.

During October 2015 and July/August 2016 we performed optical observations and spectroscopy at MPG/ESO 2.2 m telescope located at La Silla observatory in Chile. We researched hot inner parts of bubbles S1, S73 and S74. Among other results we found a double peaked profile of [NII] emission (bubble S74), which corresponds to local maxima in the HI spectrum. This probably mirrors approaching and receding walls of S74 bubble, both in HI and optical spectra. This result is another evidence that interstellar bubbles are real 3D structures.

MASARYKOVA UNIVERZITA

Abstrakt

Přírodovědecká fakulta
Ústav teoretické fyziky a astrofyziky

Doktorské studium

Bubliny v mezihvězdném prostředí

Lenka Zychová

Hmotné hvězdy spektrálního typu O a B zahřívají a ionizují okolní mezihvězdnou látku, která expanduje a šíří rázovou vlnu do přilehlého plynu. Expandující plazma prostupuje skrz okolní prostředí a nabírá chladný neutrální plyn, který se často pozoruje mezi ionizační a šokovou frontou. Tento fenomén se označuje jako mezihvězdná bublina.

Mezihvězdné bubliny byly poprvé objeveny a zkoumány v infračervených pozorováních. Nicméně, systematická studie, zabývající se rozložením neutrálního vodíku (HI) v bublinách, dosud chyběla. Náš výzkum je proto zaměřen na analýzu a hledání protějšků mezihvězdných bublin v pozorováních čáry HI a oxidu uhelnatého (CO), s využitím existujícího katalogu infračervených bublin. Z 24 objektů, přesahující mezní úhlovou velikost, jsme objevily 20 HI protějšků mezihvězdných bublin. Popsaly jsme jejich morfologické znaky, porovnaly jejich atomický a molekulární obsah a vypočítaly jejich základní vlastnosti, jako jsou rozměry, vzdálenost, hmotnost, hustota a expanzní rychlost. Pomocí těchto parametrů jsme odhadly jejich věk a energii potřebnou k jejich vzniku.

Přestože se dle našich výsledků zdá, že molekulární plyn mezihvězdných bublin vytváří plochý prstenec, HI data jasně ukazují, že mezihvězdné bubliny jsou trojrozměrné objekty. Některé studované mezihvězdné bubliny jsou v HI datech zřetelně viditelné jako jasné obálky, některé jsou rozpoznatelné pouze jako díry (absence HI emise v centrálních částech). Poprvé, díky této práci, byly objeveny obálky, které jsou viditelné v absorpci.

Podle našich výsledků předpokládáme, že se atomární plyn během expanze shromažďuje, ale pravděpodobně efektivně nevytváří H_2. V souladu s našimi odhady luminozit a vstupních energií předpokládáme, že většina bublin vzniká díky působení hvězd spektrálního typu B na své okolí.

Samostatně jsme se věnovaly mezihvězdnému prostředí v okolí bublin N115, N116 a N117. Objevily jsme dvě nové bubliny viditelné především v HI emisi a identifikovaly dva nezávislé systémy bublin, které leží na různých vzdálenostech. Oba systémy se zdají být podobné: každý z nich obsahuje dvě velké bubliny (20 – 30 pc v poloměru) a jednu malou bublinu ($\sim$ 4 pc v poloměru), která leží v místě dotyku větších bublin. Oba páry velkých bublin se pravděpodobně srážejí, což vede ke vzniku hvězd v místě

srážky. Předpokládáme, že takové kolize jsou důležitým procesem a mohou zvyšovat pravděpodobnost další tvorby hvězd.

Během října 2015 a července/srpna 2016 jsme provedly optická pozorování a spektroskopii na 2.2 m dalekohledu MPG/ESO umístěném na observatoři La Silla v Chile. Pozorování jsme zaměřily na horké vnitřní části bublin S1, S73 a S74. Kromě jiných výsledků jsme objevily dvojitý profil čáry [NII] (u bubliny S74), který odpovídá dvojitému profilu v HI spektru. Tento výsledek ukazuje, že přední i zadní stěna bublin může být viditelná jak v HI, tak v optickém spektru. Mezihvězdné bubliny jsou tudíž reálné 3D struktury.

Acknowledgements

Before I thank all people who were standing beside me through my doctoral studies, I need to thank **Prof. Jiří Krtička**, who was my supervisor throughout my undergraduate studies. Thanks to him I got interested in interstellar matter and after finishing my master degree studies, he was the one who suggested Soňa Ehlerová to be my mentor during my doctoral studies. I feel more than grateful for his help in directing my research.

I would like to express my sincere gratitude to my supervisor **Dr. Soňa Ehlerová** for her motivation, patience, great ideas and immense knowledge about the bubbling content of our Galaxy. Her guidance helped me in all the time of research, writing of our publication and this thesis. Thanks to her I could visit a wonderful observatory La Silla, observe with 2.2 m telescope, meet new scientists and get inspired by their enthusiasm and work. She taught me how to survive in the chaotic waters of neutral hydrogen data and through her brilliant talks she showed me how to communicate science of interstellar matter to general public.

There was one more exceptional observing period during my doctoral studies – the internship at RT4 radiotelescope in Piwnice, Poland. Those three weeks of excitement, observing with 32 m radiotelescope and analysing methanol spectra would have never happened, if **Dr. Jan Janík** had not arranged the internship for me. I am very thankful to him for his help, encouragement and making one of the best times in my life happen. Huge thanks belongs also to **Dr. Pawel Wolak**, who was my mentor during the stay and was incredibly patient to answer all my questions and inspire me in studying, at least for a while, methanol masers.

My sincere thanks also go to **doc. Miloslav Zejda**, **Prof. Zdeněk Mikulášek**, and **Prof. Rikard von Unge**, who provided me with an opportunity to do outreach for our department. This widened my horizons, taught me new skills and ensured me in continuing my outreach activities. I am more than grateful to each of them, to **doc. Miloslav Zejda** for his help and new ideas, for consulting each detail of my work, to **Prof. Zdeněk Mikulášek** for his support not only in astronomy, but also in music, and to **Prof. Rikard von Unge** for his incredible support in my ideas and helping me to make one of my dreams come true – founding an astronomy club for children. Here, I would like to thank **Hvězdárna a planetárium Brno** for letting us teach kids in the astonishing environment of their building and also to my fellow leaders: **Ondrej**, **Vašek**, **Mirek J.**, **Mirek D.**, **Bára**, **Terka**, a **Magda** for their enthusiasm to teach kids and uncover the beauty of astronomy for them. While mentioning all people standing behind me and helping me with my outreach activities, I need to thank **doc. Vladimír Štefl**, who inspired me in teaching physics and astronomy for high school students and for his ideas how to incorporate astronomy in regular classes of physics.

I would like to thank my fellow doctoral students and colleagues for their feedback, cooperation and of course friendship. Thanks to **Dr. Filip Hroch** for his indefatigable help whenever I had troubles with any program or analyzing method, thanks to **Oldřich**, who excitedly helped me with installations, thanks to **doc. Norbert Werner** for his insightful comments, encouragement, long debates about bubbles, careful listening and helping me sort out my thoughts, and thanks to **Pavel** for our long debates

about how to help new students to go through their doctoral studies full motivated and with a great source of research activities. Huge thanks go to my colleagues and friends from our office: **Lenka**, **Klára**, **Marek**, **Michal** and **Pawel** for the continuous support of my Ph.D study, all the fun we had and of course for their patience with the mess I have on my desk. I will put it in order soon.

I would like to thank my family, especially my parents **Jana** and **Tomáš**. Without their precious support through my whole life I would never have got to this point of writing a doctoral thesis. I am incredibly grateful that they did not object too much and let me study what I loved. Last, but definitely not least, I would love to express my deep gratitude to my partner, **Jochen**, who, although he has shared the life with me just for a few months, supports me in all my activities and especially in writing my thesis. His help with English, pointing out unclear formulations and unsustainable questions about my research made me work harder and hopefully better. He is the best support I could ever have and I am deeply thankful for it.

Contents

Introduction

The interstellar medium is both beautiful to observe and attractive to study. The Galaxy is tangled with curved filaments of gas decorated with glaring star forming regions, expanding areas of ionized gas, thick molecular clouds hiding stars in visual, but shining at millimeter wavelengths, glossing planetary nebulae and supernova remnants mirroring violent events, which stand behind their creation. All these objects and features of interstellar medium are ubiquitous and known to both professional and amateur astronomers. Among all these loops, curves and filamentary structures, some circle-like shapes are striking at every infrared image. These are interstellar bubbles, objects surrounding young and massive stars with their hot and ionized regions.

There are different types of bubbles, created by different processes (such as stellar feedback, explosion of supernova, or high velocity cloud infall) and reaching various diameters. The bubbles we are interested in and which our research is dedicated to, are mostly observable in infrared radiation and reach diameters from fractions to few tens of parsecs. Our study is mainly based on publications by Churchwell et al. [1, 2] and Deharveng et al. [3]. The progenitors of interstellar bubbles, which are the main topic of the publications mentioned above, are mainly OB stars. A region of ionized gas is forming around these stars, starts to expand and builds a bubble of hot gas, surrounded by a layer of collected neutral medium. There is an abundance of evidence of ongoing star formation in the vicinity of bubbles, even in their envelopes. Ultra compact HII regions, methanol masers, or small and probably young bubbles are often found in the rims of larger bubbles. These observations drive an attractive, but yet unanswered question: do bubbles trigger star formation?

Our study is focused on an area, which was not yet satisfactorily covered: searching for gaseous content of interstellar bubbles. Most of the studies in this field are analyzing infrared images and observations of carbon monoxide (CO) molecule. This is not surprising, interstellar bubbles are best observable at infrared wavelengths due to thermal radiation of dust particles, whose temperature reaches tens to hundreds Kelvins. Molecular gas, which was found to be associated with most of bubbles and represents their molecular content, is observable due to CO molecule emission. However, observations of bubbles in neutral hydrogen (HI), thus of warm neutral medium, are not common at all. Our motivation is to uncover bubbles in HI observations, describe them, compare their characteristics to those from CO observations, compute their distances and masses, estimate ages and energy input involved in their creation, and, finally, prepare a complete sample of bubbles, which can contribute to further detailed studies and which can conceivably help to find the answer to the question of triggered star formation.

The thesis is divided into two main parts: a summary of the current knowledge of interstellar bubbles, and our own research. The summary is given in the first two chapters. The first chapter (Interstellar bubbles) deals with the morphological and dynamical aspects of bubbles and their evolution. The second chapter (Multiwavelength observations of ISM and bubbles) is dedicated to observations of interstellar bubbles, especially in the wavelengths we are interested in: 8 μm (dust content), 2.6 mm (molecular content), 21 cm (atomic content), and additionally, 24 μm (hot inner parts) and 870 μm (cold dust condensations). The most extensive part of the thesis is devoted to the results we have attained during my doctoral studies. The third chapter (Searching for an atomic and a molecular component of infrared bubbles) is focused on analysis, morphology description and derivation of basic properties of interstellar bubbles. During our analysis we got interested by the surroundings of bubbles N115, N116 and N117, which resulted in an extended research of the location. This research is described in the fourth chapter (Colliding interstellar bubbles) and the results were published in Zychová and Ehlerová [4]. The fifth chapter (Observations of hot inner parts of bubbles S1, S73 and S74) is describing our side project – optical spectroscopy of the inner hot parts of interstellar bubbles. Each of these chapters has its own discussion and the most important results are summarized in the last chapter (Conclusions).

Chapter 1

Interstellar bubbles

Shells, supershells, superbubbles, bubbles, wind-blown bubbles, interstellar bubbles, infrared bubbles, HI holes, HI envelopes... This ocean full of bubbling terms and names is often confusing. Most of the terms are interlaced and could be replaceable, but, for a clarity, this chapter explains most of them surreptitiously while describing the formation and evolution of bubbles, their morphology and other processes associated with them. Nevertheless, shells (or supershells) are well known among scientists studying interstellar matter (ISM). These structures are large, reaching tens to hundreds of parsecs and they are best observable in neutral hydrogen (HI) emission. Their smaller cousins, interstellar bubbles, which are the theme of this thesis, are reaching diameters of fractions to tens of parsecs and are best observable in infrared emission.

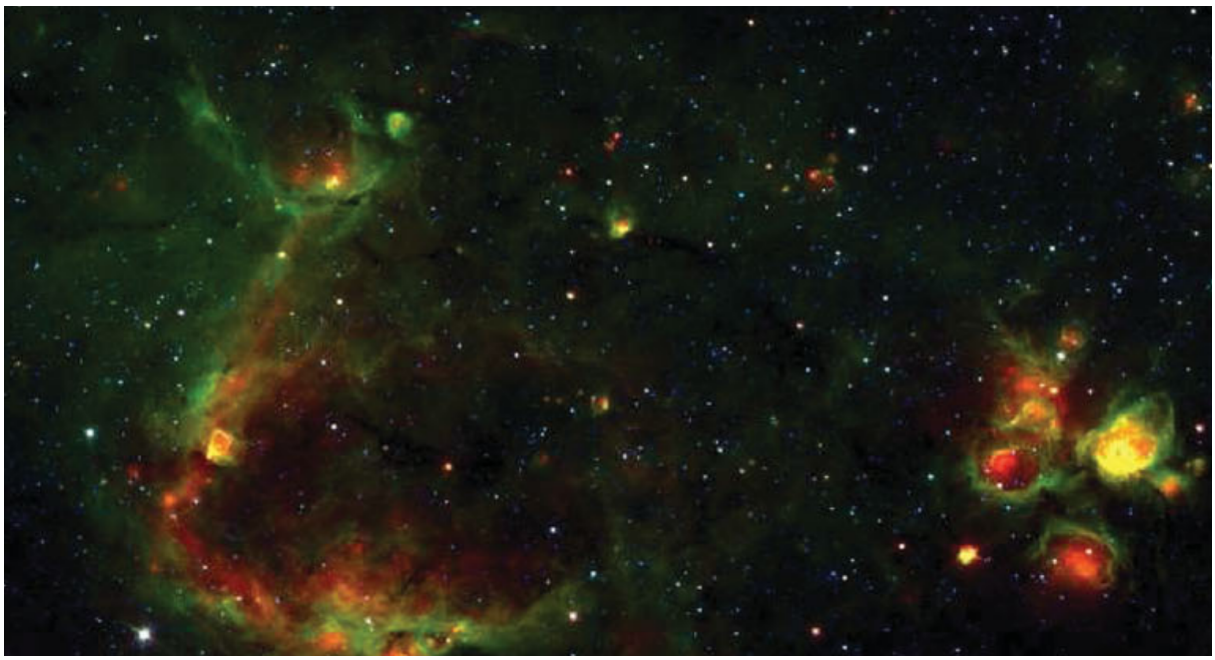

Figure 1.1: A region full of interstellar bubbles towards $l = 18.8°, b = -0.13°$. The image (GLIMPSE and MIPSGAL [5]) is a composition of three colors: red = 24 μm, green = 8.0 μm and blue = 4.5 μm. Hot inner parts of bubbles are visible at 24 μm, the envelope of a bubble at 8.0 μm.

The interstellar bubbles are distributed in the galactic disc and are strongly connected to star forming regions. Their progenitors are mostly massive (OB) stars. The evolution of bubbles is usually driven by an expansion of ionized hydrogen (HII) gas. The stellar winds are important only in a case of a very massive star ($\sim$ 100 $M_\odot$), or with highly clustered massive stars. During the growth of a bubble, two fronts are created: a shock front and an ionization front. As the bubble expands, cold ambient gas is gathered between these two fronts. This cold matter is then compressed and, due to different processes, can trigger star formation. The alternative is that the expansion of a bubble only relocates clumps, which are already forming stars or would be even without any interaction with a bubble. The problematics of triggered star formation (TSF) is broad, and therefore we dedicated a separate section to this problem.

1.1 Progenitors of bubbles

The most probable progenitors of interstellar bubbles seem to be massive stars, especially O and B spectral type stars. These stars are responsible for the existence of HII regions (regions of ionized hydrogen). The feedback of OB stars, together with the expansion of HII regions, appears to be the driving source of a bubble formation. Substantial verification of this assumption was demonstrated by Churchwell et al. [1], who found that the angular scale height of interstellar bubbles (0.63°, equivalent to a scale height of 44 pc at a distance of 4 kpc) are similar to those of HII regions (0.60°, found by Wood and Churchwell [6]). Contrary, the scale heights found for planetary nebulae ($\sim$ 500 pc) and for supernova remnants ($\sim$ 130 pc) by Becker et al. [7] significantly differ from the bubble scale height determined by Churchwell et al. [1]. Therefore, it seems that the interstellar bubbles, at least those with diameters of a few to tens of parsecs, are associated with HII regions and young OB stars.

Another supportive argument was given again by Churchwell et al. [1], who found that only three bubbles from their large sample of 322 bubbles are associated with supernova remnants and none of them with Wolf-Rayet stars or planetary nebulae. However, only 83 of their bubbles (25% of total) overlap known HII regions, of which only 30 contain cataloged near- or mid-IR stellar clusters. Therefore it seems to be reasonable that Churchwell et al. [1] came to a simple conclusion: "the majority of interstellar bubbles are produced by B4-B9 stars". According to their work, these stars have enough UV radiation capable to excite dust particles and strong winds to create a dust-free cavity around the progenitor star(s). Considering the data they used, the whole assumption seems to be plausible and understandable. But it is necessary to mention another important work by Deharveng et al. [3]. The team led by Lise Deharveng compared infrared bubbles with radio-continuum sources in the MAGPIS (the Multi-Array Galactic Plane Imaging Survey) and VGPS (the VLA Galactic Plane Survey). These surveys, contrary to the catalog by Paladini et al. [8] used in the work of Churchwell et al. [1], contain ultra compact and compact HII regions. After investigating how many interstellar bubbles overlap HII regions, they reached opposite results: at least 86% of 102 bubbles from their sample enclose HII regions (see a selection of examples in Fig. 1.2). Thus, the conclusion by Churchwell et al. [1] that only 25% of

bubbles surround HII regions is underestimated.

There is a wide range of suggestions trying to look for other progenitors of interstellar bubbles. One of these is post-asymptotic giant branch stars [9]. These stars could be surrounded by circumstellar dust shells emitting at mid-IR wavelengths [10], therefore a possible source of interstellar bubbles. However, Lagadec et al. [9] showed that a majority of dust shells of post-asymptotic giant branch candidates are unresolved. Therefore they should appear only as reddened point sources in the GLIMPSE (Galactic Legacy Infrared Midplane Survey Extraordinaire) images, which were the basis of Churchwell's and Deharveng's research. Considering this result, it seems that post-asymptotic giant branch stars are only minor, probably negligible sources of interstellar bubbles.

In the search of other possible progenitors of interstellar bubbles, one can be inspired by a broad variety of research dedicated to HI shells (or supershells). These shells are larger siblings of interstellar bubbles (more details about these structures are in the section 1.2.2). Their existence and evolution is associated mainly with massive star formation. During their development, fed by radiation and probably strong stellar winds, they are gradually enlarged by supernova events, as the stars from the progenitor cluster or association are evolving into their latest phases. This all can be described as feedback from OB stars, which was already mentioned as a probable source of interstellar bubbles. However, more exotic mechanisms can be involved in a creation of HI shells, such as high velocity cloud infalls [11], gamma-ray bursts [12], or inflation by radio jets [13]. So far, none of these mechanisms were found to be a source of any interstellar bubble, as they are forming structures with larger sizes than the typical ones of interstellar bubbles.

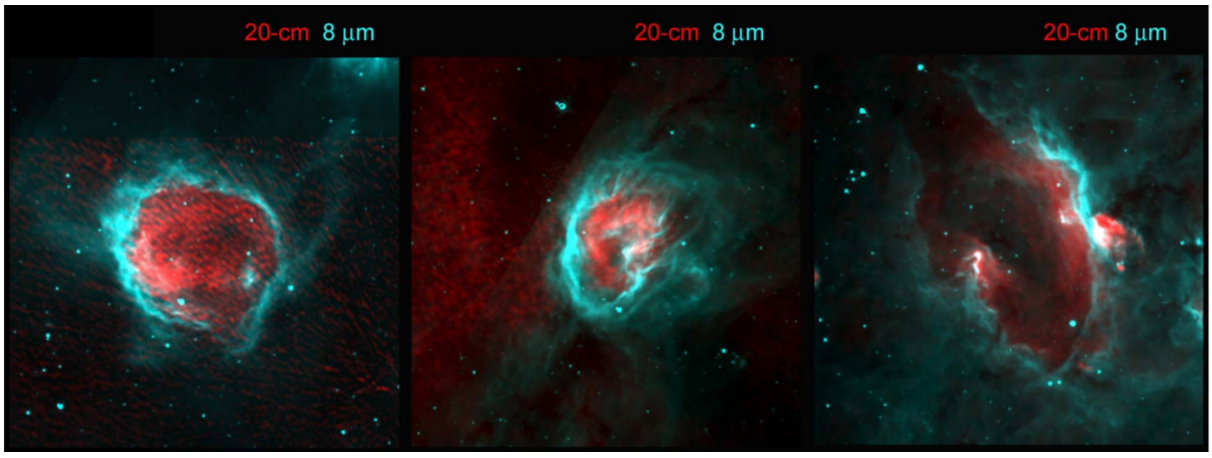

Figure 1.2: The picture from Deharveng et al. [3] shows examples of infrared bubbles (blue, Spitzer) whose interiors are filled by radio-continuum emission (red, MAGPIS), thus HII regions.

1.2 Evolution of a bubble

As it is described in the previous section, the formation and evolution of interstellar bubbles is dependent on the feedback of OB stars. During the first phase of a bubble evolution the central progenitor star is rapidly ionizing the neutral ambient medium. This phase is short, lasting only a few tens of years. The speed at which the radius of ionized region increases, is much greater than the speed of sound in the ionized gas (about 10 kms^{-1}). Thus the ionized gas cannot react as fast to the sudden change of pressure (the pressure increases with photoinization as described below) and stay in rest. Therefore, the bubble in this stadium is not expanding, as the densities of neutral and ionized gases are the same. The diameter of this pre-bubble (Strömgren sphere) is only a fraction of parsec. Considering O6V star, this first stage of a bubble would last only about 50 years and reach a diameter of about 0.15 pc [14].

As the massive hot star photoionizes the surrounding interstellar medium, it increases the gas temperature from about 10^2 K to 10^4 K. The number of gas particles is also increased by ionization process. As a result, the pressure of ionized gas becomes much greater and, after the short phase, the ionized region starts to expand supersonically. The shock front forgoes the ionization front and a neutral ambient material starts to accumulate between these two fronts, forming a layer of a denser material (Fig. 1.3). With time, this layer becomes massive. In 1 Myr a molecular gas shell of the order of 10^4 $M_\odot$ is formed around one massive star [15]. The photodissociation region (PDR) is formed outside the HII region, as the dissociation front moves faster than the

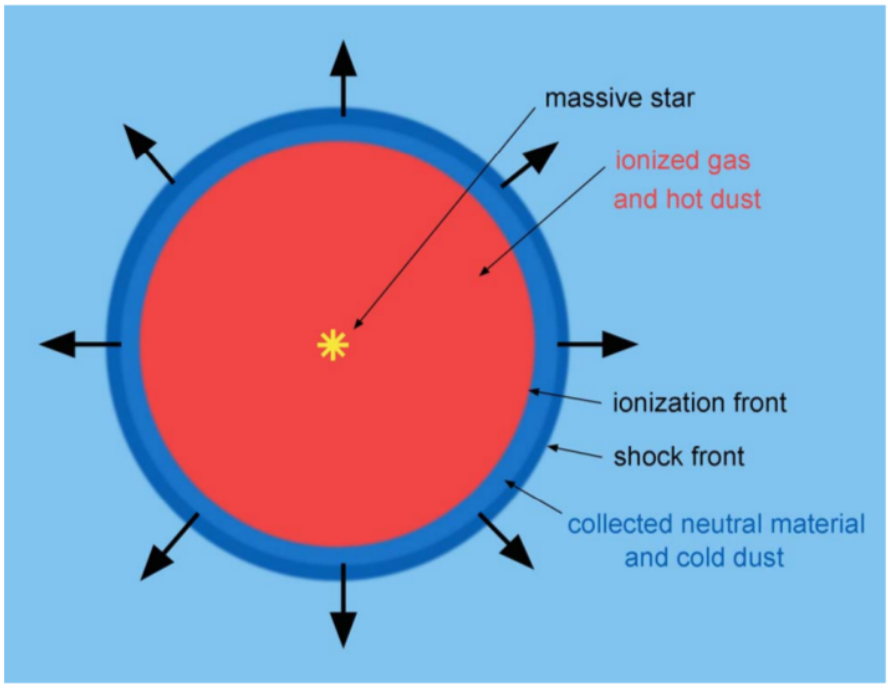

Figure 1.3: Model of a bubble filled with ionized gas (HII region) and expanding into a homogeneous medium. Between ionization and shock front neutral gas is collected [3].

ionization front. Spectroscopic observations of compact and evolved HII regions and the PDRs surrounding them show that the gas temperatures in the PDRs are between 100 K – 500 K and densities between 10^4 cm^{-3} and 10^6 cm^{-3} [16].

The expansion stops when the ionized gas and the surrounding neutral gas reach pressure equilibrium. Usually, the equilibrium is not reached before the death of the central exciting star. For example, a bubble evolving around O6V star stops its expansion after 80 Myr [14], which is much longer than the lifetime of this massive star, i.e. 8 Myr [17]. If the surrounding medium is very dense, the expansion can decrease much sooner.

There are also processes, which can distort the bubble's envelope during its evolution, and result in a change of bubble's shape. Among all, let us mention the main two processes: a fragmentation of an envelope and a triggered star formation. The star formation in the rims of a bubble can lead to the formation of new bubbles, which significantly changes the original shape of the older bubble. More about triggered star formation is written in a separate section 1.3.

Of course, hardly any bubble is evolving in a homogeneous medium. At first, the medium is turbulent [18, 19], which can result in formation of clumps. These clumps can be squeezed during the bubble's expansion and collected into the compressed layer [20]. Moreover, there is density stratification in the Galaxy, which can vary on both small and large scales. Then the shape of a bubble depends of a location of the progenitor star. If the star is located in a medium with a strong density gradient, or simply if the star is situated next to a molecular clump, the bubble will expand in the direction of a lower density medium. The shape of these bubbles then looks opened towards a particular direction. The inner ionized gas can leak farther from the source star and result in blowout (more details are described in Franco, Tenorio-Tagle, and Bodenheimer [21]). Fig. 1.4 shows significantly irregular shapes of bubbles.

Figure 1.4: The picture shows two examples of irregular bubbles: a tripolar bubble S109+S110+S111 (the left panel) and a flocculent bubble N100 (the right panel). GLIMPSE images taken from Churchwell et al. [1].

1.2.1 Wind-blown bubbles as pearls in a pond of ionized gas

From many simulations (such as Capriotti and Kozminski [22] or Freyer, Hensler, and Yorke [23]) it seems that the stellar winds are not significant in the expansion of HII regions (and therefore interstellar bubbles). The stellar winds from stars with masses smaller than 50 $M_{\odot}$ only slightly increase the initial pressure of an HII region. Only for a very massive star ($\sim$ 100 $M_{\odot}$), or highly clustered massive stars, or in higher density medium, the effect of stellar winds becomes significant [24].

However, although strong stellar winds from OB stars apparently do not influence the evolution of an interstellar bubble, they can drive a new type of a bubble – a wind-blown bubble (see an example in Fig. 1.5). It is a consequence of the interaction of stellar winds with the surrounding ionized medium. These stellar winds (the result of a stellar mass loss) expand and collide with the ionized gas inside an interstellar bubble. This creates a wind-blown bubble, with extreme inner temperatures of T$\sim 10^6$ K, who sits inside the larger interstellar bubble. The wind-blown bubbles also expand and can later reach diameters of the interstellar bubbles during their evolution [25], but do not significantly help with expansion of the interstellar bubble, as the pressure contribution from the stellar wind is low.

The evolution and dynamics of wind-blown bubbles are described in an early work of Weaver and Williams [26] and recently of van Marle, Meliani, and Marcowith [25].

Figure 1.5: Bubble nebula (NGC 7635) is a wind-blown bubble, lying inside a larger interstellar bubble, created by expansion of an HII region. The image is composed from narrow band image data of hydrogen and oxygen by Bernard Michaud.

Weaver and Williams [26] show that if the star moves supersonically through the HII region then the wind-blown bubble drives a bow shock in the direction of the motion.

1.2.2 Supershells as larger cousins of interstellar bubbles

Formation of a bubble is not limited to a single or a few OB stars. Bubbles can be created around much intensive star-forming regions and thus reach diameters of tens to hundreds parsecs [27], in some cases even kiloparsecs [30]. These structures are further called not "bubbles", but "shells" or "supershells". Shells and supershells are identified mainly in neutral hydrogen observations, therefore they are also known as HI shells (for more details about their observations see the section 2.4). They appear as

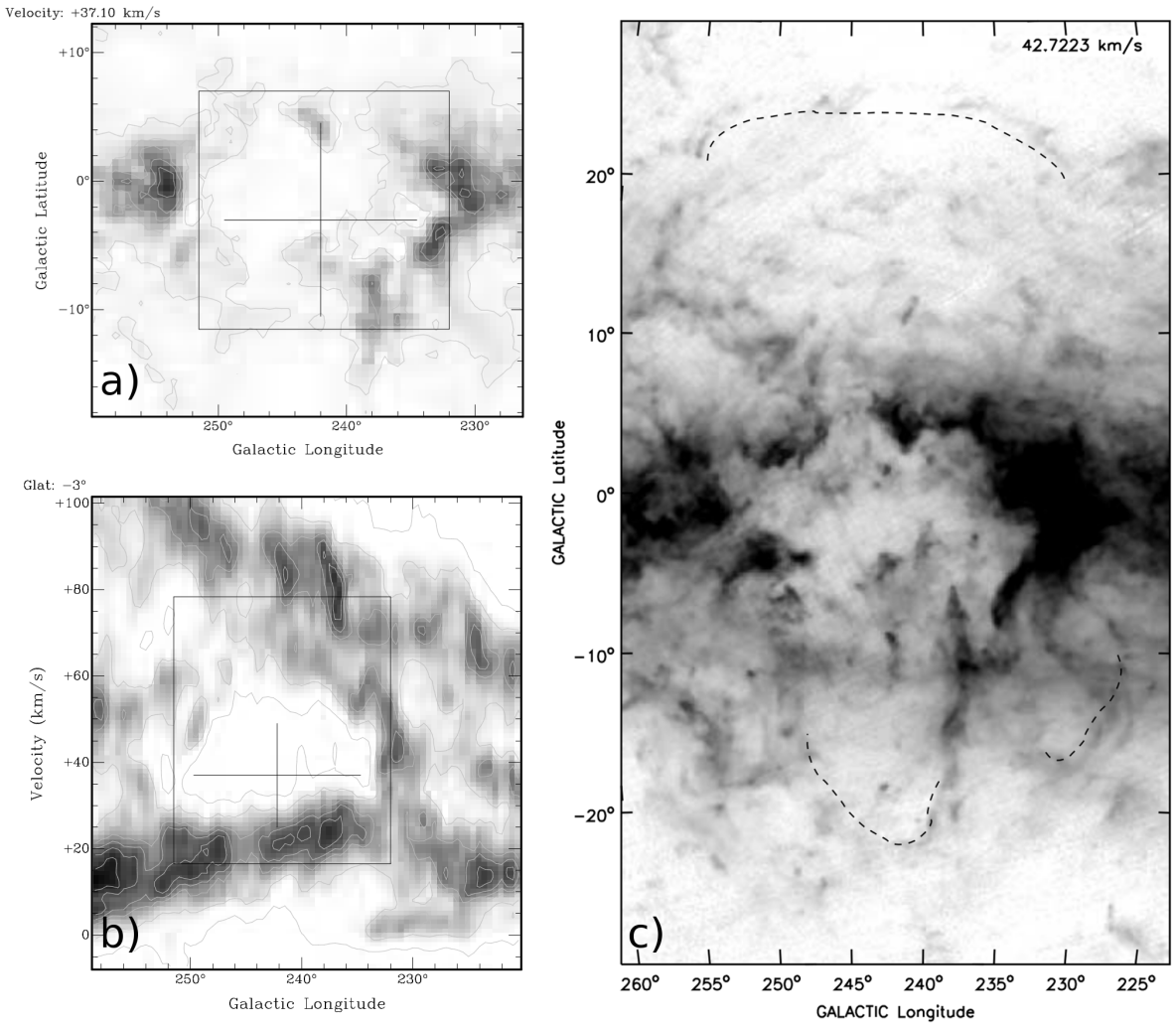

Figure 1.6: Left: HI shell GSH243.5-02.5+043.3 from the LAB survey. The black cross shows the original identification by Heiles [27] and the box shows an identification by Ehlerová and Palouš [28]. The upper panel (a) shows lb-map, the lower panel (b) is the lv-diagram. Right: HI velocity channel map of "chimney" GSH 242-03+37 from McClure-Griffiths et al. [29]. The caps of the chimney are also visible and marked with dotted lines.

holes, cavities or voids in HI distribution, with different forms of shapes, from spherical to elongated ones (an example is in the left panel of Fig. 1.6). The formation of supershells is driven by a collection of stellar feedback, including processes as stellar winds from OB stars, which evolve to the Wolf-Rayet phase after the main-sequence phase, and followed by more energetic supernova explosions. The energy input of shells are in a range of $10^{51} - 10^{53}$ ergs (which is about the same or hundred times more than for one single supernova event) and with their lifetimes of tens of millions years [27] they could, in some cases, serve as an star formation indicator long after the progenitor stars exploded as supernovae.

The combined effect of different types of stellar feedback from massive stars in an OB association is one possible source of energy and way of formation of such large objects. There are also other possibilities how to create a hole in neutral hydrogen distribution, such as an infall of high velocity cloud (HVC) to the galactic disc, as it was recently observed in Milky Way by Park et al. [31].

As the shell is evolving, it is going through a medium with a different density stratification. Some of the shells are prolonged in z-direction during their formation, this stage is also known as "a worm" [32]. In some cases, growing supershells can exceed the scale height of the HI disk, rapidly expand into lower-density medium and even break out. These structures, which are called "chimneys", then release the inner hot gas (if it is still there together with the progenitor stars) and let it flow into the galactic halo. This process may distribute hot gas and metals away from the galactic disk into the galactic halo [33]. Some of the chimneys even have their "caps" located nearby (see the right panel of Fig. 1.6). These are remnants of the HI walls of a shell, which later evolved into a chimney.

1.3 Distribution and morphologies of bubbles

There are two fundamental studies trying to analyze distribution and morphologies of bubbles: the first research is by Churchwell et al. [1, 2] and the second by Simpson et al. [5]. There is also the publication by Deharveng et al. [3], whose results are mentioned here as well. However, some results by Churchwell et al. [1] and Deharveng et al. [3] differ significantly (such as distance or type of progenitor stars, as mentioned in previous chapters). Therefore we find it useful to review both, and leave it up to the reader to draw his or her conclusions.

Churchwell et al. [1, 2] have cataloged nearly 600 bubbles in the Galactic plane by visually searching for ring-shaped, complete or partially broken structures in infrared images from GLIMPSE. The first results were published by Churchwell et al. [1] and include position, radius, thickness, eccentricity and other properties of 322 partially or fully enclosed bubbles at $|l| = 10^\circ - 65^\circ, |b| < 1^\circ$. These results were augmented with a sample of 269 mid-infrared bubbles observed and visually discovered in the inner Galactic plane, complementing the previous longitude range [2].

A new catalog by Simpson et al. [5] expands those by Churchwell et al. [1] and Churchwell et al. [2] by nearly an order of magnitude and therefore represents a far more complete sample. The new catalog includes 5106 infrared bubbles, which were

identified via visual inspection of the GLIMPSE and MIPSGAL survey images. This visual identification and classification was part of the citizen science Milky Way Project (MWP), where each bubble had been independently measured by at least five individuals, producing basic parameters of each identified structure.

Nearly all the bubbles from Churchwell et al. [1] and Churchwell et al. [2] are smaller than 10′, 88% of them are smaller than 4′. Only 2% of the bubbles were larger than 10′. Other large bubbles were not detected, probably due to their lower brightness and the strong background emission. A large fraction of the bubbles are highly eccentric, mostly having values between 0.6 and 0.8 [1]. This result differs from that by Simpson et al. [5], who found that the eccentricity peaks at ~ 0.35.

The linear sizes are linked to the distance of bubbles. As written below, the near and far kinematic distances are sometimes hard to be determined. However, from the statistics presented by Churchwell et al. [1, 2], we see that the interstellar bubbles can reach diameters from 0.1 to 66 pc and that the average diameter is ~ 11 pc. It would be useful to perform statistics with MWP bubbles, but unfortunately, so far, the distances were determined only for $\sim 4\%$ of the bubbles. Probably the results would lower the average size of interstellar bubbles, as MWP is more sensitive to angularly smaller bubbles.

As we mentioned in the previous section, hardly any bubble is evolving in an absolutely homogeneous medium. Therefore there exists a wide range of different shapes and sizes among the family of bubbles. Deharveng et al. [3] found that bubbles, which are nice and circular, keep smaller sizes (an average diameter of 3.6 pc), while open bubbles are much larger (with an average diameter of 21.4 pc). This sounds possible, as the smaller bubbles are probably evolving in more homogeneous regions than the larger ones. The larger bubbles thus seem to be influenced by the density stratification of the Galactic disk. Fig. 1.7 shows a few examples of different shapes of bubbles.

More than 50% of the bubbles from GLIMPSE and MWP catalogs show evidence for blowouts. The orientation of these blowouts has no significant tendency to be oriented away from the Galactic plane [5]. Therefore, the orientation of breaks or blowouts in

Figure 1.7: Different shapes of bubbles: 1) a closed bubble (N12) - the left panel, 2) an open bubble (N2) - the middle panel, 3) a bipolar bubble (N39) - the right panel. The red arrows on the right picture show the probable directions of expansion of the ionized gas (GLIMPSE and MIPSGAL images from Deharveng et al. [3]).

bubbles depends mostly on the local distribution of interstellar matter rather than on the large-scale gradient of the interstellar matter in the latitude direction [1]. The fact that the variation of local pressure and the density inhomogeneities in the maternal cloud are more important than the average gradient of ambient interstellar pressure in the latitude direction, could also explain why there is no significant dependence on latitude for any other bubble parameters, such as their size, thickness, eccentricity, or orientation of the major axis.

There is a wide discussion buzzing around the conclusion made by Beaumont and Williams [34]. They conclude that most of structures called interstellar bubbles are actually in a form of a ring, not in a form of a spherically symmetric bubble (Fig. 1.8). They support their conclusions by CO observations, where only a ring of gas with thickness of few parsecs is visible, but no approaching or receding walls of a bubble. Deharveng et al. [3] agree that some of the front or back walls of bubbles may be missing, but if conclusion by Beaumont and Williams [34] is correct, then there should be many more bipolar infrared bubbles observed, than there are. Kendrew et al. [35] recently have shown that there are dust clumps, visible at 870 μm, which are projected towards bubbles' interiors; and therefore they could be associated with the front or back walls of the bubbles. Obviously, studying molecular content of bubbles is important in answering many questions, from the ones which are arguing about the actual shape of bubbles, to those debating triggered star formation and molecularization of swept-up atomic gas.

Comparing the northern to the southern half of the Galactic plane, there is an asymmetry in the distribution of bubbles. The southern part is more plentiful in bubbles: 59% of the GLIMPSE bubbles are lying in the southern half [1]. This should not be so surprising, as the asymmetry is found likewise in the distribution of other objects, such as regions of massive star formation [36], clusters [37], or in the distribution of neutral hydrogen [38], and molecular clouds [39].

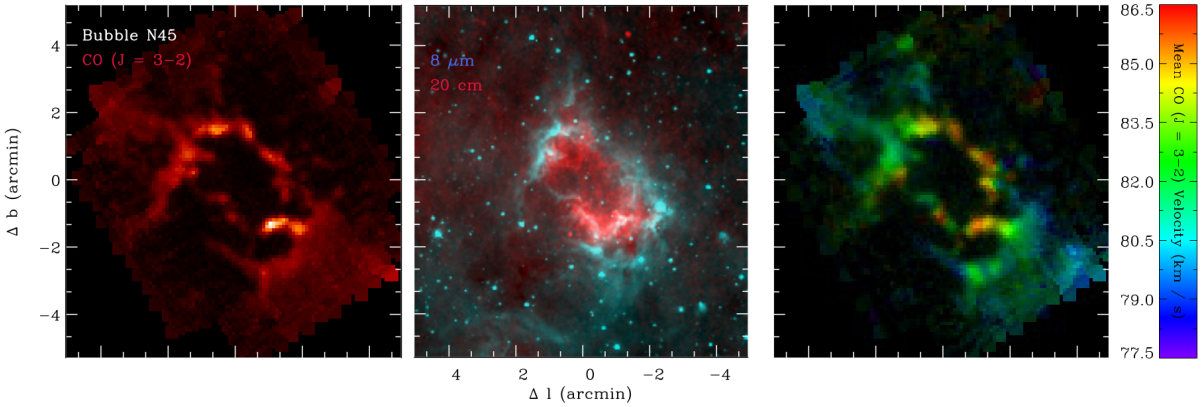

Figure 1.8: An examples of bubble N45 from data set of Beaumont and Williams [34]. The left panel shows the peak intensity of the CO emission. The center panel shows Spitzer 8 μm emission in blue, and VLA 20 cm emission in red. The right panel shows the first moment of the CO emission.

The longitude distribution was studied by Churchwell et al. [1], who found no significant tendency, except of that difference between the northern and the southern halves of the Galactic plane. However, systematical decrease from longitude 10° to 2° was found in Churchwell et al. [2]. This drop of the bubble number near the Galactic center can be physical, thus real, but it could also be caused by increasing diffuse background brightness, or opacity towards the Milky Way center. These results were refined by Simpson et al. [5], who found more details in longitude distribution of bubbles and showed that "the number of bubbles across the range of Galactic longitude appears to derive from the large-scale structure of the Milky Way." Simply said, in the locations of spiral arms, or regions with a massive star formation, a higher number of bubbles is found. This can be seen in Fig. 1.9, where apart from the longitude distribution of bubbles, several notable Galactic line-of-sight features are marked in red boxes.

Distances of the bubbles cannot be determined by analyzing infrared images. A majority of authors cross-match the positions of bubbles with catalogs of HII regions, young stellar clusters or observations of molecular clouds in particular emission lines. Churchwell et al. [1] claims that the more distant bubbles are not easily observable due to the foreground emission. Therefore, the near kinematic distances of bubbles are most likely to be the right ones, rather than the far kinematic distances. However, Deharveng et al. [3] have shown that 68% of bubbles in their sample are lying at the far kinematic distance, only 26% are lying at the near kinematic distance and the rest is located at the tangent point. Simpson et al. [5] found distances to 185 bubbles from their larger sample of bubbles, which is, comparing to the total number of bubbles identified in MWP, too small for any direct statistics.

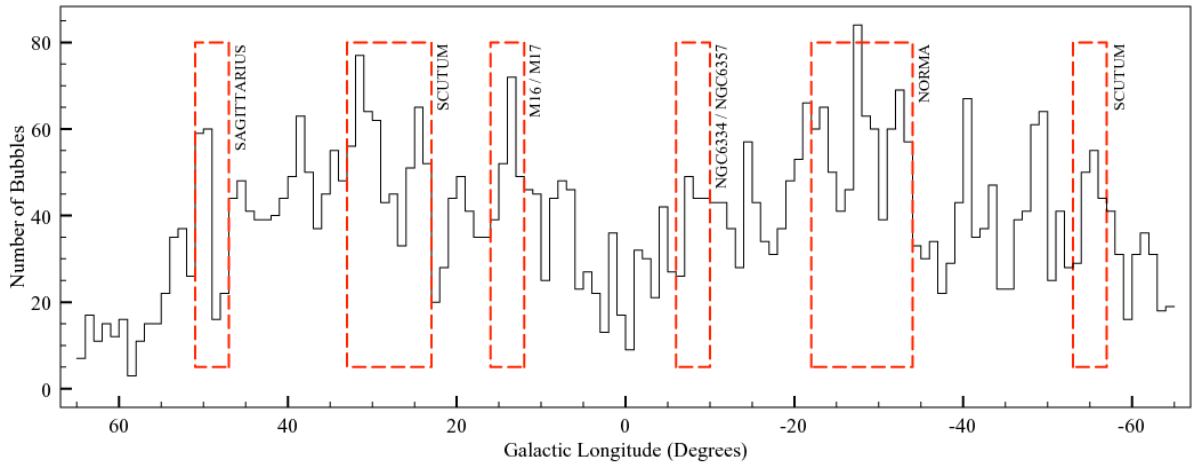

Figure 1.9: Longitude distribution of bubbles from Simpson et al. [5]. Notable features, mainly connected to the large-scale structure of the Milky Way, are marked in red boxes.

1.4 Triggered star formation in walls of expanding bubbles

Triggered star formation (TSF) is an extremely attractive concept for many scientists, so it is not surprising that many TSF publications, both observational and theoretical, constantly flood the ISM community. Unquestionably, the conditions in the walls of bubbles should be appropriate for possible star formation, as the collected gas between ionization and shock front has a low temperature and can reach high density. The collection of material during the expansion of a bubble is an important mechanism for gathering matter, which can result in star formation. However, right from the very beginning, we have to warn that some carefulness should be kept in mind. There are studies, such as by Walch et al. [40], which show that a shell-like configuration of massive clumps does not have to be a consequence of an accumulation of gas, but simply relocation of pre-existing clumps.

Nevertheless, there are numerous observational studies reporting evidence of ongoing star formation near massive young stars and clusters, or on the periphery of large bubbles (for a few examples see Fig. 1.10). For example, Rahman and Murray [41] found that giant HII regions were arranged on the rims of large mid-IR bubble structures. Deharveng et al. [3] found that at least 16% of bubbles from their sample contain compact or ultra compact HII region in the direction of their PDRs, suggesting triggered star formation. Simpson et al. [5] also found conforming evidence of star formation in the vicinity of bubbles: "29% of the Milky Way Project catalog bubbles lie on the rim of a larger bubble, or have smaller bubbles located within them."

This leads to the question; what are the mechanisms capable to trigger star formation in the walls of bubbles? There are three main processes, which can occur in many variations and can take place simultaneously:

1) a compression of pre-existing clouds

2) an accumulation of gas into a shell

3) a collision of clouds

Pre-existing clouds can be generally compressed by various processes such as a transit of spiral density waves [42], galaxy-galaxy tidal interactions [43], protostellar outflows [44], supernova explosions [45], or massive stellar winds [46]. These last two mentioned stellar feedback processes are part of those which contribute to formation or evolution of a bubble. Thus this process plays and important role when considering triggered star formation in the walls of bubbles. Also pressure of the ionized gas from the inside of a bubble can compress pre-existing condensations [47, 48]. This mechanism, when the shock front passes through pre-existing clouds and compresses them, is called "radiation-driven implosion".

The second mentioned mechanism of an accumulation of gas is actually a process, which forms a shell due to the expansion of the ionized inner parts of a bubble. A thick shell of collected gas can fragment and gravitationally collapse, which can lead to the formation of stars of all masses [11, 49]. Low-mass stars can form from small-scale

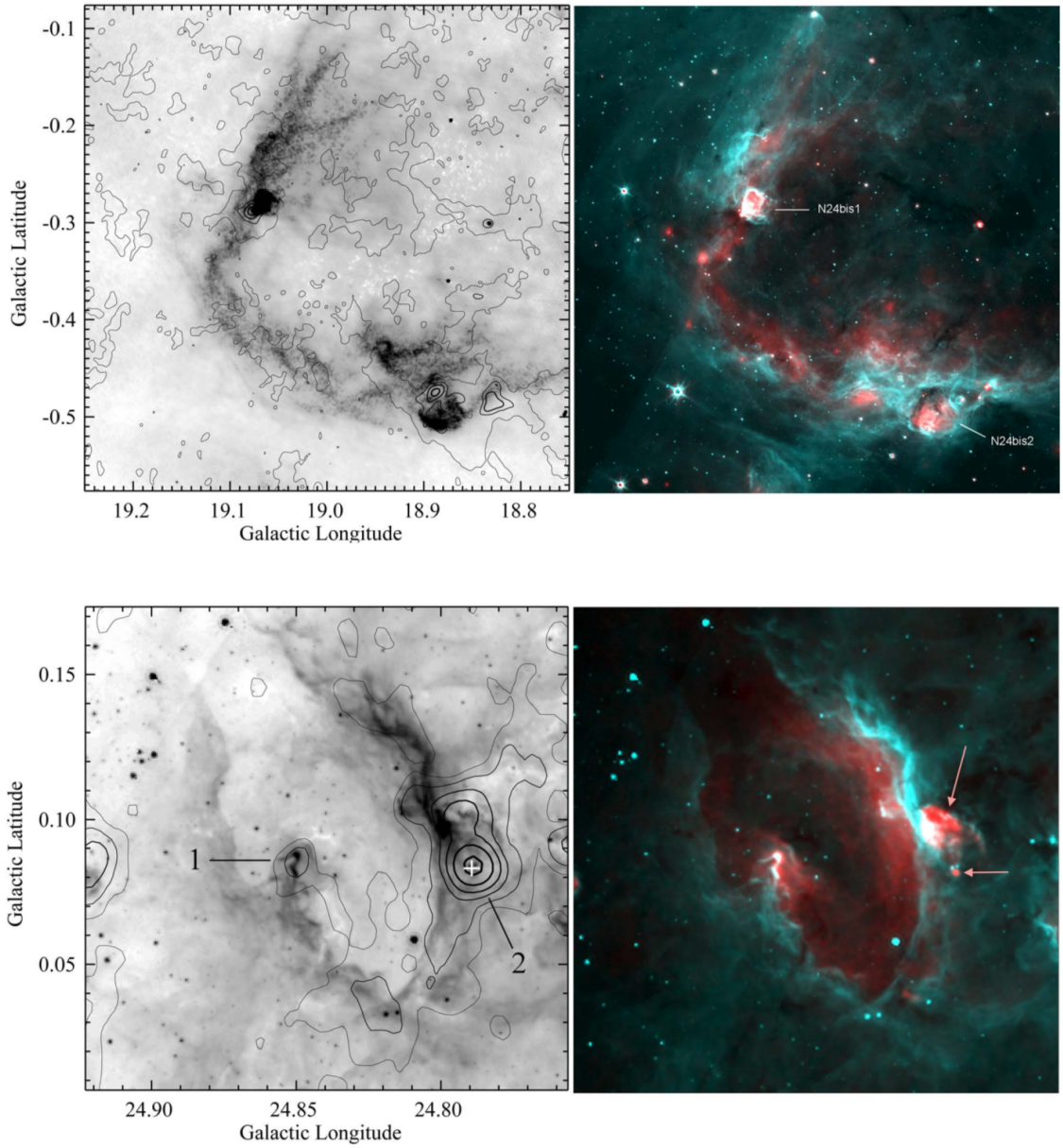

Figure 1.10: Two examples of bubbles with ongoing star formation in their rims: bubble N24 with its second-generation compact HII regions, N24bis1 and N24bis2, the top row, and bubble N36 with compact and ultra compact HII regions in its rims (marked with arrows), the bottom row [3]. The figure shows 870 μm contours superimposed on the MAGPIS radio-continuum image at 20-cm (left panel) and color composite image, with red for the Spitzer-MIPSGAL emission at 24 μm and turquoise for the Spitzer-GLIMPSE emission at 8.0 μm (right panel).

gravitational instabilities (such as Jeans instabilities), massive-star formation can occur due to large-scale gravitational instabilities and formation of massive fragments. This process is called 'collect & collapse' [50]. The third mechanism, the collision of clouds [51], occurs in the astrophysics of bubbles in its variety: shell collisions [52].

Establishing whether the star formation was actively triggered by the 'collect & col-

lapse' process or by the 'radiation-driven implosion' process is challenging. However, according to Deharveng and Zavagno [53], there are some features which can differ between these two mechanisms. For example, the radiation driven compression of pre-existing condensation causes a difference between the velocity of dense condensations and the velocity of the ionization front. Furthermore, the dense condensations can protrude inside the ionized region, on the contrary to condensations created by the 'collect & collapse' process, which are sitting in the walls of bubbles and do not protrude inside the ionized region.

However, there is one more complication in determining how the stars were triggered. According to Dale, Haworth, and Bressert [54], the main question is not "How the stars were triggered?", but "Which of them were actually triggered?" Recently, Dale, Haworth, and Bressert [54] have shown in their hydrodynamical simulations that it is not easy to identify triggered from spontaneously-formed stars. They found that: "none of the correlations with shells, ionization fronts or pillar structures were of substantial help in winnowing out the triggered objects. Neither were relative ages or geometrical distribution of stars." In their simulations it is clearly seen that the triggered and spontaneously formed stars are spatially mixed, which makes them difficult to differentiate (see Fig. 1.11). They have shown that there is an approximately 40% chance to be wrong when declaring which of the stars at the edges of bubbles were triggered. Positions of spontaneously-formed stars are mixed with those who were triggered by the expansion of a bubble and the reason why the spontaneously formed stars are also sitting at the edges is simply that they have been redistributed during the

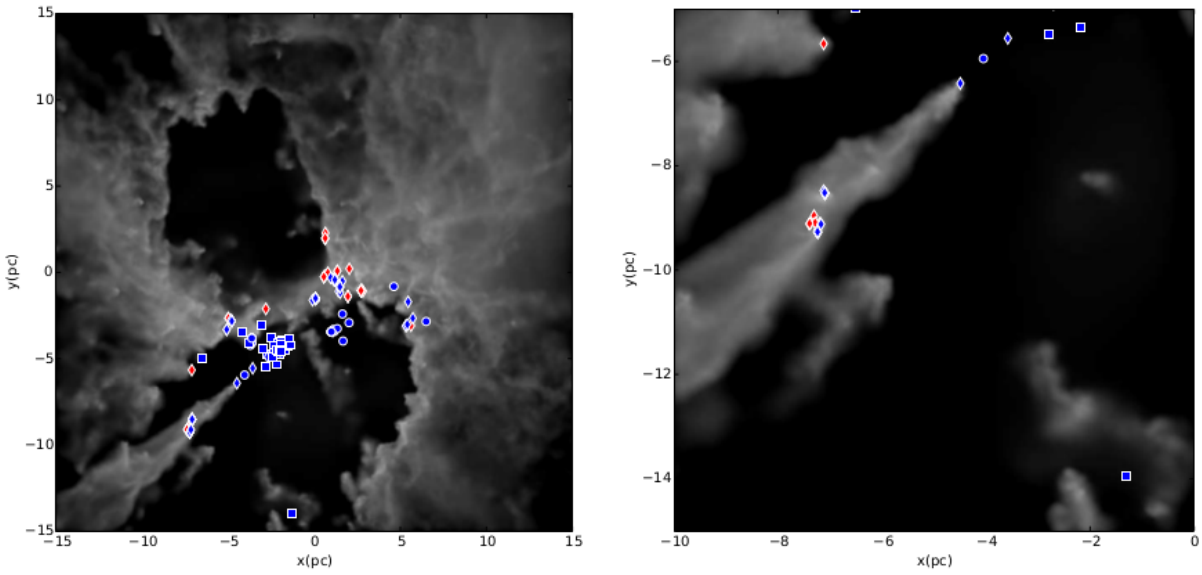

Figure 1.11: The picture shows a cloud from simulations by Dale, Haworth, and Bressert [54] in the left panel and a zoom on the prominent pillar in the right panel. Red sinks are triggered particles, blue sinks are spontaneously–formed particles, which would form even without an expanding bubble in their vicinity. Symbol shapes denote sink ages: diamonds (age $<$ 1 Myr); circles (1 Myr $<$ age $<$ 2 Myr); squares (2 Myr $<$ age).

expansion of a bubble by the strong pressure of ionized medium.

The feedback does not have to be just positive, in a sense of triggering star formation, but can also be negative, in terms of the rates at which gas is converted to stars. Smoothed particle hydrodynamics simulations show both positive (triggering) and negative (halting of star formation) effects by massive stellar feedback [55–59]. The UV and FUV radiation from massive stars ionize and heat up the parental molecular cloud, thus nearby star formation can be quenched [60, 61]. Additionally, stellar feedback may remove gas from the protostars' surroundings, thus halting collapse or accretion [55, 62–64]. According to Murray and Rahman [65] and Lee, Murray, and Rahman [66], the expansion of bubbles can be an important driver of turbulence in the interstellar medium. Turbulence resulting from ionizing radiation and winds can be a crucial regulator of a molecular cloud star formation's efficiency [67, 68] and can prevent further protostellar collapse over larger distances [69].

The triggering of a star formation by expanding bubbles is still an unanswered question. Some investigations show evidence of triggered star formation at the edges of bubbles and large shells, some simulations and theoretical studies urge that the effect of stellar feedback is mainly negative and quenching star formation. Other publications point out that the star forming regions were just relocated due to the expansion of a bubble and would form even without stellar feedback.

Chapter 2

Multiwavelength observations of ISM and bubbles

There are five phases of ISM: molecular medium, cold neutral medium, warm neutral medium, warm ionized medium, and hot ionized medium. The gas content of interstellar bubbles can be found in different phases and therefore is observable at various wavelengths. The molecular content can be traced, e.g., in millimeter wavelengths of CO molecule, cold neutral medium is observed in HI absorption, warm neutral medium is detectable in HI emission line, and warm ionized gas is visible at radio-continuum or in optical emission lines, such as H_α. Dust particles are, when heated, emitting at infrared wavelengths, cold dust particles are emitting at submillimeter wavelengths.

Interstellar bubbles are most visible in infrared observations, in both thermal and non-thermal radiation. They were defined in 8 μm observations, therefore we focus on this particular wavelength in the next sections. Hot inner parts of bubbles are visible at 24 μm and in radio-continuum. Cold and dense content of bubbles is mostly traced by emission of CO molecules and dust condensations in 870 μm. Although HI shells, structures similar to interstellar bubbles, are well studied in HI data, the warm neutral content of interstellar bubbles, however, is not well analyzed.

This chapter introduces the reader to the phases of ISM and to the multiwavelength observations of bubbles, from radio to optical wavelengths.

2.1 Phases of interstellar medium

Interstellar medium accounts for $10 - 15\%$ of the total mass of the Galactic disk. ISM is mainly distributed in the Galactic plane and concentrates along the spiral arms. Approximately half the interstellar mass exists in a form of discrete clouds, which fill up only $\sim 1\%$ of the interstellar volume. The interstellar medium in the Galaxy shows a broad range of densities and temperatures. These characteristics define diverse types of phases of ISM. There are five different phases, which define the components of ISM [70, 71]:

Molecular Medium (MM)

Cold Neutral Medium (CNM)

Warm Neutral Medium (WNM)

Warm Ionized Medium (WIM)

Hot Ionized Medium (HIM)

Molecular Medium

The molecular medium is formed by cold and dense molecular clouds. The temperature of MM is typically about 20 K and the volume density is about 10^3 cm^{-3} (however, the density range is wider, as discussed below). Despite the fact that molecular gas contains as much mass as the atomic hydrogen, only a small fraction of the interstellar volume is occupied with MM. Therefore, this phase has the lowest volume filling factor of all phases, $f \sim 1\%$. The discrete molecular gas clouds are organized hierarchically from small dense cores to giant complexes. Small dense cores have sizes of a few tens of a parsec, with masses about $0.3 - 10^3$ M$_\odot$ and a mean hydrogen number density of about $10^4 - 10^6$ cm^{-3}. The giant complexes reach sizes of a few tens of parsecs, masses up to 10^6 M$_\odot$ and relatively lower densities, compared to small dense cores, $\sim 100 - 1000$ cm^{-3} [76]. The best tools for studying the molecular medium are CO line observations (an example of molecular gas survey is in Fig. 2.1, the top panel).

Cold Neutral Medium

High-resolution maps of the 21-cm emission show that the cold neutral medium, which itself is traced in absorption of HI line, is distributed in sheets or in a form of rather dense filaments or clouds. It is primarily associated with molecular gas. The typical hydrogen density in cold HI clouds is about $20 - 50$ cm^{-3} and the temperature is between 50 and 100 K. This phase is also occupying a minor fraction of the ISM, about $2 - 4\%$, thus slightly larger volume than MM fills up. To trace CNM, a background of either continuum sources or HI emission is needed. In the latter case, HI self-absorption (HISA) can occur. HI emission from warm background gas can be absorbed by colder foreground gas and result in observations of CNM clouds.

Warm Neutral Medium

Warm neutral medium is observed in HI emission line (see an example of HI survey in Fig. 2.1, the second panel from the top). This phase of warm neutral medium, with temperatures of about 6000 – 10000 K, is more diffuse and sometimes is referred as intercloud medium. It is also, usually, radially most extended component of the ISM in galaxy disks. The volume filling factor is about 30%. Compared to CNM, the density is some two orders of magnitude smaller, ~ 0.3 cm^{-3}.

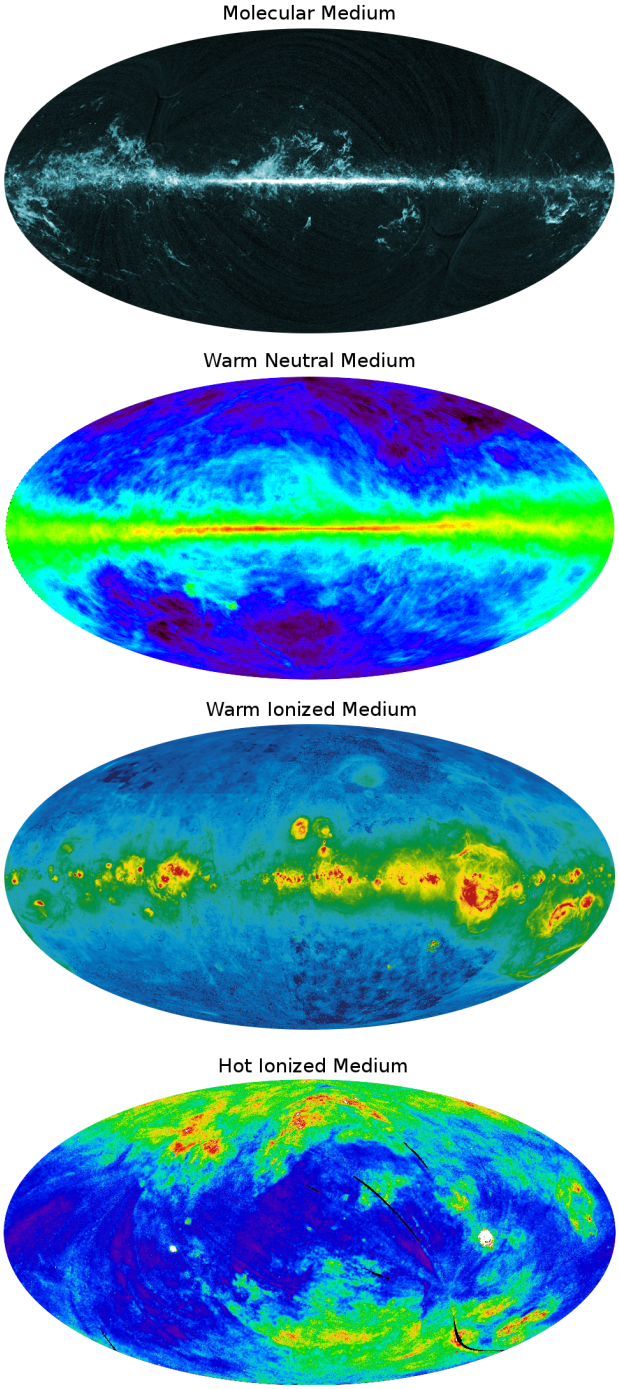

Figure 2.1: All-sky distribution of ISM phases in the Milky Way: **Molecular Medium**: CO map, Planck [72], **Warm Neutral Medium**: neutral hydrogen map, LAB survey [73], **Warm Ionized Medium**: H_α map, the Wisconsin H-Alpha Mapper (WHAM), the Virginia Tech Spectral-Line Survey (VTSS), and the Southern H-Alpha Sky Survey Atlas (SHASSA) [74], **Hot Ionized Medium**: soft X-ray map of diffuse background at 1/4 keV, the ROSAT all-sky survey [75]. Each frame is centered on the Galactic center, the Galactic equator bisects each frame in the center horizontally.

Warm Ionized Medium

Warm ionized medium was mainly associated with HII regions, but, as it was shown already in 1938 by Struve and Elvey [77] and confirmed by observations by Reynolds [78], WIM is presented also outside well-defined HII regions. The temperature of this ISM phase is about 8000 K. This is the equilibrium temperature, set by a balance between radiative cooling and photoelectric heating [79]. The typical densities are about $0.2 - 0.5$ cm^{-3} and the volume filling factor about 15%. Warm ionized gas emits a wide range of optical emission lines, between which H_α and [NII] are the most easily detectable in the Galaxy (a full sky H_α map is shown in Fig. 2.1, the third panel from the top). The WIM also emits thermal radio-continuum emission (free-free radiation) as well as recombination lines.

Hot Ionized Medium

Hot ionized medium is produced by supernova explosions and it spreads into the Galactic halo. It is also known as "coronal gas" and it occupies a large fraction of the ISM volume, the volume filling factor is about 50%. Its density is about 10^{-3} cm^{-3} and temperature about 10^6 K. HIM emits both in a Bremsstrahlung continuum and in the 0.1 to 2 keV energy band, due to complex line radiation of electronic transitions in highly excited atoms (an example of an X-ray survey is shown in Fig. 2.1, the bottom panel).

2.2 Infrared observations

Interstellar dust is a crucial element of the Galaxy. Most of the visible and UV radiation in galaxies from stars is obscured by interstellar dust, which is then heated and excited. The absorbed energy is reradiated in the infrared part of the spectrum, as the dust is heated to temperature of about few tens to hundreds Kelvins. The interstellar dust emits in continuum, but also produces strong emission bands. This is a consequence of different emission mechanisms and various sizes of dust grains, as described below.

Emission in infrared continuum is caused by thermal radiation. The thermal radiation is observed in the 1 – 60 μm range, small grains are heated, and in wavelengths larger than 100 μm, larger grains are heated. The thermal radiation from the intermediate wavelengths, from 60 to 100 μm, is also observed and it is produced by both types of grains.

Interstellar dust also produces strong infrared emission bands at 3.3, 6.2, 7.7, 8.6, and 11.3 μm. This emission corresponds to the carbon–hydrogen or carbon–carbon bond vibrations in aromatic (benzene-ring) molecules, such as polycyclic aromatic hydrocarbon (PAH) particles.

2.2.1 Emission at 8.0 μm

The interstellar bubbles are best observable in the infrared emission. As the pioneering publications of Churchwell et al. [1, 2] have shown, the infrared images taken by Spitzer telescope in the 8 μm band are literally bubbling with loops, arcs and bubbles. The 8 μm band is dominated by the 7.7 and 8.6 μm features, which are often attributed to PAH particles [80]. These PAH particles are accumulated in a thin shell during the evolution of a bubble, and as they are excited by the progenitor star(s), they emit in the 8 μm band and make bubbles visible in infrared images.

Most of the bubbles show an absence of 8 μm emission in their central regions (although there is some small contribution due to the front and back walls of the bubble). The 8.0 μm emission usually stops where the 20-cm radio-continuum emission begins (Fig. 2.2, the right panel), which essentially implies that PAHs are easily destroyed in the hard radiation field [3]. Conforming examples are shown in the studies by Cesarsky et al. [81] and Povich et al. [82], who studied M17 HII region with ISOCAM and Spitzer-IRS, respectively. They obtained spectra in two directions: towards the HII region itself and towards the adjacent molecular cloud. The spectra obtained towards the cloud displays the 7.7 μm and 8.6 μm PAH features, contrary to the spectra of the HII region, where these features are almost absent.

The lack of 8.0 μm emission of PAH particles inside HII regions does not depend on a mass of exciting star(s). A wide range of bubbles show the presence of PAHs in their walls, together with the absence of PAHs in their inner parts: from bubbles which are excited by cluster of early-type O stars (e.g., RCW 79), through those which are excited by two late-type O stars (e.g., RCW 82), to bubbles with faint or no radio-continuum

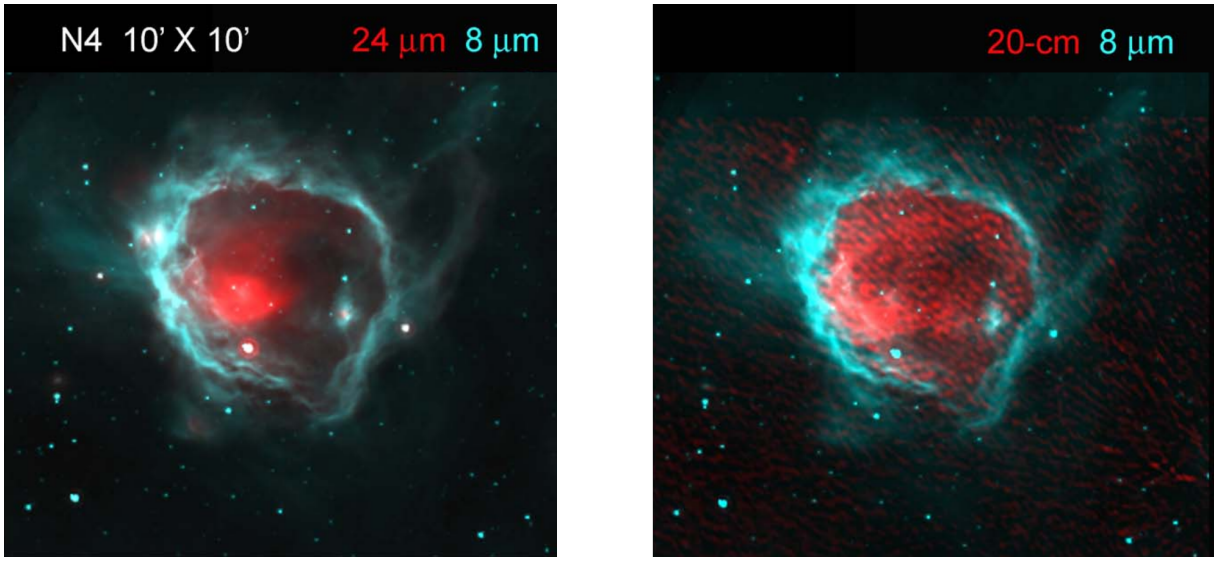

Figure 2.2: The figure shows a difference between distribution of 24 μm emission (the left panel) and radio-continuum emission (the right panel) in a case of the bubble N4 [3]. 24 μm is in general more central peaked than radio-continuum emission. Spitzer-GLIMPSE 8.0 μm emission is in turquoise, red color shows Spitzer-MIPSGAL 24 μm emission (the left panel) and MAGPIS 20-cm emission (the right panel).

emission inside their walls (e.g., N8) [3].

The absence of PAHs inside interstellar bubbles implies that they are destroyed by the hard radiation field. However, the mechanism remains unclear. Large PAHs (more than 50 carbon atoms) may survive in radiation field in HII regions [83]. Small PAHs are, on the other hand, destroyed by photodissociation processes, which include energies less than 13.6 eV. Therefore, the PAH destruction does not stop exactly at the ionization front but continues further to PDR. This is probably the reason why it is possible to observe bubbles with faint or no HII inside [3] - the destruction of PAHs does not require photons more energetic than necessary to ionize hydrogen.

2.2.2 Emission at 24 μm

The emission at 24 μm is a continuum emission and it is attributed to dust [84]. The origin and form of these dust particles is still not clear. It seems that it originates in either very small grains with sizes between 1 to 10 nm, which are probably carbon dominated, or in big dust grains with sizes of a few tens to a few hundreds of nm, which are mainly formed by coated silicates. The emission from very small grains dominates the continuum emission near 24 μm rather than emission from PAHs [85]. Very small grains have to be out of thermal equilibrium, reaching temperature of hundreds of K, to be able to radiate in the near- and mid-IR. However, amorphous silicate grains, with a small contribution from amorphous carbon grains, also emit at similar wavelengths [86]. These big grains have to be in thermal equilibrium and heated to temperatures between 85 K and 145 K for amorphous silicate grains, and between 110 K and 200 K for amorphous carbon grains.

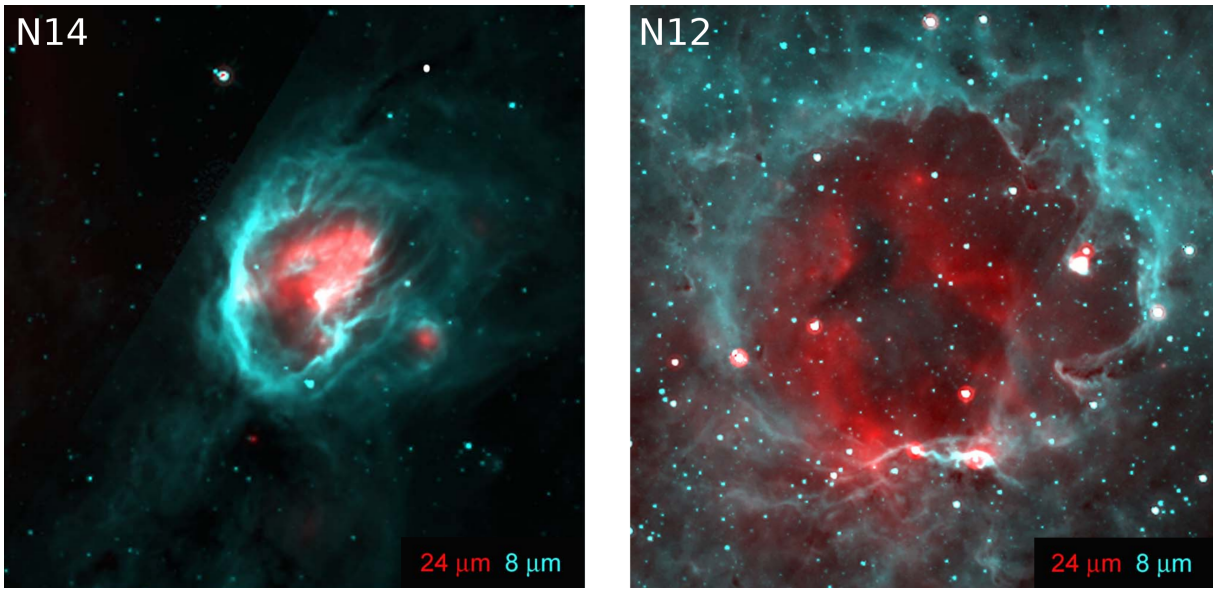

Figure 2.3: Two different distributions of 24 μm emission [3]: 1) bright emission towards the center of a bubbles (e.g. the bubble N14 in the left panel), 2) faint emission located in a shell along the inner rim of a bubble (e.g. the bubble N12 in the right panel). Spitzer-GLIMPSE 8.0 μm emission is in turquoise, Spitzer-MIPSGAL 24 μm emission is in red.

The 24 μm emission is present inside the vast majority (about 98%) of interstellar bubbles [3]; therefore, hot dust grains must be present in the ionized gas. The emission is observed in two different locations and forms: 1) bright emission in the direction of the center of the bubbles, or 2) faint emission located in a shell along the inner boundary of the 8 μm bubbles (Fig. 2.3). In most cases, 24 μm emission comes from the first location, a center of the bubble. Comparing to radio-continuum emission, this emission is much more central peaked (Fig. 2.2), presumably in the direction of the central star or cluster responsible for producing the bubble.

The latter location of 24 μm emission, along the inner boundary of bubbles, can be caused by stellar winds emitted by the central exciting stars, or alternatively by radiation pressure of these stars. A beautiful example is the bubble N49, which shows a central hole not only in 24 μm emission, but also in radio-continuum emission (Fig. 2.4). In the direction of the hole an O5V star is lying, a possible progenitor of the bubble [87]. The 24 μm emission can be therefore useful, helping to locate and identify central exciting stars of bubbles.

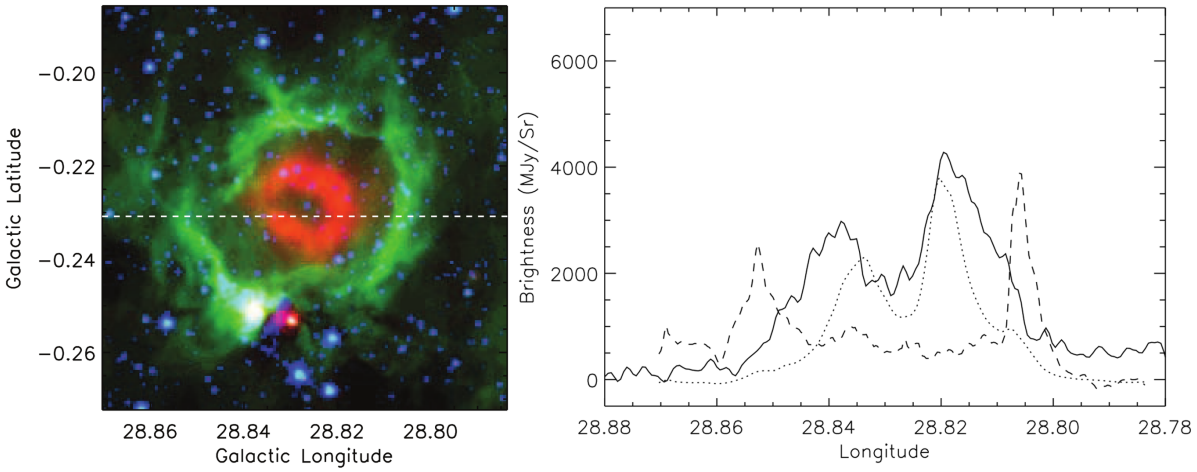

Figure 2.4: The left panel shows an infrared image of N49 (24 μm in red, 8 μm in green and 4.5 μm in blue). The white dashed line indicates the location of the cross-cut in the right panel. The right panel shows a slice at $b = -0.23°$, the solid line shows radio-continuum emission (magnified 10^6 times), the dotted line shows 24 μm emission, and dashed line shows 8 μm emission (magnified 5 times). A hole in both 24 μm and radio-continuum emission is clearly visible in both panels [87].

2.3 Submillimeter observations

Because the bubble is expanding, a cold neutral material is compressed between an ionization and a shock front. This includes mainly atomic and molecular hydrogen, however, also cold dust particles are accumulated in the walls of bubbles. This cold dust thermally emits in continuum at 870 μm. This dust continuum emission is not only a tracer of cold material, but also most reliable tracer of the earliest phases of star

formation since it directly probes the dense interstellar material from which the stars form [88].

Nearly half of interstellar bubbles (about 40%) are surrounded by a collected material emitting at 870 μm [3]. Numerous dust condensations are distributed in the direction of PDR of bubbles, the 870 μm is overlapping the emission in 8 μm. As the dust condensations are following rims of bubbles, they are sometimes referred as "necklaces" of condensations (Fig. 2.5). It seems that these dust condensations can be a consequence of the collect process. However, it is also possible that they pre-existed in the vicinity of a forming bubble and have been compressed by a passing shock front at a later time. Nevertheless, these two different origins are hardly distinguishable in observations.

Another confirmation of the connection between dust condensations and interstellar bubbles was recently shown by Kendrew et al. [35]. 48% of cold dust clumps in or near the inner Galactic plane are located in the vicinity of infrared bubbles (the study worked with a large sample of bubbles from the Milky Way Project [5]). The smaller bubbles tend to have stronger overdensities of 870 μm clumps towards their interiors than larger bubbles.

2.4 Neutral hydrogen observations

Cold neutral medium is observed in absorption and warm neutral medium in emission of 21-cm line of atomic hydrogen. This emission/absorption is caused by spin flip of electrons in neutral hydrogen atoms. The ground state of atomic hydrogen is split into two hyperfine levels, depending on if electrons have spin parallel (angular momentum F=1) or antiparallel to the proton (angular momentum F=0, true ground state). The energy difference between these two levels is 6×10^{-6} eV, thus the pho-

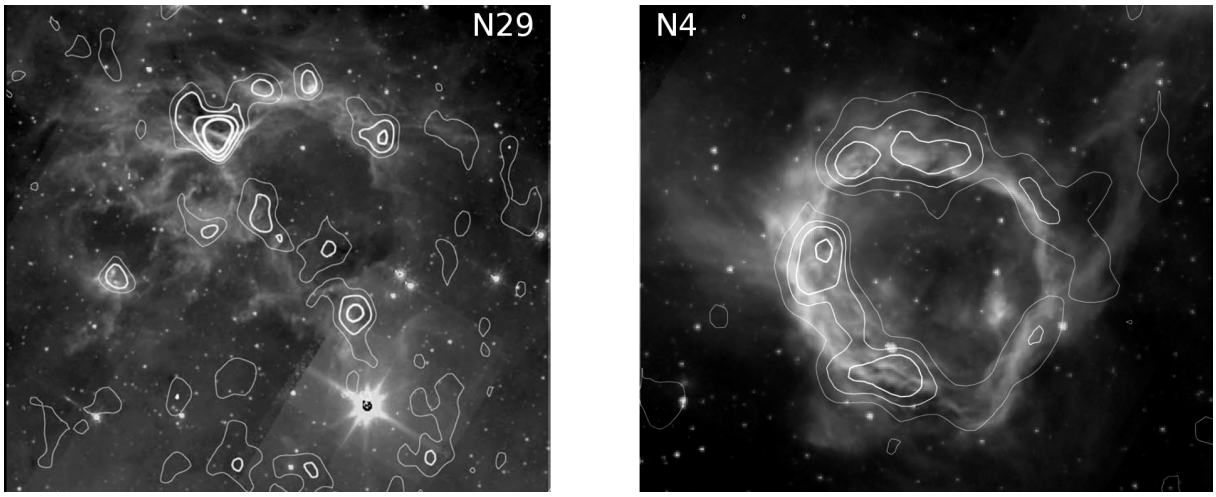

Figure 2.5: Contours of the 870 μm emission (ATLASGAL) superimposed on the 8.0 μm images (Spitzer) of bubbles N29 (the left panel) and N4 (the right panel). The condensations are following the rims of the bubbles, forming "necklaces" of dust condensations [3].

tons with frequency 1420.4 MHz (corresponding to wavelength of 21.105 cm) mediate transitions between the two levels.

Interstellar bubbles are rarely studied in HI. However, larger, but similar structures, HI shells or supershells (see the section 1.2.2), are widely studied. They were discovered by Heiles [27], who found many arc-like or shell-like structures, and discovered that many of them change their size with velocity in the way that an expanding shell would do. These structures were named "shells" and the largest ones (with energy input more than 3×10^{52} erg) "supershells". At least one of the walls of the structure, either the approaching or the receding one, was observed, which supported the idea of an HI shell as an expanding object. However, some of the shells are not expanding anymore. Those with no measurable expansion velocity do not change their shape through velocity channels, while expanding bubbles do. They appear small, then reach their maximum size and get back small again, while going through velocity channels.

The discovery of HI shells was followed by a large number of studies and catalogs of HI shells, such as by McClure-Griffiths et al. [89], Ehlerová and Palouš [91], Suad et al. [92], or Ehlerová and Palouš [28]. McClure-Griffiths et al. [89] have discovered 19 new HI shells in the Southern Galactic Plane Survey (six examples are in Fig. 2.6). The radii of these bubbles is between 40 and 700 pc, expansion velocities between 6 and 20 kms^{-1}, and expansion energies between 10^{51} and 10^{53} ergs, which corresponds to the results by Heiles [27]. Two interesting features about space distribution of HI shells was found: 1) many shells are located between spiral arms of the Galaxy, 2) large and

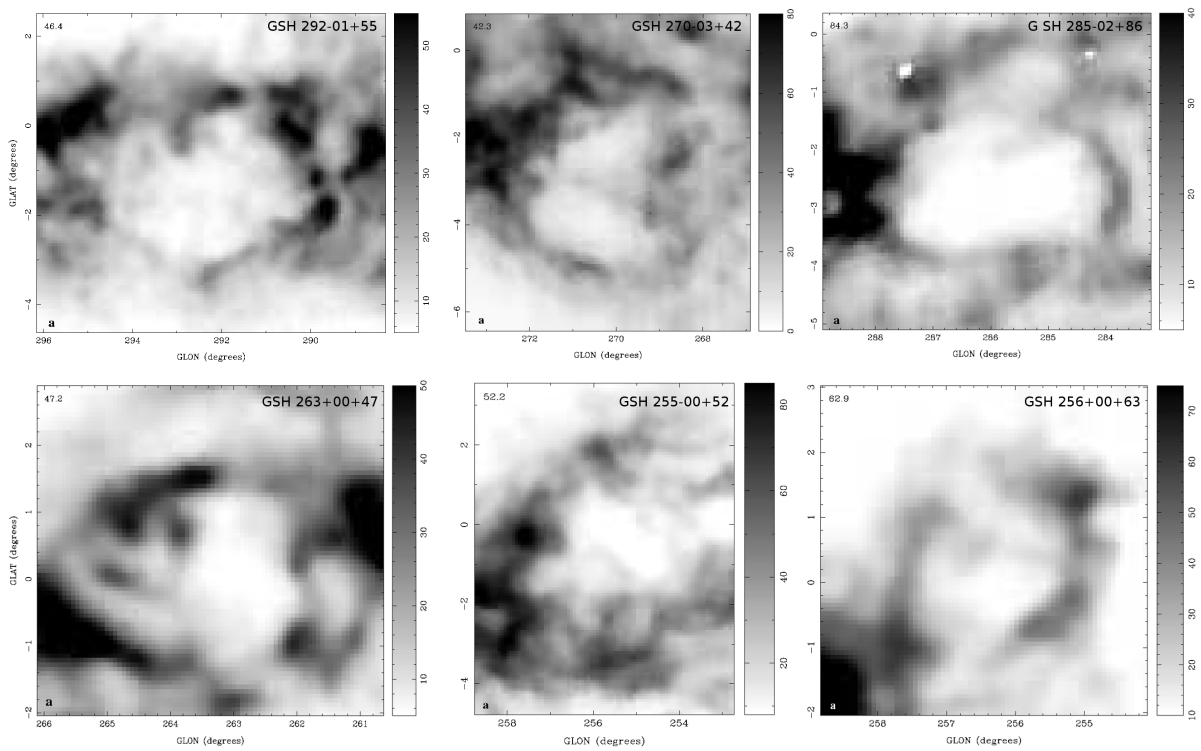

Figure 2.6: A sample of HI shells identified by [89] in The Southern Galactic Plane Survey [90].

energetic shells are located at large galactocentric radii (this spatial distribution was also observed in external galaxies [93]). The asymmetry in distribution of shells between the second and third Galactic quadrants was discovered by Ehlerová and Palouš [28], who published one of the most extended catalog of HI shells. They identified 333 shells in the Leiden/Argentine/Bonn (LAB) Survey [94] and found that shells at distances greater than 19 kpc are observed only in the second quadrant, contrary to the third quadrant, where no shells at these or further galactocentric distances were observed. The asymmetry was confirmed by Suad et al. [92], who found also an imbalance in the amount of shells between the second and the third quadrant: 347 shells from the total number of 566 bubbles (about 61%) in their catalog are located in the second quadrant, while the rest was found in the third one.

HI shells have non circular shapes, their δl is higher than δb. According to Heiles [27], the possibility that the shape is elongated due to the galactic rotation is unlikely, because a significant elongation occurs typically after 50 Myr or longer, which is longer than, or at least comparable to, the expected lifetimes of large HI shells. However, computational models investigating the role played by differential galactic rotation on shells, e.g. Tenorio-Tagle and Palouš [98] and Palouš, Franco, and Tenorio-Tagle [99], found that there is a deformation of shells caused by galactic differential rotation. The shear stretches the shape of a shell into an elliptical one – the major axis becomes larger and rotates, with respect to the direction of the galactic center.

Shells are detected not only in the Milky Way, but also in other galaxies, including the closest spiral ones such as M31 [100, 101] and M33 [102], and in dwarf galaxies such as Holmberg II [103]. Shells in other galaxies are quite common [104], their sizes can reach up to 2 kpc and their age ranges from units to tens Myr. The biggest shells

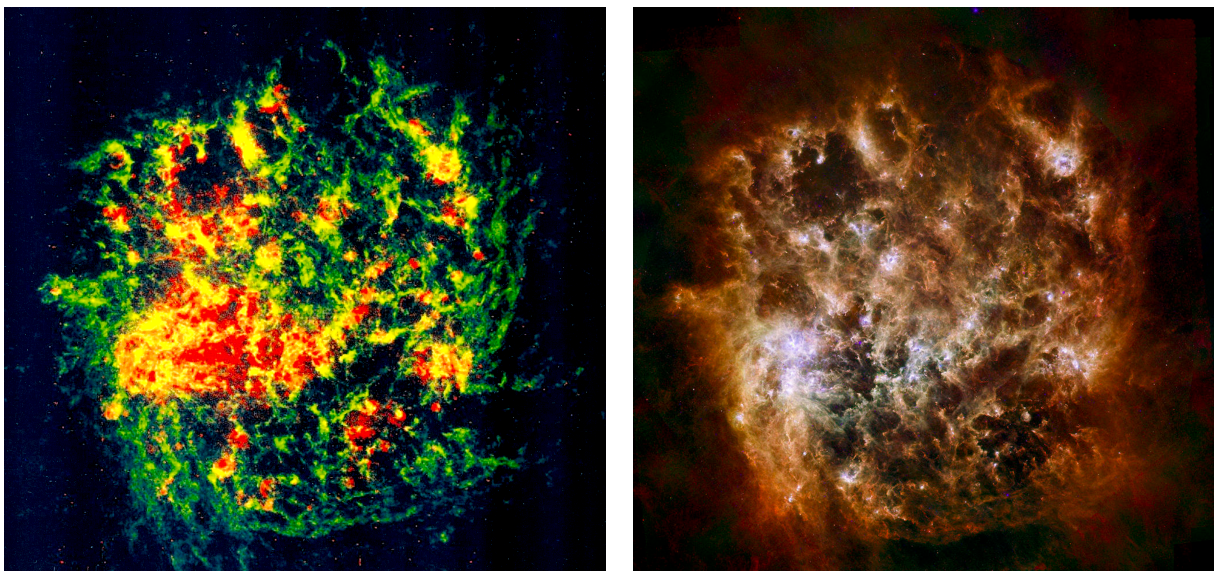

Figure 2.7: Large Magellanic Cloud in HI surface brightness map (green) with overlaid H_α image (red) from Kim et al. [95] is shown in the left panel. The right panel shows LMC in observations by Herschel [96] in green and red, while blue color represents observations from Spitzer [97]. Just from a first glance it is obvious that the ISM of LMC is crisscrossed with shells of various sizes.

with diameters of few kpc were found by Kamphuis, Sancisi, and van der Hulst [105], Chaboyer and Vader [106], and Irwin and Seaquist [107]. A shell with 1.5 kpc in diameter and expansion velocity of 50 kms^{-1} was detected in M101, two times larger shell is located in NGC 1620 and other kpc-size shells, some of them opened to the halo, were identified in NGC 3079. These named galaxies are all spiral galaxies. Nevertheless, one of the best places to study HI shells are Large and Small Magellanic Clouds (LMC and SMC). There are about 23 supershells (whose extent is much larger than the HI scale height), and about 103 shells (with radii less than the scale height of the HI gas) in LMC [95]. Figure 2.7 shows the bubbling interstellar medium of Large Magellanic Cloud in HI and infrared observations.

2.5 CO molecule observations

There are about 150 known interstellar molecules, from which the H_2 and CO molecules are the two most abundant. The hydrogen molecule is not straightly observable at radio wavelengths. It has no permanent electric dipole moment and has a small moment of inertia. However, the second most abundant molecule, carbon monoxide (CO), is observable at radio wavelengths. There are three main transitions used for observation and surveys of CO emission: $^{12}CO(1-0)$ at 115.27 GHz, $^{12}CO(2-1)$ at 230.54 GHz and $^{13}CO(1-0)$ at 110.20 GHz. Emission in CO lines comes mainly from spiral arms, where it is connected to giant molecular clouds (GMC). Thus CO surveys are the primary way of identifying giant molecular clouds and their properties. CO emission is much clumpier and shows a different global structure than the wide HI distribution. There is an interesting morphological feature between atomic (HI) and molecular (CO) distribution in molecular clouds: molecular clouds seen in CO emission are usually surrounded by HI envelopes. There are two possibilities of the origin of HI envelope: 1) H_2 molecules of the outer parts of molecular clouds are photodissociated and therefore we see envelope of the atomic hydrogen or, 2) the envelope is a remnant after the formation of GMC from HI.

Some HI shells and supershells are associated with CO emission, which is, unlike HI emission, clumpy. According to Ehlerová and Palouš [108] and Dawson et al. [109], it seems that formation of HI shells can lead to increase of molecular mass, thus amount of CO clumps. Interstellar bubbles are also observed in CO emission lines and as it was mentioned in the case of molecular content of HI shells, there is a speculation that some of CO clumps associated with interstellar bubbles are triggered by the expansion of bubbles as well [110].

One of the latest observational studies has shown that relatively young bubbles do not have any Massive Young Stellar Objects (MYSOs) associated with their molecular content. However, their older and larger counterparts do, and the associated CO clumps are full of MYSOs [110]. This would imply a possible evolutionary sequence, from young MYSOs–missing bubbles to older MYSOs–associated bubbles.

Chapter 3

Searching for an atomic and a molecular component of infrared bubbles

3.1 Methods

3.1.1 Data

For our study, we use the following surveys:

The Spitzer-GLIMPSE survey

We used *Spitzer*-GLIMPSE survey for infrared images of the region. GLIMPSE (Galactic Legacy Infrared Mid-Plane Survey Extraordinaire, Benjamin et al. [97]) is extended from $l = 295^\circ$ to 65° and from $b = -1^\circ$ to $b = 1^\circ$, while using Spitzer Infared Array Camera (IRAC) with a pixel resolution of $1.2''$. The filter used for the GLIMPSE survey is centered at 8.0 μm.

The VGPS survey

Both observations of the region in HI line and in radio-continuum we took from VGPS (VLA Galactic Plane Survey, Stil et al. [111]). The survey is extended from $l = 18^\circ$ to 67°, while b differs from -2.6° to 2.6°. VGPS contains interferometric observations by the VLA at 21 cm with the angular resolution of $1'$. The channel width for HI is 1.2 kms^{-1}.

The GRS survey

To find the molecular component we used the ^{13}CO (J = 1-0) GRS survey (Galactic Ring Survey, Jackson et al. [112]). This survey extends from $l = 17^\circ$ to 56° and from $b = -1^\circ$ to 1°. The GRS survey is based on observations by SEQUOIA multi-pixel array receiver on the FCRAO 14 m telescope with the angular resolution of $46'$. The channel width is 0.2 kms^{-1}.

Cold gas tracers

To trace cold and dense gas we used "BGPS clumps" from Dunham et al. [113] and APEX Telescope Large Area Survey of the Galaxy (ATLASGAL survey) from Schuller et al. [88]. BGPS clumps are sources detected at 1.1 mm in the Bolocam Galactic Plane Survey and in the NH_3 line by the Green Bank Telescope. We used them to trace distribution of cold phase of interstellar medium in the research of Colliding interstellar bubbles (Chapter 4). ATLASGAL survey is covering $\sim$ 95 squared degrees of the Galactic plane at 870 μm, revealing $\sim$ 6000 compact sources brighter than 0.25 Jy. We used ATLASGAL maps to complement maps of CO emission.

3.1.2 Searching for HI and CO structures

To find HI envelopes associated with studied IR bubbles, we constructed a ring-shaped masks using the ds9 tool – Smithsonian Astrophysical Observatory [114]. The masks were made according to the appearance and the shape of infrared bubbles (see the example in Fig. 3.1). We applied these manually constructed masks to the HI and later to the CO data cubes in the directions of studied bubbles. The aim was to find regions with significant difference in the brightness temperature of the ring (the HI/CO matter lying in the mask) and brightness temperatures outside and inside the ring.

The bubbles are supposed to show a high contrast between brightness temperature of the ring and inside of it, as the inner parts of bubbles are ionized and therefore causing a drop in brightness temperature. The outside temperature is supposed to be lower than the temperature of the mask, but with not such a high contrast as in the case of inside temperature.

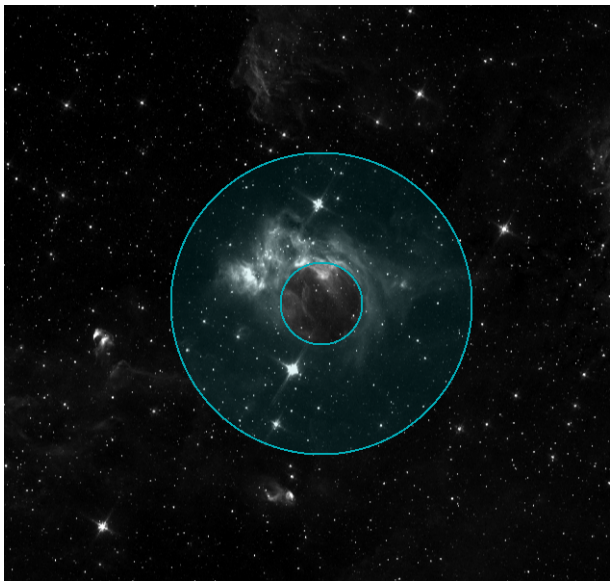

Figure 3.1: The example of a mask for the bubble N115.

To test how results change according to the size of a mask, we applied wider and narrower masks as well (each about 25% larger or smaller than the original masks).

The results did not change significantly, therefore we used the original masks based on the look of bubbles in the IR data. Then we controlled the regions visually and compared results from HI and CO data cubes.

3.1.3 Determination of bubble's properties

While knowing the radial velocity V_r of a bubble lying at the Galactic longitude l and using the flat rotational curve $V(R) = V(0)$, the two solutions of far and near kinematic distance can be determined by:

$$d = R_0 \cos(l) \pm \sqrt{R^2 - R_0^2 \sin(l)^2}, \tag{3.1}$$

where R_0 is the Galactocentric radius of the Sun and R is the Galactocentric radius of the bubble:

$$R = R_0 \sin(l) \frac{V(0)}{V_r + V_0 \sin(l)}, \tag{3.2}$$

where V_0 is the orbital velocity of the Sun around the Galactic center.

We derived separately masses of the atomic and molecular component by using formulas from Rohlfs and Wilson [115]. The neutral hydrogen column density N_{HI} is derived by:

$$N_{\mathrm{HI}} = 1.8 \times 10^{18} \int T_{\mathrm{b}} \mathrm{d}v, \tag{3.3}$$

where T_{b} is the observed brightness temperature of the HI line. The ^{13}CO column density $N_{^{13}\mathrm{CO}}$ is derived by:

$$N_{^{13}\mathrm{CO}} = 2.6 \times 10^{14} \frac{T_{\mathrm{ex}}}{1 - \mathrm{e}^{-T_0/T_{\mathrm{ex}}}} \int \tau(v) \mathrm{d}v, \tag{3.4}$$

where T_{ex} is the excitation temperature, which we assume to be 30 K. T_0 for the frequency 110 GHz of the ^{13}CO ($J = 1 - 0$) is 5.3 K. τ is the optical depth derived by the formula:

$$\tau = -\ln \left[1 - \frac{T_{\mathrm{b}}}{T_0} \left[(\mathrm{e}^{T_0/T_{\mathrm{ex}}} - 1)^{-1} - (\mathrm{e}^{T_0/T_{\mathrm{CMB}}} - 1)^{-1} \right]^{-1} \right], \tag{3.5}$$

where T_{b} is observed brightness temperature of the CO line and T_{CMB} is the cosmic microwave background temperature of 2.7 K. The GRS survey provides maps of the antenna temperature T_{A}, which has to be converted to the brightness temperature by: $T_{\mathrm{b}} = T_{\mathrm{A}}/\eta_{\mathrm{MB}}$, where $\eta_{\mathrm{MB}} = 0.48$.

We derived the original (primordial) density of the medium into which the bubble expanded, using separately both mass results (from HI and CO data). We assume that the whole matter lying in the bubble's walls was inside its volume before the expansion. This leads us to two separate results, one is the density computed only from the mass of neutral hydrogen (n_{HI}) and second density result is computed from the mass of the molecular component ($n_{\mathrm{H_2}}$). We assume that the value of the primordial

density is lying between those limits, probably more to the higher value. To compute the age of the bubble we used formulas from Chevalier [116]: the age of the bubble created around an OB star is

$$t_{\mathrm{OB}} = \frac{3}{5}\frac{r}{v_{\mathrm{ex}}} \tag{3.6}$$

and the age of the bubble created by supernova event is

$$t_{\mathrm{SN}} = \frac{2}{5}\frac{r}{v_{\mathrm{ex}}}, \tag{3.7}$$

where r is the radius of the bubble and v_{ex} is the expansion velocity of the shell. While knowing the primordial density of the parental cloud n [cm^{-3}], radius of the shell and the expansion velocity, we derived the total energy input E_{tot} using Chevalier's formula [116]:

$$\frac{E_{\mathrm{tot}}}{\mathrm{erg}} = 5.3 \times 10^{43} \left(\frac{n}{\mathrm{cm}^{-3}}\right)^{1.12} \left(\frac{r}{\mathrm{pc}}\right)^{3.12} \left(\frac{v_{\mathrm{exp}}}{\mathrm{kms}^{-1}}\right)^{1.40}. \tag{3.8}$$

From the total energy input and the age of the bubble we estimated the luminosity of the progenitor star, in the case where the shell was created by an HII region expansion. E_{tot} also shows if the bubble could have been created by a supernova explosion. Comparing the results with the grids of stellar models by Schaller et al. [17] we estimated the spectral type of the progenitor star. The energies and luminosities are only order estimations, helping us to decide if the structures were created by a supernova event or by expansion of an HII region.

3.1.4 Describing morphology of bubbles

To describe the shape of HI envelopes we use following distribution:

a partial bubble - filling up $0-25\%$ of the assumed shape of the bubble

a loop - filling up $25-50\%$ of the assumed shape of the bubble

an open bubble - filling up $50-75\%$ of the assumed shape of the bubble

a closed bubble - filling up $75-100\%$ of the assumed shape of the bubble

To be able to determine these characteristics, we manually constructed a counterpart to each HI envelope (as seen in the example in the left panel of Fig. 3.3) and compute the filling factor of HI emission f_{HI}. The shapes of HI envelopes are schematically shown in the left panel in Fig. 3.2. The same figure, but the right panel, shows cardinal directions, which we use for the description of bubbles, locations of features and so forth. We computed also the ratio $\frac{T_{\mathrm{b(i)}}}{T_{\mathrm{b(o)}}}$ between the brightness temperature in the HI walls ($T_{\mathrm{b(i)}}$) and outside it ($T_{\mathrm{b(o)}}$). For each bubble we measured it in 5 different locations and then determine the average ratio.

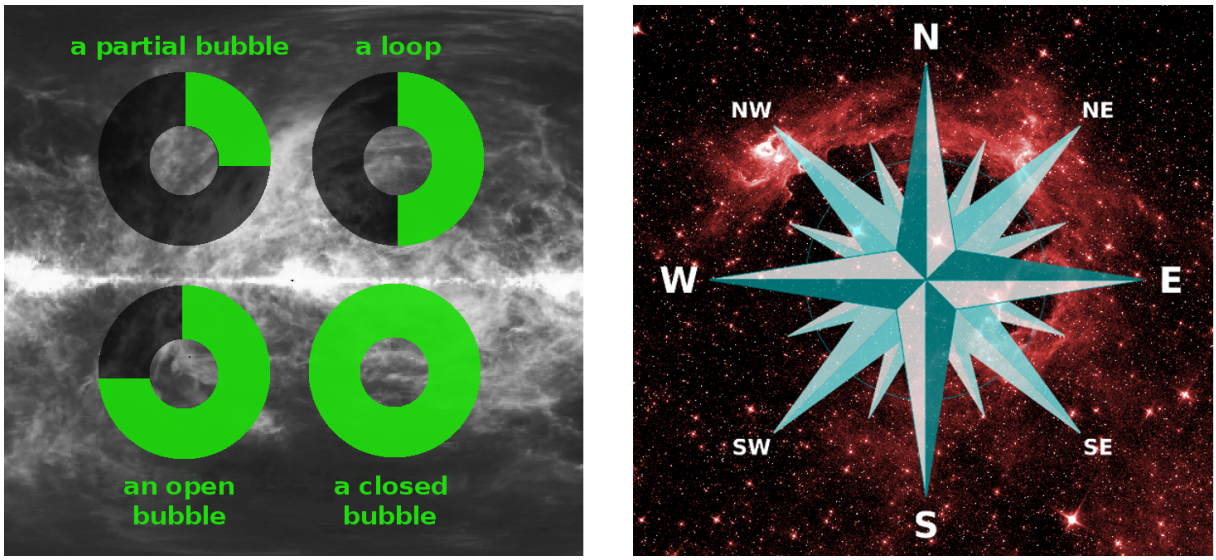

Figure 3.2: The panel on the left shows the classification we use for describing shapes of HI envelopes. The panel on the right shows cardinal directions, which we use for describing the directions and locations of observed features.

To describe the morphology of bubbles seen in CO emission, we computed several parameters, according to the overlapped areas of an HI envelope and CO emission, compared to the full area of CO emission (see the example in the right panel of Fig. 3.3): the relative area of CO emission lying outside the HI envelope (S_{COout}), the relative area of CO emission lying in the (walls of) HI envelope (S_{COinw}), the relative area of CO emission lying inside the HI envelope (S_{COins}), and the relative area of CO emission complementing the HI envelope (S_{COcom}). Then we computed the filling factors of CO emission according to their overlap with particular areas: the filling factor of CO emission lying inside the HI envelope compared to the inner area of the HI envelope (f_{HIins}), the filling factor of CO emission lying in the walls of the HI envelope compared to the full area of the HI envelope (f_{HIinw}), and the filling factor of CO emission complementing the HI envelope compared to the manually constructed counterpart of the HI envelope (f_{HIcom}).

The interpretation of the morphology of bubbles, described in the following sections, is affected by an uncertainty in the categorization. There are two ideal models of the bubble's structure: a spherical model and a "blister" model (see Fig. 3.4). The spherical model is ideal: infrared emission surrounds the hot inner parts of a bubble and marks the heated surface of molecular clouds. Molecular clouds are distributed homogeneously in an envelope, while more diffuse HI gas is spread further. The blister model differs mainly in the distribution of molecular clouds, which are concentrated at the edge of a bubble. In that case the bubble tends to expand into regions of lower density and create a blister-like shape.

The image of the bubble we see (and our description of its shape and relative positions of HI, CO and IR) depends on the viewing angle towards the bubble. The blister bubble looks differently from various angles (as seen in Fig. 3.5). Contrary, a bubble following a spherical model should look from different angles the same. However, we

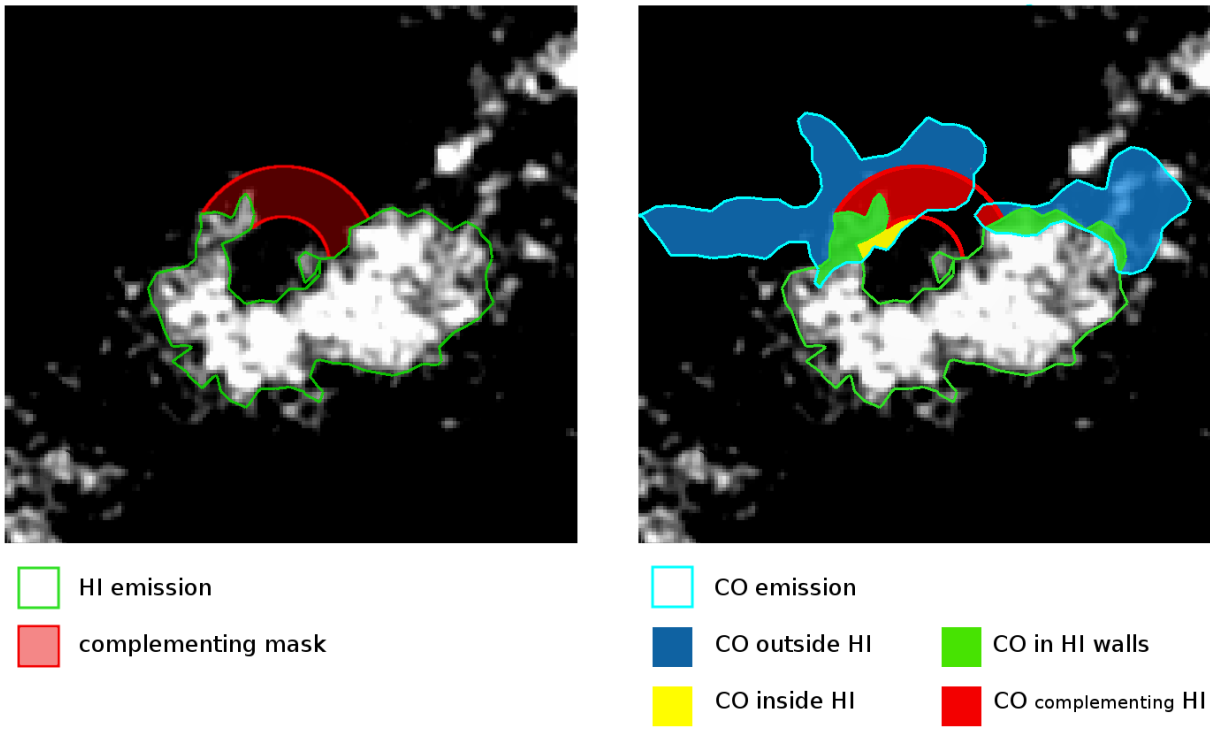

Figure 3.3: The left panel shows an HI envelope (N115) surrounded by a green line. The manually constructed counterpart is in red. The right panel shows the same region, but together with CO emission, which is bordered by a turquoise line. The blue area marks CO emission lying outside the HI envelope, the green area marks CO emission lying in the HI envelope, the yellow area marks CO emission lying inside the HI envelope, and the red area marks CO emission complementing the HI envelope.

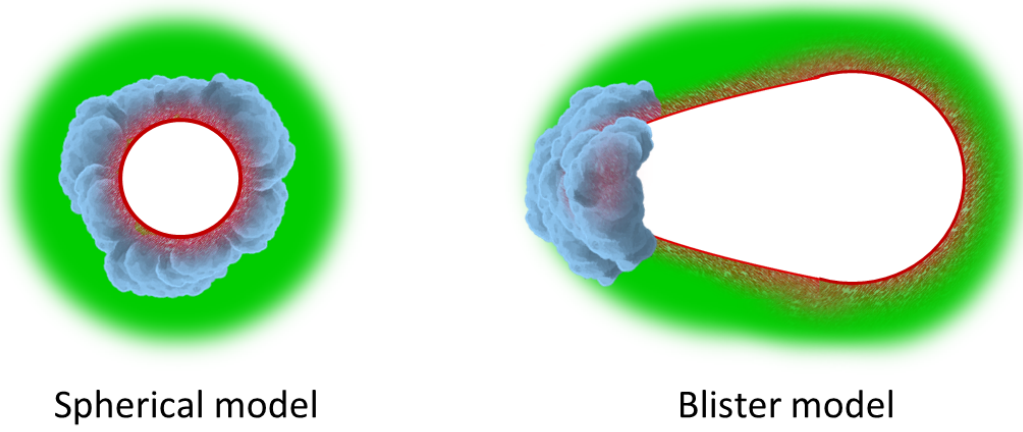

Figure 3.4: Cartoons of two different models: a spherical model (left) and a blister model (right). HI gas is pictured as green, emitting dust particles at 8 μm as red and molecular clouds as blue clouds.

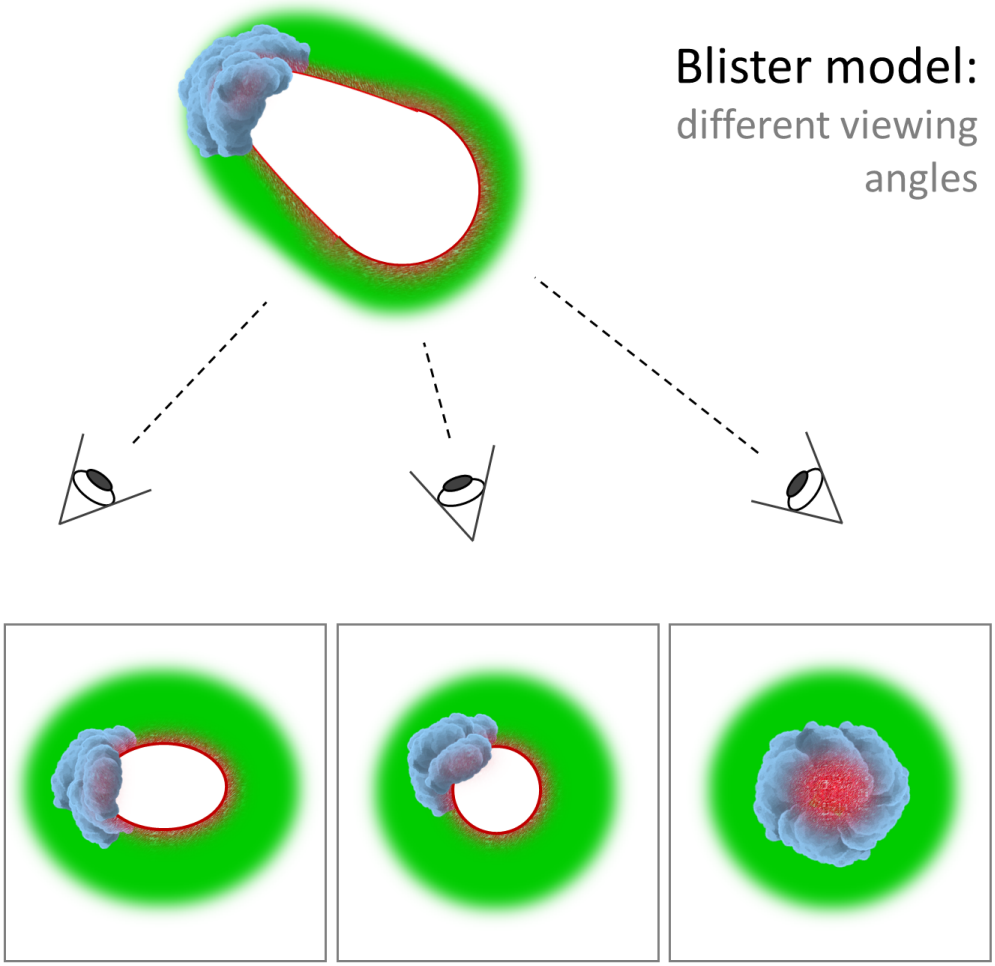

Figure 3.5: The change in a viewing angle causes a difference in observations (cartoons bordered by squares). A blister bubble can look different from various angles.

cannot change the viewing angle and some features stays projected and can be interpreted in contrasting ways. I.e., the fact that the CO cloud seems to be located inside a bubble, does not mean, it is really sitting there. It can be a blister model (the right-hand option in Fig. 3.5) and the CO cloud can only appear to be inside a bubble. The CO emission is scattered into few velocity channels, so we cannot distinguish between a cloud sitting inside a bubble, and a back (or front), non-expanding wall. We want to remind to the reader that all the morphology descriptions are relative to a viewing angle and sometimes even to a considered model.

3.2 Sample of studied bubbles

We have chosen 24 bubbles from the list of infrared bubbles provided by Churchwell et al. [1], which we planned to find in HI data according to the angular size of the infrared bubbles compared to the resolution of the HI data. The angular resolution of VGPS survey is 1′, therefore we have chosen bubbles with angular radius higher than 1′. From these bubbles we have found 18 bubbles both in HI and CO data. We have also found 3 of Churchwell's bubbles (N113, N116 and N117), which we did not plan to investigate. Their angular radius is smaller than 1′ and we found them because of their position close to other bubbles from our list. Two of these bubbles, N116 and N117 were identified to be part of the same object. The full list with identified and unidentified bubbles is in the Table 3.1, together with some basic properties we determined, such as distance and radius.

Chapters 3.3, 3.4 and 3.5 are dedicated to morphology of bubbles; morphology of HI envelopes is discussed in chapter 3.3, morphology of CO emission is discussed in chapter 3.4 and morphological features of each studied bubbles are discussed in chapter 3.5. Following chapter 3.6 is dedicated mostly to dynamical properties of bubbles and correlations with size, galactocentric distance or mass of the bubbles.

3.3 HI envelopes compared to their IR counterparts

Most of the bubbles are visible as emission envelopes surrounded by noisy background. The background emission is noisy and variable, but the envelope stays visible for a few channels. The brightness temperature of the envelope is usually 17% higher compared to the brightness temperature of the surrounding emission (Table 3.2). Some of the bubbles are clearly visible as bright envelopes, such as N35. Some bubbles have only a part of their envelope brighter than the surroundings, but the other parts are indistinguishable from the ambient medium. There are bubbles, especially the bubble N119, whose HI envelopes are hard to be distinguished and they look more like holes in the HI emission. The maximum difference between T_b in walls of a bubble and T_b of the surroundings was 44%, while the minimum was about 2%, which is mainly pointing out to bubbles, which are detectable mostly because of the lack of HI emission in their inner parts (holes).

We discovered an interesting and probably new type of HI envelopes of bubbles, which are observed in absorption. Unlike most of the bubbles, these bubbles do not show their envelope in emission, but in absorption. We identified the gaseous content of these bubbles in CO data first and afterwards we found out that the bubbles are visible in HI data as well, but not as emission envelopes, but as absorption ones. These bubbles (marked with $*$ in the Table 3.2) are on average about 40% less bright than its surroundings and they seem to be much more compact than bubbles visible in the emission (examples of an emission and an absorption envelope are in Fig.3.6).

Furthermore, these absorption HI envelopes copy their infrared counterparts better than the emission HI envelopes. It is visible in the ratio of r_{IR} and r_{HI}, which are both average radius of the external border of the bubble, the first one of HI envelopes and

Sample of studied bubbles with basic parameters

Bubble	l [deg]	b [deg]	V_{LSR} [kms^{-1}]	d [kpc]	r [pc]	Bubble	l [deg]	b [deg]	V_{LSR} [kms^{-1}]	d [kpc]	r [pc]
N35	24.513	0.241	117.3	6.5	3.9	N97	46.951	0.312	-	-	-
				8.9	5.3						
N36	24.837	0.090	107.4	6.1	8.5	N99	48.540	0.468	-	-	-
				9.4	13.0						
N59	33.071	-0.075	79.2	5.0	14.0	N100	48.821	-0.557	57.5	5.6	7.7
				9.3	26.0						
N61	34.157	0.140	58.1	3.8	3.6	N107	50.972	0.078	42.2	3.7	11.9
				10.3	9.9					7.0	22.4
N62	34.334	0.216	57.9	3.8	1.7	N108	51.766	0.471	1.0	0.1	0.1
				10.3	4.7					10.4	15.3
N63	34.652	-0.412	-	-	-	N109	51.982	0.562	4.4	0.4	2.5
										10.1	62.6
N64	34.760	-0.669	-	-	-	N111	52.204	0.751	4.5	0.4	0.1
										10.1	3.6
N68	35.543	0.011	51.6	3.4	5.0	N113	52.229	0.737	1.0	0.1	0.0
				10.4	15.3					10.3	3.1
N69	36.187	0.648	77.3	5.1	6.2	N114	52.253	0.706	5.1	0.4	0.2
				8.7	10.6					10.0	5.4
N71	38.290	0.007	-	-	-	N115	53.556	-0.014	24.1	2.1	4
N76	38.955	-0.731	80.2	6.0	6.8	N116*	54.091	-0.088	40.0	5.0	4
				7.2	8.2						
N81	42.003	-0.512	69.4	5.3	13.0	N117*	54.112	-0.064	40.0	5.0	4.0
				7.3	17.9						
N91	44.211	0.050	-	-	-	N119	55.157	0.130	38.1	4.1	5.0
										5.6	6.8
N94	44.818	-0.500	47.1	3.5	4.7						
				8.6	11.5						

Table 3.1: Bubbles, which were not found in HI or CO have "-" in columns of V, d and r. V is a radial velocity of a channel in HI data, where the bubble is centered, d is a distance from Sun (near kinematic distance is in a first row, far kinematic distance is in a second row for each bubble), r is radius of the bubble. Bubbles N116 and N117, both marked with * were identified to be one object.

the second one of the IR bubbles. For the absorption bubbles the average ratio is 0.99, but for the emission ones it is about two times more - the average ratio is 1.91. We can clearly see here that those bubbles which envelopes are observed as an absorption are about the same size as the infrared bubbles. The emission envelopes are on average two times larger than their infrared counterparts, which is probably due to the phase of HI gas - the emission ones are formed by WNM and the absorption ones may be formed by CNM, which is denser and colder. Some of the HI envelopes are very extended: the HI envelope of N36 is 2.6 times larger than the one in IR, in a case of N111 the HI envelope is 2.8 times larger and for N113 the HI envelope is even 4.6 times larger than its counterpart in infrared observations. Among absorption bubbles there is even a case (bubble N100), where the HI envelope is 0.76 times less extended than the IR bubble.

There is no correlation between the ratio of the brightness temperature in the walls of HI bubbles and of the surrounding medium ($T_{\mathrm{b(i)}}/T_{\mathrm{b(o)}}$), with the radius, the mass, the energy input, the galactocentric distance, nor the age of the bubbles. There is no correlation between the HI envelope extension ($r_{\mathrm{HI}}/r_{\mathrm{IR}}$) and the mass, the energy in-

Morphological parameters of studied bubbles

Bubble	r_{IR}	r_{HI}	$\frac{r_{HI}}{r_{IR}}$	$\frac{T_{b(i)}}{T_{b(o)}}$	f_{HI}	S_{COins}	f_{HIins}	S_{COcom}	f_{HIcom}	S_{COout}	S_{COinw}	f_{HIinw}
N35	3.9′	6.8′	1.7	1.4	100.0%	21.7%	56.9%	0.0%	0.0%	4.8%	73.5%	33.0%
N36	3.3′	8.6′	2.6	1.2	89.9%	40.7%	54.6%	18.0%	94.7%	20.3%	21.0%	3.6%
N59	7.5′	9.0′	1.2	1.2	98.3%	2.4%	31.5%	0.0%	0.0%	71.8%	25.8%	19.1%
N61	3.8′	4.7′	1.2	1.1	96.2%	2.7%	14.5%	0.0%	0.0%	72.8%	24.5%	29.8%
N62	1.7′	4.4′	2.6	1.2	96.4%	15.9%	75.0%	4.2%	90.5%	6.6%	73.3%	58.5%
N68	5.1′	5.8′	1.1	1.1	93.6%	11.2%	39.9%	1.3%	30.0%	57.8%	29.7%	46.7%
N69*	10.2′	11.0′	1.1	0.6	54.6%	6.7%	7.7%	44.5%	78.9%	18.1%	30.7%	45.2%
N76*	4.6′	5.2′	1.1	0.8	38.0%	5.1%	6.7%	17.0%	28.7%	49.4%	28.5%	78.9%
N81*	10.3′	10.5′	1.0	0.7	89.0%	14.2%	22.2%	0.0%	0.0%	58.5%	27.3%	38.8%
N94	4.4′	5.6′	1.3	1.0	88.4%	3.9%	3.0%	0.0%	0.0%	41.9%	54.2%	12.6%
N100*	5.5′	4.2′	0.8	0.8	67.7%	1.0%	2.1%	9.4%	27.3%	72.0%	17.6%	24.4%
N107	12.6′	20.1′	1.6	1.1	95.8%	2.3%	2.3%	0.0%	0.0%	19.0%	78.7%	20.9%
N108	4.9′	7.1′	1.5	1.2	74.5%	20.5%	19.1%	11.4%	9.8%	2.9%	65.2%	17.2%
N109	16.8′	19.6′	1.2	1.2	70.4%	3.1%	2.9%	7.2%	23.6%	18.8%	70.9%	30.4%
N111	1.2′	3.4′	2.8	1.2	86.3%	24.0%	61.0%	13.5%	68.3%	0.0%	62.5%	50.4%
N113	0.7′	3.2′	4.6	1.2	97.5%	54.1%	53.0%	0.0%	0.0%	0.0%	45.9%	13.3%
N114	1.8′	3.7′	2.1	1.0	80.7%	0.0%	0.0%	49.4%	98.9%	0.0%	50.6%	24.3%
N115	3.5′	10.9′	3.1	1.3	71.2%	7.1%	16.0%	16.8%	80.0%	61.2%	14.9%	18.5%
N116(7)	0.9′	2.1′	2.3	1.1	94.9%	47.2%	60.7%	0.0%	0.0%	0.0%	52.8%	19.2%
N119	5.1′	8.8′	1.7	1.2	96.6%	56.8%	97.3%	7.1%	79.7%	0.0%	36.1%	14.3%

Table 3.2: This table shows some morphological features and parameters determined while comparing HI envelopes to IR bubbles and CO distribution to HI envelopes. Bubbles marked with $*$ are those which HI envelope is visible in absorption. r_{IR} is an average external radius of infrared bubbles adopted from Churchwell et al. [1]; r_{HI} is an average external radius of HI envelopes; r_{HI}/r_{IR} shows, how much an HI envelope is extended compared to an infrared bubble; $T_{b(i)}/T_{b(o)}$ is a ratio between the brightness temperature in HI walls and outside of them. This ratio shows, how bright the HI envelope is compared to its surroundings. f_{HI} shows the fulfillment of the HI envelope; S_{COins} shows how much of the total CO emission is inside the HI envelope; f_{HIins} shows how much of HI cavity is filled with CO emission; S_{COcom} shows how much of the total CO emission complements the HI envelope; f_{HIcom} shows how much CO emission complements the HI envelope; S_{COout} shows how much of the total CO emission is outside the HI envelope; S_{COinw} shows how much of the total CO emission is in the walls of HI envelope; f_{HIinw} shows the fulfillment of the HI walls by the CO emission.

put, nor with the galactocentric distance of the bubbles. However, there is a correlation with the size and the age of bubbles (the size and the age are proportional (see Eq. 3.6), therefore we show the correlation with the size of bubbles as an example in Figure 3.7). Both correlations seem to be power laws: smaller bubbles have larger HI envelopes, as well as younger bubbles. This can be caused by the fact that young bubbles could be still surrounded by the primordial cloud or remnants of said cloud. Therefore, we can observe bigger envelopes in the case of smaller/younger bubbles.

75% of studied HI envelopes are mostly closed, with average filling factor f_{HI} of 84.5% (see Tab. 3.2). Only 20% of the bubbles are open and only 5% (one studied bubble) assume the form of a loop. Interestingly, the bubbles with lowest f_{HI} are three of four absorption bubbles. The fourth absorption bubble N81 is observed as a closed HI envelope (89.0%). If we ignore all four absorption bubbles from our sample, then all emission bubbles can be designated as closed bubbles (average filling factor would be 91.3%).

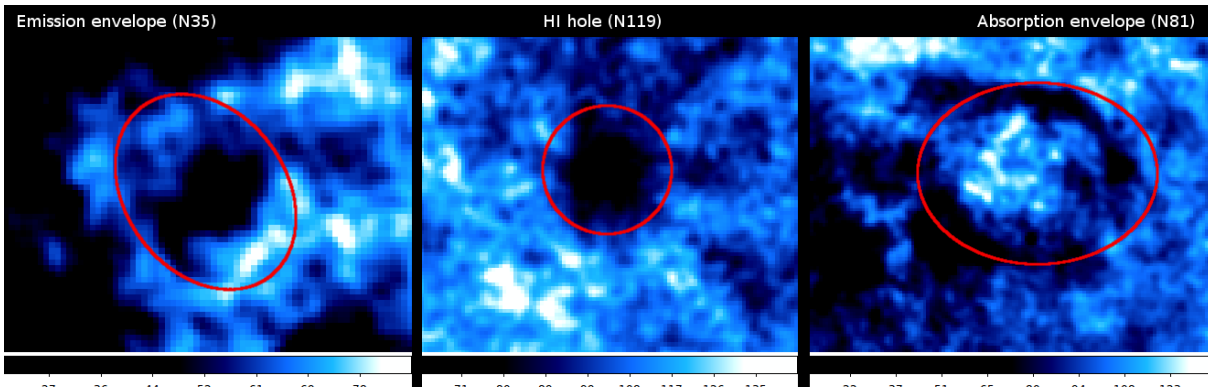

Figure 3.6: The panel on the left shows an example of an HI emission envelope, where the brightness temperature of the envelope is much higher than the brightness temperature of the surrounding media. The central panel shows an example of a bubble with not well defined HI envelope. These kind of bubbles look more like holes in HI data. The panel on the right side shows a new type of HI envelopes, which are seen in absorption. These absorption envelopes are more concentrated towards the IR rims than the more diffused emission envelopes. HI data are in blue, red line marks the rims of IR bubbles.

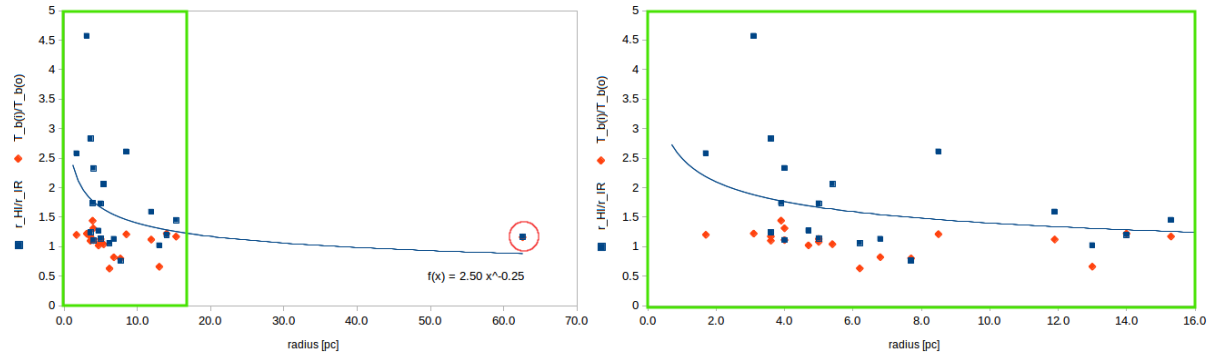

Figure 3.7: The correlation between the HI envelope extension ($r_{\mathrm{HI}}/r_{\mathrm{IR}}$) and the physical size of bubbles. There is no correlation with the brightness of the envelope ($T_{\mathrm{b(i)}}/T_{\mathrm{b(o)}}$). The data for bubble N109 are marked in a red circle. This bubble is exceptional in its size, therefore we show also the correlation without it (marked in a green rectangle).

3.4 Distribution of CO emission

Most of the CO emission is in a form of clumps, located along the rims of infrared bubbles. Nice examples of bubbles, where CO emission is following the infrared rims well, are bubbles N68 and N109 (Fig. 3.8). Compared to HI emission, CO emission is more compact (HI seems to be more diffuse). We looked at the distribution of CO emission 1) in the HI walls, 2) outside the HI walls (or in a case of open HI envelopes or HI loops, we looked at the outskirts of the complemented shape of the bubble), 3) inside the HI envelopes (in the HI cavity, where the lack of HI emission is caused mainly due to ionized hydrogen), and 4) in missing parts of HI envelopes (simply, we looked how much CO emission complements HI envelopes). The details about the description method are in the section 3.1.4, the results are in Table 3.2. All of the studied bubbles show that at least some part of their CO emission lies in the HI envelopes (the

definition of "outside", "inside" and "in" the HI walls is shown in Fig. 3.3). Nearly half of them (about 45% of bubbles) has most, more than 50%, of their total CO emission lying in the HI walls. Still, if we look only at these bubbles, where CO emission is mainly concentrated in HI walls (bubbles N35, N62, N94, N107, N108, N109, N111, N114 and N116), their CO emission is covering only about 30% of their HI envelope. These results show that the CO emission is not well correlated with HI emission and the reason is not only the clumpiness of the CO emission, but also a fact that most of the bubbles (55% of them) have a majority of their CO emission distributed somewhere else, than in the HI walls (S_{COinw} is lower than 50%).

The majority of studied bubbles show some CO emission inside the HI cavity, but 50% of them show only a small fraction of CO emission in the HI cavity (less than 10% of the total CO emission). 20% of bubbles (bubbles N36, N113, N116 and N119) have more than 25% of their CO emission lying inside the HI cavity, from which bubbles N113 and N119 are reaching the highest concentration (about 54%, 56% respectively). In the case of N113, the CO clouds are lying inside the HI envelope due to the large extension of HI envelope and a large cavity. They are filling up about 53% of the cavity, but they still correspond to the infrared emission (just to remind to the reader, all depends on the viewing angle as described in the section 3.1.4). But in the case of N119 it is clearly seen that almost the whole HI cavity is filled with CO emission (the filling factor f_{HIins} is about 97%) and the CO emission does not correspond to the IR emission. Similarly, bubble N116+N117 is showing a CO cloud sitting inside the HI cavity (Fig. 3.9, the upper row).

About 60% of the studied bubbles show that some of their CO emission complements the HI envelope (this is expressed in the relative area S_{COcom}). However, there are only six bubbles out of the twenty, where the CO emission is nearly fully complementing the HI envelope. Especially nice examples are bubbles N69 and N115 (Fig. 3.9,

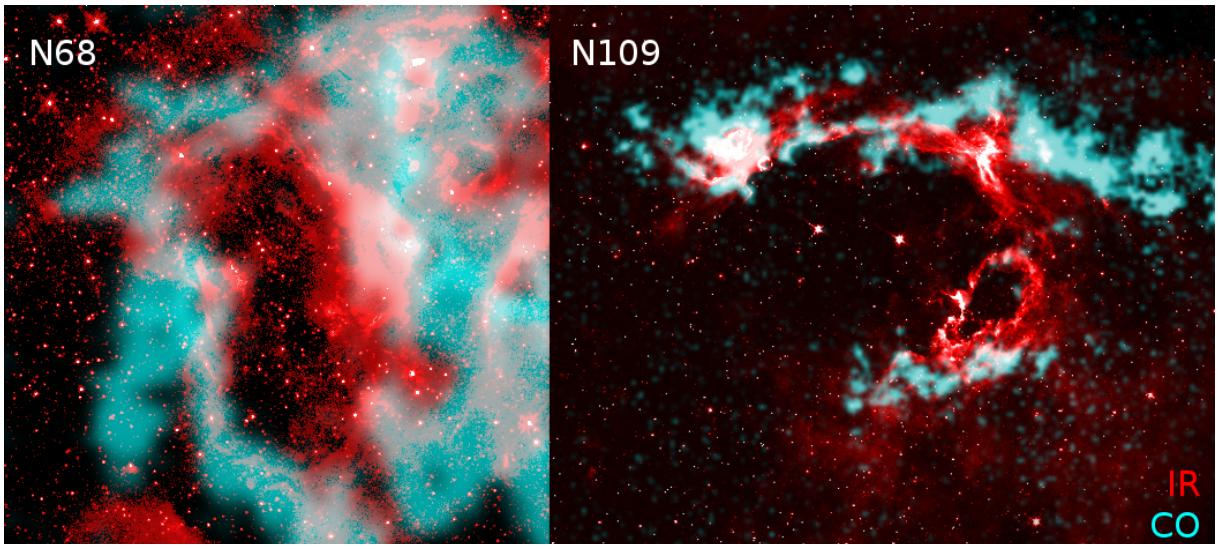

Figure 3.8: These two bubbles are nice examples, where CO emision (GRS, blue) traces, or at least partly follows the infrared structure of the bubble (Spitzer, red).

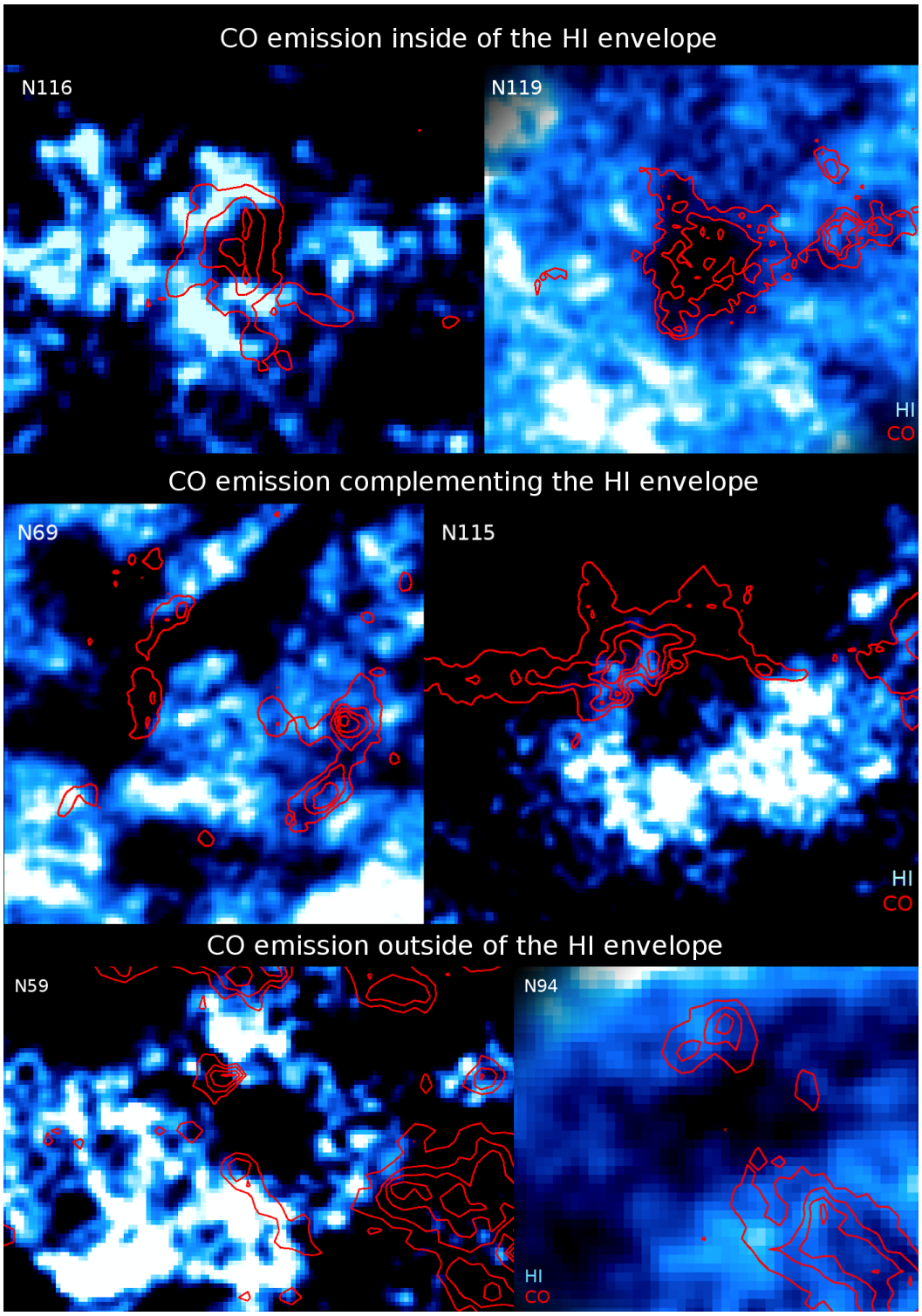

Figure 3.9: The first row shows two examples of bubbles, which HI cavity is filled up with CO emission. The middle row shows two bubbles, which CO emission is complementing HI envelopes, both emission (the right panel) and absorption ones (the left panel). The lower row shows two examples of bubbles with extended CO emission. HI emission is in blue, red contours are from CO observations.

the middle row). While in the case of N115 the CO emission is complementing the HI emission envelope, in the case of N69 the CO emission is complementing the HI absorption envelope.

75% of all bubbles has their CO emission distributed outside the HI envelope (this is expressed in the relative area S_{COout}). Among the bubbles there are two examples, bubbles N59 and N94 (Fig. 3.9, the lower row), which show extended CO emission. Bubble N59 shows an extended CO cloud attached to the infrared bubble, as well as bubble N94, which large CO cloud (in the southeastern direction) seems to be surrounded by HI emission. The inner parts of the cloud, however, miss HI emission.

There is no correlation between the CO morphology features and radius, age, mass nor galactocentric distance. The CO morphology of bubbles probably depends mainly on the local conditions of the interstellar media.

3.5 Morphology of the studied bubbles

3.5.1 N35

HI envelope of N35 is closed, filling about 100% of the shape, nicely copying the shape of IR bubble (especially the southern part). The HI envelope is more extended, the radius of the HI envelope is about 74% larger than the outer radius of the IR bubble. The IR bubble seems to be more prolonged towards the northwestern direction, this is because of a lack of IR emission in those parts. Contrary, in HI data we can observe HI emission spreading over the northwestern edge of the bubble, entering slightly the inner parts of the IR bubble, which makes the HI envelope look more rounded than the IR one. The central parts of the bubble are fulfilled with radio-continuum emission (Fig. 3.11).

CO emission is mainly in the form of two loops, the western one is not bright, contrary to the eastern loop, which includes most of the molecular mass. The shape of the CO emission distribution is prolonged towards the northwestern direction and most of the emission, about 74%, lies in the walls of the HI envelope. Just a little fraction, about 5% of the emission lies out of the HI envelope, whereas about 22% of the CO emission lies inside the HI envelope, which covers about 57% of the cavity. The CO emission is nicely visible along most of the velocity channels of the HI envelope, especially from the channel 117.7 to 124.0 kms^{-1} the change of the bubble's shape (its shrinking) is clearly visible.

3.5.2 N36

N36 is a complicated object. Churchwell et al. [1] identified this bubble as a bubble with a high eccentricity of 0.75. However, comparing the IR image of N36 and its surroundings with HI, CO and radio-continuum emission (Fig. 3.11), we suggest that N36 is a much bigger bubble, with a complicated shape (Fig. 3.10). The most striking feature is the "central bar" (originally in Churchwell et al. [1] it is an eastern edge of the bubble). We marked this feature (Fig. 3.10) as a central bar, because its position

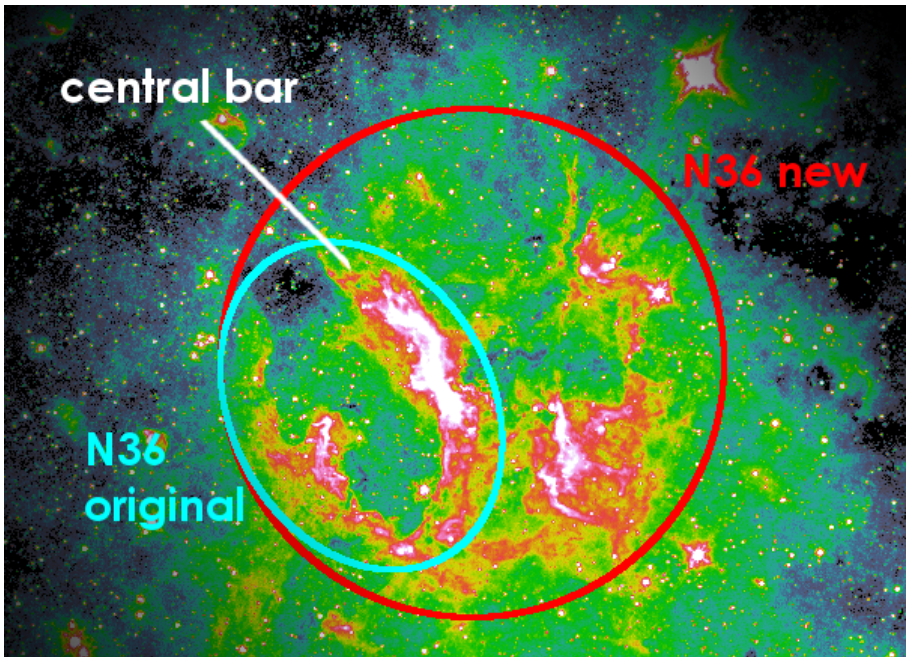

Figure 3.10: Comparison of an originally suggested shape of N36 (in blue) with a new one (in red). The background map is 8μm infrared map from Spitzer.

is projected in the center of the bubble's shape we suggested. It does not mean it is sitting in the very center of the bubble, it can be a part of the approaching or receding wall. It is bright in IR, radio-continuum, but also in CO emission and submillimeter observations. However, contrary to the CO emission, the central bar in the HI data is associated with a deep lack of HI emission. It seems that the central bar is the source of ionizing radiation and probably ongoing star formation. This region seems to be dynamical, as the expansion velocity from HI observations is about 9 kms^{-1}, which is the highest in the total studied sample of bubbles.

The CO emission also illustrates the complexity of this bubble. Only about 6% of the CO emission lies in the walls of the HI envelope, while 41% lies inside the HI cavity, filling up about 55% of its space. This is caused by the central bar. Although the HI envelope is defined as a closed bubble (see Fig. 3.2), 10% of the fulfilled shape is actually missing. This 10% is nearly fully packed with CO emission. The structure of radio-continuum emission is also more complicated than in most of the other cases of studied bubbles. It shows four bright spots, from which the two brightest are filling up the original (Churchwell's) shape of N36. However, the other two spots, located eastwards from the brightest regions, are complementing the shape of the bigger, by us suggested, shape of N36.

3.5.3 N59

N59 seems to be a multi-bubble, with the bubble [SPK2012] MWP1G033176-000097 sitting in its northwestern edge (Fig. 3.12). The bubble N59 is much better visible in CO observations than in HI observations, where the HI envelope is closed, but not

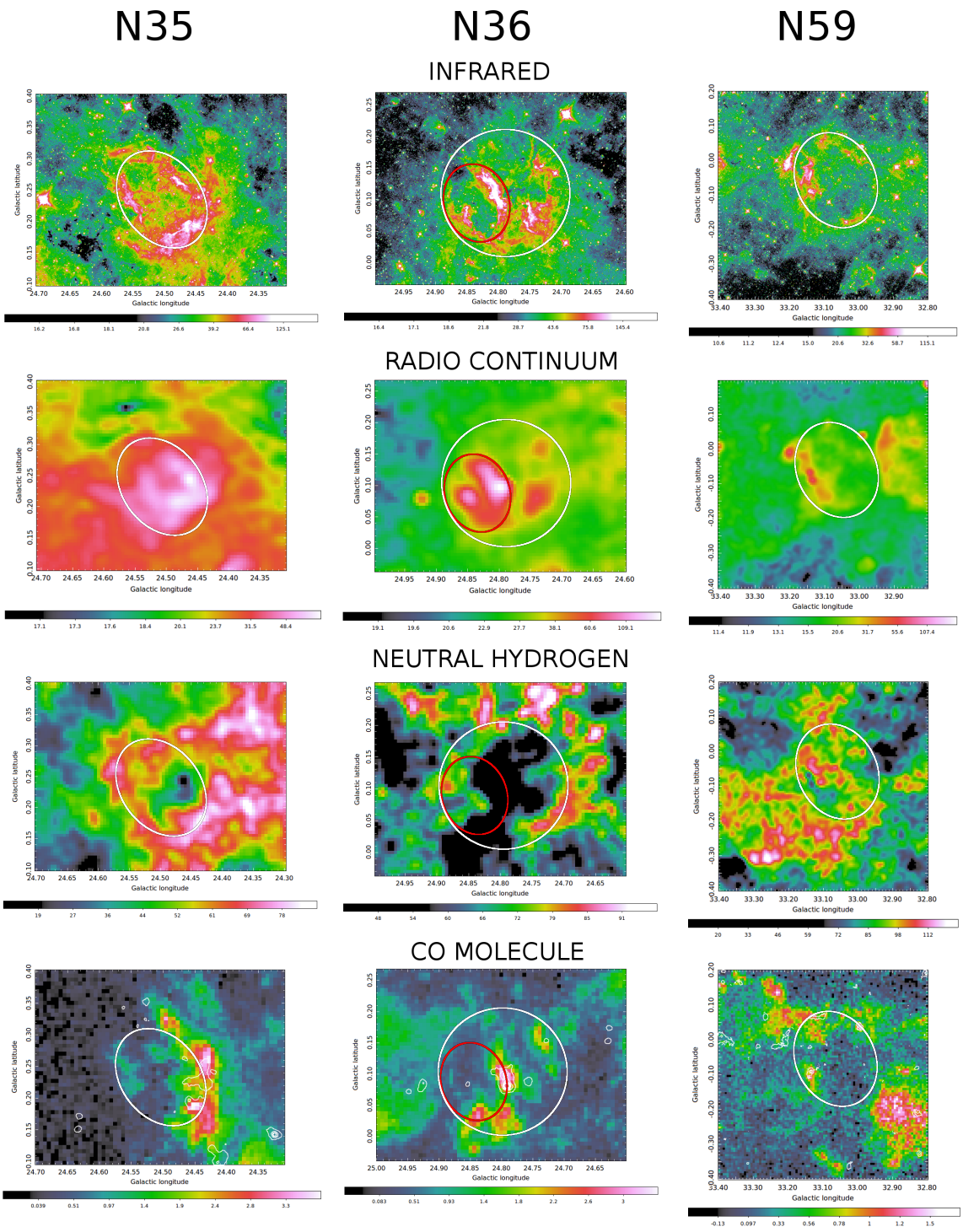

Figure 3.11: Multiwavelength images of bubbles N35, N36 and N59. Images of HI and CO emission are centered on the velocity channel from Tab. 3.1. CO emission images are overlapped with contours of submillimeter emission.

copying well the northeastern edge of the IR bubble. The northeastern edge of the HI envelope is lying inside the infrared one. This can be caused by an extra HI emission from a different distance. In that case, probably a part of the real northeastern edge can be seen on the northern side of the strayed emission. The inner parts of the HI envelope are fulfilled with radio-continuum emission, which is not spread into the rest of the cavity inside the IR bubble. It is mostly concentrated along the western edge of the bubble, which is including the brightest parts of the IR bubble, as well as the smaller bubble MWP1G033176-000097 (Fig. 3.11).

The western edge of N59 is best visible in CO data around the channel 77.7 kms^{-1}, together with the smaller bubble MWP1G033176-000097. The whole bubble is nicely visible through channels 77.7 to 80.9 kms^{-1}, with a similar structure and a shape as it is observed in IR data. The fact that the CO emission is not copying well the shape of the HI envelope is reflected in the morphology results: about 72% of the CO emission is lying outside the HI envelope - mainly the northeastern parts, together with the CO emission coming from the walls of the smaller bubble MWP1G033176-000097.

3.5.4 N61

N61 is an open bubble according to Churchwell et al. [1], with a bright HII region [KJB2003] G34.255+0.145 located just next to its western edge. HI observations show an HI envelope located at 58.1 kms^{-1}, which, contrary to its IR counterpart, seems to be closed ($f_{HI} = 96\%$). However, the northeastern edge of the HI envelope is protruding into the inner parts of the IR bubble. This contrasts with the CO emission, which

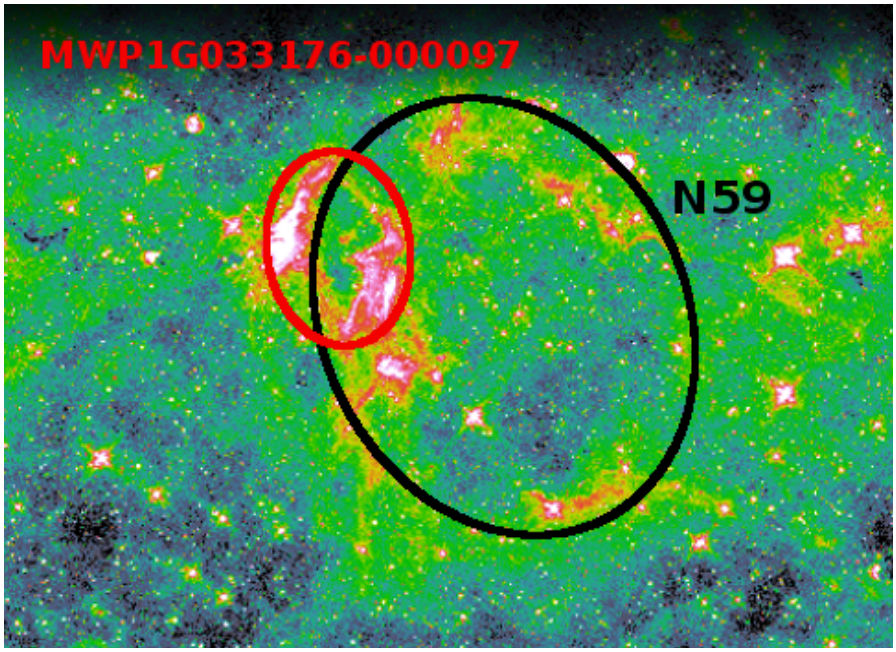

Figure 3.12: The position of the bubble N59 (marked in black) superimposed on the IR map from Spitzer. The bubble marked in red is the bubble MWP1G033176-000097.

is following most of the IR shape of the bubble. The inner parts of the bubble are fully filled with radio-continuum emission. The brightest IR emission coming from the western edge of the bubble is associated with a bright emission seen both in HI data, and in CO data. There is a drop in radio-continuum emission in the location of the western edge (Fig. 3.14).

Similarly as in the case of the bubble N59, about 73% of the CO emission is lying outside the HI envelope and about 25% is lying in the walls of the HI envelope. Interestingly, there is a CO cloud at the southern part of the bubble's edge, which is outlined by the IR emission just from the western side, from the direction of a probable location of the ionizing source.

3.5.5 N62

The HI envelope of N62 is located at 57.9 kms^{-1} and it is a closed bubble ($f_{HI} = 96.4\%$). The HI envelope is 2.6 times larger than the infrared bubble. It seems that the infrared edges are lying inside the HI envelope, just along the HI borders. There is a significant drop of HI emission inside the infrared bubble. At the same place we can observe bright radio-continuum emission, which is filling up the whole infrared bubble and it is prolonged towards the southeastern edge of the bubble (Figure 3.14). Churchwell et al. [1] suggested the shape of the infrared bubble to be quite circular (with eccentricity of 0.38), but we suggest that the bubble is actually prolonged, as it is visible in other wavelengths. Fig. 3.13 shows the infrared image of the bubble (red) superimposed on the CO emission map (blue). The circle marks the position and suggested shape of the bubble by Churchwell et al. [1]. It is clearly visible that the bubble in CO data is prolonged, and actually, the prolonged shape is mirrored in the infrared image as well.

The CO emission is clearly visible from the channel 56.9 to 58.8 kms^{-1}. It mostly

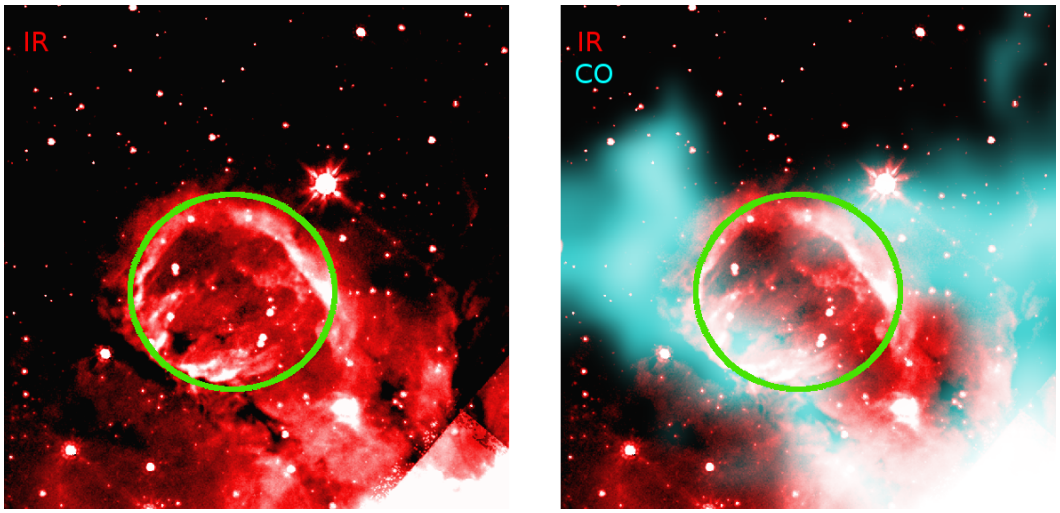

Figure 3.13: The Spitzer infrared image (red) of the bubble N62 superimposed on the GRS CO emission map (blue). The circle marks the position and suggested shape of the bubble by Churchwell et al. [1]. The bubble seems to be elongated contrary to what Churchwell et al. [1] suggested.

resembles a rectangular shape. It is partly open towards the northern direction, where one of the brightest HI emission sits. 73% of the CO emission is lying in the walls of the HI envelope and about 16% of the total CO emission lies inside the HI envelope. The submillimeter emission follows properly the southwestern edge of CO emission.

3.5.6 N68

N68 is one of the best examples of bubbles, whose gaseous content is incredibly well visible in CO emission (Fig. 3.14). The shape of the CO envelope is perfectly copying the shape of the infrared bubble. The two brightest regions located at the edges of the bubble visible in the infrared image coincide with the brightest CO emission. These regions are lying opposite each other, the brightest one is lying at the eastern edge, the second one at the western edge. The radio-continuum emission is filling up the inner parts of the infrared bubble, but it is obvious that it consists of two bright spots, which are spreading from the eastern and western edges of the bubble towards the center and along the rims of the bubble. Therefore, it is possible that the bubble is created by stellar feedbacks from these two locations.

The bubble in HI data seems more like a hole. The envelope is distinguishable but, comparing the brightness temperature in the walls and outside them, we see that the difference is about 13%. This number is that high due to some of the better distinguishable parts of the envelope, the most of the envelope seems to be as noisy as its surroundings. The inner parts of the HI envelope show lack of HI emission, which is fulfilled well by radio-continuum emission.

3.5.7 N69

The bubble is visible in HI as an absorption (from 75.2 to 79.3 kms^{-1}), copying the shape of the infrared bubble well. It is more open than in the infrared observations, but in the same eastern direction. There is also discontinuity in the HI absorption walls, at the southwestern edge. The highest absorption is associated with the brightest infrared emission at the northwestern edge of the bubble. The radio-continuum emission is not filling up the whole infrared bubble/HI absorption envelope, but it is distributed among two main regions - northern and southern. The northern one is associated with the bubble, due to its position being related to the brightest infrared emission of the bubble (Fig. 3.18).

The CO emission does not coincide with the HI absorption walls, but it complements the walls. Especially on the eastern side, where the bubble is open (both in IR and HI), the CO emission is particularly bright. The bubble in CO observations seems to be also open, but in the southwestern direction. The lack of CO emission is at the same southwestern location, where the discontinuity in HI walls is visible as well. The western part of CO walls is partly lying in the HI wall, partly outside it.

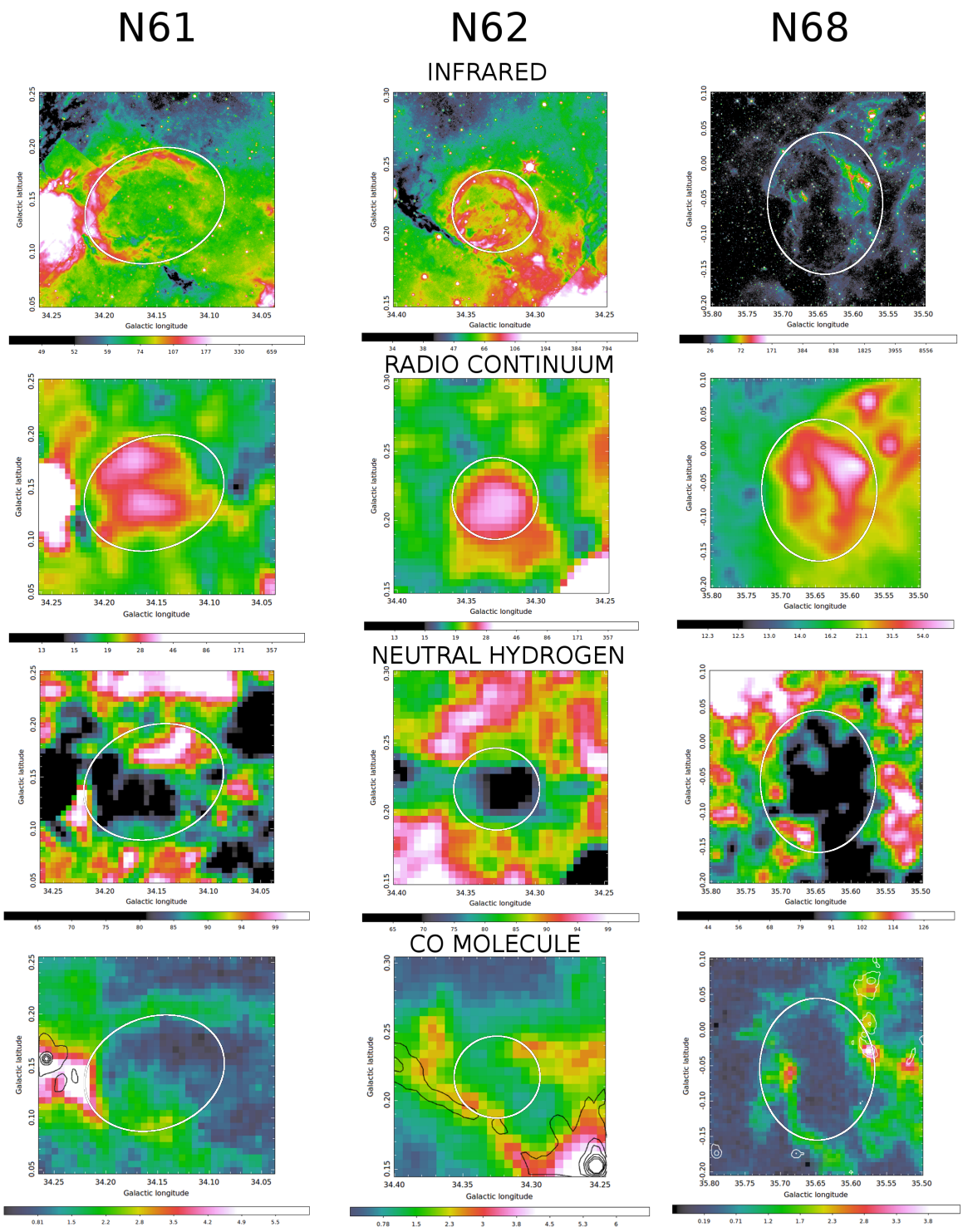

Figure 3.14: Multiwavelength images of bubbles N61, N62 and N68. Images of HI and CO emission are centered on the velocity channel from Tab. 3.1. CO emission images are overlapped with contours of submillimeter emission.

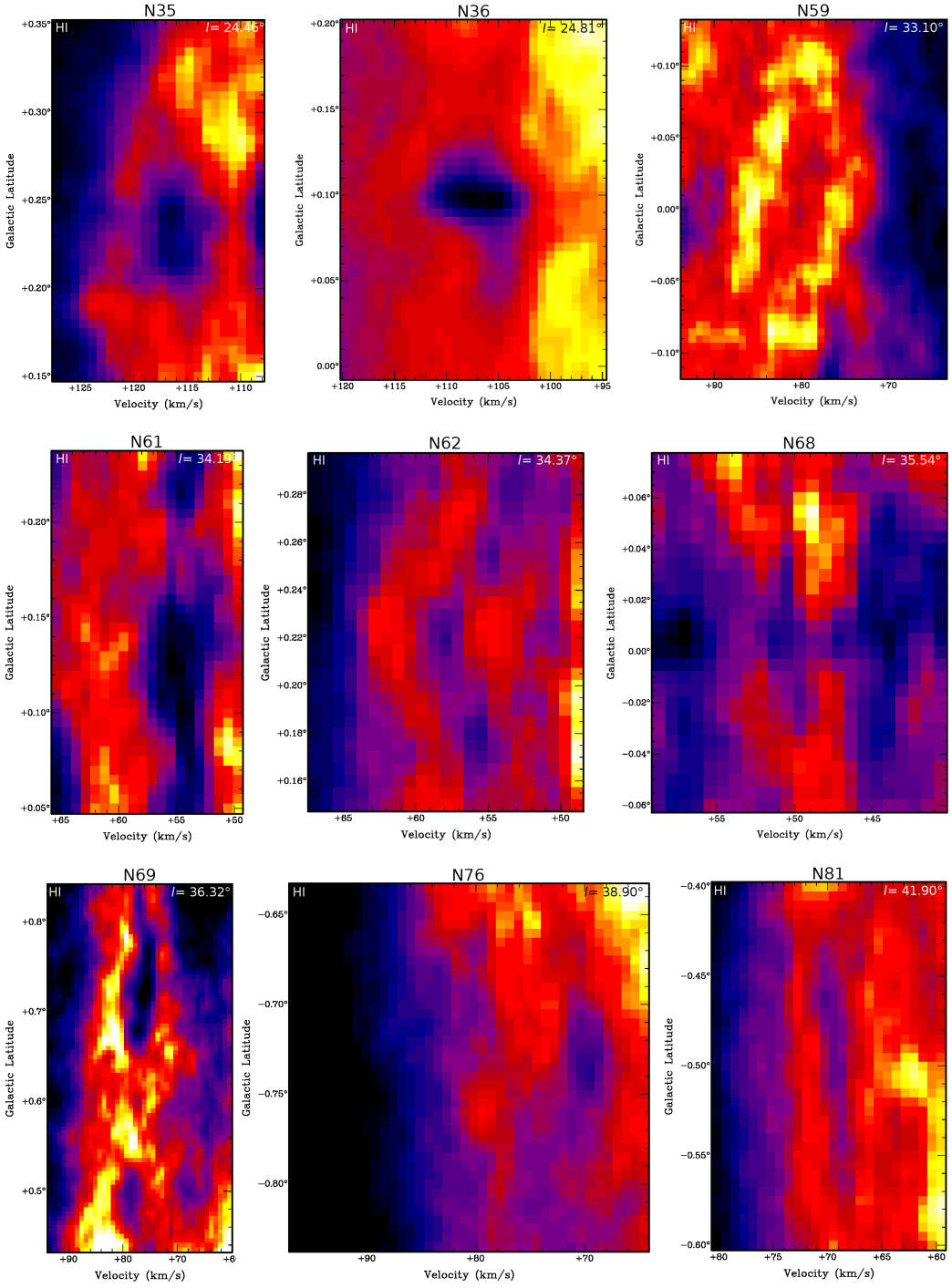

Figure 3.15: Position-velocity diagrams for bubbles N35, N36, N59, N61, N62, N68, N69, N76 and N81.

3.5.8 N76

Bubble N76 is visible as an HI absorption envelope in the range of $78.5 - 82.6$ kms^{-1}. The HI envelope is not complete, it is fragmented and open in the northwestern direction (slightly resembling the shape of the IR bubble, where the northwestern part of the bubble is faint). The strongest absorption is accumulated in two regions, one lies towards the northeastern direction, the second one spreads around the southeastern part of the bubble. The second region coincides with the strongest IR emission. Over all, the IR bubble and HI absorption shell match together. It seems that the bubble is not filled with ionized hydrogen, due to faint radio-continuum emission in the direction of the bubble (Fig. 3.18).

The CO emission is mainly lying in and outside the walls of the HI absorption envelope, which looks like the HI absorption is wrapped inside the CO emission. However, the strong HI absorption lying in the northeastern direction just partly coincides with the local CO emission and makes the CO bubble look open in the northern direction, instead of the northwestern direction, as is the case with the HI envelope. The other strongest HI absorption region lying at the southern edge of the bubble coincides with the strongest CO emission. This part of the bubble seems to be strong in IR and CO emission, as well as in HI absorption.

Interestingly, the bubble is visible also in emission, but at different channels (see Fig. 3.16). It is visible as an emission bubble from 75.2 to 77.7 kms^{-1}, then turns into an absorption envelope, and from 84.3 kms^{-1} it goes back into an emission envelope (the full development is shown in Fig. 3.28 in section 3.6.2 Expansion velocity). It is possible that the envelope is made of both types, cold and warm neutral medium, but the WNM is visible in more velocity channels due to higher thermal motion of HI atoms. It is also possible that the bubble is expanding, but mostly its WNM phase, probably due to its lower density. The CNM envelope seen in absorption should be denser and therefore more resistant against expansion. There is also a possibility that the absorption envelope is in a reality a CNM ring, sitting between two WNM lobes.

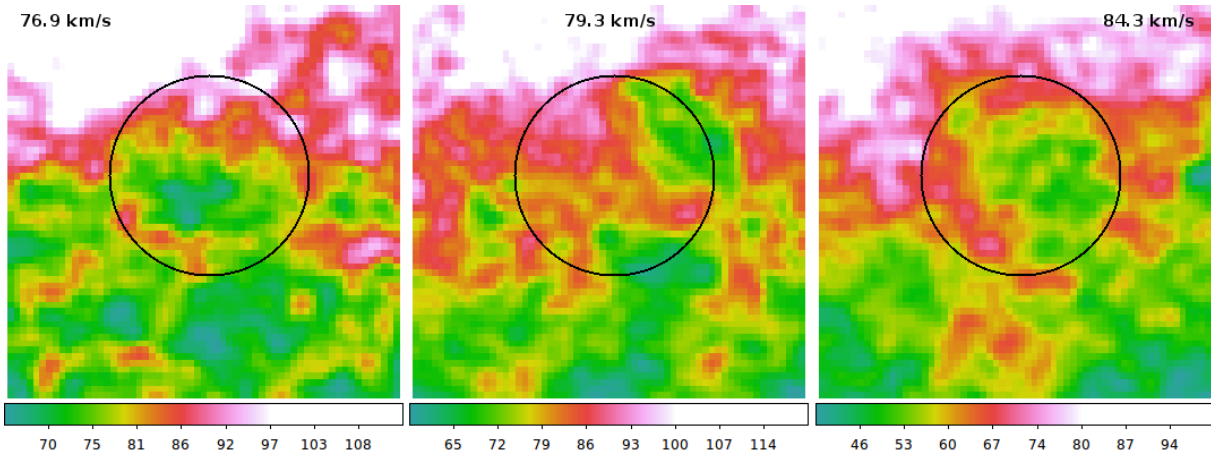

Figure 3.16: The bubble N76 at three different velocity channels. Panels on the left and right side show the bubble as an HI envelope, while the panel in the middle shows it as an absorption envelope.

3.5.9 N81

The HI envelope comes out as an absorption feature at the channel 67.8 kms^{-1} and continues to appear as a nearly complete envelope till 71.9 kms^{-1}. This HI absorption bubble seems to have thin, and probably dense walls. The HI absorption envelope is surrounding the radio-continuum emission, which is filling up the inner parts of the infrared bubble as well (Fig. 3.18). The absorption envelope includes two hole-like features, whose location coincide with two smaller bubbles sitting at the edge of the IR bubble. The first and bigger one is the infrared bubble N82, located at the southwestern edge of the N81 bubble (Fig. 3.17). It is visible as an HI hole from 58.7 to 71.9 kms^{-1}. The smaller bubble N83 is visible as an HI hole at channels 55.4 to 64.5 kms^{-1}. Both smaller bubbles are visible also in the radio-continuum data as bright sources (Fig. 3.18).

The CO emission does not seem to form a convincing shell. There are some features, sitting in the HI walls or outside it, following the shape of the infrared bubble. However, one of those features is definitely connected to the bubble, especially with the smaller infrared bubble N82, which is sitting in the wall of N81. This small IR bubble has a nice CO counterpart. The CO emission surrounding the N82 starts at 65.2 kms^{-1} and goes until 69.0 kms^{-1}, from where a huge CO cloud slowly appears on the western side of the bubble. Until 72.2 kms^{-1} it stretches and forms a thin loop surrounding the southwestern edge of the N81 bubble. There is no significant coincidence with the HI absorption bubble and local CO emission.

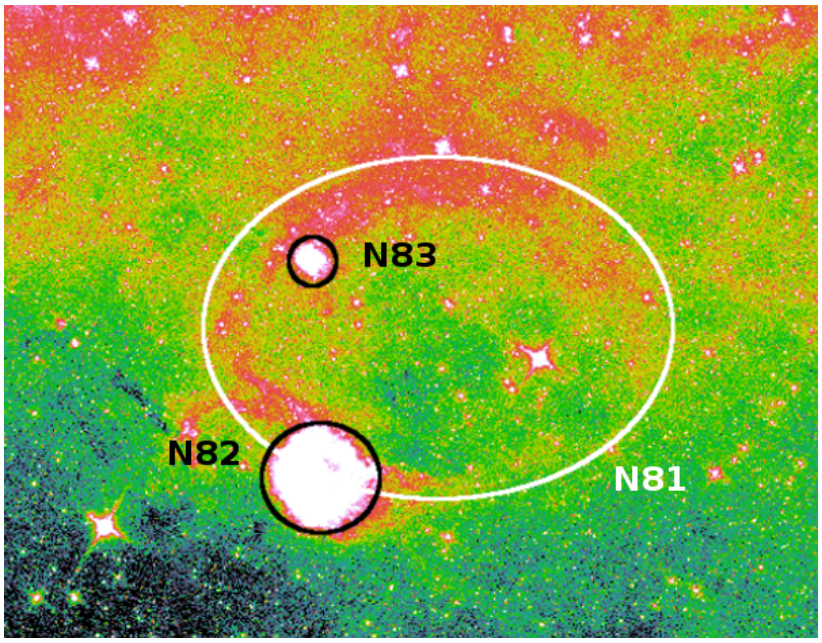

Figure 3.17: The position of the bubble N81 (marked in white) superimposed on the IR map from Spitzer. The bubbles marked in black are bubbles N82 and N83.

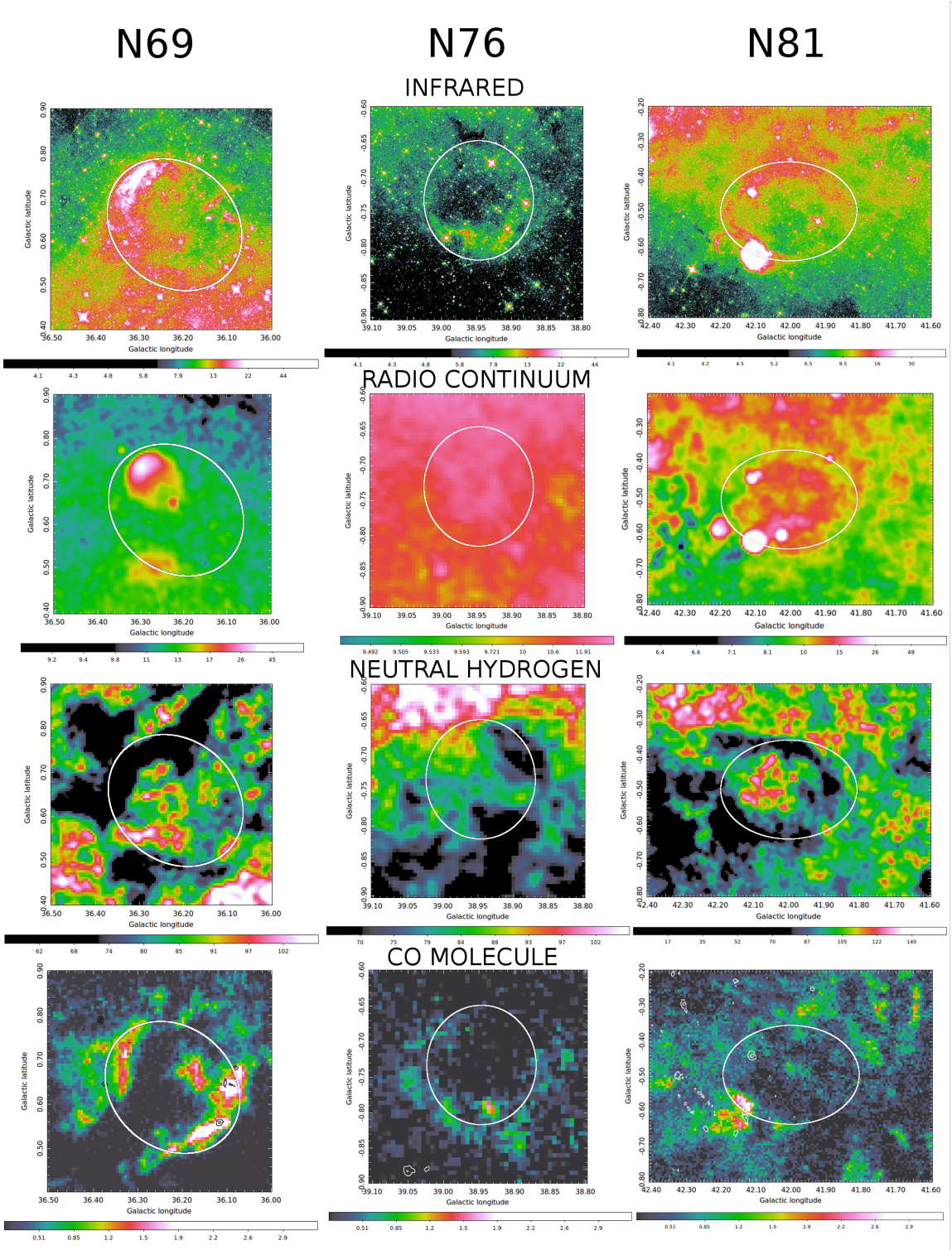

Figure 3.18: Multiwavelength images of bubbles N69, N76 and N81. Images of HI and CO emission are centered on the velocity channel from the Table X. CO emission images are overlapped with contours of submillimeter emission.

3.5.10 N94

N94 is a closed bubble ($f_{HI} = 88.4\%$). It copies the infrared bubble properly, although the HI envelope is about 27% larger. The envelope consists mainly of two bright walls, the first in the northwestern direction, the second in the southeastern direction. These walls are also bright in the infrared radiation. The inner parts of the infrared bubble, as well as the HI envelope are filled with mostly uniform radio-continuum emission, which shows a slight increase towards the northwestern direction (Fig. 3.20).

Both bright IR rims/HI walls are also connected to the CO emission. The bubble in the CO data does not show any bubble-like shape. It consists mainly of two bright CO clouds, the larger one lying in the southeast (towards the brightest wall), and the second one in the northwest direction (towards the second wall). The brightest cloud, located in the southeast, is huge and takes up most of the molecular mass. Due to the presence of this huge CO cloud, 42% of the total CO emission is lying outside the HI envelope.

3.5.11 N100

Bubble N100 is visible as an absorption feature from 55.4 to 60.4 kms^{-1} (the feature is best visible at 57.1 and 57.9 kms^{-1}). The absorption copies the shape of the bubble from IR observations quite well, mainly the brightest part stretching from the northwestern to the eastern side of the bubble. Furthermore, there is an other loop visible in HI absorption, lying at the southwest, which partly complements the infrared bubble. The bubble or any of its parts are not visible in the HI emission. In the central parts of the bubble there is always an emission, which probably comes from different distances, as well as most of other emission coming from the direction of the bubble. There is no radio-continuum emission associated with the bubble (Fig. 3.20).

The CO emission is closely surrounding the HI absorption, although they do not complement each other. There is only a small portion of CO emission lying in the HI walls. The main concentration of CO emission is in three clouds, the first sitting at the southeastern, the second at the southern, and the third one at the northwestern edge of the bubble, where another, much smaller infrared bubble MWP1G048870-005100S lies (Fig. 3.19). The bubble is visible just in a few channels in the HI observations (as an absorption), but in more channels in CO observations.

3.5.12 N107

It is an open bubble according to Churchwell et al. [1], it opens towards the southwest. However, the HI envelope is closed ($f_{HI} = 95.8\%$). The brightest HI emission is copying the brightest infrared rim (Fig. 3.20) and spreads more outwards - the HI envelope is about 59% larger than the infrared one. The same rim is visible in the CO data as a loop spreading from the north to the south. About 78% of the CO emission is lying in the walls of the HI envelope. The eastern part of the CO loop is copying the eastern rim of the infrared bubble well (Fig. 3.20). The radio-continuum is filling most of the inner parts of the HI envelope, especially the western parts. However, the radio-continuum

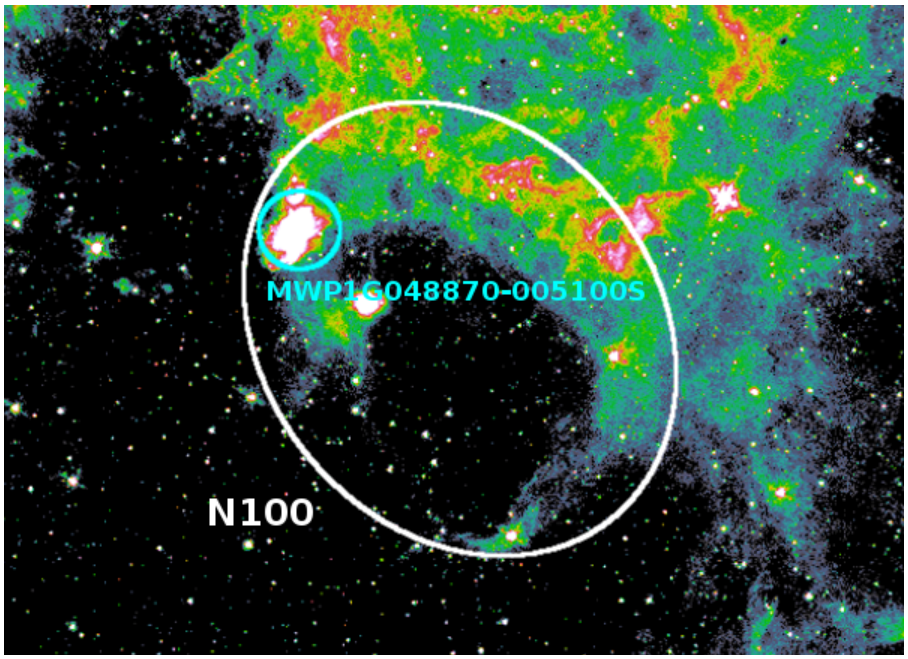

Figure 3.19: The position of the bubble N100 (marked in white) superimposed on the IR map. The bubble marked in turquoise is the bubble MWP1G048870-005100S.

emission seems to combine the emission from bubble N107 and the feature lying towards the southwestern direction. This infrared feature is probably associated with GAL 051.4-00.0 HII region. However, it is probably not connected to bubble N107 as it is not visible neither in the HI, nor in the CO data at the velocity channel of 42.2 kms^{-1}, where the bubble is located.

The infrared bubble N107 was studied in details by Sidorin et al. [117]. Although the derived properties of bubbles are discussed in following sections, let us comment on N107 already here. Sidorin et al. [117] studied the bubble in HI, CO, IR and radio-continuum data as well and they have found similar results to ours. They also ran simulations of evolution of the bubble and found two possible scenarios: 1) the bubble was evolving in an oblate molecular cloud with energy input rate of $\approx 2.7 \times 10^{50}$ erg/Myr and the evolution time of 1 Myr, 2) the bubble was evolving in a prolate molecular cloud with energy input rate of $< 0.4 \times 10^{50}$ erg/Myr and the evolution time of 1.75 to 2.25 Myr (more details in Sidorin et al. [117]). The second simulation result corresponds with our results of derived properties (total energy input of 2.1×10^{50} erg and the age of 1.4 Myr).

3.5.13 N108

Bubble N108 is a part of a system of bubbles around the larger N109 bubble. It is located at similar velocity channels both in HI and CO data, therefore we suggest that the bubbles N109 and N108 are physically connected. N108 is lying in the eastern wall of much bigger bubble N109. The bubble is closed, although the HI envelope is open towards the western direction. This HI empty region is filled with radio-continuum

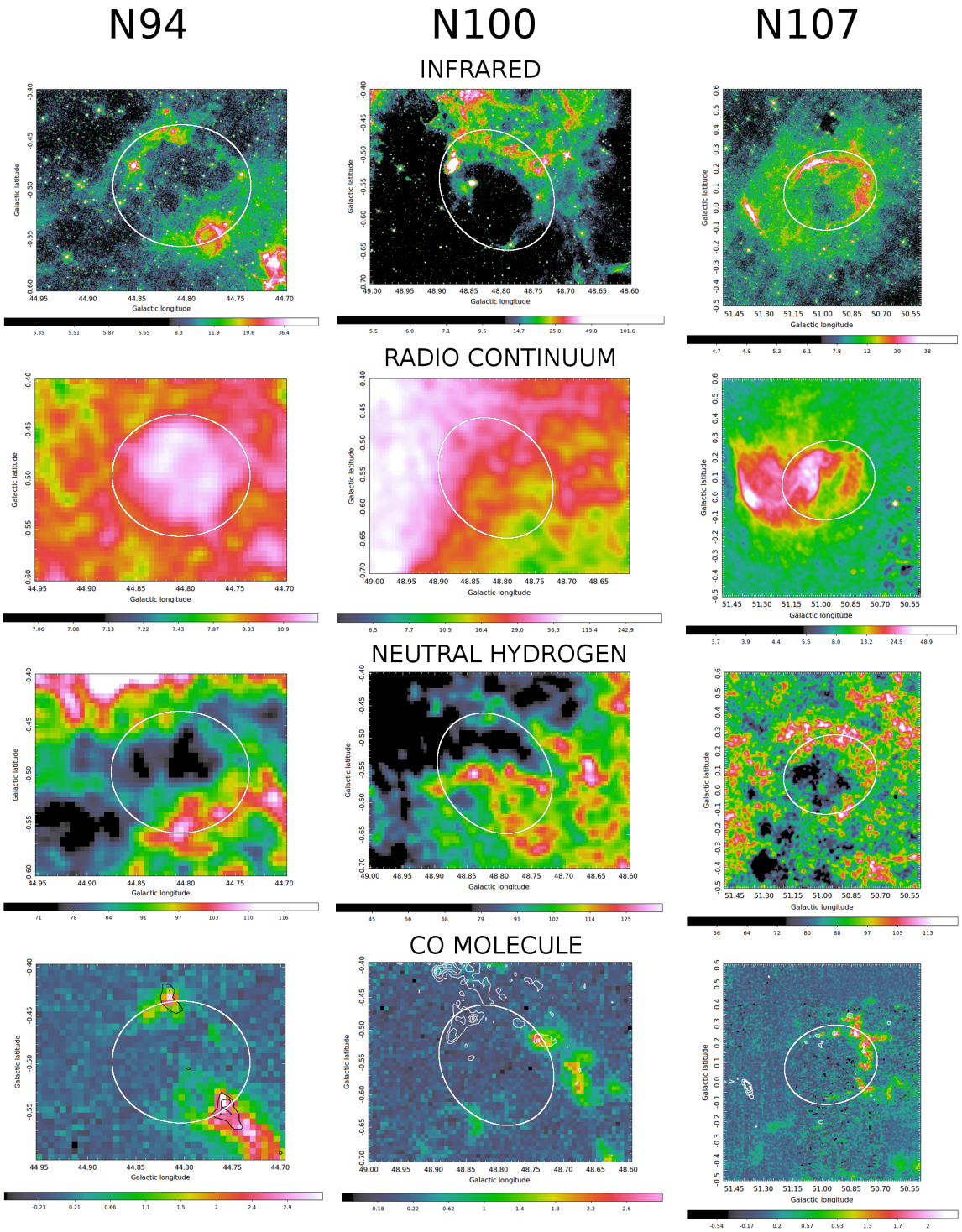

Figure 3.20: Multiwavelength images of bubbles N94, N100 and N107. Images of HI and CO emission are centered on the velocity channel from Tab. 3.1. CO emission images are overlapped with contours of submillimeter emission.

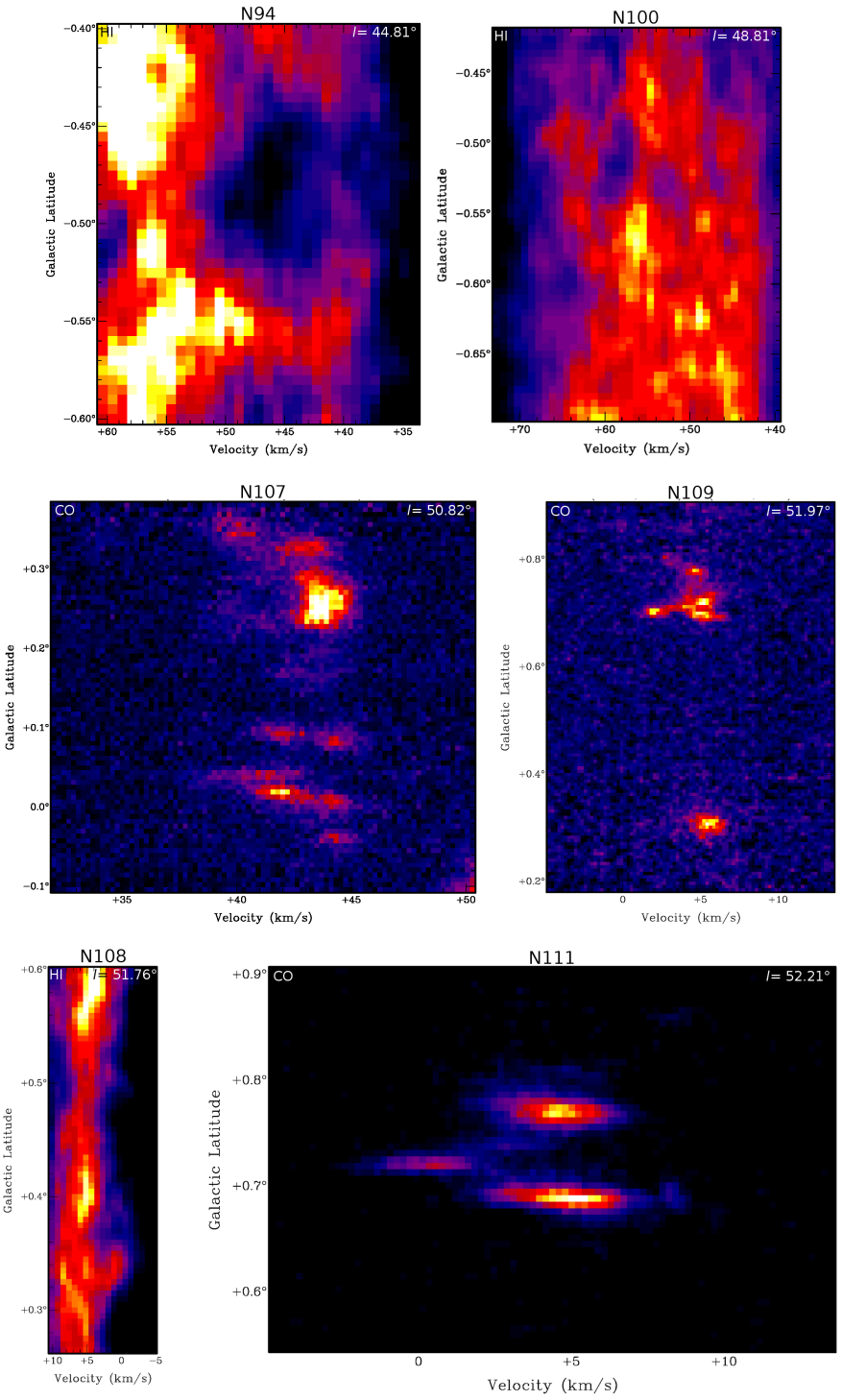

Figure 3.21: Position-velocity diagrams for bubbles N94, N100, N107, N108, N109 and N111.

emission, which is spread along the rims of the infrared bubble. Right at the western edge (which is missing in HI data) the radio-continuum emission is bright and seems to be associated with a bright infrared feature at the western edge. The feature is curved and the same curvature is visible in IR as well as in radio-continuum emission (Fig. 3.22).

The emission in CO is not so strong, but it follows the rims of the HI envelope, especially in the southern parts. 65% of the total CO emission is lying in the walls of the HI envelope and about 21% are protruding inside. The strongest HI emission is mostly in the northern parts of the bubble, while the strongest CO emission is located in the opposite direction. Together with the 870 μm emission, one can clearly see the shape of the IR bubble in the CO data, as well as in the HI data.

3.5.14 N109

This large bubble is actually a multi-bubble complex, which includes smaller (and younger) bubbles spread along its rims: bubbles N108, N110, N111, N112 and N113. From these bubbles we were able to find only N108, N111 and N113 in HI and CO data. The others (N110 and N112) were not visible in our data. All these bubbles are lying at the same distance, i.e. they are not just projected into N109's rims. The HI envelope is copying the shape of the IR bubble quite accurately. Just like its infrared counterpart, it is an open structure, towards the southwestern direction. The HI envelope is just slightly, about 17%, more extended than the IR envelope. N109 is nicely visible also in radio-continuum data. The emission is not filling the central parts of the bubble as it does in most of the cases of studied bubbles, but it is lying along the inner edge of the HI envelope/IR bubble (Fig. 3.22).

The CO emission is copying the IR emission properly and most of it, about 71%, is lying in the walls of the HI envelope. Although the distribution of HI and CO emission is similar, there is a difference in a concentration. The CO emission is more concentrated towards the IR rims, while HI is more extended (which is not surprising, as the infrared emission tracks heated dust particles in molecular clouds).

3.5.15 N111, N113 and N114

Bubbles N111, N113 and N114 lie angularly close to each other. The whole complex seems to be active, which can be seen on the infrared image (Fig. 3.23). The brightest bubble is the bubble N113, which is also associated with the brightest radio-continuum emission. This radio-continuum emission is filling the inner parts of N113's HI envelope, which is centered at 1.0 kms^{-1}. This HI envelope is closed (98%) and is extremely extended, reaching approximately 4.6 times larger radius than its infrared counterpart. The CO emission is mostly concentrated around the western edge of the IR bubble and it is visible from -2.2 to 8.2 kms^{-1}. In the Fig. 3.23 (first column, fourth row) centered around 1.0 kms^{-1} we can see a CO cloud towards the southeastern direction. This is probably a cloud associated with the bubble N112, according to its position.

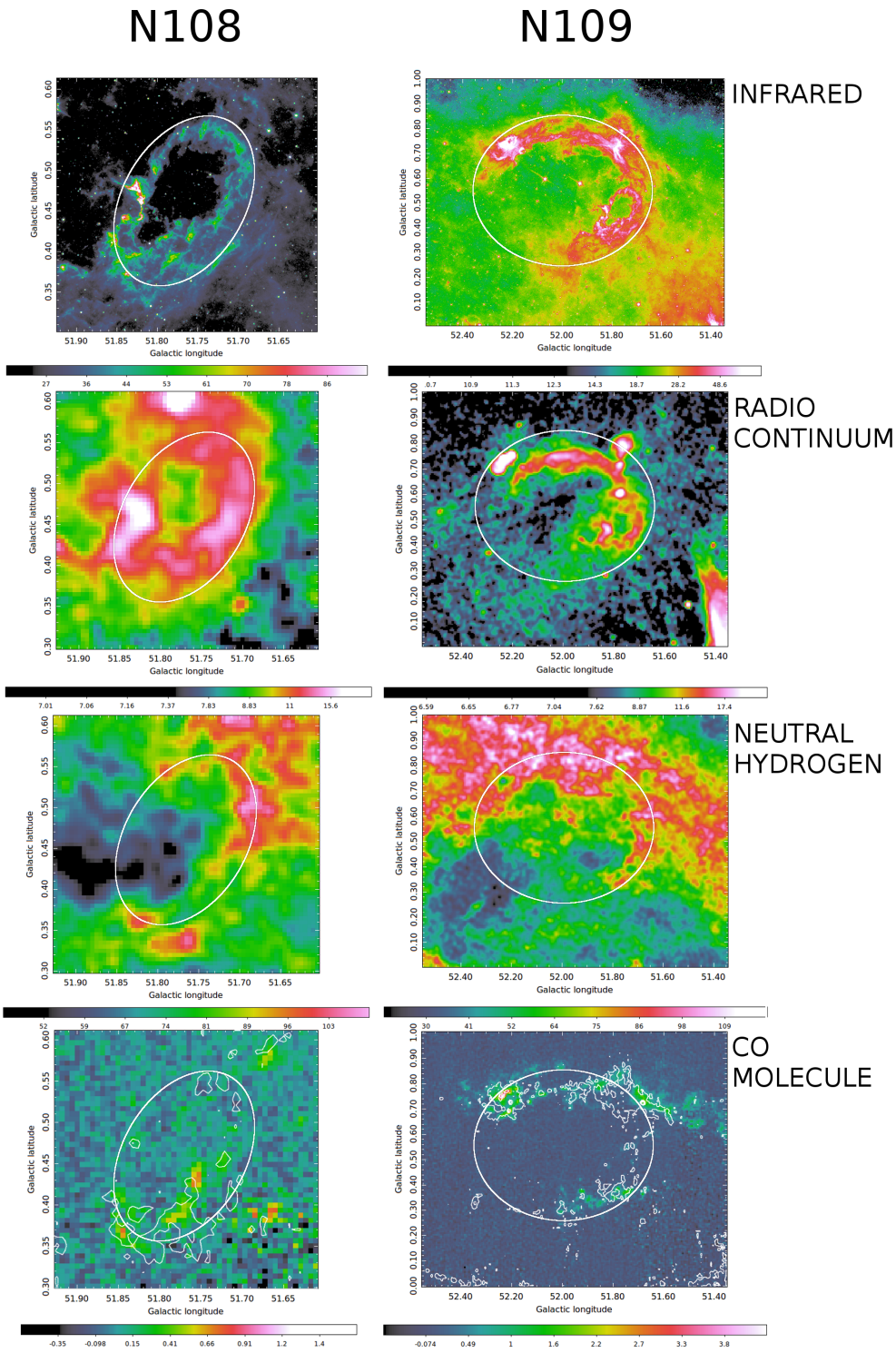

Figure 3.22: Multiwavelength images of bubbles N108 and N109. Images of HI and CO emission are centered on the velocity channel from Tab. 3.1. CO emission images are overlapped with contours of submillimeter emission.

N111, as well as N114, is visible at less HI and CO velocity channels and both bubbles are clearly visible in the HI data at about 5 kms^{-1} (Fig. 3.23, second column, third and forth row). The HI envelope of N111 is also very extended, about 2.8 times more than the infrared one, but not as much as in the case of N113. Parts of the bubble are nicely seen also in CO data, especially around 5 kms^{-1}. Contrary to N113, N111's CO emission is mostly lying in the walls of its HI envelope and partly complementing it. Both bubbles show that their CO emission lies also inside the HI envelope, especially the N113's CO emission, which fills up about 53% of its HI cavity. The HI envelope of N114 is also extended, about 2 times more than the infrared one. Nearly a half of CO emission lies in the HI walls, the second half complements the HI envelope.

3.5.16 N115

Sec. 4.2.2 (Foreground system) is dedicated to the bubble N115 (Bubble F) in more details; therefore, to follow this chapter about morphology, please see the Fig. 4.6). The HI envelope of N115 is very bright, about 30% brighter than the surrounding media. This envelope is mainly concentrated towards the southern direction, while the infrared bubble is obviously brighter in its northern part. The inner parts of the HI envelope/IR bubble are filled with radio-continuum emission.

The CO emission is copying the infrared emission accurately. It is seen as a loop (or a huge CO cloud) sitting at the northern part of the bubble, with the brightest part towards the northwestern edge of the bubble. This part of the CO emission is complementing the HI envelope for about 90%. The majority of the CO emission, about 61%, is lying outside the HI envelope (in this case outside the complementary part of the HI envelope) and only about 18% is lying in the walls of the HI envelope. It seems that the northern part of the bubble consist of a molecular cloud, where probably all, or most of the hydrogen is in its molecular form (that could be the reason why there is an decrease of HI emission).

3.5.17 N116+N117

Sec. 4.2.1 is dedicated to the bubbles N116 and N117 (Bubble C) in more details; therefore, to follow this chapter about morphology, please see the Fig. 4.4. According to Churchwell et al. [1], these two infrared bubbles seem to be two different objects. But looking at the radio-continuum, HI and CO data, we suggest that these bubbles are one and the same object. The bubble N116+N117 has an extended, closed HI envelope, more than two times larger than its infrared counterpart (both infrared bubbles put together). The inner parts of the HI envelope are filled with radio-continuum emission. The radio-continuum emission has its brightest spot in the central-northern part, at the position of the brightest infrared emission.

About 53% of the CO emission is lying in the walls of the HI envelope, but the brightest part, about 47% of the total CO emission, is lying inside the HI envelope, filling about about 61% of the HI cavity. The CO emission does not resemble a bubble, but it is more like a huge clump sitting over the western half of the bubble.

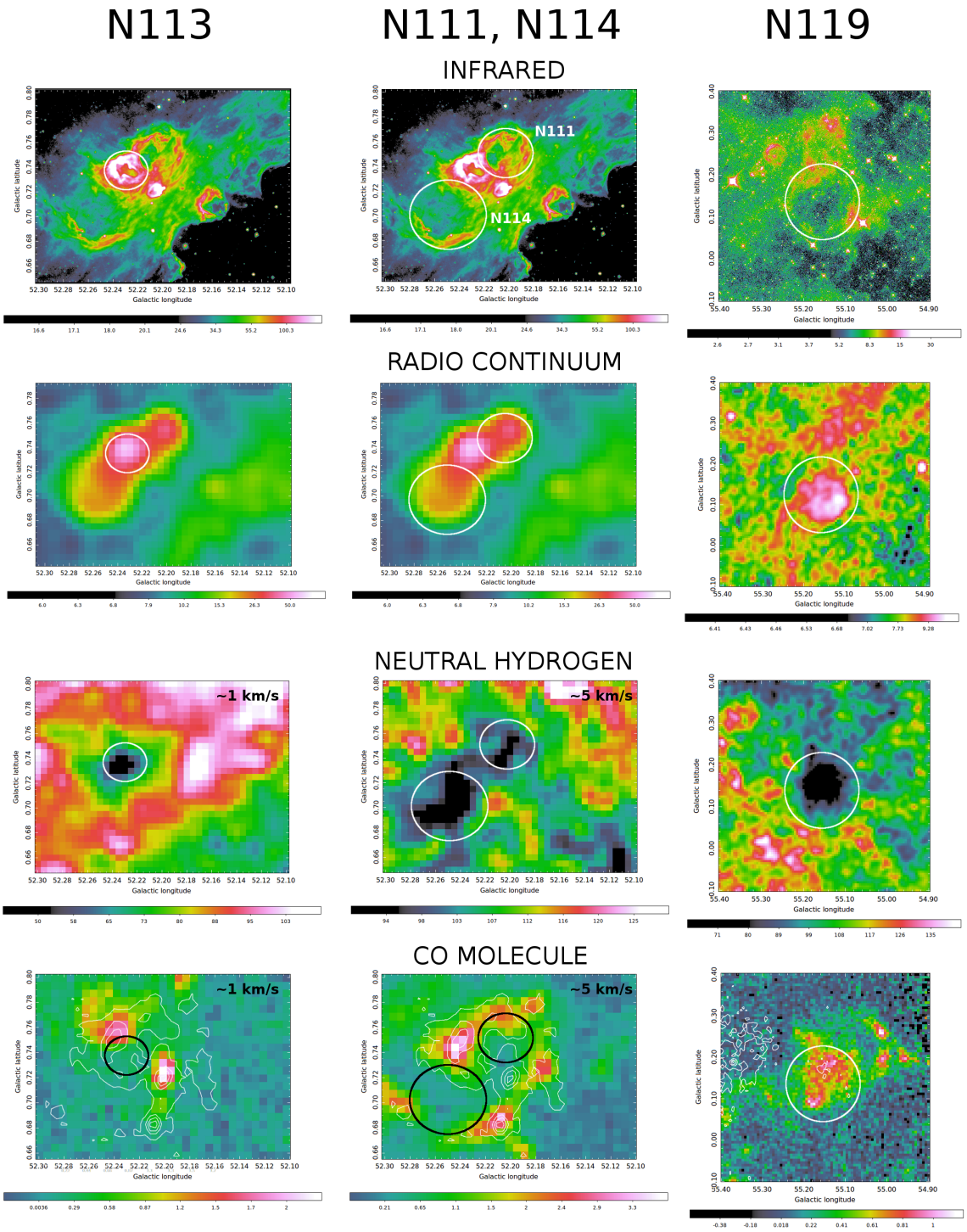

Figure 3.23: Multiwavelength images of bubbles N111, N113, N114 and N119. Images of HI and CO emission are centered on the velocity channel from Tab. 3.1. CO emission images are overlapped with contours of submillimeter emission.

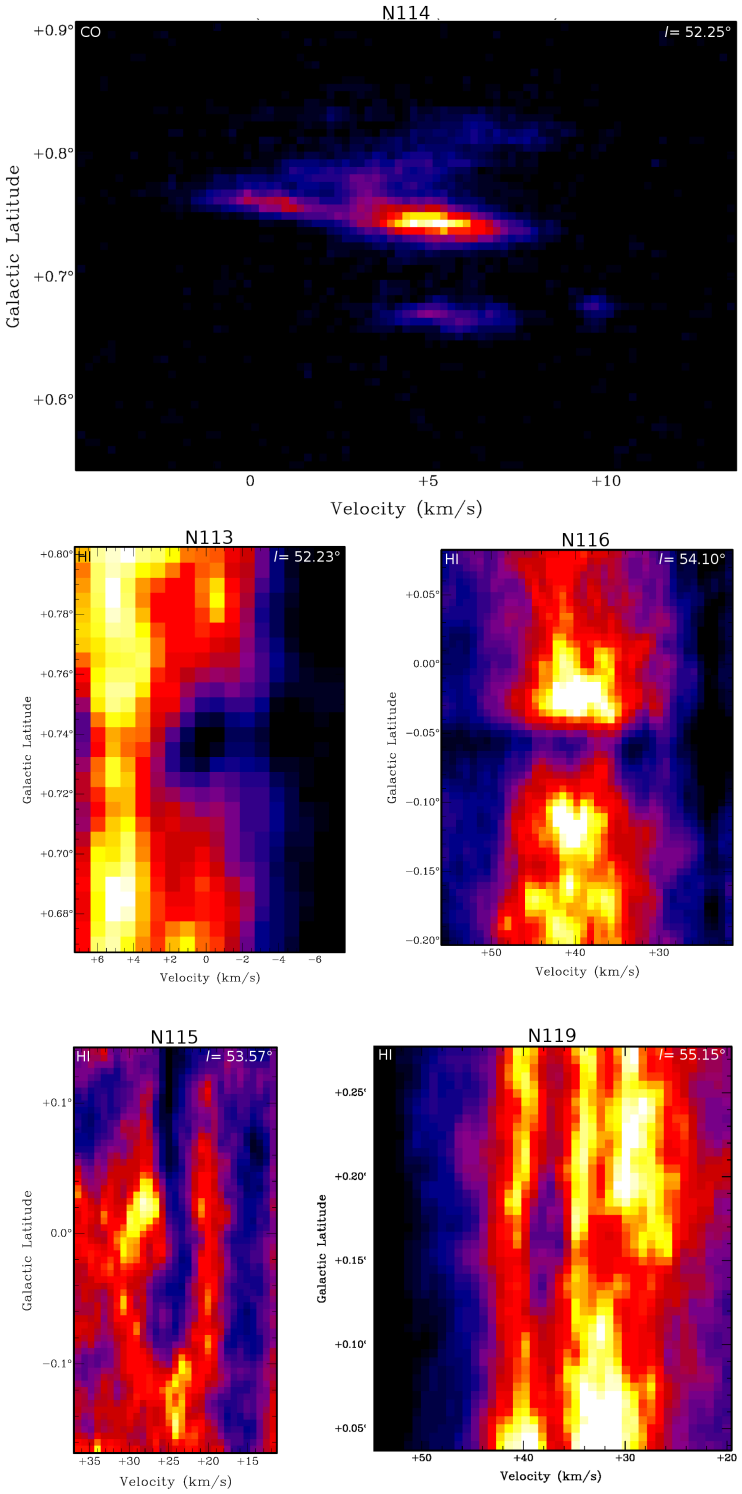

Figure 3.24: Position-velocity diagrams for bubbles N113, N114, N115, N116 and N119.

3.5.18 N119

N119 is a faint infrared bubble, with a bright circular radio-continuum emission filling the inner parts of the bubble. This radio-continuum emission perfectly matches with a lack of HI emission in HI data (Fig. 3.23). This hole is surrounded by a fuzzy (and not convincing) HI envelope. The size of the HI envelope is uncertain, the bubble looks in the HI data more as just a hole surrounded by noisy surroundings ($T_{\mathrm{b(i)}}/T_{\mathrm{b(o)}} = 1.08$).

Interestingly, most of the CO emission, about 57%, is lying inside the bubble. The cloud is spreading from the velocity channels 35.8 to 39.9 kms^{-1}, sitting exactly on the position of the radio-continuum emission. It is possible that the CO cloud is actually sitting on different kinematic distance. However, it is also possible that the cloud is physically connected to the bubble and probably is located in approaching or receding wall (following a blister model, Fig. 3.4).

3.6 Properties of the studied bubbles

In the following sections we describe each determined property of the studied bubbles, looking for correlations between size, mass, age, energy and galactocentric distance. Tab. 3.3 shows all the results, all of them computed for both near and far kinematic distance. In most cases we cannot determine, which of the distances, near or far, is correct; therefore we decided to use the results determined for near kinematic distances, as they could be more likely. Therefore, for statistics and correlations we take in account the results for near kinematic distance. The only exceptions are the multi-bubble N109 and its smaller bubbles (N108, N111, N113 and N114), whose far kinematic distance is more probable.

3.6.1 Size

95% of the studied bubbles have a radius smaller than 15 pc, while the average value is 9.5 pc. This value is mostly influenced by the extremely large bubble N109 with its radius of nearly 63 pc. The median value is 5.0 pc, which is reflected by the fact that 50% of studied bubbles have their radius between 2.5 and 5 parsecs.

There is no clear correlation between the size of bubbles and their distance from Sun, neither the galactocentric distance (see Fig. 3.25). However, the radius of the bubbles and their age are proportional. This is not surprising as the age was derived from the radius. The correlation between radius and mass (and density) are discussed in following sections.

3.6.2 Expansion velocity

All of the studied bubbles are visible as parts or full envelopes in more than three HI velocity channels. This scattering into more velocity channels is caused by the thermal motion of particles and (if existing) expansion velocity of a bubble. The typical velocity of the thermal motion of HI atoms (producing HI emission lines) is about 7 kms^{-1}.

Properties of the studied bubbles

Bubble	R_{gal} [kpc]	r [pc]	n_{HI} [cm^{-3}]	n_{H_2} [cm^{-3}]	M_{HI} [10^3M$_{sol}$]	M_{H_2} [10^4M$_{sol}$]	t_{SN} [10^6y]	t_{OB} [10^6y]	E_{inp} [erg]	L_* [10^3L$_{sol}$]
N35	3.7	3.9	500	7500	3.1	4.6	0.2	0.4	$1.15{\cdot}10^{51}$	27.37
		5.3			5.7	8.7	0.3	0.5	$2.98{\cdot}10^{51}$	52.3
N36	3.9	8.5	50	460	3.2	2.9	0.4	0.6	$8.89{\cdot}10^{50}$	13.4
		13.0			7.5	6.9	0.6	0.8	$3.35{\cdot}10^{51}$	32.9
N59	5.1	14.0	16	180	4.4	5.0	0.9	1.3	$8.82{\cdot}10^{50}$	5.7
		26.0			15.3	17.3	1.6	2.4	$6.09{\cdot}10^{51}$	21.1
N61	5.8	3.6	34	4300	0.2	2.1	0.3	0.5	$2.78{\cdot}10^{50}$	4.9
		9.9			1.2	15.2	0.9	1.3	$6.53{\cdot}10^{51}$	41.8
N62	5.8	1.7	160	14000	0.1	0.7	0.3	0.4	$4.48{\cdot}10^{49}$	0.9
		4.7			0.6	5.3	0.7	1.1	$1.07{\cdot}10^{51}$	8.0
N68	6.1	5.0	31	1400	0.4	1.8	0.3	0.5	$2.96{\cdot}10^{50}$	4.8
		15.3			4.4	16.4	1.1	1.6	$9.71{\cdot}10^{51}$	50.9
N69	5.3	6.2	38	1200	0.9	2.9	0.7	1.0	$2.70{\cdot}10^{50}$	2.3
		10.6			2.7	84.5	1.1	1.7	$1.44{\cdot}10^{51}$	7.1
N76	5.4	6.8	21	120	0.7	0.4	0.4	0.6	$6.41{\cdot}10^{49}$	0.9
		8.2			1.0	0.6	0.5	0.7	$1.15{\cdot}10^{50}$	1.3
N81	5.8	13.0	17	210	3.8	4.7	0.8	1.1	$8.84{\cdot}10^{50}$	6.4
		17.9			7.2	8.9	1.0	1.6	$2.40{\cdot}10^{51}$	12.6
N94	6.5	4.7	27	120	0.3	0.1	0.3	0.4	$2.28{\cdot}10^{49}$	0.5
		11.5			1.7	0.8	0.6	0.9	$1.38{\cdot}10^{50}$	1.3
N100	6.15	7.7	20	280	0.9	1.3	0.6	0.8	$1.80{\cdot}10^{50}$	1.8
					0.9	1.3	0.6	0.8	$1.80{\cdot}10^{50}$	1.8
N107	6.8	11.9	27	110	4.7	1.9	1.0	1.4	$2.13{\cdot}10^{50}$	1.2
		22.4			17.0	6.8	1.8	2.7	$1.53{\cdot}10^{51}$	4.7
N108	8.5	0.1	13	13	0.0	0.0	0.0	0.0	$3.35{\cdot}10^{43}$	0.0
		15.3			4.9	0.5	0.8	1.2	$7.67{\cdot}10^{49}$	0.5
N109	8.3	2.5	1	7	0.1	0.0	0.2	0.4	$6.00{\cdot}10^{46}$	0.0
		62.6			35.6	17.4	5.8	8.7	$1.39{\cdot}10^{51}$	1.3
N111	8.5	0.1	100	4100	0.0	0.0	0.0	0.0	$3.71{\cdot}10^{45}$	0.0
		3.6			0.5	2.0	0.3	0.5	$2.66{\cdot}10^{50}$	4.7
N113	8.5	0.0	860	5700	0.0	0.0	0.0	0.0	$2.30{\cdot}10^{44}$	0.0
		3.1			2.6	17.5	0.2	0.3	$4.42{\cdot}10^{50}$	14.1
N114	8.3	0.2	42	770	0.0	0.0	0.0	0.0	$2.77{\cdot}10^{45}$	0.0
		5.4			0.7	1.2	0.7	1.1	$8.10{\cdot}10^{49}$	0.6
N115	7.5	4.0	20	2300	0.1	1.5	0.4	0.6	$1.60{\cdot}10^{50}$	2.3
					2.1	25.4	1.5	2.3	$1.12{\cdot}10^{52}$	40.3
N116/7	6.9	4.0	54	5100	0.4	3.4	0.4	0.6	$4.00{\cdot}10^{50}$	5.6
					0.4	3.4	0.4	0.6	$4.00{\cdot}10^{50}$	5.6
N119	7.0	5.0	60	350	0.8	0.5	0.6	0.9	$3.02{\cdot}10^{49}$	0.3
		6.8			1.4	0.8	0.8	1.2	$7.89{\cdot}10^{49}$	0.5

Table 3.3: The first column shows galactocentric distance R_{gal} of a bubble, while the other columns show derived properties of individual bubbles for near (first row) and far kinematic distance (second row): , r is radius of the bubble, n_{HI} is primordial density computed from HI mass, n_{H_2} is primordial density computed from H_2 mass, M_{HI} is HI mass, M_{H_2} is H_2 mass, t_{SN} is the age of a bubble in case the progenitor was a supernova, t_{OB} is the age of a bubble in case the progenitor was/were OB star(s), E_{inp} is energy input, L_* is luminosity of probable ionizing OB star.

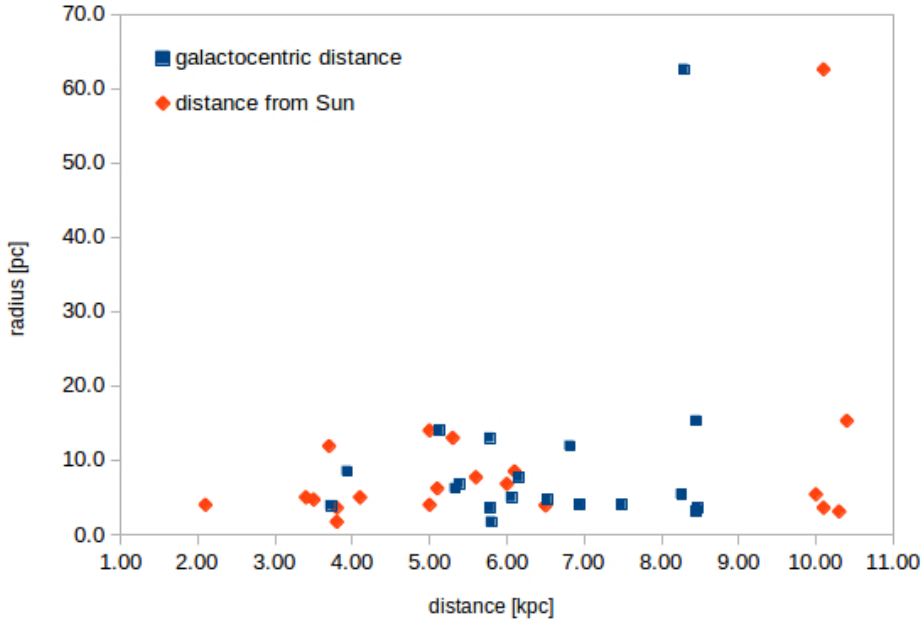

Figure 3.25: The graph shows non-correlation between the radius of the bubbles and their distance (galactocentric in blue, distance from Sun in red).

Only one of the studied bubbles has a significantly higher expansion velocity than this value - bubble N36 with its expansion velocity of 9 kms^{-1}. All the other bubbles show smaller values, between 5 and 7 kms^{-1}, therefore it is possible that they are not significantly expanding and their image is mainly scattered by the thermal motion.

The expansion of a bubble can be recognized as well in the way how the shape of a bubble is changing through velocity channels. If an HI envelope is "frozen" in a few velocity channels, it is probably not expanding. If there is a significant change of its shape (ideally, the envelope is getting larger until it reaches the central velocity channel, and getting smaller through the following channels), it is highly possible that the bubble is expanding. From the sample of studied bubbles, only two bubbles significantly show this behavior - bubble N35 and the already mentioned N36. Both bubbles show expected change of the shape, especially through higher velocity channels. A good example of such a development is shown in Fig. 3.26, where an evolution of the bubble N35 is seen through 15 velocity channels. Other studied bubbles seem to be more static, appearing mostly in the same shape through several channels ($v_{\mathrm{exp}} \simeq (5-7)$ kms^{-1}). A good example is bubble N107, which shows similar shape through 6 velocity channels (Fig. 3.27).

There is a special development in a case of the absorption bubble N76. It seems to be evolving through two stages: it appears as an emission envelope through the channels of 75.2 to 77.7 kms^{-1}, changing into an absorption envelope at channels of 78.5 to 82.6 kms^{-1}, at 85.5 kms^{-1} something like a transition phase is visible, and from the channel of 84.3 kms^{-1} it gets back into an emission envelope, getting smaller until it reaches 87.6 kms^{-1} (see Fig. 3.28). Contrary, the other absorption bubbles seem to be

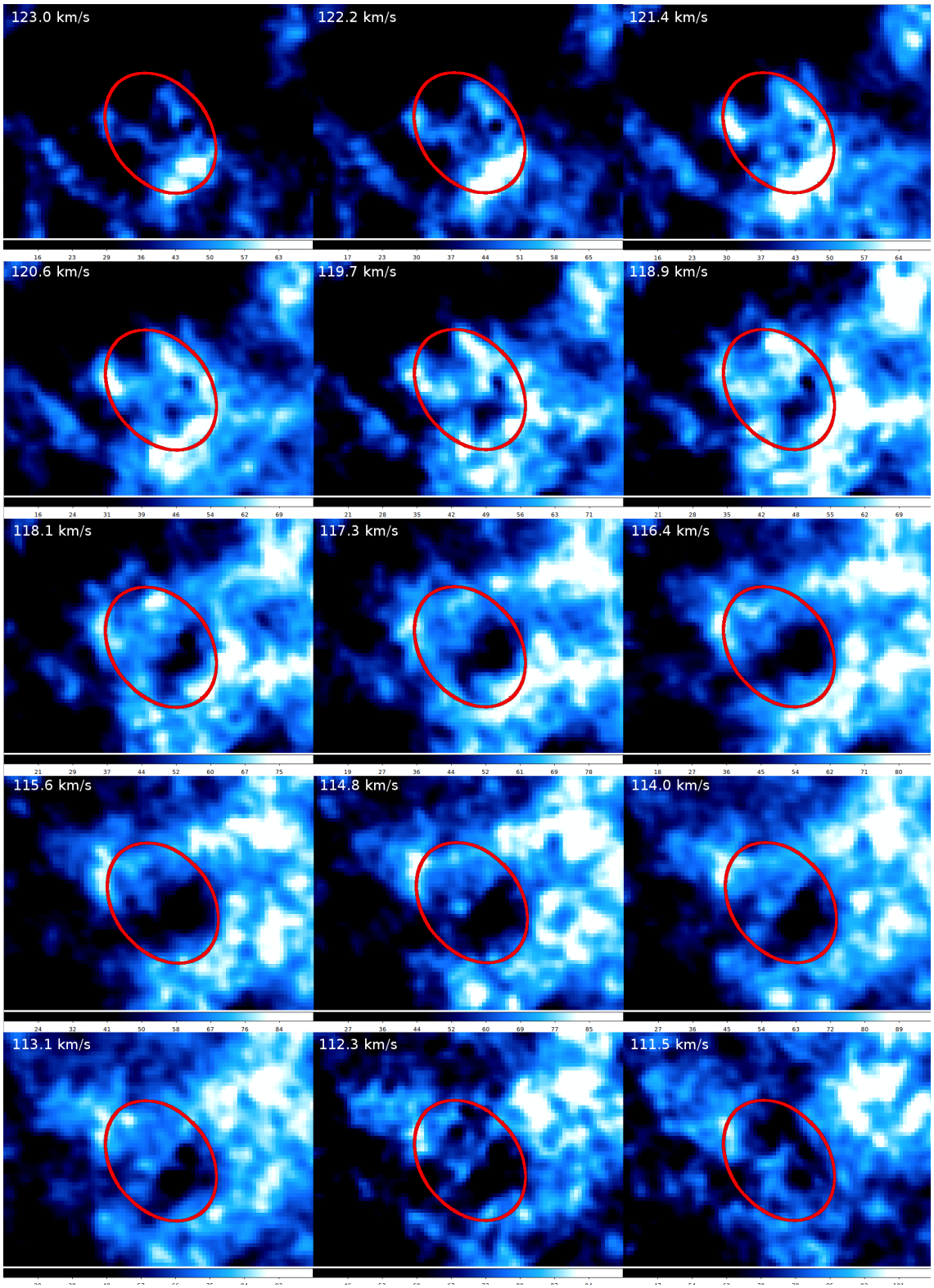

Figure 3.26: The bubble N35 and its change through 15 velocity channels. HI data are in blue, red ellipse marks the infrared bubble.

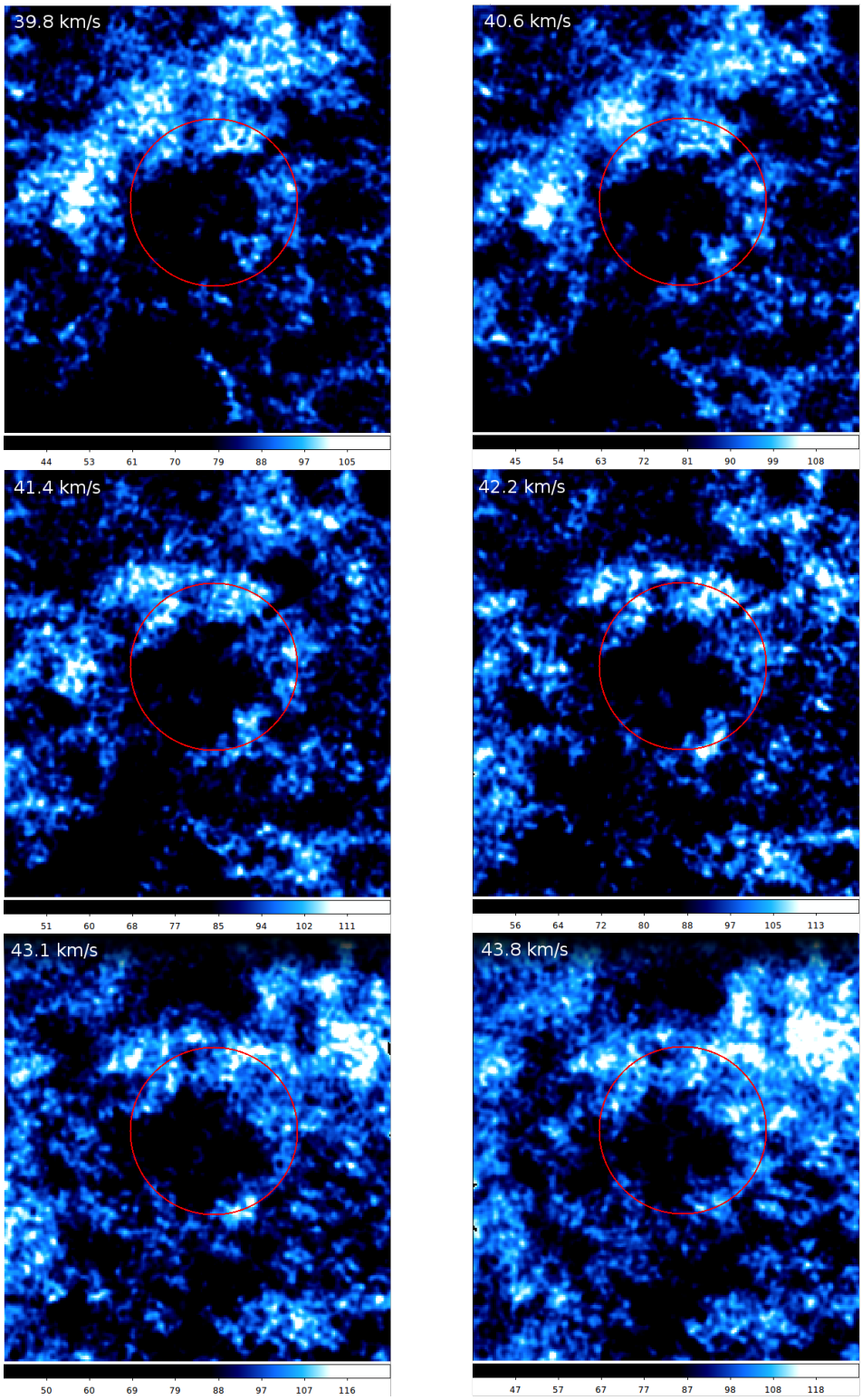

Figure 3.27: The bubble N107 as an example of non-expanding bubble, showing the same shape of an envelope through several velocity channels. HI data are in blue, red ellipse marks the infrared bubble.

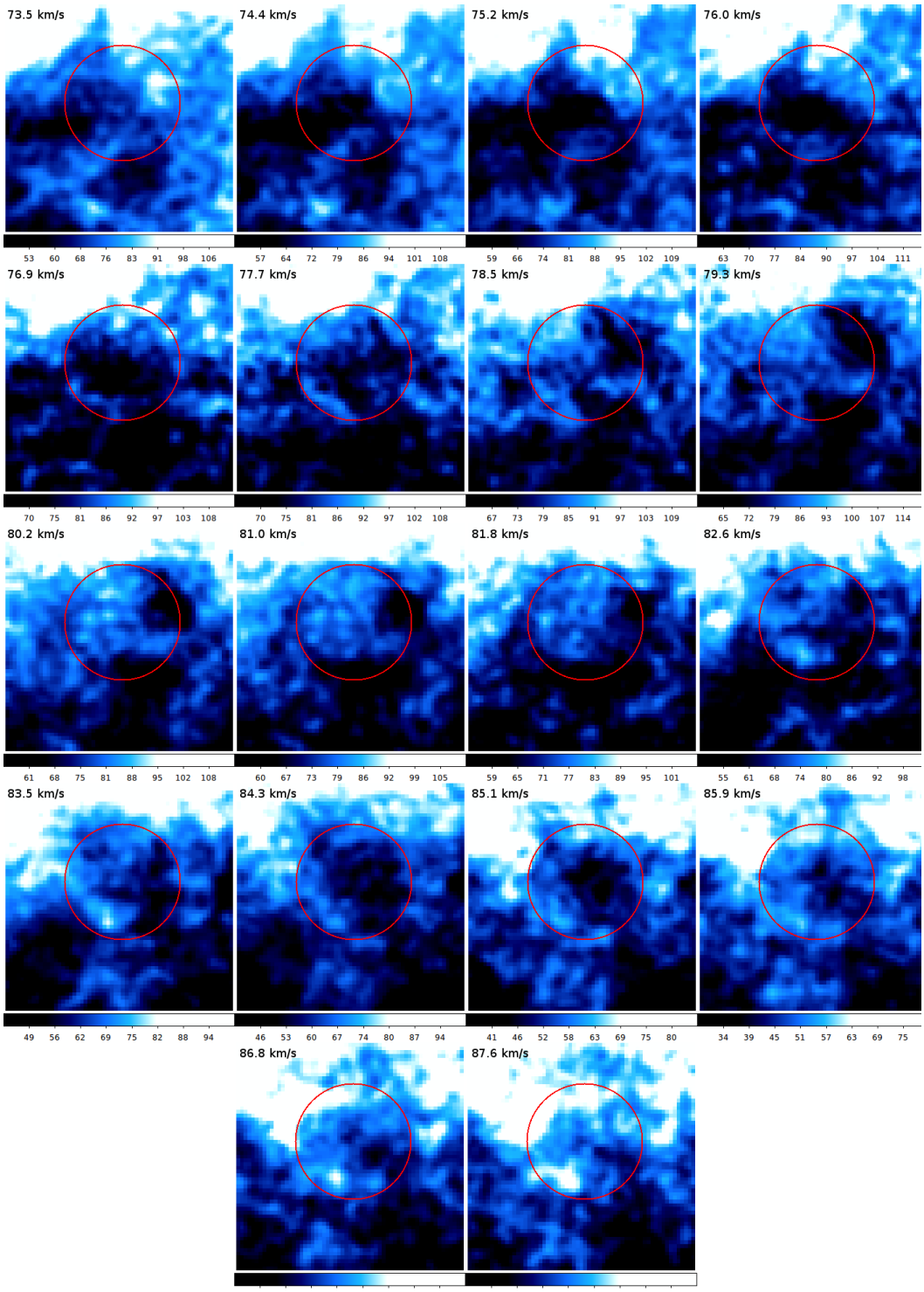

Figure 3.28: Development of the bubble N76, which changes the forms of its envelope - first the bubble is visible as an emission envelope from 75.2 to 77.7 kms^{-1}, then as an absorption envelope from 78.5 to 82.6 kms^{-1}, and then back as an emission envelope. HI data are in blue, red ellipse marks the infrared bubble.

static and do not show such behavior.

The bubbles are also visible in position-velocity diagrams, such as *bv* diagrams, which are shown in Fig. 3.15, 3.21 and 3.24 from the previous sections. The best examples are shown in Fig. 3.29. Most of the bubbles are nicely visible in HI *bv* diagrams, but some of them are more clearly visible in CO *bv* diagrams. The absorption bubbles are also visible, especially N69 is a good example.

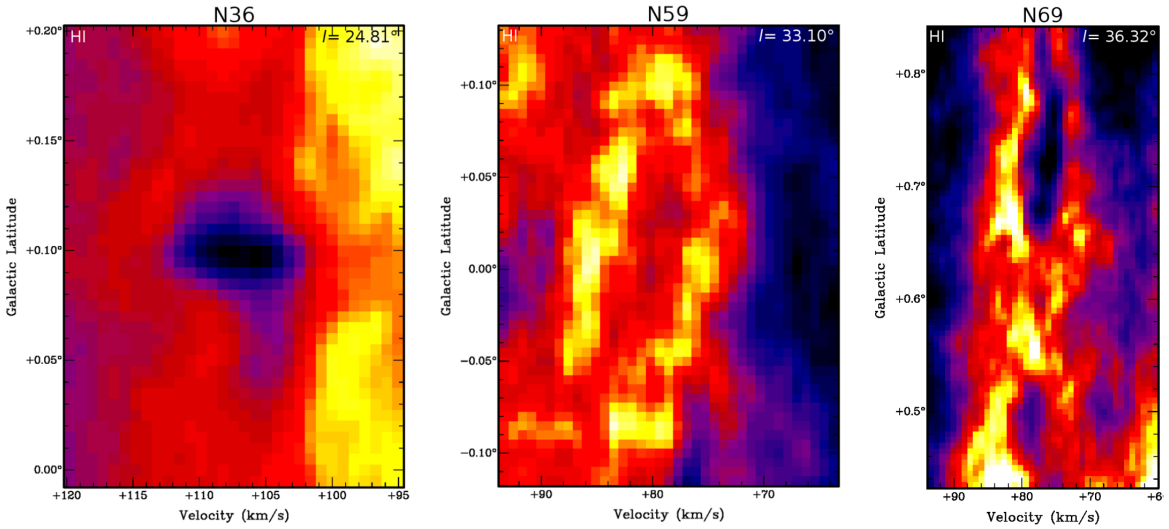

Figure 3.29: Three examples of position-velocity diagrams: the left panel shows a "hole" in the HI emission (N36), the middle panel shows a bubble with significant walls (N59), and the right panel shows the absorption walls of N69. It is obvious that there is no approaching, nor receding wall in the case of the absorption bubble N69.

3.6.3 Bubbles or rings?

Compared to HI observations, CO emission seems not to be evolving, or significantly changing its distribution with a change in velocity channels. The emission is usually visible in a few velocity channels (usually in a smaller velocity range than HI emission). The CO emission appears in a similar shape through those channels and unlike some of the HI envelopes, which are showing clear (or at least some) expansion, CO distribution does not change much from each channels (with one exception, see below). It seems that the molecular content of the studied bubbles is distributed in a flat ring, rather than in a 3D bubble. This idea is not new, Beaumont and Williams [34] already suggested that the majority of bubbles are actually rings (Fig. 3.30). But their work is based on observations of molecular gas, but not on neutral hydrogen observations. As described above, there are bubbles with HI emission development. The other bubbles, with no significant expansion, can be in a reality bubbles as well, not rings as Beaumont and Williams [34] suggested. Neutral hydrogen gas is more diffuse than molecular gas, therefore there is no reason, why bubbles should be just rings, not full spheres. However, molecular gas is more clumpy, filamentary and condensed, so there

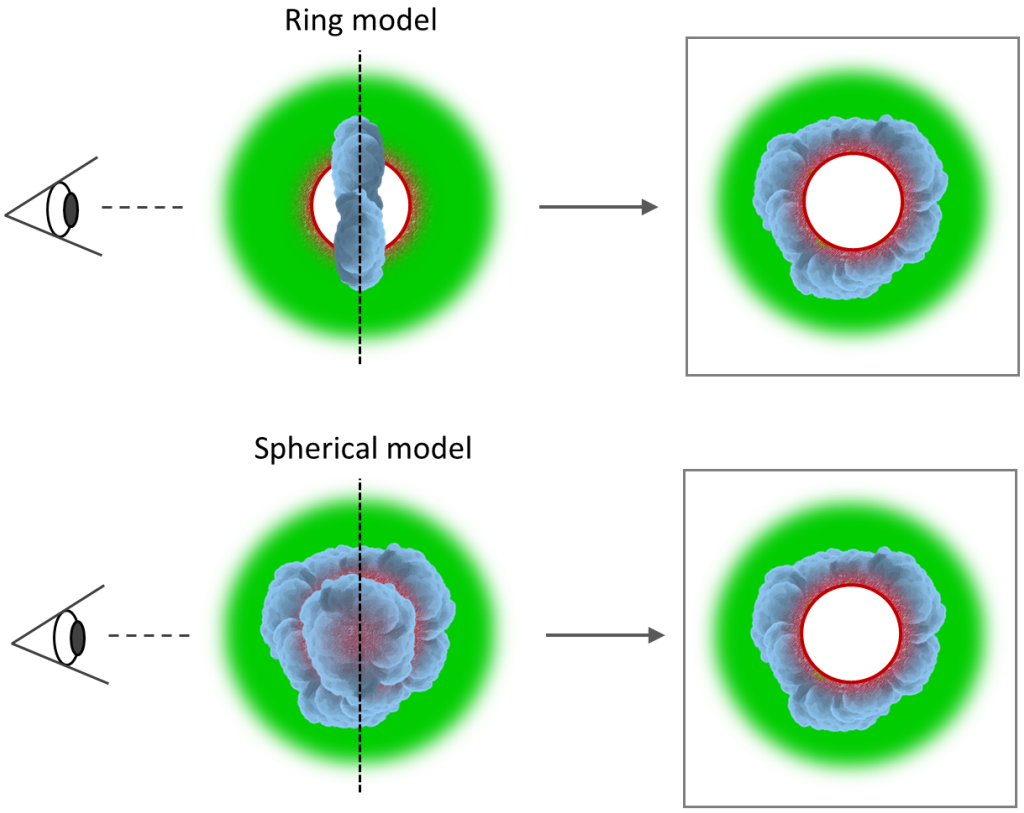

Figure 3.30: The map of CO emission would look the same at the central systemic velocity channel in both cases: in the case of a ring model (the upper row) and in the case of a spherical model (the bottom row). The green color shows HI emission, the red one IR emission and the blue clouds show CO emission.

is a possibility that the studied bubbles have rings of molecular gas, with no (or faint) front and back wall, but in HI they are still bubbles.

3.6.4 Mass

We determined the mass of atomic (HI) envelopes as well as molecular (H_2) envelopes (Tab. 3.3). 60% of HI envelopes are less massive than 10^3 $M_\odot$. The average mass of an HI envelope is about 3.4×10^3 $M_\odot$, while the median value is about 0.9×10^3 $M_\odot$. The difference between the average and the median value is caused by one extreme value of about 3.6×10^4 $M_\odot$, associated with the bubble N109. This bubble is also extremely massive in H_2 - about 1.7×10^5 $M_\odot$, which rises the average value of H_2 envelope to about 2.8×10^4 $M_\odot$, while the median is about 1.9×10^4 $M_\odot$. Almost all bubbles, except of N109, have H_2 mass lower than 5×10^4 $M_\odot$, from which 63% are less massive than 2×10^4 $M_\odot$.

Interesting is the range of the value M_{H_2}/M_{HI} (see Tab. 3.4), which shows the ratio between the mass of H_2 and HI envelopes. The range is between 1 to 130, the average

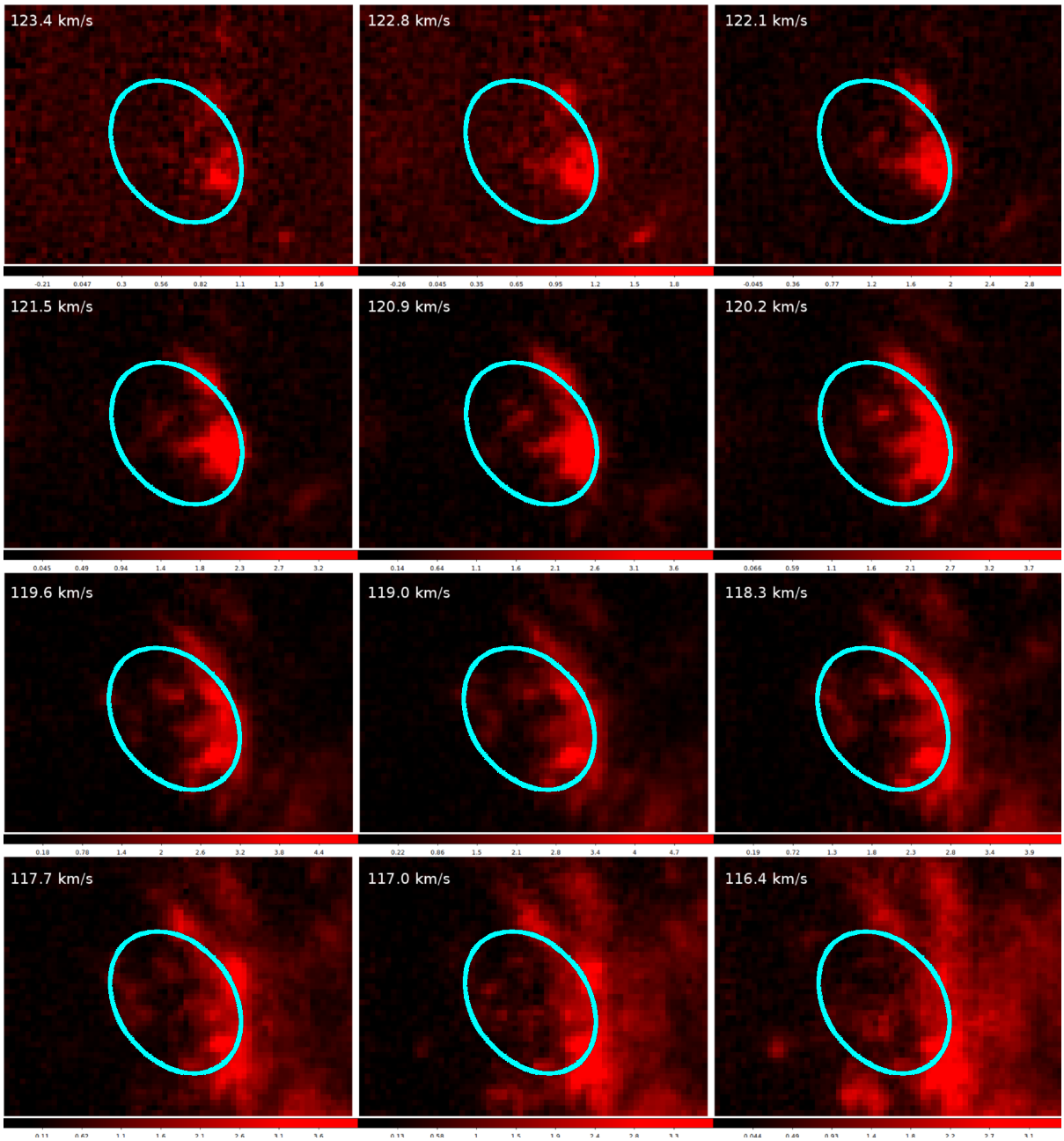

Figure 3.31: Development of the bubble N35 in CO emission. IR bubble is marked in turquoise ellipse, CO emission is in red.

value is about 33, while the median value is about 14. The higher value of average ratio is due to two extremes: the bubble N61 ($M_{H_2}/M_{HI} \cong 127$) and the bubble N115 ($M_{H_2}/M_{HI} \cong 115$). The ratio of most of the bubbles, about 65% of them, is lower than 20. Both bubbles showing the extreme values of the ratio between M_{H_2} and M_{HI} have similar morphology - both have a massive molecular cloud connected to the edge of their HI envelope. The majority of the mass is therefore located in the molecular cloud, but not along the envelope (see Fig. 3.34).

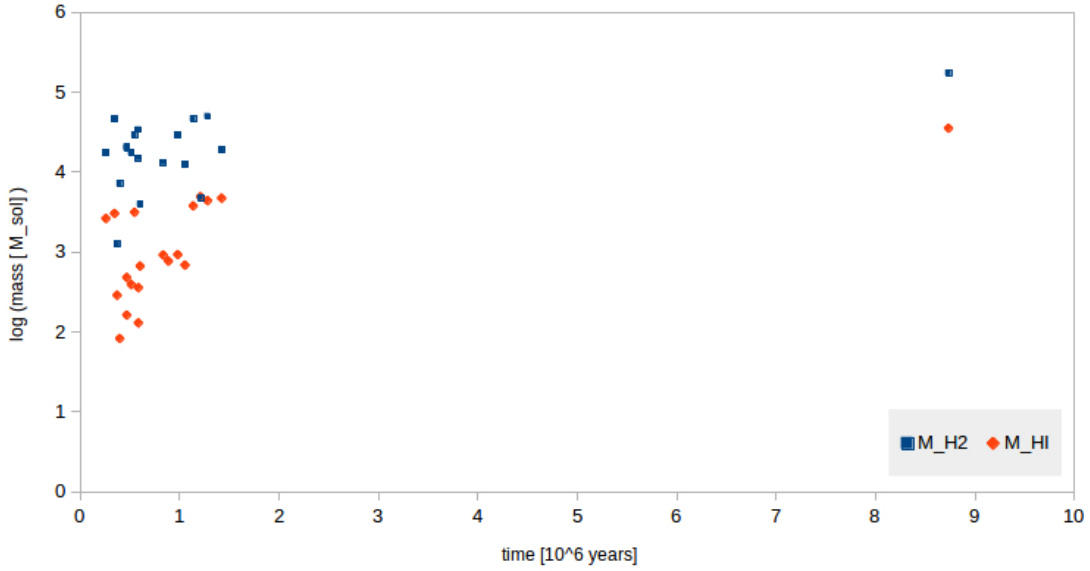

Figure 3.32: Relation between (logarithm of) mass of an envelope (HI in red, H_2 in blue) and its age.

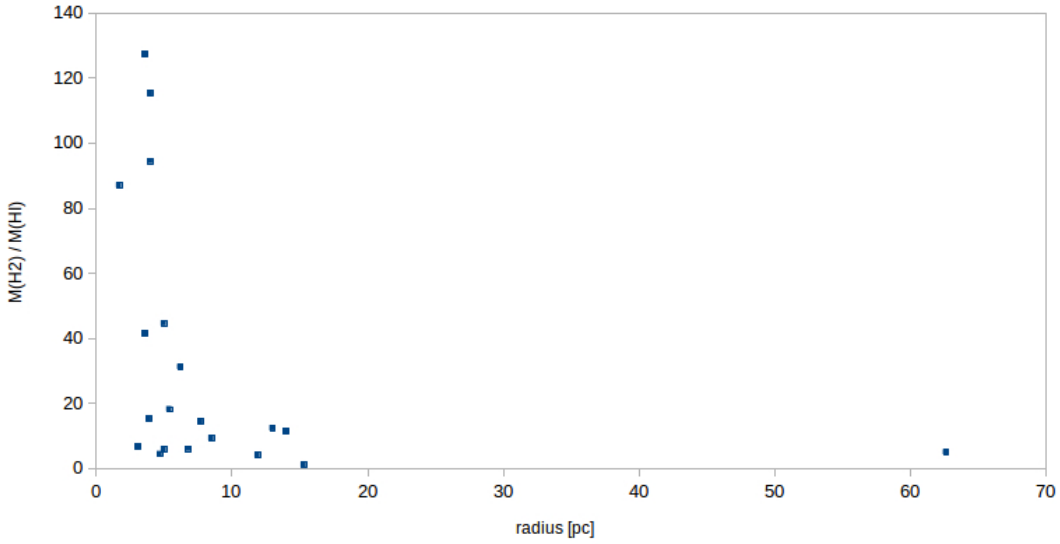

Figure 3.33: Relation between the ratio M_{H_2}/M_{HI} and the radius of bubbles.

There is a correlation between the mass of an envelope, both HI and H_2, with the radius and age of the bubbles. The older (and bigger) the envelope is, the more massive it gets (Fig. 3.32). However, from Fig. 3.33 it is visible that smaller and also younger bubbles have much more molecular gas associated with them compared to their HI envelopes, than larger bubbles (the correlation between the ratio M_{H_2}/M_{HI} and the radius of bubbles follows a power law). This can be caused by the fact that smaller

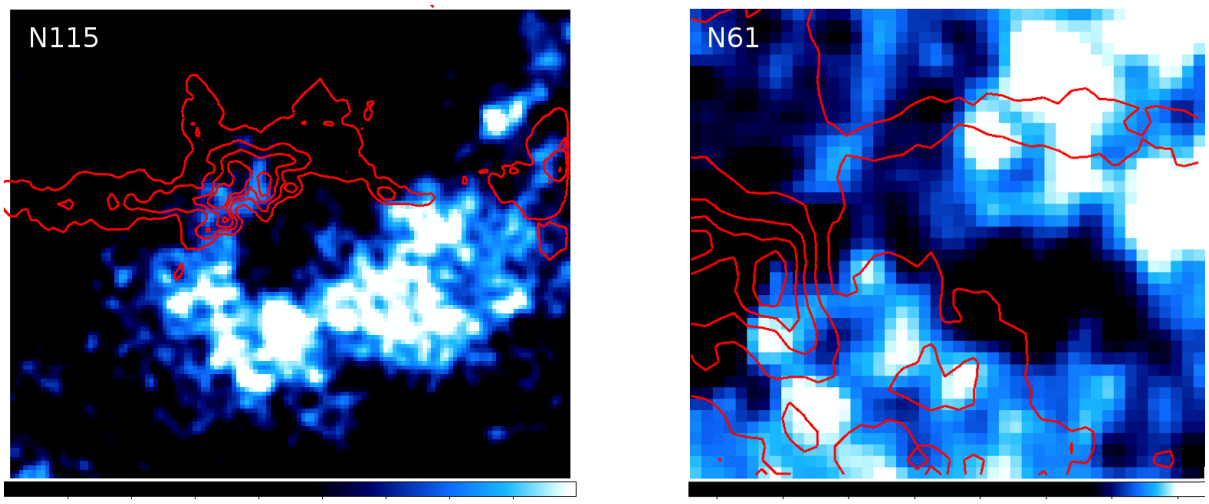

Figure 3.34: Bubbles N115 and N61 with the highest ratio of M_{H_2}/M_{HI}. HI emission is in blue, CO contours are in red.

bubbles are still embedded in (parts of) their maternal cloud, which rises the H_2 mass. However, this correlation can also show that there is no significant molecularization of atomic gas during the bubble expansion - the ratio M_{H_2}/M_{HI} is decreasing with the radius/age of bubbles and, as described in the following chapter, H_2 column densities are decreasing with the radius of bubbles, while HI column densities are increasing. Therefore, HI matter is probably being accumulated during the expansion, but probably does not effectively form H_2.

Column densities of studied bubbles

Bubble	N_{HI} [cm^{-2}]	N_{H_2} [cm^{-2}]	$\frac{n_{H_2}}{n_{HI}}$	$\frac{M_{H_2}}{M_{HI}}$	Bubble	N_{HI} [cm^{-2}]	N_{H_2} [cm^{-2}]	$\frac{n_{H_2}}{n_{HI}}$	$\frac{M_{H_2}}{M_{HI}}$
N35	$1.1{\cdot}10^{21}$	$1.4{\cdot}10^{22}$	12.5	15.2	N100	$1.1{\cdot}10^{21}$	$1.9{\cdot}10^{21}$	1.8	14.3
N36	$1.3{\cdot}10^{21}$	$1.2{\cdot}10^{22}$	9.2	9.2	N107	$8.3{\cdot}10^{20}$	$3.8{\cdot}10^{21}$	4.5	4.0
N59	$9.7{\cdot}10^{20}$	$8.2{\cdot}10^{21}$	8.4	11.3	N108	$8.6{\cdot}10^{20}$	$1.1{\cdot}10^{21}$	1.3	1.0
N61	$3.6{\cdot}10^{20}$	$1.4{\cdot}10^{22}$	37.8	127.4	N109	$7.5{\cdot}10^{20}$	$5.1{\cdot}10^{21}$	6.7	4.9
N62	$2.8{\cdot}10^{20}$	$7.4{\cdot}10^{21}$	26.5	87.0	N111	$4.1{\cdot}10^{20}$	$5.4{\cdot}10^{21}$	13.0	41.4
N68	$8.8{\cdot}10^{20}$	$1.2{\cdot}10^{22}$	13.1	44.5	N113	$5.9{\cdot}10^{20}$	$1.3{\cdot}10^{22}$	21.8	6.6
N69	$3.4{\cdot}10^{20}$	$3.6{\cdot}10^{21}$	10.6	31.1	N114	$3.6{\cdot}10^{20}$	$4.1{\cdot}10^{21}$	11.2	18.2
N76	$5.0{\cdot}10^{20}$	$0.9{\cdot}10^{21}$	1.8	5.9	N115	$5.2{\cdot}10^{20}$	$2.4{\cdot}10^{22}$	45.5	115.4
N81	$8.9{\cdot}10^{20}$	$5.4{\cdot}10^{21}$	6.0	12.3	N116/7	$7.5{\cdot}10^{20}$	$5.1{\cdot}10^{22}$	68.0	94.4
N94	$6.6{\cdot}10^{20}$	$4.4{\cdot}10^{21}$	6.7	4.4	N119	$5.3{\cdot}10^{20}$	$2.7{\cdot}10^{21}$	5.1	5.8

Table 3.4: Column densities of studied bubbles determined in HI: N_{HI}, and in H_2: N_{H_2}, ratios between primordial densities and between masses determined in H_2 and HI for each of studied bubbles.

3.6.5 Densities

We determined column densities as well as primordial densities both for atomic and molecular hydrogen. The HI column densities range from $2.8 \times 10^{20} - 1.3 \times 10^{21}$ cm^{-2},

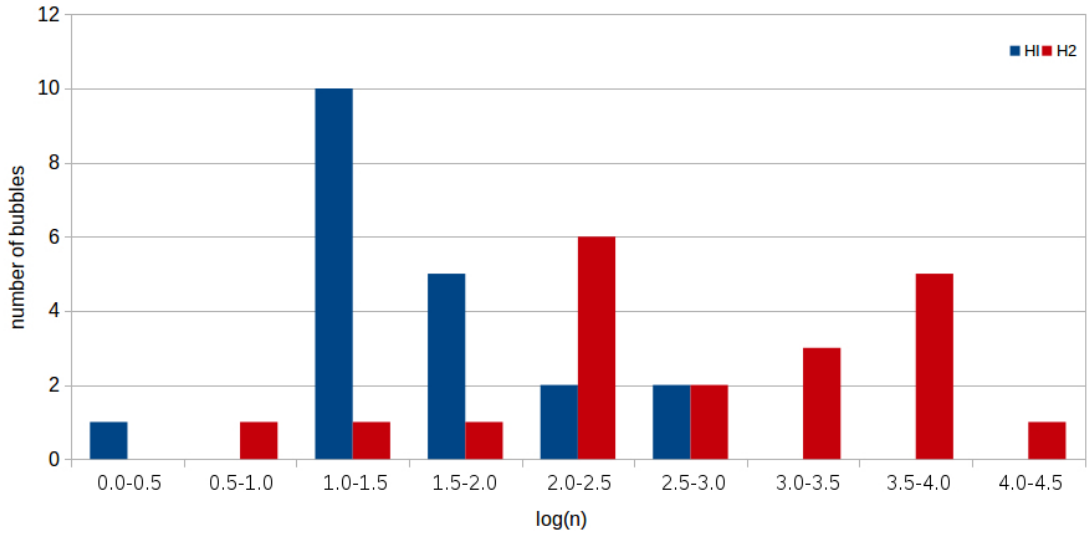

Figure 3.35: Bar chart showing the number of bubbles reaching particular densities of atomic (HI) and molecular (H_2) hydrogen.

while the average value is 7.0×10^{20} cm^{-2}. The range of H_2 column densities is from $9.0 \times 10^{20} - 5.1 \times 10^{22}$ cm^{-2}, while the average value is 9.6×10^{21} cm^{-2}. The range of HI primordial densities is from $1 - 860$ cm^{-3}, while the average value is about 2420 cm^{-3}. The range of H_2 primordial densities is from $7 - 14200$ cm^{-3}, while the average value is about 105 cm^{-3}. The correlation of primordial densities with radius is predictable as seen in Fig. 3.37, the bigger bubbles seem to expand into a lower density medium, than the smaller ones.

This is reflected also in Fig. 3.36, which shows the relation between (logarithm of) primordial densities of HI (n_{HI}) and H_2 (n_{H_2}). It seems that there is a limit of density values we can detect in CO (corresponding to n_{H_2}), as the increase in n_{H_2} becomes constant. Colors of the data relate to sizes of bubbles, going from red (the smallest) to purple (the largest bubbles). It is clearly visible that the smaller bubbles are expanding in denser medium (both reflected in n_{HI} and n_{H_2}).

However, the correlation between column densities and the radius of bubbles is different - while the H_2 column densities are decreasing with a higher radius, values of HI column densities are increasing as seen in Fig. 3.38. Perhaps, this can be a result of HI accumulation during the bubble expansion, while H_2 is not being accumulated and its column density is getting lower as molecular gas is spreading out along the bubble's edges.

3.6.6 Energy

The range of input energies is from 2.3×10^{49} erg to 1.4×10^{51} erg, the average input energy is 4.0×10^{50} erg. 90% of studied bubbles have their input energy lower than the supernova canonical value ($\sim 10^{51}$) erg, which shows that major progenitors of studied bubbles should be OB stars. It does not mean that the progenitors of bubbles with

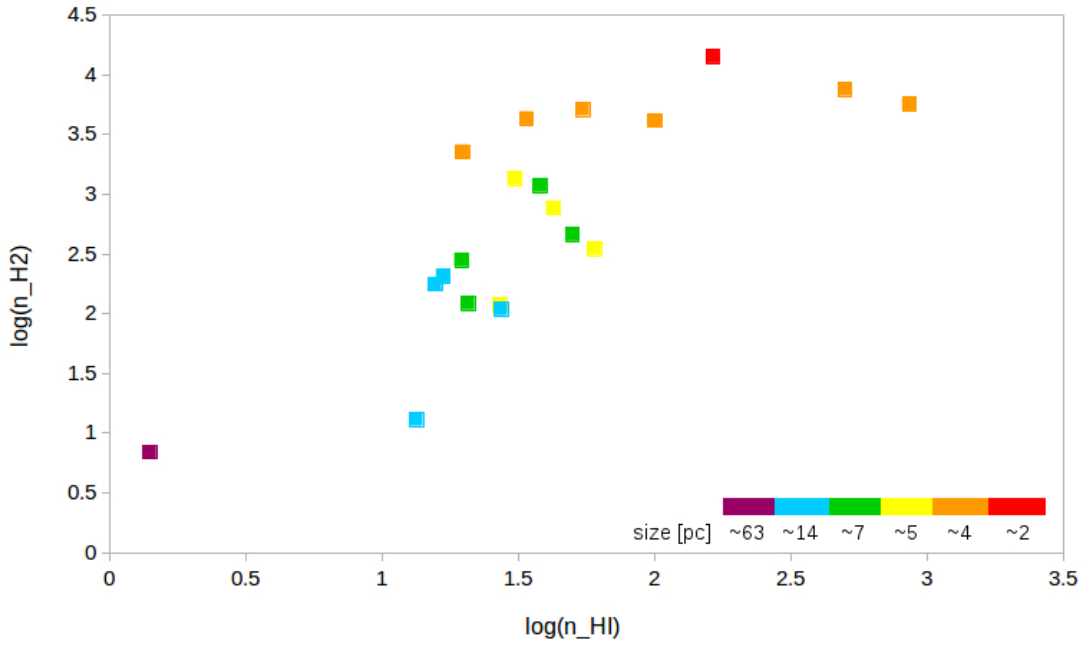

Figure 3.36: The relation between logarithm of primordial densities of HI (n_{HI}) and H_2 (n_{H_2}).

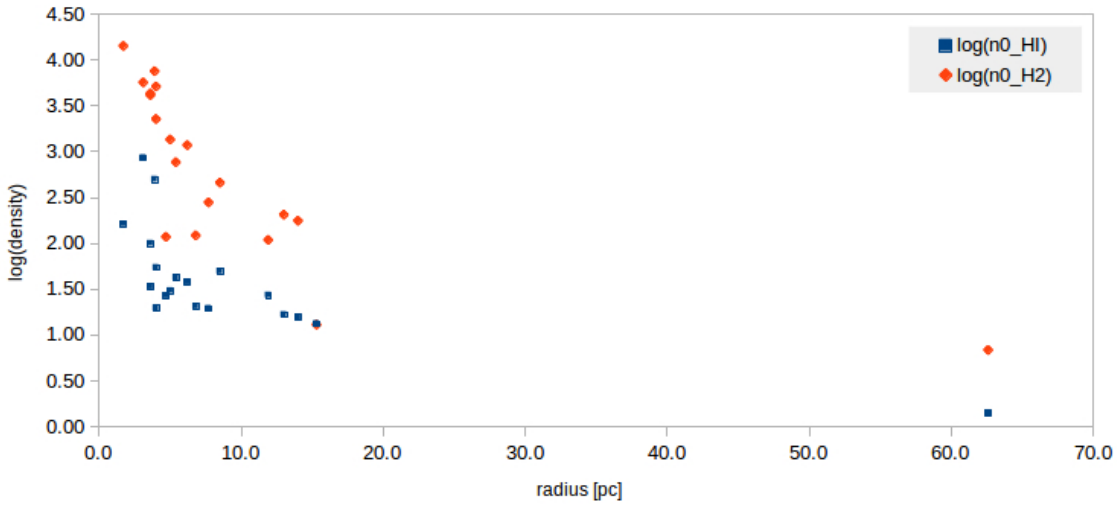

Figure 3.37: Correlation between primordial HI (blue), H_2 (red) densities and radius of bubbles.

input energy values similar to supernova have to be supernova events themselves (in our sample these are bubbles N35 and N109). The progenitors of these high energy bubbles could be even B stars, if the bubbles have enough time to expand. From estimated luminosities of progenitor stars (Tab. 3.3) we can see that the major progenitors are B type stars (luminosities between 100 and 15000 $L_\odot$). There is only one case, bubble N35, one of the two most energetic bubbles, whose progenitor star can be an O type star. In this case, but also in all other cases, it is possible that the ionizing star is

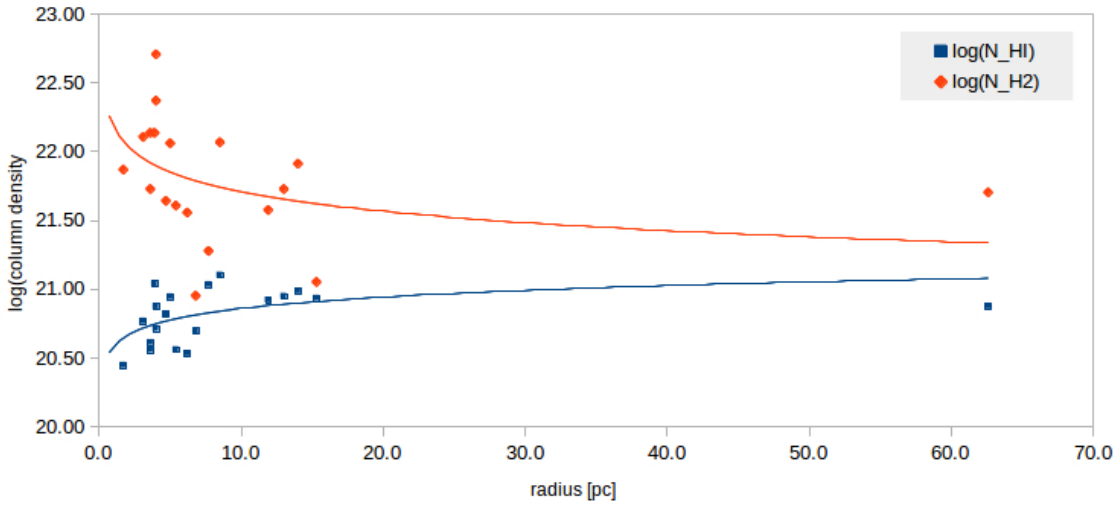

Figure 3.38: Correlation between column HI (blue), H_2 (red) densities and radius of bubbles.

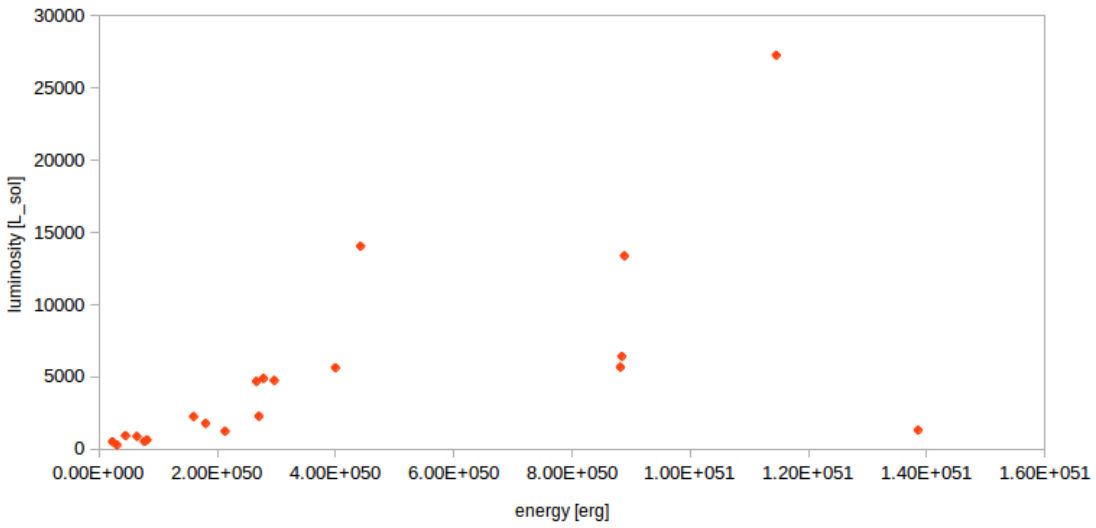

Figure 3.39: Correlation between estimated luminosity of progenitor star and energy input of a bubble.

not single. It could be several B stars ionizing the inner parts of N35 bubble. It is also important to notice that these luminosities, energies and ages are only estimates. The range of luminosities is from about 500 to 27300 $L_\odot$), while the average value is about 5000 $L_\odot$).

3.6.7 Age

We estimated two different possibilities of age of the studied bubbles. The first estimate is based on the fact that the progenitor of a bubble would be a supernova t_{SN}, the

second estimate assumes that the progenitor is an OB star t_{OB}. According to energy input requirements we assume that most (probably all) of the bubbles are created by a stellar feedback of OB stars that is why we use t_{OB} as a more probable result. The range of ages is from 0.3 to 8.7 millions of years, the average value is 1.1 million years, while the median value is 0.6 million years. There is no correlation between age of a bubble and its energy input. As expected, more energetic bubbles are produced by more luminous stars (Fig. 3.39).

3.7 Discussion

We studied the atomic and molecular content of interstellar bubbles. HI counterparts of IR bubbles have various forms. Some of the bubbles are clearly visible as bright envelopes, forming a nice shell against the noisy background. Some bubbles are recognizable in HI data only as holes, without any convincing HI envelope. Interestingly, some bubbles are found in a form of absorption envelopes, reflecting probably the fact that these envelopes are formed of CNM (Fig. 3.6).

Most of the HI envelopes, which we found, are closed. Only one fifth of the bubbles are open and only one bubble from our sample is a loop. Smaller (and younger) bubbles tend to have larger HI envelopes, compared to their IR size. This is probably caused by the fact that younger bubbles are still evolving in the primordial cloud, or its remnants. We assume that their HI envelopes are formed not only by the collected neutral medium, but also by the surrounding material, through which the shock front did not pass yet. As a bubble grows, the ratio between radius of an HI envelope and an IR bubble, according to our results, lowers down (see Fig. 3.7). An HI envelope of a small bubble, with r_{IR} of 1 pc, would be 2.5 times larger. An HI envelope of a large bubble with r_{IR} of 30 pc would be only 1.1 times larger. This leads us to a conclusion that, as the evolution of a bubble continues, there is more shocked, thus compressed, material in the HI envelope. Therefore there is a decrease of r_{HI}/r_{IR} with an increasing size/age of a bubble.

The majority of bubbles have a radius smaller than 15 pc, while the typical radius is about 5 pc. We cannot determine which of the bubbles are expanding, as we usually do not detect any signs of an expansion. Most of the bubbles reach expansion velocities between 5 and 7 kms^{-1}. This value is comparable to thermal velocity of hydrogen atoms, therefore it is not clear, whether the bubbles are expanding or not. There is only one exception, the bubble N36, whose expansion velocity reaches $\sim$ 9 kms^{-1} (see the position-velocity diagram in Fig. 3.15).

Compared to HI emission, CO emission is more compact and located along the rims of infrared bubbles. It seems that CO emission is not well correlated with HI emission. Although all of the studied bubbles show that at least some part of their CO emission lies in the HI envelopes, it is covering only about 30% of their HI envelopes. The majority of CO emission is distributed somewhere else than in the HI walls.

It seems that the molecular content of bubbles is distributed in a ring, rather than in a 3D bubble, which corresponds to Beaumont and Williams [34]. The star formation takes place in molecular clouds, which have a filamentary structure. When the

bubble is evolving in such a medium, it is possible that it soon reaches the edges of the cloud. Then, as Beaumont and Williams [34] suggested, the distribution of molecular gas would resemble more a ring than a bubble, with a thickness of the primordial cloud. From our results, at least 75% of studied bubbles show CO emission highly concentrated along IR rims, however still fragmented, not following the full circuits of the IR bubbles. Neither approaching, nor receding walls are observed in CO emission. There is only one example of a bubble, which shows a clear development throughout velocity channels (bubble N35, see the development is Fig. 3.31). Therefore, it is possible that the molecular content of bubbles, in general, is distributed in a ring. An alternative explanation is that the approaching and receding walls are simply hard to detect, as the column densities would be too low. We have to point out that this possible ring distribution applies only to the molecular content of bubbles, not the atomic content.

The typical mass of an HI envelope is about 1×10^3 $M_\odot$, while the molecular content has typically about 2×10^4 $M_\odot$. There is one extreme bubble, whose derived properties exceeded most of the average results. It is the bubble N109, whose HI content has about 4×10^4 $M_\odot$ and molecular content about 12×10^5 $M_\odot$. The correlation between radius and M_{H_2}/M_{HI} (Fig. 3.33) shows that the smaller (and also younger) bubbles have larger amount of molecular gas associated with them compared to their HI envelopes, than their larger counterparts. This can be caused by the fact that smaller bubbles are still embedded in their maternal cloud, which rises the H_2 mass.

There were hypotheses that accumulation of HI gas can lead to molecularization of the collected gas during an expansion of a bubble. However, according to our results, we do not see any evidence of this process. The ratio M_{H_2}/M_{HI} is decreasing with the radius/age of bubbles, which is mirrored in decreasing H_2 column densities and increasing HI column densities with the radius/age. Therefore, we suppose that the atomic matter is being collected and accumulated during the expansion, but probably does not effectively form H_2. The decrease in H_2 column density during the expansion of a bubble is probably caused by spreading out of molecular gas along the bubble's edges.

According to energy input requirements we assume that most (probably all) of the bubbles are created by the stellar feedback of OB stars. 90% of the studied bubbles have their input energy lower than the supernova canonical value of $\sim 10^{51}$ erg. Based on our estimates of luminosities, we suggest that B type stars are the main progenitors of interstellar bubbles.

Along with our analysis of atomic content of interstellar bubbles, we discovered an interesting and probably new type of HI envelopes of bubbles. These envelopes are not observed in HI emission, but in HI absorption. They seem to be much more compact than the envelopes detected in HI emission, and they copy their infrared counterparts better than the HI emission envelopes. These absorption envelopes are probably formed by CNM, much colder and denser gas than WNM, which is responsible for HI emission envelopes. We found that four out of twenty bubbles from our sample show this type of an absorption envelope, which makes it an important feature to be studied in future.

Chapter 4

Colliding interstellar bubbles

During the research of infrared bubbles N115, N116 and N117 we found that both bubbles are lying on the rims of a larger infrared shell G053.9+0.2. We decided to study this region in more details and soon we found out that its structure is more complicated. It contains two different systems of six bubbles in total, two of them newly discovered by our research. These systems lie separately at different distances and only due to infrared and radio-continuum images it seems that they are overlapping. Furthermore, these two independent systems seem to be similar: both are formed by three bubbles, of which the two largest ones seem to collide. In the position of the collision the third and smallest bubble is sitting, revealing recent star formation.

In the following sections we first provide a brief summary of what is known about the studied region. Afterwards, we characterize each system, together with a detailed description of individual bubbles. We portray both regions according to the calculated properties and discuss possible progenitors of bubbles.

4.1 Previous studies of the region

One of the most dominant feature of the region is a supernova remnant SNR G54.4-0.3, studied by Junkes, Fuerst, and Reich [118] (see Fig.4.4, the left-hand panel). This bright radio remnant is connected to the CO emission at $v_{\mathrm{LSR}} = 40.0$ kms^{-1}.

There is another large radio object in the vicinity of SNR G54.4-0.3. It is a radio loop G053.9+0.2, discovered by Leahy, Tian, and Wang [119] as a large-scale shell in 1420 MHz radio-continuum VLA observations. It was found that this radio loop has its counterpart in the infrared data, which itself is associated with few HII regions and CO emission. These associated regions show velocities around $v_{\mathrm{LSR}} = 40.0$ kms^{-1}.

The progenitor of the radio loop was extensively researched, but with no definite result. There is a pulsar wind nebula projected to the rims of the radio loop, but according to Leahy, Tian, and Wang [119], this nebula is not physically associated with the radio loop, as it most likely lies at a different radial velocity (53 kms^{-1}). The progenitor of the pulsar wind nebula is a young pulsar (about 2900 years old) PSR J1930+1852, which was lately found to be connected to the supernova remnant SNR054.1+0.3 [120].

The infrared bubbles N115, N116, and N117, discovered and cataloged by Churchwell et al. [1], seem to lie precisely on the borders of the radio loop G053.9+0.2. The CO and the HII regions in the radio loop's neighborhood were broadly studied by Xu and Ju [121]. They showed that the bubbles N116 and N117 are connected to the larger radio loop. According to their results, the radial velocity of N116/7 is $\sim$ 38 kms^{-1}. Contrary, bubble N115 is not associated with the radio loop, due to its different velocity: $v_{\rm LSR} = 24.0$ kms^{-1} [122].

For a good comparison between the knowledge of the region before and after our research, we illustrate the region in the Fig. 4.1, according to results of Xu and Ju [121]. This figure shows that the radio loop G053.9+0.2 was known to be connected to bubbles N116 and N117. Although the radial velocity of the SNR G54.4-0.3 was known as well, it was not associated with neither the radio loop G053.9+0.2, nor bubbles N116 and N117. The panel also shows the isolation of N115, lying on a different distance.

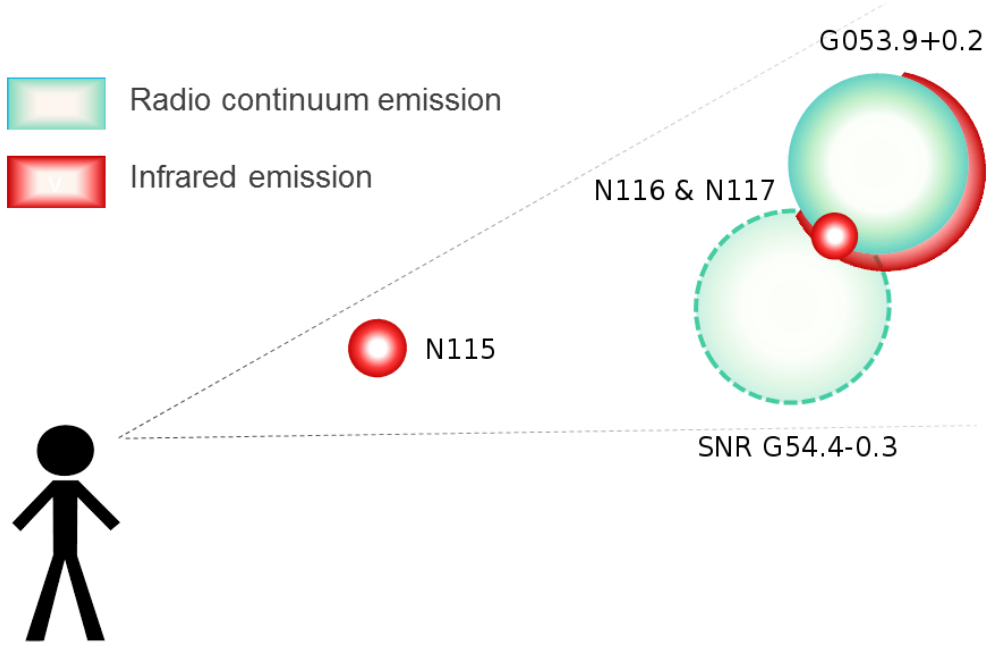

Figure 4.1: Cartoon of the region surrounding G053.9+00.2 according to Xu and Ju [121]: N116+117 connected to the radio loop G053.9+0.2 and the independent N115 and SNR G54.4-0.3.

Name	l [deg]	b [deg]	v_r [kms^{-1}]	d [arcmin]	Prominent data	System	Alternative name
Bubble A	53.885	+0.180	41.4	39	radio continuum	B	Leahy's large-scale bubble
Bubble B	54.498	-0.303	40.0	45	radio continuum	B	SNR G54.4-00.3
Bubble C	54.089	-0.087	40.0	5	IR emission	B	N116 & N117
Bubble D	53.821	+0.302	25.0	78	HI line	F	-
Bubble E	53.257	-0.419	24.9	54	HI line	F	-
Bubble F	53.556	-0.014	24.1	13	IR emission	F	N115

Table 4.1: Measured properties of the studied bubbles: positions, radial velocities, and diameters, together with wavelengths, where the bubble is nicely seen or where it was previously detected and described. 'B' and 'F' stands for the background or foreground system.

4.2 Results

We confirmed the connection of bubbles N116+N117 with Leahy's large-scale radio-continuum bubble [121], all having a radial velocity around $v_{\rm LSR} \simeq 40$ kms^{-1}. We assume that these bubbles are also connected to the second radio bubble, SNR G54.4-00.3. All these bubbles are therefore lying at the same distance, which is about 5 kpc. This distance corresponds to the tangential point, due to their radial velocity of 40 kms^{-1} being close to the terminal velocity in the considered direction. For clarity we named this system the background system and we named its member bubbles Bubble A (Leahy's large-scale bubble), Bubble B (SNR G54.4-00.3) and Bubble C (N116 & N117; according to our results we think that bubbles N116 and N117 are in fact one bubble. Details are given below). The cartoon of our image of the region is in Fig. 4.2.

According to our results, the bubble N115 is lying at the radial velocity of $v_{\rm LSR} \simeq$ 24 kms^{-1}, whose kinematic distance can be both near (2.1 kpc) and far (8.0 kpc). We adopt the near kinematic distance, as most of the authors did. In following chapters we describe reasons for our choice based on our calculated results. Because the distance of N115 is smaller than the distance of N116+N117 and its surrounding bubbles, we named the system of N115 the foreground system. Interestingly, we found that in the vicinity of the bubble N115 two large bubbles exist. These bubbles are best visible in HI data and they are about five times larger than the bubble N115. For clarity we named these bubbles Bubble D, Bubble E and Bubble F (N115).

All is summarized in two tables: Tab. 4.1 gives an overview of the identified bubbles, their positions, radial velocities, diameters, wavelengths of best visibility, system membership and alternate names. Tab. 4.2 summarizes the main properties of all bubbles: dimensions, derived masses and densities (Eqs. 3.3-3.5), and energy input (Eq. 3.8).

The most interesting fact from our results seems to be a possible collision of bubbles from both systems. Just from a first glance it is obvious, how both systems are similar. They are formed by two large bubbles, with radii around 20 – 30 pc and ages of a few million years, and a smaller ($\sim$ 4pc) and younger (less than a million years old) bubble. These smaller bubbles (Bubble C in the case of the background system and Bubble F in the foreground system) are sitting in the place, where larger bubbles interact with each other. It is therefore possible, as discussed later, that large bubbles are in fact colliding. In the place of collision a recent star formation takes place and results in a creation of new bubbles (Bubble C, Bubble F). Fig. 4.2 illustrates the distribution of the systems together with their member bubbles.

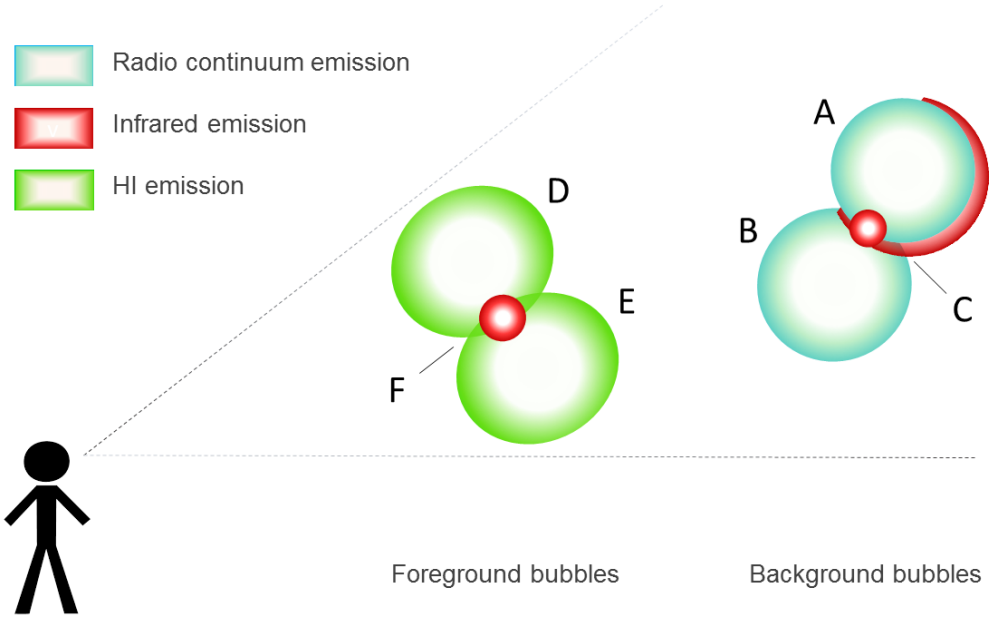

Figure 4.2: Cartoon of the region with all previously known and newly identified bubbles. There are two systems: a foreground system (larger Bubbles D and E and a small Bubble F = N115); and the background system (bubbles A = a radio loop GS053.9+0.2, B = SNR G054.4-0.3 and small C = N116+117).

The following chapters are describing both systems separately, together with their member bubbles and derived properties.

Bubble	R [pc]	v_{exp} [kms^{-1}]	M_{HI} [M$_\odot$]	M_{H_2} [M$_\odot$]	n_{HI} [cm^{-3}]	n_{H_2} [cm^{-3}]	E [10^{50}erg]	age [Myr]
A	28	7	$2.4{\cdot}10^4$	$1.4{\cdot}10^5$	13	31	4.0	2.7
B	32	50 *	$1.2{\cdot}10^4$	$1.4{\cdot}10^5$	3.4	19	26.0	0.3*
C	4	4	360	$3.4{\cdot}10^4$	160	$7.5{\cdot}10^3$	> 0.028	0.5
D	23	5	$2.4{\cdot}10^3$	$5.6{\cdot}10^4$	1.8	20	0.19	3.6
E	17	6	$2.1{\cdot}10^3$	$3.0{\cdot}10^4$	3.9	26	0.21	2.3
F	4	4	130	$1.5{\cdot}10^4$	23	$1.3{\cdot}10^3$	> 0.008	0.6

Table 4.2: Properties of identified bubbles. R is the mean radius, v_{exp} is the expansion velocity, M_{HI} is the mass of the bubble in HI, M_{H_2} is the molecular mass derived from CO observations, n is the density of the medium into which the bubble was expanding (derived from HI and CO), and E is the energy needed to create the bubble. Bubble B is the special case: its expansion velocity does not come from our measurements and its age is likely to be greater (see the Section 3.1.1).

4.2.1 Background system

The background system is centered around Bubble C at the radial velocity of about 40 kms^{-1}. This velocity corresponds to a distance of approximately 5 kpc. The diameters of large bubbles A and B are 39′ and 45′, respectively. The typical size in all studied spectral regions of Bubble C is 5′. In linear dimensions, A corresponds to 56 pc, B to 65 pc, and C to 7 pc. The best spectral region to see all bubbles of the background system is the radio-continuum emission. In the other data, mainly Bubble C is well observed, the other bubbles show only parts of their structure or no significant structure at all (i.e. Bubble B is not recognized in HI data and in CO there are only hints of associated emission). The detailed description of bubbles and their visibility in multiwavelength observations is included in the following sections. The results and comments about determined properties, such as mass or density, are in the last section.

Bubble A

Bubble A is visible in the radio-continuum images as a closed irregular ring. The bubble is seen also in the infrared data, where the northeastern part matches its counterpart from the radio-continuum image (see Fig. 4.4, left-hand panel, the upper bubble). The outline of the infrared emission borders the radio-continuum emission, making it inside the infrared bubble. Although Leahy, Tian, and Wang [119] suggested that the radio bubble and the infrared bubble are two different objects, due to the spatial shift of the infrared walls, we suggest that the radio bubble and the infrared bubble are the same object. The radio-continuum emission comes from the inner parts of the bubble and the infrared emission comes from its walls.

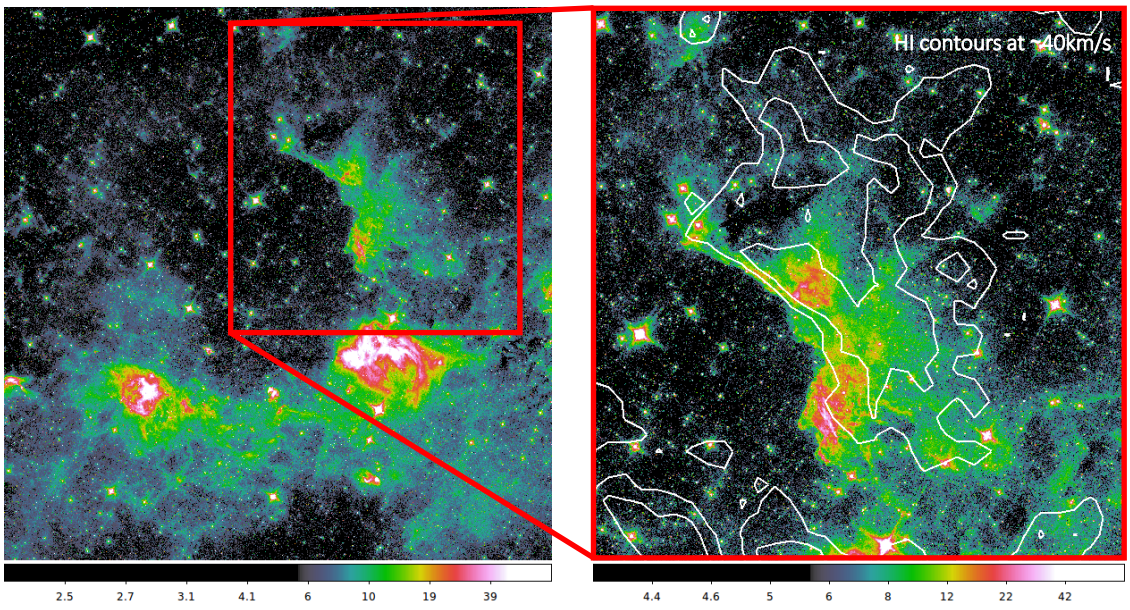

Figure 4.3: The northeastern part of Bubble A is visible both in IR and HI data. This feature is located at $\sim$ 40 kms^{-1}. The background image is infrared, countours are from HI data, with levels of 90 and 100 K.

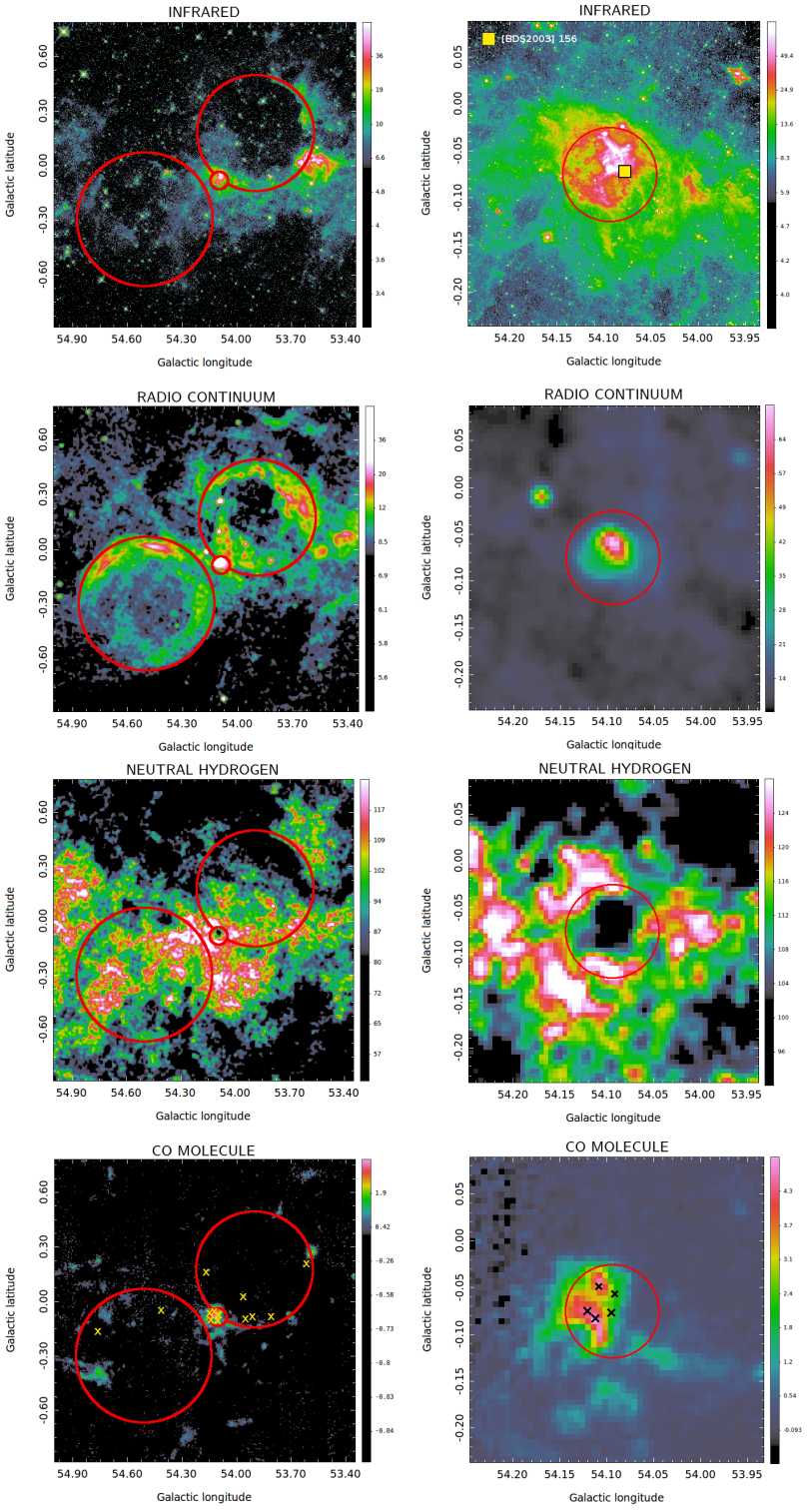

Figure 4.4: Multiwavelength image of the background system (left: the total system, right: the small central region). Positions of bubbles A (G053.9+0.2, upper right), B (SNR G54.4-0.3, lower left), and C (N116+N117, small in the middle) are overlaid. The HI is summed over the velocity interval: 38.9 kms^{-1} $< v_{LSR} <$ 42.2 kms^{-1} (left) and 39.8 kms^{-1} $< v_{LSR} <$ 42.2 kms^{-1} (right), the CO over the interval: 38.6 kms^{-1} $< v_{LSR} <$ 41.6 kms^{-1} (left) and 38.4 kms^{-1} $< v_{LSR} <$ 41.8 kms^{-1} (right). Crosses in the CO maps belong to the BGPS clumps found at the corresponding velocity intervals.

The bubble is not so clearly visible in HI data as in radio-continuum. It is probably caused by a strong background emission. However, the counterpart of the northeastern infrared loop is visible in HI data and morphologically copies the infrared emission (see comparison of the infrared image with contours of HI emission in Fig. 4.3). We found some CO emission in the walls of the bubble, but most of the emission is in a form of a huge CO cloud, which lies at the southwestern edge of Bubble A, where Bubble C is located. There are six BGPS clumps with velocities from 32.8 to 44.2 kms^{-1} lying in the vicinity of Bubble A.

Bubble B

Bubble B is a supernova remnant SNR G54.4-00.3. This region is prominent in the radio-continuum emission and forms a well-defined ring (Fig. 4.4, left-hand panel, the lower bubble). It has no clear counterpart in the IR data, although there is some IR emission towards the northeastern direction. This infrared emission is however mainly connected to Bubble C, which lies at the edge of Bubble B.

The bubble was found at 40 kms^{-1} in the previous radio studies by Junkes, Fuerst, and Reich [118]. At this velocity channel there is no shell-like structure visible in the HI data we are using (VGPS survey), probably due to high background emission. However, Park et al. [123] found neutral gas corresponding to the bubble's walls at velocities 53 to 108 kms^{-1} in I-GALFA data and determined the expansion velocity of 50 kms^{-1}. For further calculations we adopted this value of expansion velocity.

There is some CO emission visible at the systemic velocity of 40 kms^{-1}, which is again connected mainly to Bubble C. Hints of arcs of molecular gas are rising from a huge molecular cloud surrounding Bubble C. Other two tracers of cold dense matter, BGPS clumps, are found in the vicinity of Bubble B's walls. These clumps have velocities of 31.5 and 37.5 kms^{-1}, which slightly differ from the velocity of the bubble. It can be caused by their position in the closer wall of the bubble.

Bubble C

Bubble C was discovered by Churchwell et al. [1] as two separate bipolar infrared bubbles N116 and N117. The bubble N116 is cataloged as incomplete, with the mean radius of 0.82′. N117 is classified as a closed bubble, with the mean radius of 1.66′. However, in other data these bubbles look as one object. E.g., the bubble looks like a small hole in the HI data, surrounded by a fragmented and denser wall. This hole is filled with the radio-continuum emission (Fig. 4.4, the right-hand half). Therefore, we assume that this region is in fact a single bubble - Bubble C.

There is a bright CO emission lying close to Bubble C at around $\sim$ 40 kms^{-1}. As described before, there are CO arcs protruding from this bright region and partly copying the shape of the larger bubbles. The vicinity of Bubble C is also rich in other tracers of cold and dense gas, BGPS clumps. There are four BGPS clumps with velocities from 38.3 to 40.8 kms^{-1} lying in the bubble's walls.

The HI spectrum through the center of Bubble C is shown in Fig. 4.5, together with a spectrum taken through the brightest CO emission. The CO emission lies partly inside

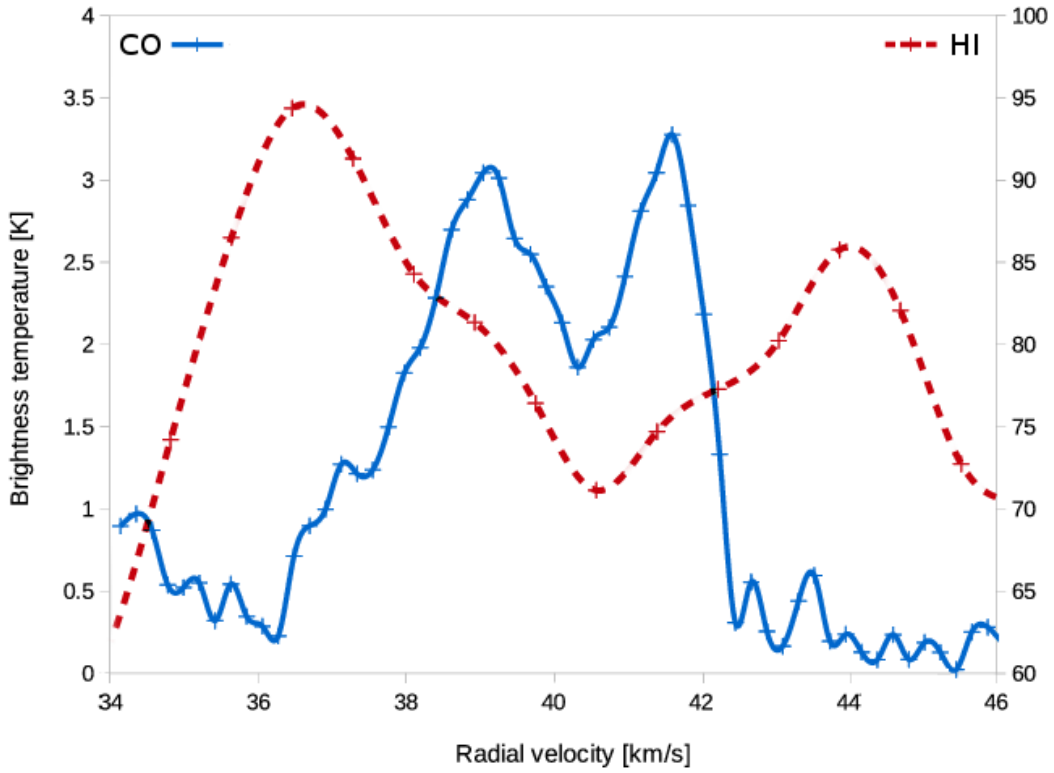

Figure 4.5: CO (a solid blue line, the left y-axis) and HI (a dashed red line, the right y-axis) spectrum of bubble C (the background system). The HI spectrum is taken at the position (54.087°, −0.068°), the CO spectrum at the position (54.123°, −0.103°).

the HI envelope and due to its slight off-center position it seems that the CO expansion velocity is smaller than the HI expansion velocity.

Properties of the background system

Using Eqs. 3.3 – 3.8 we calculated basic properties of the bubbles, all values can be found in Tab. 4.2. The mass of Bubble A and B are in fact the same, about 1.4×10^5 $M_\odot$, the mass of the smaller Bubble C is 3.4×10^4 $M_\odot$. The minimum energy needed to create the bubbles differs even in the case of the two large structures: Bubble A's energy input is $\sim 4 \times 10^{50}$ erg, and Bubble B's energy input is nearly 10 times higher, $\sim 2.6 \times 10^{51}$ erg. The high value in the case of Bubble B corresponds with the origin of the bubble, whose nature is a supernova remnant. Bubble A is also very energetic. Leahy, Tian, and Wang [119] suggested that it could be an old supernova remnant. However, even one very massive or a few less massive stars could supply the bubble with enough energy.

The minimum energy needed to create Bubble C is $\sim 3 \times 10^{48}$ erg (this minimum energy is determined from n_{HI}), however the maximum of energy input is $\sim 4 \times 10^{50}$ erg, if we use $n_{\mathrm{H_2}}$ in the Eqs. 3.8. The ages of bubbles are 2 Myr for Bubble A, 0.3 Myr for Bubble B, and 0.5 Myr for Bubble C. The young age of Bubble B is due to its high

expansion velocity of 50 kms^{-1}, adopted from Park et al. [123].

Striking feature of this system (and as we will see later, the same is applicable to the foreground system) is that the small Bubble C is sitting exactly at the place of the contact of the two large bubbles. Bubbles A and B are seen as rings of warm ionized gas in the radio-continuum image, where Bubble C is seen as a bright spot located at the touch of both bubbles (see Fig. 4.4, left-hand half, second row). Bubble C is more compact, with thick dense walls made of both atomic and molecular hydrogen. It is possible that large bubbles interact with surrounding gas, as seen in the distribution of cold molecular and atomic gas in their walls. As both bubbles probably collect (or collected) neutral gas from their vicinity and as they seem to be close to each other, they will presumably collide. During this collision the swept-up neutral hydrogen is being compressed and probably turns into its molecular form. This compression can lead into a star formation. If massive stars were born there, they could form another bubble, adequately younger and smaller. And this is actually what we observe. Bubble C is smaller and younger (0.5 Myr).

However, one can object that Bubble B is, according to our results, younger than Bubble C. And that assumption would be correct. It is a supernova remnant, which is probably very young (about 0.3 Myr). A supernova remnant is a remnant after an explosion of a massive star and massive stars produce bubbles during their lifetime. It is therefore plausible that this supernova remnant evolved inside a pre-existing interstellar bubble [123, 124], and is still residing inside it. In that case it would be the former interstellar bubble that collided with Bubble A and helped star formation to take place in the place of the collision.

4.2.2 Foreground system

The foreground system is centered around Bubble F at the radial velocity of $\sim 24\,\mathrm{kms}^{-1}$. This velocity corresponds to a near kinematic distance of 2.1 kpc. The diameters of large bubbles D and E are 1.3° and 0.9°, respectively. The typical size in all studied spectral regions of Bubble F is 13′. In linear dimensions for an assumed near kinematic distance, Bubble D corresponds to 46 pc, Bubble E to 34 pc, and Bubble F to 8 pc. For a far kinematic distance of 8 kpc, the sizes of Bubbles D and E would be comparable to the thickness of the HI disk, their diameters would be around 140 pc. From Fig. 4.6 we see that the bubbles are not influenced by the vertical density gradient. Furthermore, the energy needed to create such bubbles would be in order of 10^{52}erg, which would mean that the bubbles would have been very energetic. This can be still possible, but because of lack of radio-continuum emission inside these large bubbles, we assume that the bubbles are less energetic and therefore lying at the near kinematic distance.

The best spectral region to see all bubbles from the foreground system is the HI emission (see Fig. 4.6). In the other data mainly Bubble F is well visible, especially in IR and CO data. There is some faint radio-continuum emission inside the large bubbles, but again, the most prominent bubble in radio-continuum is Bubble F. The detailed description of bubbles and their visibility in multiwavelength observations is included in the following sections. The results and comments about derived properties, such as mass or density, are in the last section.

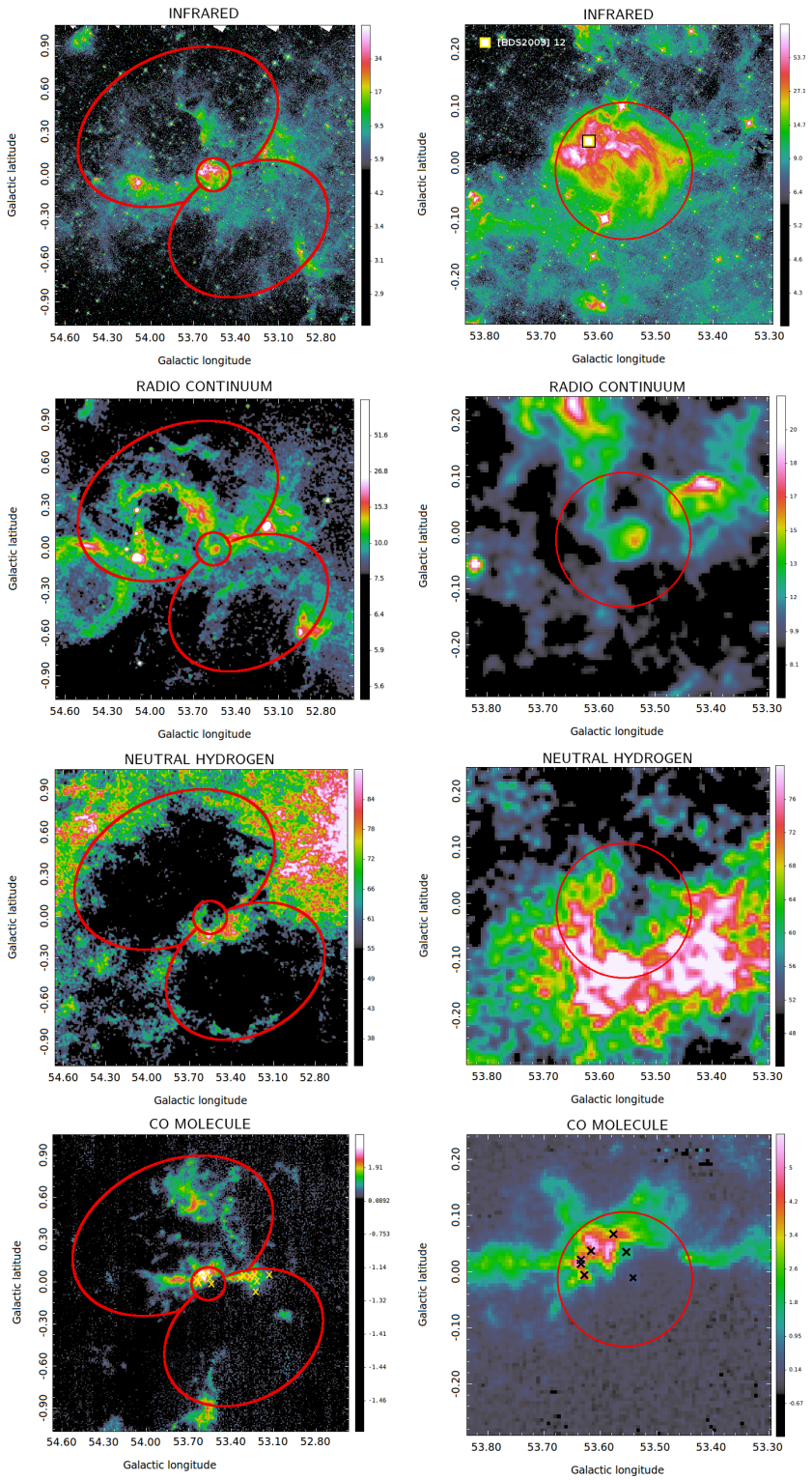

Figure 4.6: Multiwavelength image of the foreground system (left: the total system, right: the small central region). Positions of bubbles D (upper left), E (lower right) and F (N115, small in the middle) are overlaid. The HI is summed over the velocity interval: 23.3 kms^{-s} $< v_{LSR} <$ 24.9 kms^{-1} (left) and 23.3 kms^{-s} $< v_{LSR} <$ 24.1 kms^{-1} (right), the CO over the interval: 23.8 kms^{-s} $< v_{LSR} <$ 25.0 kms^{-1} and 23.9 kms^{-s} $< v_{LSR} <$ 24.8 kms^{-1}. Crosses in the CO maps belong to the BGPS clumps found at the corresponding velocity intervals.

Bubble D

We found Bubble D visually as an elliptical hole in the HI distribution. There are no prominent HI walls, only a lack of HI emission in the inner parts. The only significant part of HI emission is connected to the location of Bubble F, where Bubble D interacts with Bubble E. There is faint radio-continuum emission along the inner edges of Bubble D (Fig.4.6, left-hand half), but comparing it to e.g. Bubble A from the background system, this is significantly dimmer.

Bubble D is not properly visible in infrared data. The only part which is visible is the one connected to Bubble F. A bright infrared region occurs at the southeast of the bubble's border, between Bubble D and E (see Fig. 4.7). It is an infrared bubble MWP1G053174+001497 [5] and according to Bronfman, Nyman, and May [125] and Anderson et al. [126], it lies at the radial velocity 6.6 $\text{kms}^{-1} \leq v_{LSR} \leq 8.3\ \text{kms}^{-1}$. These velocities are not consistent with the systemic velocity of Bubble D. The position of the MWP bubble seems to be only projected to the edge of Bubble D.

The position of the bubble at $\sim$ 24.0 kms^{-1} is also supported by the velocities of three associated BGPS clumps. The velocity range of these clumps is from 23.7 to 24.8 kms^{-1}. The cold dense gas is visible also in the CO data, but only half of the envelope is observed - the part which surrounds Bubble F and the whole first and second quarter of the envelope (Fig.4.6). The most interesting fact about the CO distribution is that the emission lies inside the HI hole, specifically along the inner edge. The possible scenario, which can explain this unconventional distribution, is that the shock wave, which formed Bubble D, was not strong enough to fully dissolve molecular gas, but it was strong enough to push the atomic gas.

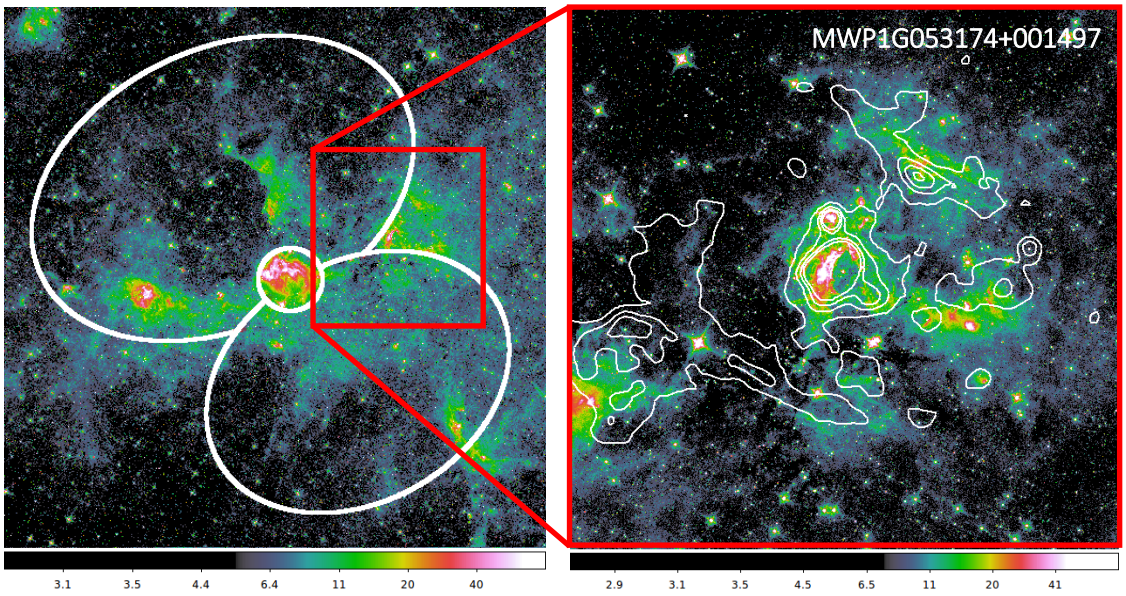

Figure 4.7: The bubble MWP1G053174+001497 seems to lie in the walls of Bubble D (and Bubble E). But it is only projected into that direction, as its radial velocity differs from the systemic velocity of the foreground system. The images are in infrared emission, the contours are from radio-continuum data, with levels of 11, 14, 17, 20 K.

Bubble E

Bubble E is a ring like structure visually found in the HI data. It shows a nice partial wall in its southern part (see Fig. 4.6, left-hand half, the third row). The bubble is not as clearly visible in the infrared as it is in the HI data. The smaller Bubble F is lying at the bubble's northern edge and the surrounding infrared emission seems to be also part of Bubble E.

The inner edges of the HI envelope are slightly traced by radio-continuum emission. The regions of ionized gas are faint, stretching from the southwest to the east, going through the north. The brightest part of the radio-continuum emission is the HII region [KC97c] G052.9-00.6 [127], which is connected to the infrared bubble MWP1G052967-006009 [5](see Fig. 4.8). Although it seems to be associated with Bubble E, it does not belong to the foreground system, due to its different systemic velocity. This bubble is associated with other objects, such as BGPS clumps or IRAS objects, lying at the distance of 5.1 kpc [128]. The distance of 5.1 kpc is the systemic velocity of the background system, but according to the position of the bubble MWP1G052967-006009, we do not assume it to be a member of the background system. The bubble MWP1G052967-006009 may be associated with pulsar PSR 1930+17 (the position of the pulsar is marked in Fig. 4.8).

There are nine BGPS clumps, which are spatially associated with the bubble, and whose velocities vary from 21.9 to 25.1 kms^{-1}. The CO emission is not as perfectly distributed as in the case of Bubble D. In fact, there are only two main CO regions connected to the walls of the HI envelope (Fig. 4.6).

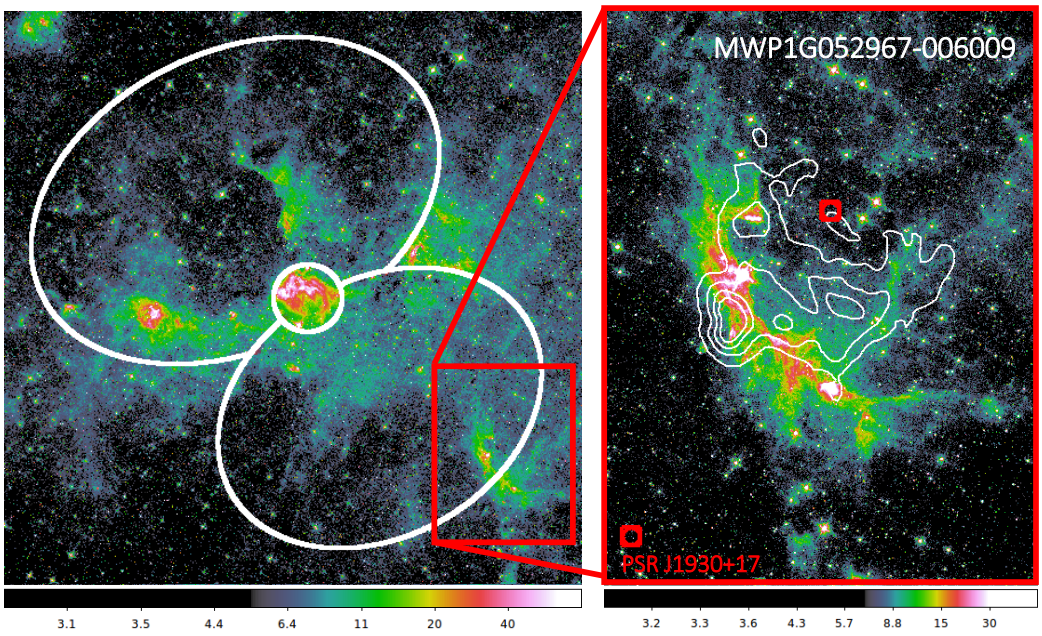

Figure 4.8: The bubble MWP1G052967-006009 seems to lie in the walls of Bubble E, but it is probably just projected into that direction. The images are in infrared emission, the contours are from radio-continuum data, with levels of 11, 14, 17, 20 K. Possible progenitor of the bubble PSR 1930+17 is marked in red.

Bubble F

Bubble F is known as bubble N115, described as a closed ring by Churchwell et al. [1]. It is the most prominent bubble in the IR data from the foreground system. The emission at 8 μm is dominating at the northern edge of the bubble, where all BGPS clumps associated with Bubble F are perched. Radial velocity of these objects is similar; it lies in the interval from 23.1 kms^{-1} to 24.3 kms^{-1}. There are also two masers associated with the Bubble F, both lying in the vicinity of BGPS clumps. The inner parts of the bubble are filled with radio-continuum emission, but in comparison with Bubble C from the background system, this radio-continuum emission is dimmer (see Fig. 4.6).

The HI emission closely follows the infrared bubble. However, the brightest regions of HI emission lie at the south edge of the envelope, at the place where the infrared emission is faint. The CO emission is clumpy and unlike the HI emission, it does not trace the whole outline. The largest CO region is located close to the brightest parts of the infrared bubble. This northern region seems to contain cold and dense gas. It is filled with CO emission, all associated BGPS clumps, and other YSO candidate objects. The latitude-velocity diagram of Bubble F in Fig. 4.10 shows how the HI and CO emission complement each other.

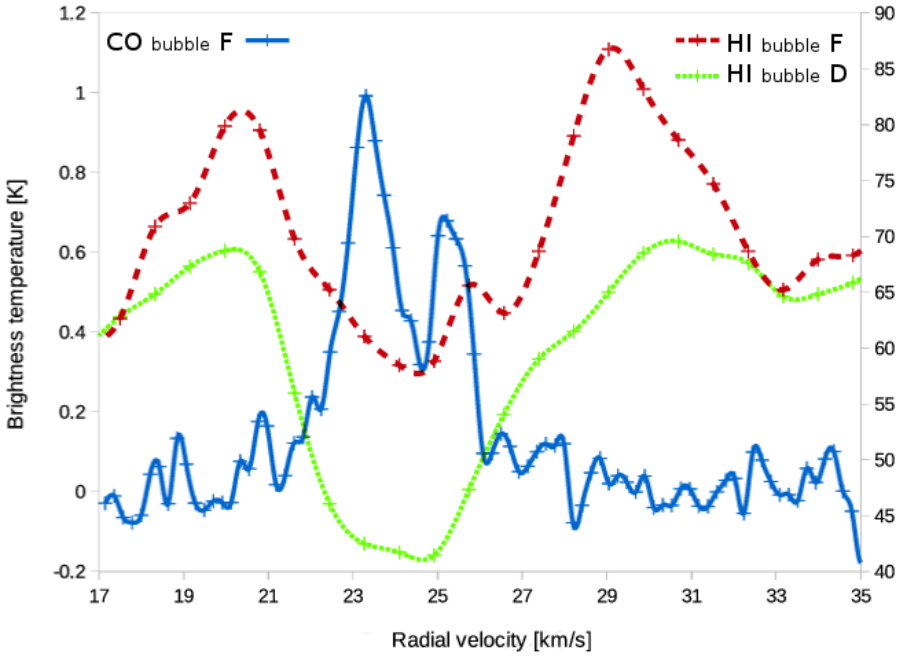

Figure 4.9: CO (solid blue line, the left y-axis) and HI (dashed red line, the right y-axis) spectrum of bubble F (the foreground system). The HI spectrum is taken at the position (53.573°, −0.059°), the CO spectrum at the position (53.558°, 0.003°). The HI spectrum of bubble D (dotted green line) is overlaid, its position is (53.56°, −0.014°).

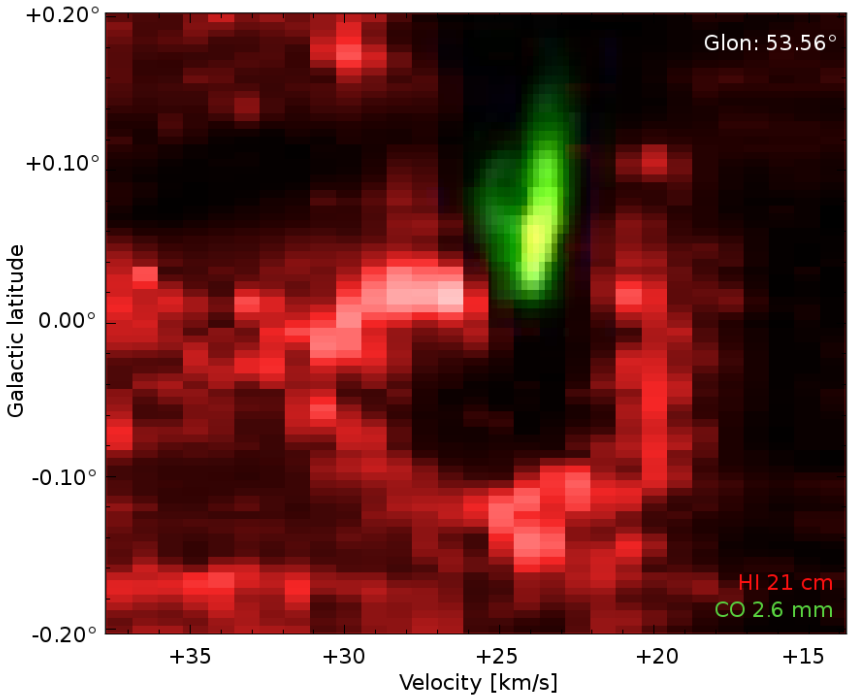

Figure 4.10: Latitude-velocity diagram of bubble F (the foreground system) at $l = 53.56°$. The red color corresponds to the HI emission, the green color to CO.

Properties of the foreground system

All calculated values of basic properties of the bubbles can be found in Tab. 4.2. The masses of Bubble D, E and F are nearly doubles: 1.5×10^4 $M_\odot$ for Bubble F, 3.0×10^4 $M_\odot$ for Bubble E, and 5.6×10^4 $M_\odot$ for Bubble D. The minimum energies needed to create the bubbles D and E are similar, 0.19×10^{50} erg and 0.21×10^{50} erg, respectively. The minimum energy needed to create Bubble F is much smaller,$> 0.008 \times 10^{50}$ erg. However, if we use n_{H_2} in the Eqs. 3.8, the maximum energy input would be way higher, $\sim 1 \times 10^{50}$ erg. We suppose that the correct value is somewhere in between these border values, probably closer to the lower one. As seen in the Figure 4.6, the CO emission of Bubble F is more concentrated on the northwestern edge of the bubble. Therefore we suppose that the bubble did not expand into an extremely dense environment, but opened in the direction of lower density.

The ages of larger bubbles are similar, 3.6 Myr for Bubble D and 2.3 Myr for Bubble E. Bubble F is much younger, about 0.6 Myr. This leads us to a similar picture as in the case of the background system. Two larger and older bubbles seem to collide, and a smaller and younger bubble sits in the interacting zone. It seems that the probability of star formation was increased by squeezing material between the two large bubbles, which resulted in star and later bubble formation. However, there is a difference between the background and the foreground system: the second system is less energetic (Tab. 4.2) according to our energy estimates and its connection to a less of ionized gas.

4.2.3 Progenitors of bubbles

Most of the bubbles (except of Bubble B, and maybe Bubble A) were according to our energy estimates, created by stellar feedback from massive stars. To find candidates to be the progenitor stars we used the study by Morales et al. [129] and looked for adequately young ($<$ 100 Myr) clusters in the studied area. We found five clusters spatially coinciding with both systems. Positions of these clusters are schematically pictured in the Fig. 4.11 and their properties are listed in Tab. 4.3. The cited radial velocities are from Morales et al. [129] and they belong to gas, which is connected to the clusters.

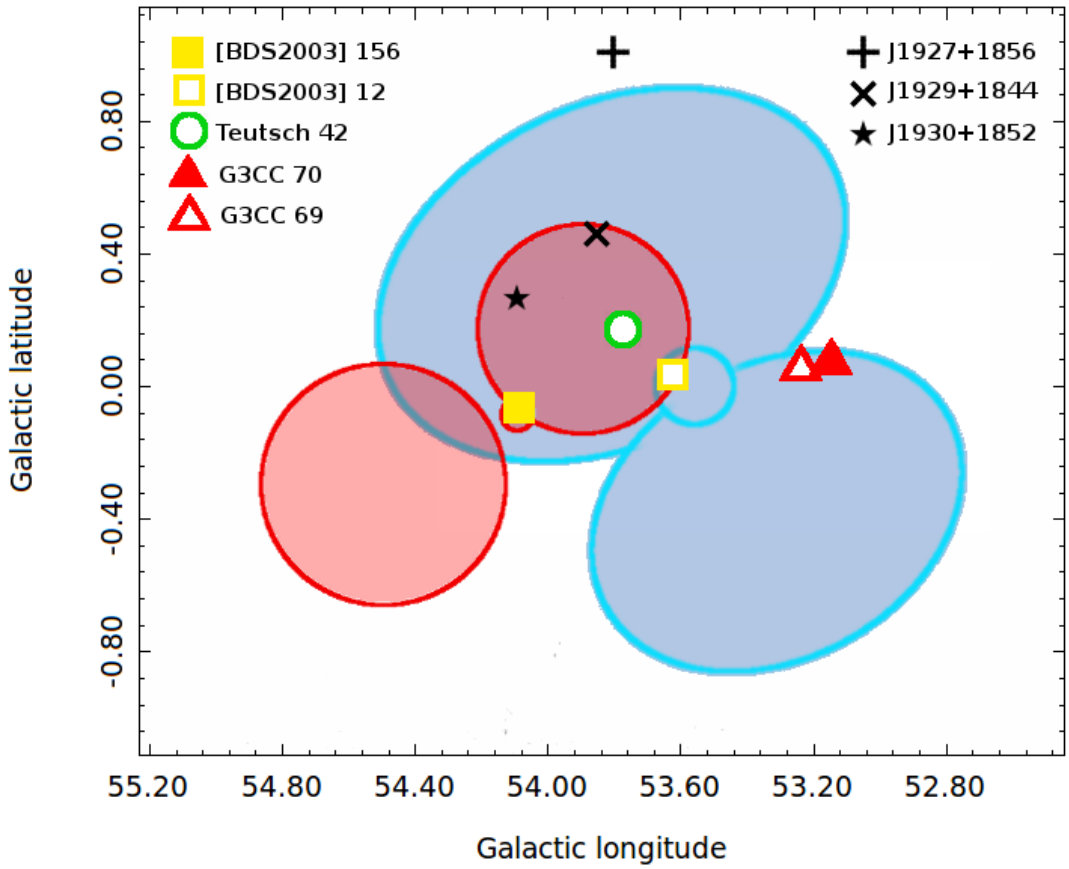

Figure 4.11: Schematic panel of the two systems, background (smaller red one) and foreground (larger blue one) with young clusters and pulsars in the area.

Bubble A

According to our energy estimates, Bubble A could be created by either feedback from massive stars or from a supernova explosion. The first possibility could be supported by the existence of the cluster Teutsch 42. This cluster has been properly studied and among all the publications many different results of age and distance can be found:

Table 4.3: Young clusters in the studied area.

Name	l [deg]	b [deg]	v_{LSR} [kms^{-1}]	age [Myr]	Type
G3CC 69	53.147	0.071	22.0		embedded
G3CC 70	53.237	0.056	23.9		partially emb.
BDS2003 12	53.622	0.039	23.7		embedded
Teutsch 42	53.771	0.164	37.7	3	exposed, assoc.
BDS2003 156	54.084	-0.069	39.9		embedded

30 Myr and 1.6 kpc [130]; 2-4 Myr and 6.5 kpc [131]; 3 Myr and 6.7 kpc [129]; and 1.3 Myr and 2.0 kpc [132].

Teutsch 42 (with its total mass of $(4-6) \times 10^3$ M$_\odot$) is in fact a good candidate to be the source of energy for Bubble A (see its position in Fig. 4.12). It contains a WR star and some O and B stars. This could be supported by the age and distance results of Hanson et al. [131] and Morales et al. [129].

We searched for pulsars in the vicinity of Bubble A to see, if there are some candidates for the second possible origin of Bubble A – a supernova event. Two pulsars with reasonable distances are located in the area of Bubble A: J1929+1844 (5.3 kpc) and J1927+1856 (4.8 kpc) [133]. The second pulsar is too old (8 Myr) to create Bubble A, however the first one has more appropriate age of 2 Myr. It is also possible that the massive star, from which pulsar J1929+1844 arose, was originally part of Teutsch 42 cluster. The neutron star would be expelled from the cluster after the supernova event, which would explain its farther location from the cluster.

All three scenarios are possible: a) the bubble was created by stellar a feedback

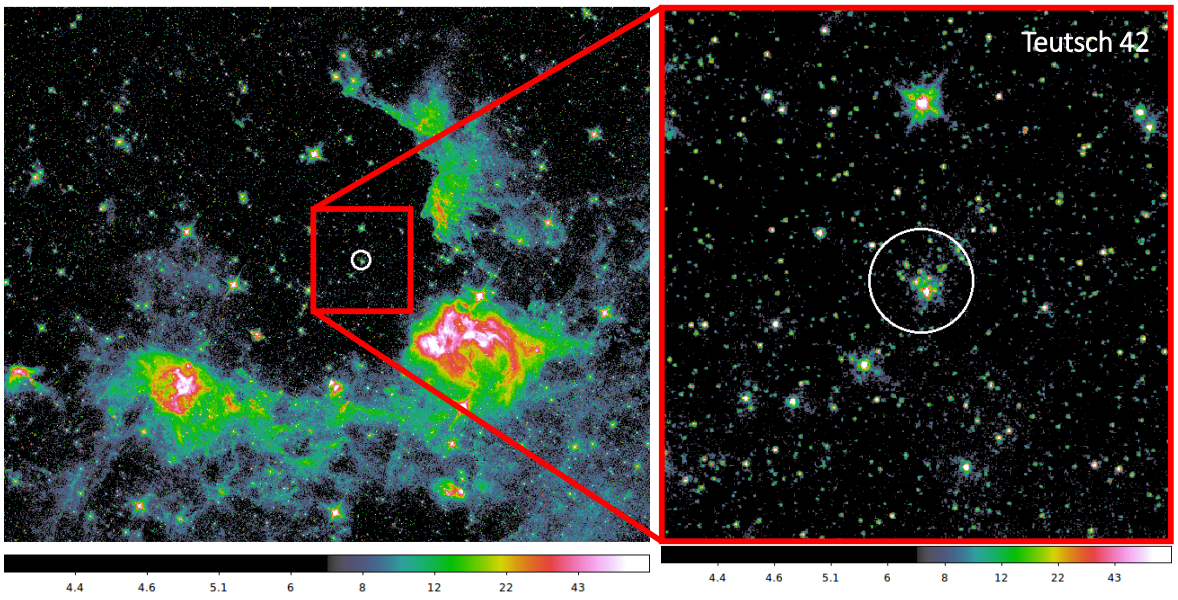

Figure 4.12: Position of Teutsch 42, a probable progenitor star cluster, with angular size of 1.0′.

of stars, probably from Teutsch 42 or another unidentified cluster; b) the bubble was created by a supernova event, from which the pulsar J1929+1844 remains; c) the bubble was created by a combination of both feedbacks, from Teutsch 42 and J1929+1844, where the pulsar was originally part of the cluster.

Bubble B

Bubble B is a known supernova remnant G54.4-0.3, however its progenitor is not known. As we described earlier, it is possible that the remnant is evolving inside an older stellar bubble. This pre-existing bubble would be created during the life of a massive star, which later exploded as a supernova and gave origin to the observed remnant.

Bubble C

The cluster [BDS2003] 156 has a radial velocity of 39.9 kms^{-1} and seems to lie inside Bubble C [129]. It is a young cluster, still embedded in the gas. There is a high possibility that this cluster is the ionizing source of Bubble C and its stars are heating the interior of the bubble (see the position and size of the cluster in Fig. 4.13).

Bubble D

The cluster Teutsch 42 was described in more details in the section about progenitors of Bubble A. However, this cluster is also projected in the direction of Bubble D (see the green mark in Fig. 4.11). One of the mentioned results of its age and distance, 1.3 Myr and 2.0 kpc by Kharchenko et al. [132], is in a good correspondence with our estimates:

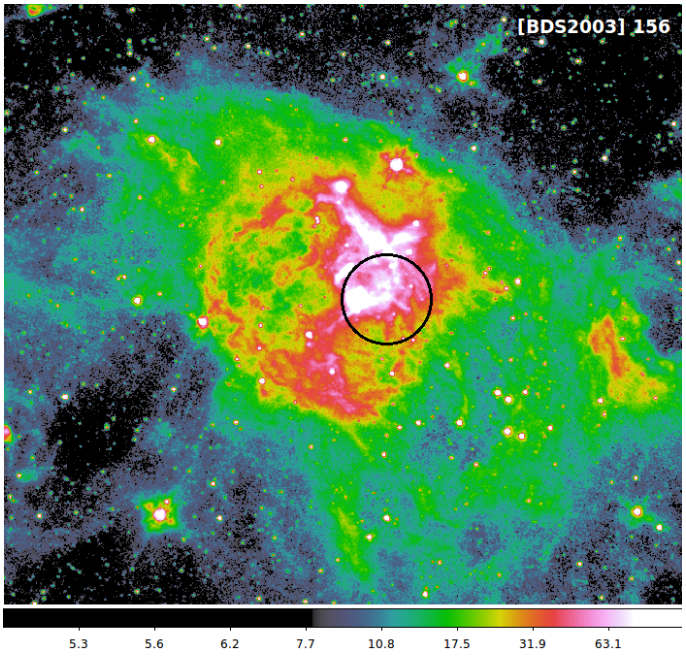

Figure 4.13: Position of [BDS2003] 156, a probable progenitor star cluster, with angular size of 1.8′.

3.6 Myr and 2.1 kpc. The only disagreement would be in energetic demands. The cluster Teutsch 42 contains several O and B stars and WR star, whose energy output into surrounding media would probably exceed the energy input of Bubble D. We estimate the energy needed to create Bubble D to be 0.19×10^{50} erg, which corresponds to one or two B stars. But it is necessary to mention that all the energetic estimates given in this chapter, are only the minimum of the energy needed to create a bubble. The maximum energy input in case of Bubble D is 6×10^{50} erg, which matches to the probable energetic output of Teutsch 42. Therefore it is possible that, if Kharchenko et al. [132] is correct, Teutsch 42 could be the progenitor cluster of Bubble D.

Bubble E

There are two clusters in the vicinity of Bubble E: clusters G3CC 69 and 70. Both of them lie at the edge of Bubble E (and Bubble D, see the red marks in Fig. 4.11). They seem to be projected into the position of the infrared bubble MWP1G053179+001558, but the connection between them cannot be confirmed. The assumed radial velocity of the bubble MWP1G053174+001497 is around 7 kms^{-1} and the assumed radial velocity of the clusters is $\sim$ 23 kms^{-1}. Therefore, they are not physically associated with the bubble MWP1G053174+001497, but probably with the foreground system (for detailed positions and sizes of the clusters see Fig. 4.14). Bubble E is a member of the foreground system. This makes us wonder whether these clusters can be the progenitors of Bubble E?

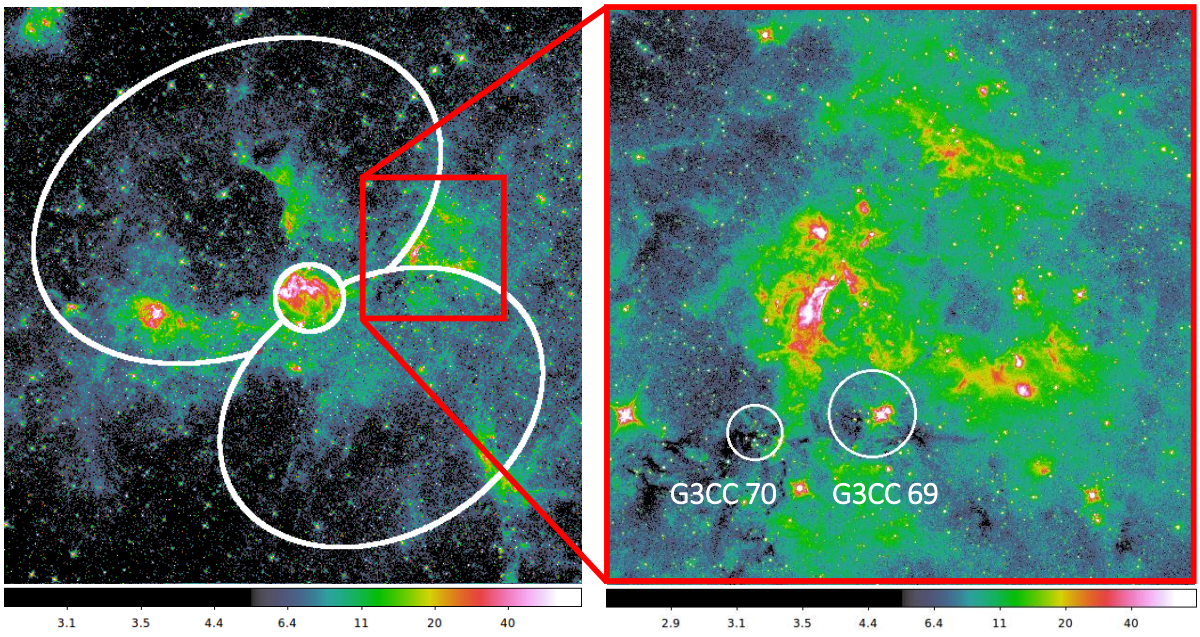

Figure 4.14: Position of clusters G3CC 69 and G3CC 70 according to the bubble MWP1G053174+001497 (the right panel) and Bubbles D and E (the left panel, the two largest ellipses). Angular sizes of clusters G3CC 69 and G3CC 70 are 1.98′ and 1.27′, respectively. The background maps are infrared maps from Spitzer.

According to Morales et al. [129], these clusters are very young, as they are still embedded in the surrounding gas. Our estimate of the age of Bubble E is 2.3 Myr, which is probably too old for young, still in gas embedded clusters. Therefore, we find three possible scenarios for the relationship between Bubble E and both clusters: a) the clusters are lying at the radial velocity found by Morales et al. [129], but they are actually lying at the far kinematic distance; b) the clusters are connected to the foreground system, physically lying in the wall of Bubble E and probably their formation could be triggered by collision of Bubble D and E; and c) the clusters are part of the foreground system and they are actually progenitors of Bubble E. One can oppose the last mentioned scenario with the energy estimates. Again, as in the case of Bubble E, the energy input given here is just a minimum value. The maximum value is 4×10^{50} erg, which would correspond better with the energy output of the clusters.

Bubble F

From the spatial location, it seems that the cluster [BDS2003] 12 is associated with Bubble F (see the yellow empty square in the Fig. 4.11). According to Morales et al. [129] the cluster is still embedded in the parental gas, therefore young. This result correlates with our estimated young age of Bubble F, which is 0.6 Myr. Furthermore, the cluster is located in the northwestern edge of the bubble, where the strongest IR and CO emission of Bubble F lies (see Fig. 4.15). We assume, according to its location and age estimate that the cluster [BDS2003] 12 is the progenitor cluster of Bubble F.

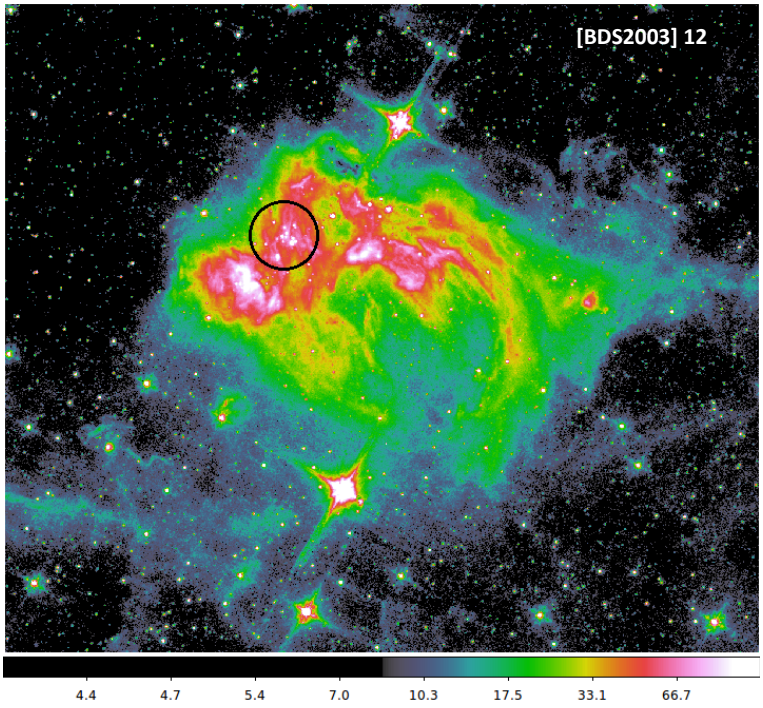

Figure 4.15: Position of [BDS2003] 12, a probable progenitor star cluster, with angular size of 1.1′.

4.3 Discussion

We identified two independent systems of bubbles, the foreground and the background system, lying at different distances (2.1 kpc and 5 kpc, respectively). These systems appear to be similar: both include two large bubbles (20 – 30 pc in radius) and one small bubble ($\sim$ 4pc in radius). It seems that both pairs of large bubbles are colliding, resulting in star formation happening in the place of the collision, and forming the smaller bubbles (see Fig. 4.4 for the background system and Fig. 4.6 for the foreground system).

Average densities of atomic and molecular hydrogen are higher in the case of smaller bubbles. The average density of atomic gas in smaller bubbles is about 90 cm^{-3}, while about 6 cm^{-3} in large bubbles. The average density of molecular gas in smaller bubbles is about 4×10^3 cm^{-3}, while only about 24 cm^{-3} in large bubbles. The smaller bubbles are also the youngest from both systems, and as the star formation takes place in the densest ISM, the younger bubbles are expected to show higher densities. As bubbles grow, they reach the less dense medium, which lowers the density in walls of older and larger bubbles.

Both systems of bubbles are similar in sizes and structure, but they differ in energy which was involved in their creation. The background system is more energetic: the energy needed to create both large bubbles, Bubble A and B, are 4×10^{50} erg and 3×10^{51} erg, respectively. Bubble B is a supernova remnant [120], which makes its input energy exceptional, according to the results from the Chapter 3 (Searching for an atomic and a molecular component of infrared bubbles). Bubble A could also be a supernova remnant, as was suggested by Leahy, Tian, and Wang [119]. Our energy estimates corresponds with this hypothesis, but it is also possible that Bubble A was created by ionizing radiation of massive stars and following expansion of an HII region. An expansion of an HII region is the most probable origin of the rest of studied bubbles: Bubble C, D, E and F.

Two young clusters are probably the sources of energy in the cases of the smaller bubbles: [BDS2003] 156 of the small Bubble C (N116+117) and [BDS2003] 12 of the small Bubble F (N115). Teutsch 42, according to its location and age, might be the progenitor of Bubble A or Bubble D. However, the progenitors of Bubble B and E are not yet known.

Perhaps the most interesting result is that both pairs of large bubbles seem to collide. At the place of the collision smaller (and younger) bubbles are located. It seems that the collision of the large bubbles increased the possibility of further star formation due to compressing gas and increasing its density. We do not suggest that a collision of bubbles is behind all triggered star formation, nor that it is the main mechanism of triggering star formation, but we propose that such collisions are important and can increase the probability of further star formation.

Chapter 5

Observations of hot inner parts of bubbles S1, S73 and S74

5.1 Introduction

5.1.1 The S1 bubble and its surroundings

The S1 bubble was identified and classified by Churchwell et al. [1] as an infrared open bubble with a mean radius of 4.51′. Two HII regions are located in the northern part of the bubble, close to the brightest infrared emission. The radial velocities of these regions are about -25 kms^{-1} [134], which agrees with our results obtained from HI data. We identified the bubble at -22 kms^{-1} in the SGPS HI survey [135].

Two open clusters are lying in the vicinity of the S1 bubble: [MCM2005b] 92 and [DBS2003] 120 [129]. According to Morales et al. [129], the radial velocity of both clusters is -25.4 kms^{-1}, corresponding to a distance of 3.46 kpc. The cluster [MCM2005b] 92 is an exposed cluster lying inside the S1 bubble. The cluster [DBS2003] 120 seems to lie on the rim of the S1 bubble, and probably therefore it is classified as a partially embedded cluster. For locations and sizes of clusters see left panel of Fig. 5.2.

The environment of the S1 bubble, which includes a large elliptical infrared loop spreading eastward (see Fig. 5.1, left panel), also seems to be interesting and worth of a further study. The infrared loop is filled with Hα emission (SHASSA survey by Gaustad et al. [136]) and is likely to be connected to the small S1 bubble. The S1 bubble may be the result of star formation triggered by the larger (and in that case older) structure or, alternatively, the larger structure may be the result of the HII region of the S1 bubble expanding into a nonuniform environment.

5.1.2 The S73 and S74 bubbles

S73 bubble was identified and classified by Churchwell et al. [1] as an infrared closed bubble with a mean radius of 3.46′. The bubble encloses RCW 98, an HII region lying at the distance of 2.6 kpc [137]. Fig. 5.1 shows the bubble in Spitzer-IRAC infrared image [97] and in Hα emission in SuperCOSMOS survey [138]. A part of the bubble is SFO75,

a bright-rimmed cloud, which is associated with the infared source IRAS 15519-5430. Its luminosity in far infrared is 3.4×10^4 $L_\odot$ [139]. This leads Urquhart et al. [140] to the conclusion that the star formation, triggered by the HII region RCW98, takes place in the rim of the bubble.

There is one cluster, [MCM2005b] 64, which is according to Morales et al. [129] associated with the HII region RCW 98. The cluster is angularly small comparing to the size of the bubble, its angular size is only 0.40′ versus 6.92′ of S73. The connection to RVW 98 and therefore the bubble S73 seems to be unclear. However, Pinheiro, Copetti, and Oliveira [137] found three stars, which could be probable sources of ionization of RCW 98. These stars are RCW98-1 (LSS 3423), which is the most probable one, RCW98-2 (ALS19480) and RCW98-3 (2MASS15554264-5439018), whose spectral types are O9.5V, O9.5V and B2.5V, respectively. These stars, together with the cluster, are marked in Fig. 5.2, right panel. The ionizing stars are driving the expansion of RCW98 region for $1 - 2.5 \times 10^5$ years [140].

The bubble S74, with a mean radius of 1.33′ [1], seems to lie in the wall of the bigger bubble S73 (see Fig. 5.1, right panel). There is not much research dedicated to this bubble and there is a question, whether this bubble is also triggered by the expansion and radiation of RCW 98, or whether S74 is not even a real bubble, but only a ring-shaped rim of the larger bubble S73.

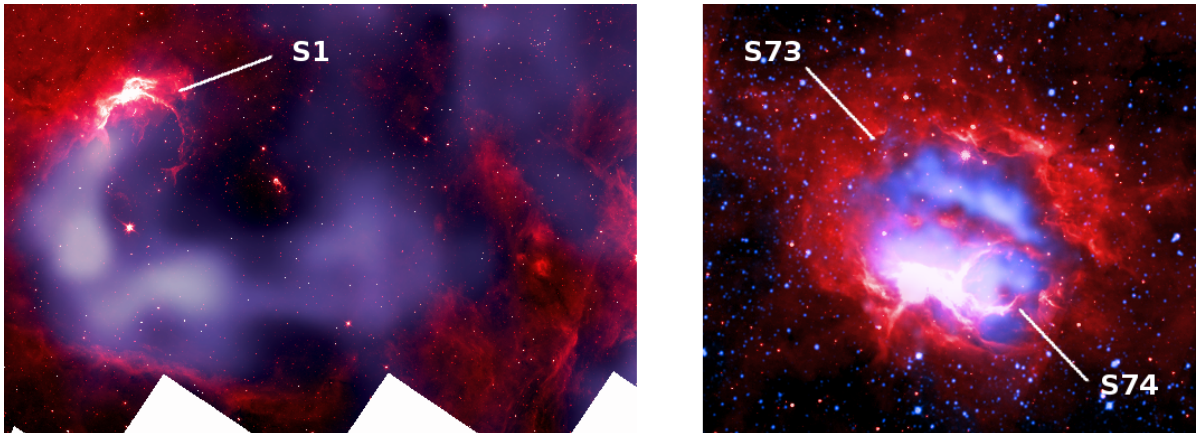

Figure 5.1: Bubble S1 and its surroundings in 8 μm (red) and in Hα (purple) - left panel. Bubbles S73 and S74 in 8 μm (red) and in Hα (blue) - right panel.

5.2 Observation goals

5.2.1 Observations of the bubble S1 and its surroundings

We proposed narrow band Hα imaging and optical spectroscopy of the ionized Hα emitting gas associated with the S1 bubble and its surroundings. We requested to perform narrow band imaging first and based on the quick look results of the narrow band image we decided final positions for spectroscopy. Refined positions (points p1,

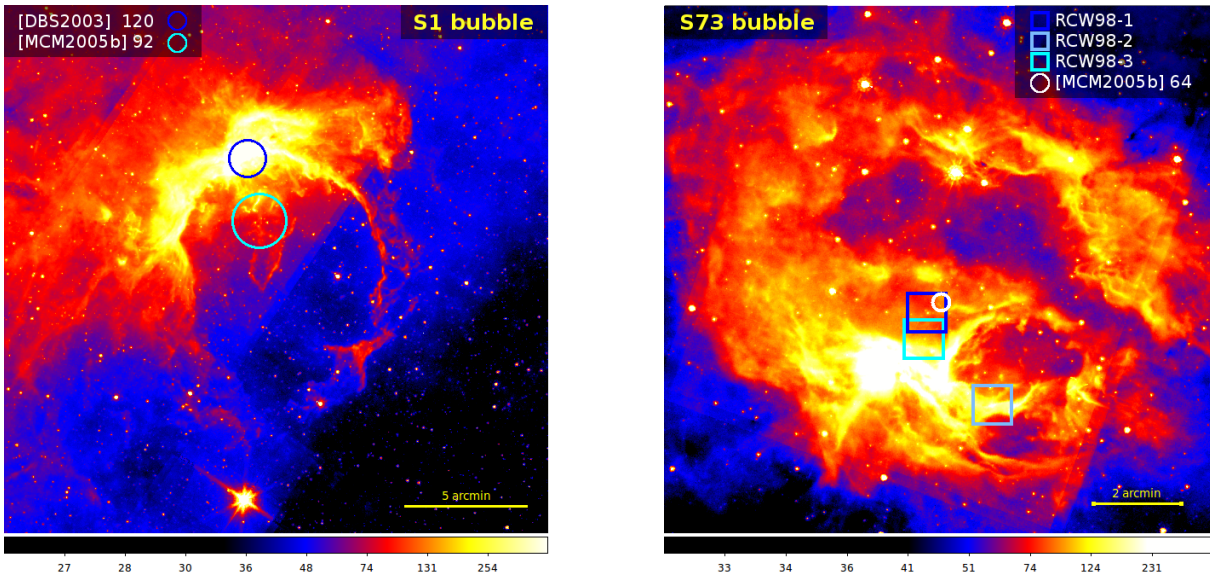

Figure 5.2: The left panel shows positions of two clusters associated with the S1 bubble: [DBS2003] 120 with angular size of 1.5′ and [MCM2005b] 92 with angular size of 2.2′. The right panel shows the position of the cluster [MCM2005b] 64 with angular size of 0.4′. The ionizing stars of RCW98 are marked in the blue squares.

p2, and p3 - see Fig. 5.3, left panel) centered on Hα enhancements, allowed us to get better S/N ration than positions based on a low-resolution image.

Even though Hα image from the SHASSA survey maps the whole region, its resolution is low to detect detailed distribution of hot gas inside the bubble S1. Therefore we proposed narrow band image of the S1 bubble and its enclosed area (marked in Fig. 5.3, left panel), which provided us with a clear view of the interface between the bubble and the ambient loop. This image would show us how the hot gas inside these structures is distributed and how it is related to the dusty walls of the bubble.

The positions of points p1, p2, and p3 were chosen in the way that one was placed inside the S1 bubble, and two additional points along the surrounding loop like structure (marked in Fig. 5.3, left panel). We wanted to compare the obtained spectra and determine the chemical abundances, temperatures, densities and ages. Combining the temperatures and densities, we could estimate the pressure inside both structures.

The goal of this observation was to clarify the origin of the S1 bubble as well as that of the surrounding loop. If the structures were created by expansion of the same HII region, the pressure of both structures would be similar and the Hα radial velocities would be the same (suggesting they are lying at the same distance). If the smaller bubble S1 was created as a result of star formation triggered by the bigger loop, the pressure inside these structures would be different, while the radial velocities would be still the same. If the bubble S1 and the ambient loop are spatially unrelated structures that are just overlapping in the sky, then their radial velocities will be different. In that case we will continue work on both regions separately.

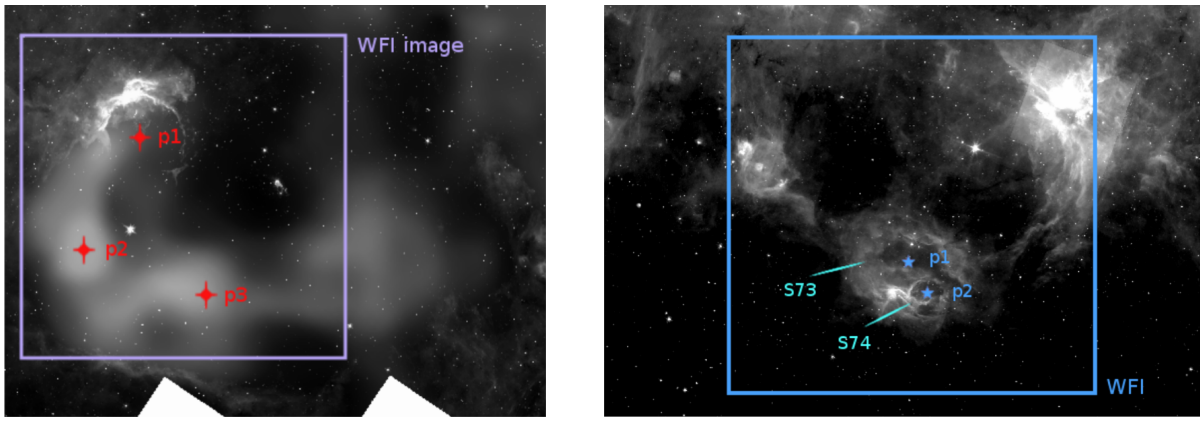

Figure 5.3: The left panel shows the position of the image we proposed to obtain by WFI for the bubble S1. The points p1, p2 and p3 mark the preliminary coordinates of the spectral measurements. The right panel shows the position of the image we proposed to obtain by WFI for the bubbles S73 and S74. The points p1 and p2 mark the preliminary coordinates for spectroscopy.

5.2.2 Observations of the bubbles S73 and S74

We proposed narrow band Hα and OIII imaging and optical spectroscopy of RCW 98, an HII region filling the interior parts of S73 bubble. We requested to perform spectroscopy of points p1 and p2 first. After spectroscopy we requested to perform narrow band OIII and Hα imaging.

Points p1 and p2 were selected so that first one lies inside the S73 bubble and the second one inside the S74 bubble (marked in Fig. 5.3, right panel). We wanted to compare the obtained spectra and determine the chemical abundances, temperatures and densities as in the case of the bubble S1. Combining the temperatures and densities, we could estimate the pressure inside both structures. This would help us to clarify the origin of both bubbles, especially it will clarify whether S74 is a real bubble or not.

The ratio between [OIII] and Hα depends on the conditions inside the ionized gas and therefore we asked for the narrow band images in OIII and Hα filters. We have the Hα map from the SuperCOSMOS [138] with the resolution about two times worse than the resolution of 2.2 m, so the Hα photometry has the lowest priority. We proposed narrow band image of the S73 bubble (marked in Fig. 5.3, right panel), which provided us with a clear view of the interface between the bubble S73 and the smaller bubble S74. This image could show us how the hot gas inside these structures is distributed and how these bubbles are connected.

5.3 Methods and Data Analysis

The next section is dedicated to the description of properties and the source of our data. The basic methods used for analysis, such as line profile characteristics, derivation of electron temperatures and densities, metallicity and abundances are characterized in following sections.

5.3.1 Data

We requested our proposals to Tycho Project, asking for observing time at 2.2 m telescope at La Silla. The telescope offers three instruments: Wide Field Imager (WFI), the Fiber-fed Extended Range Optical Spectrograph (FEROS) and Gamma-Ray Burst Optical/Near-Infrared Detector (GROND). Our data comes from FEROS, high resolution Échelle spectrograph and from WFI.

FEROS

ESO's Fibre-fed, Extended Range, Échelle Spectrograph (FEROS) provides high resolution ($R \sim 48,000$) and almost complete spectral coverage from $\sim$ 350 nm to $\sim$ 920 nm. The radial velocity accuracy is $\sim$ 25 ms^{-1}. There are two fibers providing simultaneous spectra. One is taking spectra of the object, the second one takes spectra of either sky or one of the two calibration lamps.

WFI

Wide Field Imager (WFI) is a focal reducer-type camera with field of view of $34' \times 33'$ and sensitivity from 350 nm to the near IR. It offers more than 40 filters to operate with. The detector consists of 4×2 mosaic with 2000×4000 CCDs and a pixel scale of 0.238 arcsec/pixel.

5.3.2 Line profile characterization

To be able to compute electron temperature and density, metallicity and abundances of elements in studied HII region, first we have to measure a spectral line profile of each spectral line. The important spectral lines needed for the analysis of an HII region are mainly:

OIII 4959 $\mathring{A}$, 5007 $\mathring{A}$, 4363 $\mathring{A}$

NII 6548 $\mathring{A}$, 6583 $\mathring{A}$, 5755 $\mathring{A}$

OII 3729 $\mathring{A}$, 3726 $\mathring{A}$

SII 6716 $\mathring{A}$, 6731 $\mathring{A}$

The basic parameters of a spectral line profile are the equivalent width of the line (W), the full width at half maximum ($FWHM$) and the peak intensity (I).

The equivalent width of a spectral line is a width of a rectangle formed with the height equal to that of continuum emission and with surface equal to a surface integrated under the spectral line (see Fig. 5.4). The equivalent width is measured in wavelength units and mathematically is described as:

$$W = \int (1 - \frac{I_\lambda}{I_c}) \mathrm{d}\lambda, \tag{5.1}$$

where I_λ represents the intensity across the wavelength range of the spectral line and I_c is the continuum intensity. If $W > 1$, the line is in absorption, and if $W < 1$, the line is in emission.

Full width at half maximum ($FWHM$) is the width measured at half level between the peak of the spectral line and the continuum. The $FWHM$ could be expressed in wavelength units or in speed units. Fig. 5.4 shows the $FWHM$ in a plot of a spectral line.

The peak intensity (I) is the ratio between the intensity at the center of the line I_0 and the intensity of the continuum I_c:

$$I = \frac{I_0}{I_c}. \tag{5.2}$$

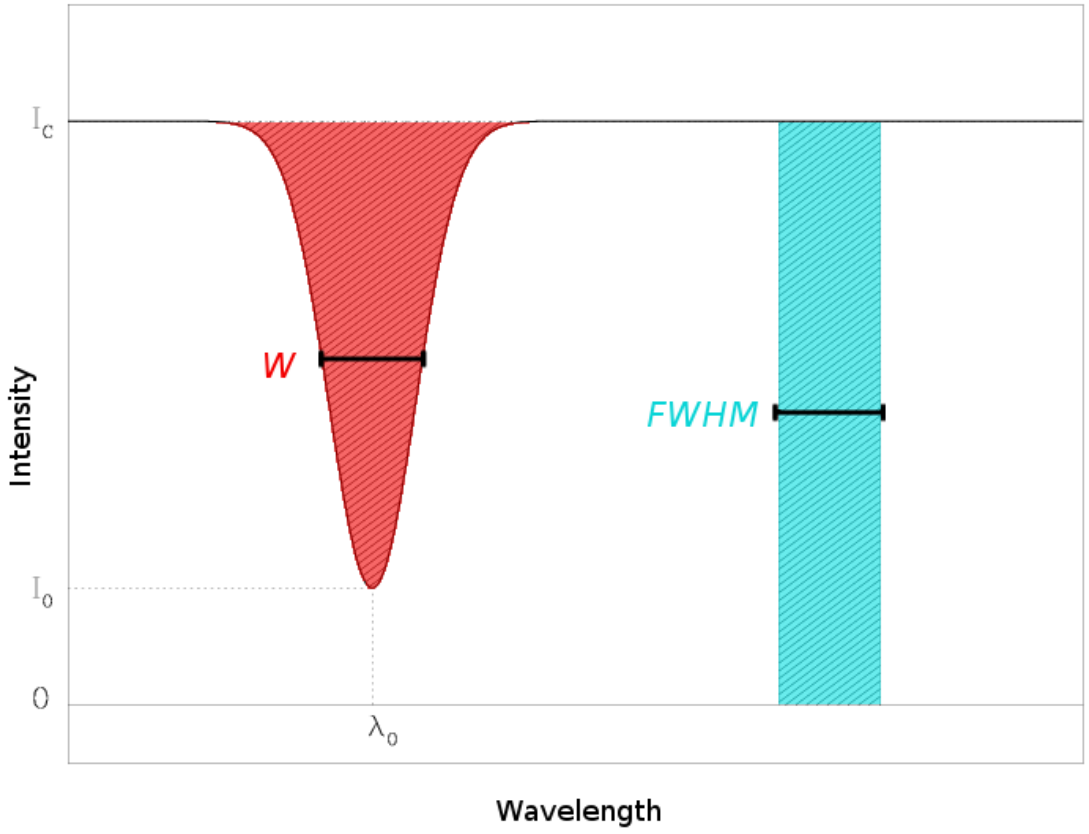

Figure 5.4: Equivalent width (W) and Full width at half maximum ($FWHM$) of a spectral line.

5.3.3 Electron temperature and density

Electron density and temperature of gas are two parameters describing the local physical condition. To derive the average density we need to measure the relative intensities of two lines which arise from a split upper level. The line ratios are excellent density diagnostics especially in the intermediate regime, between "low density regime" (where collisional deexcitation is unimportant) and "high density regime" (where the level populations are held at the ratio of their statistical weights). More theoretical details are described in Osterbrock [79]. For the basic analysis of the electron density we can use two different ratios:

$$R_{[SII]} = \frac{I(6716)}{I(6731)} \tag{5.3}$$

$$R_{[OII]} = \frac{I(3729)}{I(3726)}. \tag{5.4}$$

The ratio $R_{[SII]}$ gives good results in the range from 10^2 to 10^4 cm^{-3} for $T_\mathrm{e} = 5000 - 20000$ K. It can be observed at moderate spectral resolution. The ratio $R_{[OII]}$ works in the same regime, but the lines are closer to each other, than in the previous case. Therefore, it is necessary to use high-dispersion spectrometer for proper observations.

To derive densities from this line ratios it is mandatory to know the energy level separations, the statistical weights of the levels, and the radiative and collisional excitation and de-excitation rates. The behavior of the $R_{[SII]}$ ratio according to a change in density is shown in Fig. 5.5.

The balance between heating and cooling processes in an HII region is expressed in the electron temperature. Absorption of the ionizing radiation from the exciting star(s) is responsible for the heating, collisional excitation of electrons in the ions of heavy elements is the most important cooling mechanism. With higher metallicity there are more coolants in the gas and therefore the electron temperature gets lower.

There are two possibilities how to measure the electron temperature, using ratio of [OIII] lines or [NII] lines [79]:

$$R_{[OIII]} = \frac{I(4959) + I(5007)}{I(4363)} \approx \frac{7.73e^{32900/T_e}}{1 + 4.5 \times 10^{-4}(n_e/T_e^{1/2})} \tag{5.5}$$

$$R_{[NII]} = \frac{I(6548) + I(6583)}{I(5755)} \approx \frac{6.91e^{25000/T_e}}{1 + 2.5 \times 10^{-3}(n_e/T_e^{1/2})}. \tag{5.6}$$

Fig. 5.6 shows five different temperature sensitive emission line ratios, together with $R_{[OIII]}$ and $R_{[NII]}$. The ratio $R_{[OIII]}$ is well working at high temperatures, but not every time this ratio can be used as the line λ4363 is usually week. Contrary, the [S II] ratio is more useful in lower temperatures, below 15000 K [141].

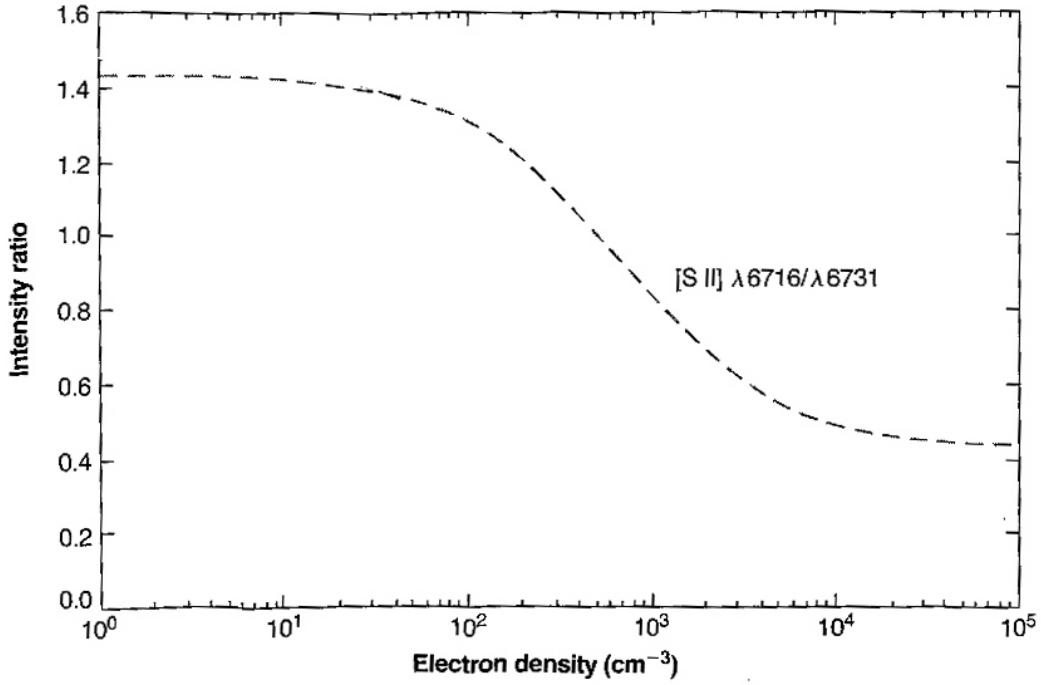

Figure 5.5: A diagram of the density sensitive emission line ratio $R_{[SII]}$ [79].

5.3.4 Metallicity

Ionic abundances N can be derived by using intensities of an ionic emission line $I(\lambda)$ and of an H recombination line $I(H_\beta)$, together with ratio of their theoretical emissivities ϵ:

$$\frac{N(X^{+i})}{N(H^+)} = \frac{I(\lambda)}{I(H_\beta)} \frac{\epsilon(H_\beta)}{\epsilon(\lambda)}. \tag{5.7}$$

The emissivity for collisionally excited ions in the low-density limit is:

$$\epsilon(\lambda) = \frac{\mathrm{hc}}{\lambda} 8.63 \times 10^{-6} (\Omega/\omega_1) T_e^{-0.5} e^{-\chi/\mathrm{k}T_e}, \tag{5.8}$$

where Ω is a collision strength for the observed transition, ω_1 is a statistical weight of the lower level and χ is the excitation energy of the upper level. The total elemental abundance is a sum of the ionic abundances. However, not always are all of the ionic states observed. Therefore there is a number of empirical formulae, which converts ionic abundances into elemental abundances. For example, in a case of oxygen, the unobserved O^{+++} state is corrected by ionic abundances of He^{++}. This correction is based on the similar value of the second ionization potential of helium (54.4 eV) with the third ionization potential of oxygen (54.9 eV):

$$\frac{O}{H} = \left(\frac{O^+}{H} + \frac{O^{++}}{H}\right) \times \left(1 + \frac{He^{++}}{He^+ + He^{++}}\right). \tag{5.9}$$

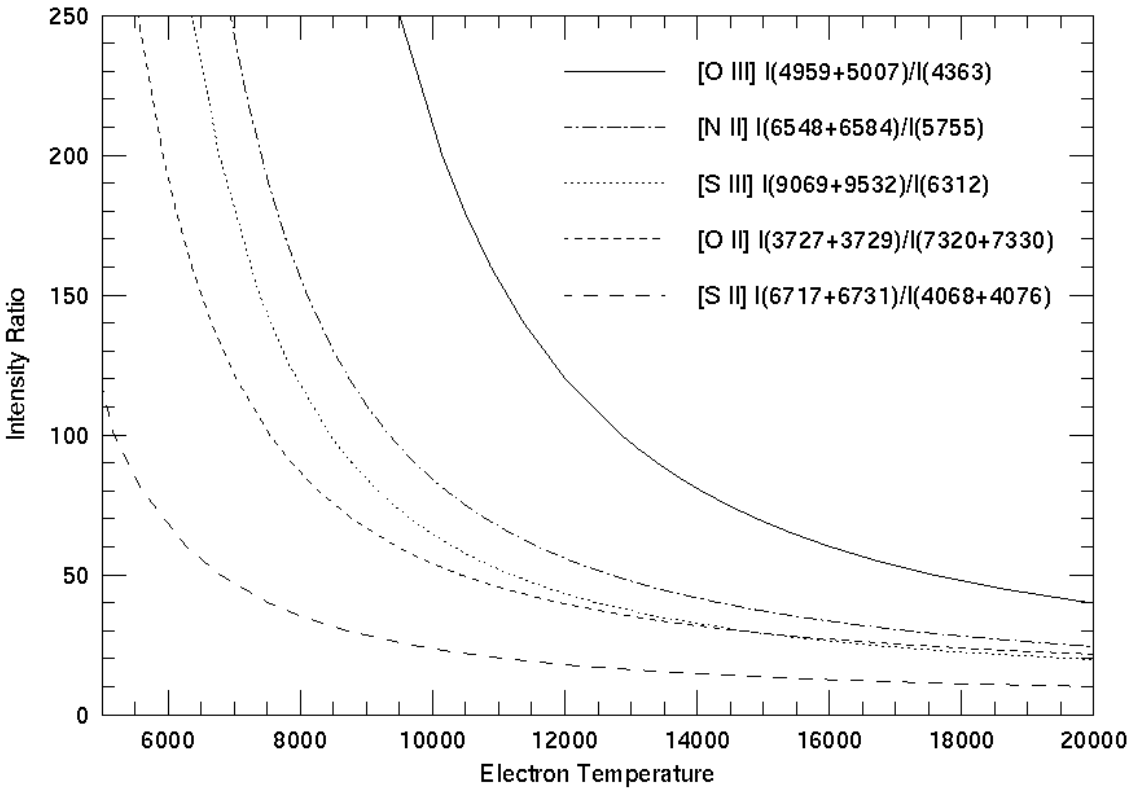

Figure 5.6: A diagram of the temperature sensitive emission line ratios, produced by Skillman [141] by using SD95 program.

However, not always are the essential emission lines from all of the relevant ionic states observable. Therefore we can use simplier methods, which allows us to determine directly the metallicity of the gas (log(O/H)+12). One of these uses N2 index, defined as the ration of the nitrogen line [N II]λ6583 and Hα:

$$N2 = \log(\frac{[NII]\lambda 6583}{H_\alpha}). \tag{5.10}$$

N2 index is very useful for calculating the oxygen abundance. There is no need for reddening corrections or flux calibration, because Hα and [N II]λ6583 are close to each other. Although N2 index could be very saturated in the high-metallicity regime, it is still sensitive to the metal content and therefore useful for determination the metallicity of the gas [142]:

$$12 + \log(\frac{O}{H}) = 8.90 + 0.57 \times N2 \tag{5.11}$$

5.4 Results

Our projects "Origin of the interstellar bubble S1 and its surroundings" and "Infrared bubbles S73 and S74" were awarded the requested 3 and 5 hours, respectively, of observing time (including overheads) on the MPG/ESO 2.2 m telescope located at La Silla Observatory in Chile. Both programs were awarded Priority category A. The first project was performed during October 2015. The spectroscopy was done for two targets (S1 (p2) and S1 (p3) from Tab. 5.1) and WFI image was taken as it was requested in H_α filter (50min, see Fig. 5.3, left panel for the location of the WFI). The second project was performed during July/August 2016 and all the observations were done by me. The spectroscopy for both targets S73 and S74 was done (Tab. 5.1). The imaging was done in OIII/8 filter, but no significant emission was measured.

Table 5.1: Spectral observations

Object	RA	DEC	l	b	t_{exp} [min]
S1 (p2)	17:22:31.3	-37:51:11.5	349.90002	-0.80005	20
S1 (p3)	17:22:18.8	-38:01:08.4	349.74013	-0.86021	30
S73	15:55:30.2	-54:36:45.6	327.55991	-0.79227	50
S74	15:55:34.8	-54:40:32.2	327.52811	-0.84771	33

All the results from the basic analysis are shown in following figures and tables. Fig. 5.8 and 5.9 are showing lines detected in the optical spectrum for each observed region. Measured properties of detected lines are listed in Tab. 5.2, upper limits of undetected lines in Tab. 5.3, kinematic properties of prominent spectral lines are in Tab. 5.4, derived properties such as temperature, electron density and metallicity are shown in Tab. 5.5. The WFI picture of the area close to the bubble S1 is visible in Fig. 5.7 in the right panel. The left panel shows Hα emission from SHASSA, which we used for locating points of interest in our proposal.

Table 5.2: Measured properties of detected lines

Object	FWHM($H\alpha$)[$\AA$]	[NII]6548/$H\alpha$	[NII]6583/$H\alpha$	[SII]6716/$H\alpha$	[SII]6731/$H\alpha$	A_V
S1 (p2)	0.42	0.059	0.227	0.055	0.048	3.09
S1 (p3)	0.54	0.106	0.332	0.113	0.084	3.79
S73	0.48	0.121	0.390	0.114	0.088	3.54
S74	0.63	0.144*	0.388*	0.112*	0.091*	2.94

S74($*$): line profiles differ between the H emission (a broad single peak) and heavier elements emission (double peaked).

Table 5.3: Upper limits of undetected lines

Object	[OII]/$H\alpha$	[OIII]/$H\alpha$	[NII]/$H\alpha$	HeI/$H\alpha$
	3726+3729	5006+4958+4931	5755	5876+4471+6678
S1 (p2)	7.2	0.1	0.02	0.09
S1 (p3)	16.0	0.2	0.03	0.2
S73	4.3	0.08	0.01	0.06
S74	2.3	0.06	0.01	0.04

Table 5.4: Kinematical properties.

Object	H		[NII]		[SII]		[OI]
	v_{LSR} [kms^{-1}]	σ [kms^{-1}]	v_{LSR} [kms^{-1}]	σ [kms^{-1}]	v_{LSR} [kms^{-1}]	σ[kms^{-1}]	σ[kms^{-1}]
S1 (p2)	-29	12	-29	9	-29	9	4
S1 (p3)	-29	13	-29	10	-26	11	4
S73	-35	12	-35	8	-33	9	4
S74	-39	14	-46	6	-46	6	4
			-32	6	-32	7	4

Table 5.5: Derived properties.

Object	$T_{[NII]}$ (K)	[SII] ratio	n_e (cm^{-3})	12+logO/H ([NII])
S1 (p2)	$<$ 34 000	1.16	300	8.53
S1 (p3)	$<$ 41 000	1.34	100	8.63
S73	$<$ 15 000	1.29	120	8.67
S74	$<$ 12 500	1.23	200	8.67

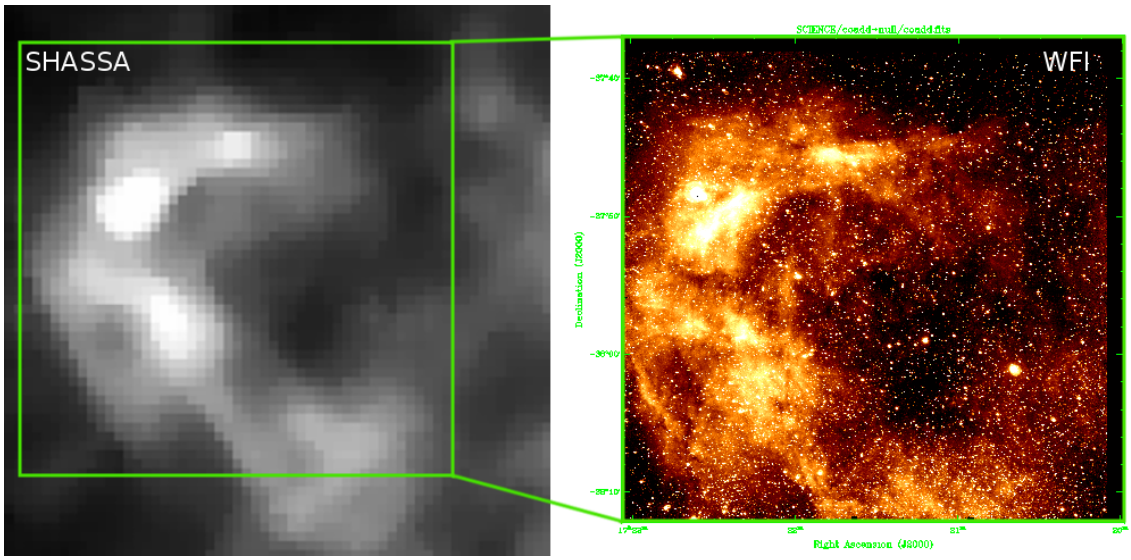

Figure 5.7: This figure shows a comparison between Hα emission captured by SHASSA (the left panel) and our WFI image (the right panel).

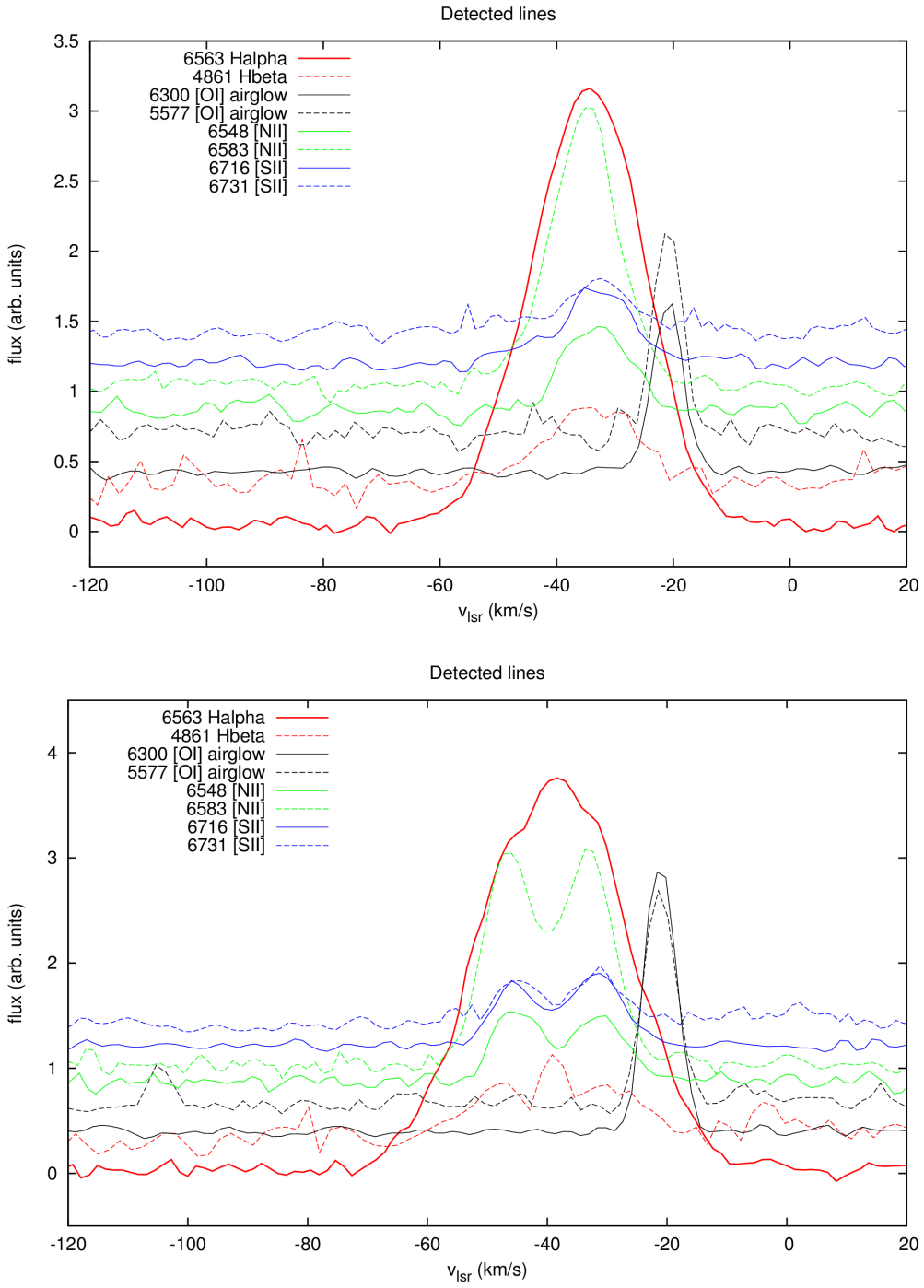

Figure 5.8: S73 and S74 infrared bubbles (RCW98): lines detected in the optical spectrum (S73: left, S74: right). Different colors denote different species: red is hydrogen ($H\alpha$, $H\beta$), green nitrogen ([NII] 6548, [NII] 6583), blue sulfur ([SII] 6716, [SII] 6731). Black is oxygen ([OI] 6300, [OI] 5577) and the emission does not originate from the HII region, but it is an airglow. Observations from the 2.2 m MPG/ESO (FEROS). Flux is in arbitrary units, unreddened, normalized to the same exposure time and shifted in the y axis.

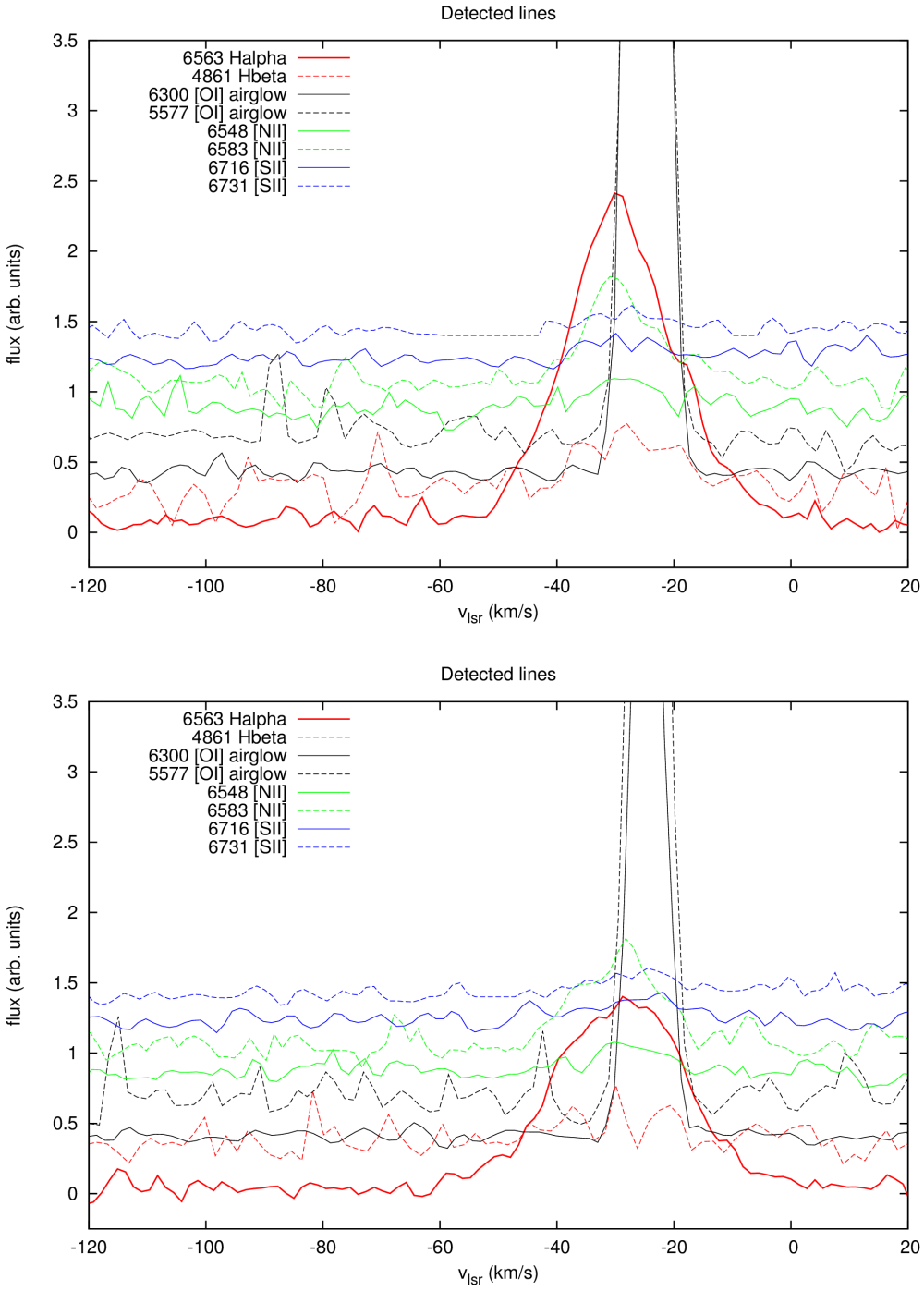

Figure 5.9: S1 infrared bubble: lines detected in the optical spectrum (position P2: left, position P3: right). Different colours denote different species: red is hydrogen ($H\alpha$, $H\beta$), green nitrogen ([NII] 6548, [NII] 6583), blue sulfur ([SII] 6716, [SII] 6731). Black is oxygen ([OI] 6300, [OI] 5577) and the emission does not originate from the HII region, but it is an airglow. Observations from the 2.2 m MPG/ESO (FEROS). Flux is in arbitrary units, unreddened, normalized to the same exposure time and shifted in the y axis.

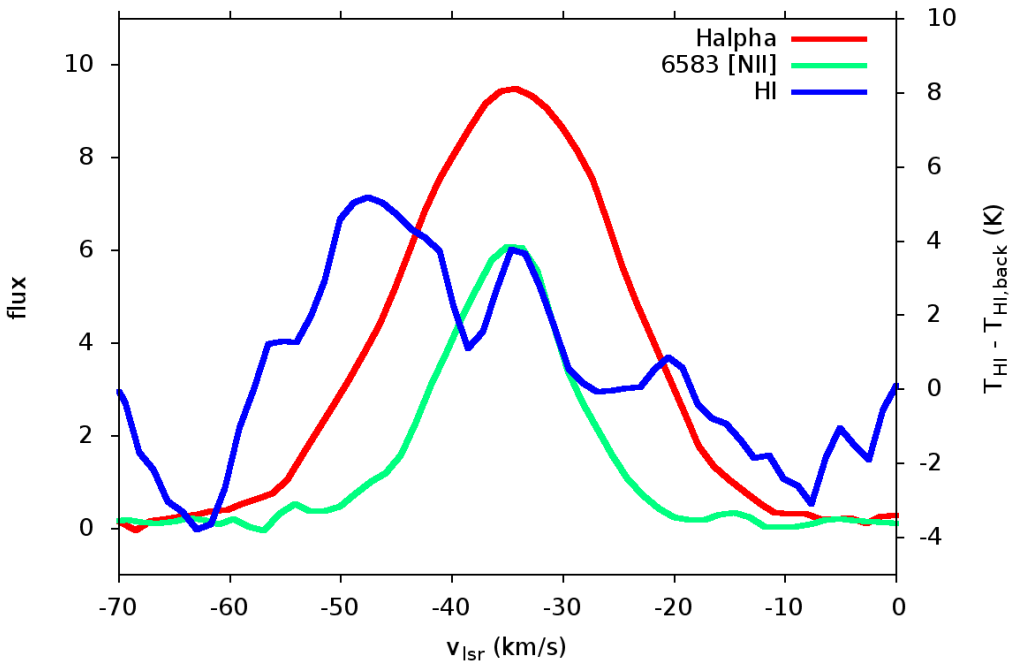

Figure 5.10: Optical (2.2 m MPG/ESO) spectrum we took from the inside of bubble S74, together with HI spectrum from HI4PI.

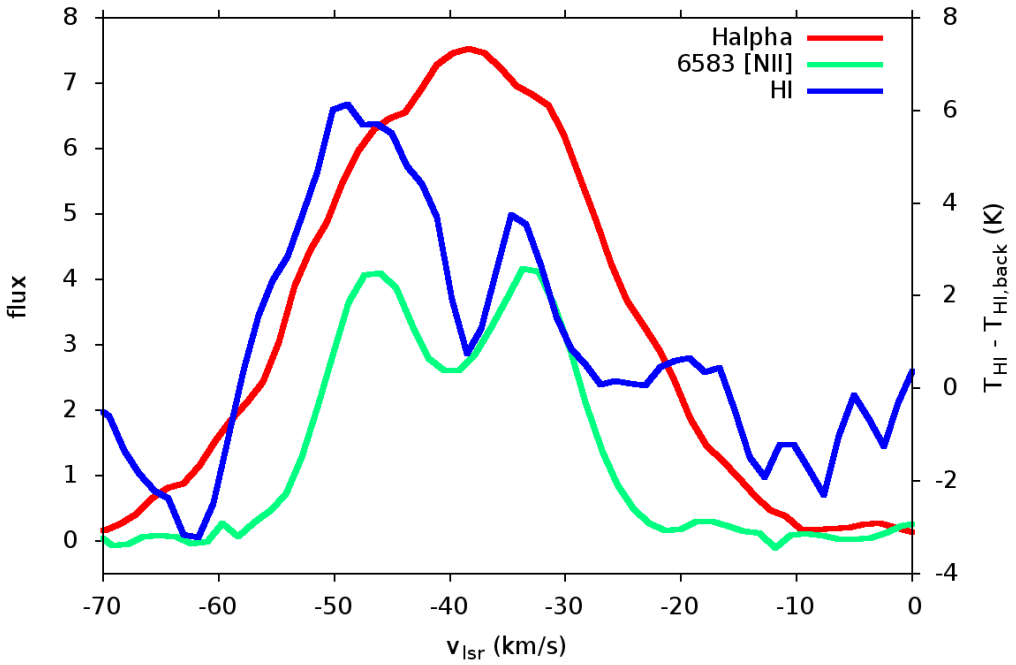

Figure 5.11: Optical (2.2 m MPG/ESO) spectrum we took from the inside of bubble S74, together with HI spectrum from HI4PI. The double peak in NII spectral line is mirrored also in HI profile.

5.5 Discussion

From all results we have got from our analysis so far, the most interesting results are the comparisons between the optical and the HI spectra of bubbles S73 and S74, especially the double peaked emission in [NII] found in the spectrum of S74.

H_α emission of S73 and S74 is centered on similar radial velocities, but their profiles are different. Spectrum of S73 shows a single peak H_α emission at -35 kms^{-1}, which is consistent with the velocity of the bright-rimmed CO cloud (-36.5 kms^{-1}). There is a single peak in optical emission, both in H_α and [NII] emission, which is consistent with the local peak in HI temperature (Fig. 5.10).

However, the optical spectra of S74 shows a different behavior. While the H_α emission profile is complex, with the central radial velocity of -39 kms^{-1}, the [NII] emission shows a double profile. Maxima of the double profile are located at -33 kms^{-1} and -46 kms^{-1}. Interestingly, this [NII] double peaked profile corresponds to local maxima in the HI spectrum (Fig. 5.11).

H_α emission traces the ionized gas, which is distributed in the whole volume of the bubble. The central part (around the central radial velocity) is probably low-density gas, while the high-density gas lies in two walls, separated by 13 kms^{-1}). This is confirmed by the [NII] emission originating primarily in high-density regions. Profiles in [NII] and HI are similar, which means that bubble walls are partly neutral and partly ionized. S74 is a good and valuable example of an expanding interstellar bubble, where approaching and receding walls are visible not just in the HI spectra, but also in the optical spectra. Urquhart et al. [140] also confirm a presence of front and back CO emission. Bubble S74 is clearly a 3D object.

Chapter 6

Conclusions

Interstellar bubbles, with diameters from fractions to a few tens of parsecs, were broadly studied especially in infrared observations during the past decade. The main goal of this thesis was an extensive study of the atomic and molecular component of these bubbles. To introduce the reader to this field of bubbling interstellar matter, we summarized the current knowledge of interstellar bubbles, their formation, evolution and observations in the first two chapters.

From our results it is obvious that smaller interstellar bubbles are evolving in a denser medium (both atomic and molecular), than the larger ones. This is expected as the star formation takes places in the densest parts of ISM, and as the bubble is evolving, it reaches a sparser medium. From our energy estimates we see that the main mechanism, which drives the expansion of interstellar bubbles, is a feedback from OB stars. We suppose, according to the luminosity estimates that the most probable progenitors are B type stars. Churchwell et al. [1] conclude that late B type stars are the main progenitors, while Deharveng et al. [3] suggest that more massive stars, O and earlier B type stars, are the main progenitors. According to our estimates, both late and early B stars are involved in the formation of bubbles.

Thanks to studying both atomic and molecular content of bubbles we could derive masses of interstellar bubbles, which vary between 10^3 to 10^5 $M_\odot$. The correlations between column densities (and also masses in HI and H_2) and size/age of bubbles give no evidence that the accumulation of HI gas would effectively form molecular gas. The distribution of CO emission does not show any change in velocity channels (except of the bubble N35), not even any approaching or receding walls. Beaumont and Williams [34] got similar results and suggested that bubbles are actually rings. It is possible that the molecular content is distributed in a ring, but neutral hydrogen is, according to our analysis, forming a bubble. Most of the bubbles have approaching and receding HI walls, therefore we stress that interstellar bubbles are 3D objects, at least their atomic content.

While we were analyzing our sample of bubbles, we found an intriguing new type of HI envelopes. We called them "absorption envelopes" (or bubbles), as they are observed not in HI emission, but in HI absorption. We found out that these envelopes are more compact and follow IR rims of bubbles better than HI emission envelopes. They also show lower f_{HI} (the filling factor of HI emission) than the HI emission envelopes.

We suggest that these absorption envelopes are formed of CNM, colder and denser gas than WNM. These structures are definitely worth of more detailed study.

During our analysis we found also another unexpected phenomenon - a collision between bubbles. While deriving basic properties of the bubbles N115, N116 and N117, we were caught by the unusual and striking neighborhood of these bubbles. This aroused our curiosity and we dedicated part of our research to the study of this complex region (the details are described in the fourth chapter). We found two independent systems of bubbles, each formed by two large bubbles (20 – 30 pc in radius) and one small bubble ($\sim$ 4 pc). It seems that the large bubbles are colliding and increasing the probability of star formation in the place of the collision. The proof of the recent star formation is in the existence of the smaller bubbles, which sit exactly at the position of the interaction between the large bubbles. We see, from all our results, that the expansion of a bubble itself is not much effective in molecularization of collected HI gas, but, probably, the collision helps to compress collected gas, molecularize it and leads to further star formation. To be able to make general conclusions we would need to study interactions between bubbles more broadly. Therefore, we would like to continue in searching for interacting interstellar bubbles and look for some evidence, which would support (or disprove) our hypothesis.

The fifth chapter is dedicated to our side project - optical observations and spectroscopy of inner parts of interstellar bubbles. We were awarded observing time at MPG/ESO 2.2 m telescope located at La Silla observatory in Chile. We performed optical spectroscopy of bubbles S1 (and its surroundings), S73 and S74. Among the basic spectroscopic analysis we came to an interesting result. We found a double-peaked [NII] emission profile towards the bubble S74, which corresponds to its profile in HI. H_α emission is complex, but with a single peak, which sits between double peaks of [NII] and HI emission. It leads us to a conclusion that H_α emission is coming from low-

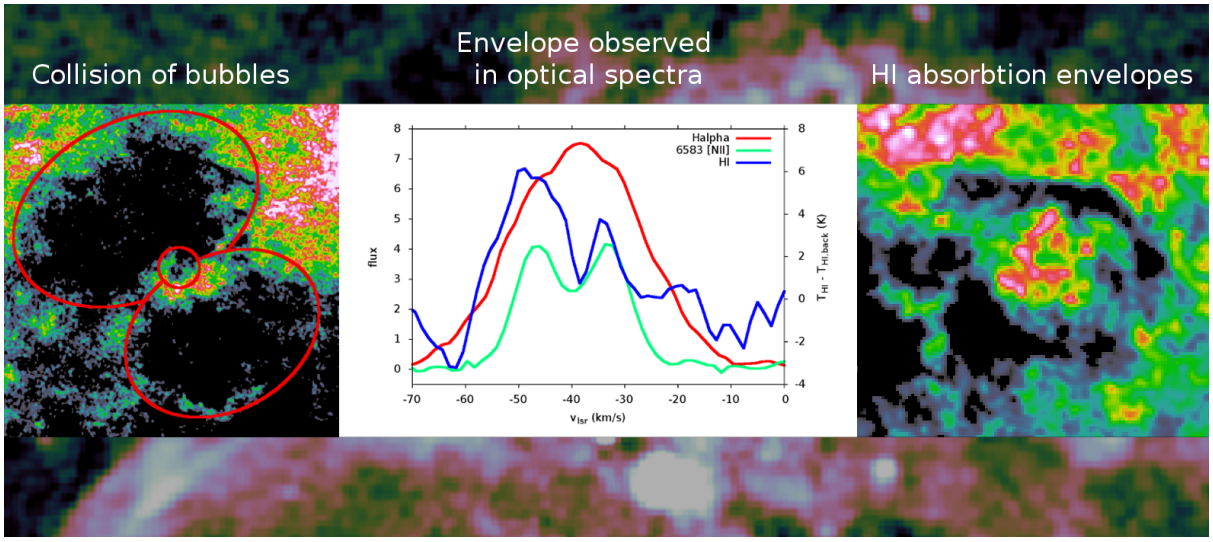

Figure 6.1: The figure summarizes the most interesting results of this thesis, besides the main analysis described in the third chapter. These are discoveries of HI absorption envelopes (the right panel), collisions of bubbles (the left panel) and observation of an envelope in an optical spectra.

density ionized gas, surrounded by walls of denser ionized gas, emitting in [NII]. The denser ionized gas seems to be close to the HI walls, which are forming an envelope around the ionized gas. This is a wonderful example, where, even in optical spectra of ionized gas, we can observe approaching and receding walls of an interstellar bubble.

We hope that this thesis, together with papers we are working on, will contribute to the growing field of interstellar bubbles research. The results probably helped to answer some of the uncertainties in the problematics of interstellar bubbles. Here is a brief summary of our conclusions: **1) smaller bubbles are evolving in a denser medium**, **2) the progenitors of bubbles are mainly B type stars**, **3) there is no evidence of effective molecularization of the swept-up atomic gas**, and **4) the molecular content of bubbles can be distributed in a ring, but the atomic gas forms a 3D bubble**. We discovered a new type of HI envelopes, **the absorption envelopes**, we found **colliding interstellar bubbles** and suggested that the collision helps further star-formation, and we observed front and back **walls of a bubble in an optical spectra**. Therefore new questions and tasks for further studies arose, such as: What are the properties of absorption bubbles? Is a collision between bubbles a common event? How effective is the collision in terms of a star formation? These and other questions are not only motivating for further research, but they also reflect how much is left to be discovered in the world of bubbling interstellar matter.

Bibliography

[1] E. Churchwell et al. "The Bubbling Galactic Disk". In: *ApJ* 649 (Oct. 2006), pp. 759–778. DOI: 10.1086/507015.

[2] E. Churchwell et al. "The Bubbling Galactic Disk. II. The Inner 20deg". In: *ApJ* 670 (Nov. 2007), pp. 428–441. DOI: 10.1086/521646.

[3] L. Deharveng et al. "A gallery of bubbles. The nature of the bubbles observed by Spitzer and what ATLASGAL tells us about the surrounding neutral material". In: *A&A* 523, A6 (Nov. 2010), A6. DOI: 10.1051/0004-6361/201014422. arXiv: 1008.0926.

[4] L. Zychová and S. Ehlerová. "Colliding interstellar bubbles in the direction of l = 54deg". In: *A&A* 595, A49 (Oct. 2016), A49. DOI: 10.1051/0004-6361/201527897.

[5] R. J. Simpson et al. "The Milky Way Project First Data Release: a bubblier Galactic disc". In: *MNRAS* 424 (Aug. 2012), pp. 2442–2460. DOI: 10.1111/j.1365-2966.2012.20770.x. arXiv: 1201.6357.

[6] D. O. S. Wood and E. Churchwell. "The morphologies and physical properties of ultracompact H II regions". In: *ApJS* 69 (Apr. 1989), pp. 831–895. DOI: 10.1086/191329.

[7] R. H. Becker et al. "A 20 centimeter survey of compact sources in the northern Galactic plane". In: *ApJ* 358 (Aug. 1990), pp. 485–494. DOI: 10.1086/169002.

[8] R. Paladini et al. "A radio catalog of Galactic HII regions for applications from decimeter to millimeter wavelengths". In: *A&A* 397 (Jan. 2003), pp. 213–226. DOI: 10.1051/0004-6361:20021466. eprint: astro-ph/0210226.

[9] E. Lagadec et al. "A mid-infrared imaging catalogue of post-asymptotic giant branch stars". In: *MNRAS* 417 (Oct. 2011), pp. 32–92. DOI: 10.1111/j.1365-2966.2011.18557.x. arXiv: 1102.4561 [astro-ph.SR].

[10] M. Meixner et al. "A Mid-infrared Imaging Survey of Proto-Planetary Nebula Candidates". In: *ApJS* 122 (May 1999), pp. 221–242. DOI: 10.1086/313215. eprint: astro-ph/9812279.

[11] G. Tenorio-Tagle and P. Bodenheimer. "Large-scale expanding superstructures in galaxies". In: *ARA&A* 26 (1988), pp. 145–197. DOI: 10.1146/annurev.aa.26.090188.001045.

[12] Y. N. Efremov, B. G. Elmegreen, and P. W. Hodge. "Giant Shells and Stellar Arcs as Relics of Gamma-Ray Burst Explosions". In: *ApJ* 501 (July 1998), pp. L163–L165. DOI: 10.1086/311468. eprint: astro-ph/9805236.

[13] Gopal-Krishna and J. A. Irwin. "Radio jet-blown neutral hydrogen supershells in spiral galaxies?" In: *A&A* 361 (Sept. 2000), pp. 888–894. eprint: astro-ph/0008251.

[14] J. E. Dyson and D. A. Williams. *The physics of the interstellar medium*. Bristol, 1997.

[15] T. Hosokawa and S.-i. Inutsuka. "Dynamical Expansion of Ionization and Dissociation Fronts around a Massive Star. I. A Mode of Triggered Star Formation". In: *ApJ* 623 (Apr. 2005), pp. 917–921. DOI: 10.1086/428648. eprint: astro-ph/0411080.

[16] E. Peeters et al. "The Prominent Dust Emission Feature near 8.9 μm in Four H II Regions". In: *ApJ* 620 (Feb. 2005), pp. 774–785. DOI: 10.1086/427143.

[17] G. Schaller et al. "New grids of stellar models from 0.8 to 120 solar masses at Z = 0.020 and Z = 0.001". In: *A&AS* 96 (Dec. 1992), pp. 269–331.

[18] E. Falgarone and T. G. Phillips. "Small-Scale Density and Velocity Structure of a Molecular Cloud Edge". In: *ApJ* 472 (Nov. 1996), p. 191. DOI: 10.1086/178054.

[19] C. Federrath et al. "Comparing the statistics of interstellar turbulence in simulations and observations. Solenoidal versus compressive turbulence forcing". In: *A&A* 512, A81 (Mar. 2010), A81. DOI: 10.1051/0004-6361/200912437. arXiv: 0905.1060 [astro-ph.SR].

[20] B. G. Elmegreen, T. Kimura, and M. Tosa. "Sequential Star Formation in OB Associations: The Role of Molecular Cloud Turbulence". In: *ApJ* 451 (Oct. 1995), p. 675. DOI: 10.1086/176253.

[21] J. Franco, G. Tenorio-Tagle, and P. Bodenheimer. "On the formation and expansion of H II regions". In: *ApJ* 349 (Jan. 1990), pp. 126–140. DOI: 10.1086/168300.

[22] E. R. Capriotti and J. F. Kozminski. "Relative Effects of Ionizing Radiation and Winds from O-Type Stars on the Structure and Dynamics of H II Regions". In: *PASP* 113 (June 2001), pp. 677–691. DOI: 10.1086/320809.

[23] T. Freyer, G. Hensler, and H. W. Yorke. "Massive Stars and the Energy Balance of the Interstellar Medium. II. The 35 M_{solar} Star and a Solution to the "Missing Wind Problem"". In: *ApJ* 638 (Feb. 2006), pp. 262–280. DOI: 10.1086/498734. eprint: astro-ph/0512110.

[24] T. Hosokawa and S.-i. Inutsuka. "Dynamical Expansion of Ionization and Dissociation Front around a Massive Star: A Starburst Mechanism". In: *ApJ* 648 (Sept. 2006), pp. L131–L134. DOI: 10.1086/507887. eprint: astro-ph/0607587.

[25] A. J. van Marle, Z. Meliani, and A. Marcowith. "Shape and evolution of wind-blown bubbles of massive stars: on the effect of the interstellar magnetic field". In: *A&A* 584, A49 (Dec. 2015), A49. DOI: 10.1051/0004-6361/201425230. arXiv: 1509.00192 [astro-ph.SR].

[26] H. Weaver and D. R. W. Williams. "The Berkeley Low-Latitude Survey of Neutral Hydrogen Part II. Contour Maps". In: *A&AS* 17 (Oct. 1974), p. 1.

[27] C. Heiles. "H I shells and supershells". In: *ApJ* 229 (Apr. 1979), pp. 533–537. DOI: 10.1086/156986.

[28] S. Ehlerová and J. Palouš. "HI shells in the Leiden/Argentina/Bonn HI survey". In: *A&A* 550, A23 (Feb. 2013), A23. DOI: 10.1051/0004-6361/201220341. arXiv: 1301.4003.

[29] N. M. McClure-Griffiths et al. "Evidence for Chimney Breakout in the Galactic Supershell GSH 242-03+37". In: *ApJ* 638 (Feb. 2006), pp. 196–205. DOI: 10.1086/498706. eprint: astro-ph/0510304.

[30] W. J. G. de Blok and F. Walter. "Evidence for Tidal Interaction and a Supergiant H I Shell in the Local Group Dwarf Galaxy NGC 6822". In: *ApJ* 537 (July 2000), pp. L95–L98. DOI: 10.1086/312777. eprint: astro-ph/0005473.

[31] G. Park et al. "A High-velocity Cloud Impact Forming a Supershell in the Milky Way". In: *ApJ* 827, L27 (Aug. 2016), p. L27. DOI: 10.3847/2041-8205/827/2/L27. arXiv: 1607.07699.

[32] C. Heiles. "H I shells, supershells, shell-like objects, and 'worms'". In: *ApJS* 55 (Aug. 1984), pp. 585–595. DOI: 10.1086/190970.

[33] J. B. Dove, J. M. Shull, and A. Ferrara. "The Escape of Ionizing Photons from OB Associations in Disk Galaxies: Radiation Transfer through Superbubbles". In: *ApJ* 531 (Mar. 2000), pp. 846–860. DOI: 10.1086/308481. eprint: astro-ph/9903331.

[34] C. N. Beaumont and J. P. Williams. "Molecular Rings Around Interstellar Bubbles and the Thickness of Star-Forming Clouds". In: *ApJ* 709 (Feb. 2010), pp. 791–800. DOI: 10.1088/0004-637X/709/2/791. arXiv: 0912.1852.

[35] S. Kendrew et al. "The Milky Way Project and ATLASGAL: The Distribution and Physical Properties of Cold Clumps Near Infrared Bubbles". In: *ApJ* 825, 142 (July 2016), p. 142. DOI: 10.3847/0004-637X/825/2/142. arXiv: 1602.06982.

[36] R. Paladini, R. D. Davies, and G. De Zotti. "Spatial distribution of Galactic HII regions". In: *MNRAS* 347 (Jan. 2004), pp. 237–245. DOI: 10.1111/j.1365-2966.2004.07210.x. eprint: astro-ph/0309350.

[37] E. P. Mercer et al. "New Star Clusters Discovered in the GLIMPSE Survey". In: *ApJ* 635 (Dec. 2005), pp. 560–569. DOI: 10.1086/497260.

[38] W. B. Burton. "Leiden-Green Bank survey of atomic hydrogen in the galactic disk. I - l, V and b, V maps". In: *A&AS* 62 (Dec. 1985), pp. 365–643.

[39] T. M. Dame et al. "A composite CO survey of the entire Milky Way". In: *ApJ* 322 (Nov. 1987), pp. 706–720. DOI: 10.1086/165766.

[40] S. Walch et al. "Comparing simulations of ionization triggered star formation and observations in RCW 120". In: *MNRAS* 452 (Sept. 2015), pp. 2794–2803. DOI: 10.1093/mnras/stv1427.

[41] M. Rahman and N. Murray. "A New Sample of Very Massive Star Forming Complexes in the Spitzer Glimpse Survey". In: *ApJ* 719 (Aug. 2010), pp. 1104–1122. DOI: 10.1088/0004-637X/719/2/1104. arXiv: 1004.3290 [astro-ph.GA].

[42] W. W. Roberts. "Large-Scale Shock Formation in Spiral Galaxies and its Implications on Star Formation". In: *ApJ* 158 (Oct. 1969), p. 123. DOI: 10.1086/150177.

[43] D. F. Woods, M. J. Geller, and E. J. Barton. "Tidally Triggered Star Formation in Close Pairs of Galaxies: Major and Minor Interactions". In: *AJ* 132 (July 2006), pp. 197–209. DOI: 10.1086/504834. eprint: astro-ph/0603175.

[44] M. Barsony et al. "Protostars in Perseus: Outflow-induced Fragmentation". In: *ApJ* 509 (Dec. 1998), pp. 733–748. DOI: 10.1086/306509.

[45] J. P. Phillips, G. Ramos-Larios, and J. A. Perez-Grana. "Wind-swept clouds and possible triggered star formation associated with the supernova remnant G357.7+0.3". In: *MNRAS* 397 (Aug. 2009), pp. 1215–1227. DOI: 10.1111/j.1365-2966.2009.14988.x. arXiv: 0909.2065.

[46] J. I. Castor, D. C. Abbott, and R. I. Klein. "Radiation-driven winds in Of stars". In: *ApJ* 195 (Jan. 1975), pp. 157–174. DOI: 10.1086/153315.

[47] P. R. Woodward. "Shock-driven implosion of interstellar gas clouds and star formation". In: *ApJ* 207 (July 1976), pp. 484–501. DOI: 10.1086/154516.

[48] H. A. T. Vanhala and A. G. W. Cameron. "Numerical Simulations of Triggered Star Formation. I. Collapse of Dense Molecular Cloud Cores". In: *ApJ* 508 (Nov. 1998), pp. 291–307. DOI: 10.1086/306396.

[49] R. McCray and M. Kafatos. "Supershells and propagating star formation". In: *ApJ* 317 (June 1987), pp. 190–196. DOI: 10.1086/165267.

[50] B. G. Elmegreen and C. J. Lada. "Sequential formation of subgroups in OB associations". In: *ApJ* 214 (June 1977), pp. 725–741. DOI: 10.1086/155302.

[51] B. G. Elmegreen. "Magnetic cloud collision fronts". In: *ApJ* 326 (Mar. 1988), pp. 616–638. DOI: 10.1086/166121.

[52] A. D. Chernin, Y. N. Efremov, and P. A. Voinovich. "Superassociations: violent star formation induced by shock-shock collisions". In: *MNRAS* 275 (July 1995), pp. 313–326. DOI: 10.1093/mnras/275.2.313.

[53] L. Deharveng and A. Zavagno. "Observations of star formation triggered by H ii regions". In: *Computational Star Formation*. Ed. by J. Alves et al. Vol. 270. IAU Symposium. Apr. 2011, pp. 239–246. DOI: 10.1017/S1743921311000457.

[54] J. E. Dale, T. J. Haworth, and E. Bressert. "The dangers of being trigger-happy". In: *MNRAS* 450 (June 2015), pp. 1199–1211. DOI: 10.1093/mnras/stv396. arXiv: 1502.05865.

[55] J. E. Dale et al. "Photoionizing feedback in star cluster formation". In: *MNRAS* 358 (Mar. 2005), pp. 291–304. DOI: 10.1111/j.1365-2966.2005.08806.x. eprint: astro-ph/0501160.

[56] J. E. Dale, I. A. Bonnell, and A. P. Whitworth. "Ionization-induced star formation - I. The collect-and-collapse model". In: *MNRAS* 375 (Mar. 2007), pp. 1291–1298. DOI: 10.1111/j.1365-2966.2006.11368.x. eprint: astro-ph/0612128.

[57] J. E. Dale, P. C. Clark, and I. A. Bonnell. "Ionization-induced star formation - II. External irradiation of a turbulent molecular cloud". In: *MNRAS* 377 (May 2007), pp. 535–544. DOI: 10.1111/j.1365-2966.2007.11515.x. eprint: astro-ph/0701497.

[58] J. E. Dale and I. A. Bonnell. "Ionization-induced star formation - III. Effects of external triggering on the initial mass function in clusters". In: *MNRAS* 422 (May 2012), pp. 1352–1362. DOI: 10.1111/j.1365-2966.2012.20709.x. arXiv: 1202.1417 [astro-ph.SR].

[59] S. K. Walch et al. "Dispersal of molecular clouds by ionizing radiation". In: *MNRAS* 427 (Nov. 2012), pp. 625–636. DOI: 10.1111/j.1365-2966.2012.21767.x. arXiv: 1206.6492.

[60] A. Whitworth. "The erosion and dispersal of massive molecular clouds by young stars". In: *MNRAS* 186 (Jan. 1979), pp. 59–67. DOI: 10.1093/mnras/186.1.59.

[61] J. P. Williams and C. F. McKee. "The Galactic Distribution of OB Associations in Molecular Clouds". In: *ApJ* 476 (Feb. 1997), pp. 166–183.

[62] C. M. Boily and P. Kroupa. "The impact of mass loss on star cluster formation - I. Analytical results". In: *MNRAS* 338 (Jan. 2003), pp. 665–672. DOI: 10.1046/j.1365-8711.2003.06076.x. eprint: astro-ph/0210378.

[63] C. M. Boily and P. Kroupa. "The impact of mass loss on star cluster formation - II. Numerical N-body integration and further applications". In: *MNRAS* 338 (Jan. 2003), pp. 673–686. DOI: 10.1046/j.1365-8711.2003.06101.x. eprint: astro-ph/0211026.

[64] N. Bastian and S. P. Goodwin. "Evidence for the strong effect of gas removal on the internal dynamics of young stellar clusters". In: *MNRAS* 369 (June 2006), pp. L9–L13. DOI: 10.1111/j.1745-3933.2006.00162.x. eprint: astro-ph/0602465.

[65] N. Murray and M. Rahman. "Star Formation in Massive Clusters Via the Wilkinson Microwave Anisotropy Probe and the Spitzer Glimpse Survey". In: *ApJ* 709 (Jan. 2010), pp. 424–435. DOI: 10.1088/0004-637X/709/1/424. arXiv: 0906.1026 [astro-ph.GA].

[66] E. J. Lee, N. Murray, and M. Rahman. "Milky Way Star-forming Complexes and the Turbulent Motion of the Galaxy's Molecular Gas". In: *ApJ* 752, 146 (June 2012), p. 146. DOI: 10.1088/0004-637X/752/2/146. arXiv: 1204.4190.

[67] C. F. McKee and E. C. Ostriker. "Theory of Star Formation". In: *ARA&A* 45 (Sept. 2007), pp. 565–687. DOI: 10.1146/annurev.astro.45.051806.110602. arXiv: 0707.3514.

[68] J. M. D. Kruijssen and S. N. Longmore. "An uncertainty principle for star formation - I. Why galactic star formation relations break down below a certain spatial scale". In: *MNRAS* 439 (Apr. 2014), pp. 3239–3252. DOI: 10.1093/mnras/stu098. arXiv: 1401.4459.

[69] C. D. Matzner. "On the Role of Massive Stars in the Support and Destruction of Giant Molecular Clouds". In: *ApJ* 566 (Feb. 2002), pp. 302–314. DOI: 10.1086/338030. eprint: astro-ph/0110278.

[70] D. Mihalas and J. Binney. *Galactic astronomy: Structure and kinematics /2nd edition/*. 1981.

[71] S. R. Kulkarni and C. Heiles. "Neutral hydrogen and the diffuse interstellar medium". In: *Galactic and Extragalactic Radio Astronomy*. Ed. by K. I. Kellermann and G. L. Verschuur. 1988, pp. 95–153.

[72] Planck Collaboration et al. "Planck 2015 results. I. Overview of products and scientific results". In: *A&A* 594, A1 (Sept. 2016), A1. DOI: 10.1051/0004-6361/201527101. arXiv: 1502.01582.

[73] P. M. W. Kalberla et al. "The Leiden/Argentine/Bonn (LAB) Survey of Galactic HI. Final data release of the combined LDS and IAR surveys with improved stray-radiation corrections". In: *A&A* 440 (Sept. 2005), pp. 775–782. DOI: 10.1051/0004-6361:20041864. eprint: astro-ph/0504140.

[74] D. P. Finkbeiner. "A Full-Sky Hα Template for Microwave Foreground Prediction". In: *ApJS* 146 (June 2003), pp. 407–415. DOI: 10.1086/374411. eprint: astro-ph/0301558.

[75] W. Voges et al. "The ROSAT all-sky survey bright source catalogue". In: *A&A* 349 (Sept. 1999), pp. 389–405. eprint: astro-ph/9909315.

[76] P. F. Goldsmith. "Molecular clouds - an overview". In: *Interstellar Processes*. Ed. by D. J. Hollenbach and H. A. Thronson Jr. Vol. 134. Astrophysics and Space Science Library. 1987, pp. 51–70. DOI: 10.1007/978-94-009-3861-8_3.

[77] O. Struve and C. T. Elvey. "Emission Nebulosities in Cygnus and Cepheus." In: *ApJ* 88 (Oct. 1938), p. 364. DOI: 10.1086/143992.

[78] R. J. Reynolds. "A measurement of the hydrogen recombination rate in the diffuse interstellar medium". In: *ApJ* 282 (July 1984), pp. 191–196. DOI: 10.1086/162190.

[79] D. E. Osterbrock. *Astrophysics of gaseous nebulae and active galactic nuclei*. 1989.

[80] A. G. G. M. Tielens. "Interstellar Polycyclic Aromatic Hydrocarbon Molecules". In: *ARA&A* 46 (Sept. 2008), pp. 289–337. DOI: 10.1146/annurev.astro.46.060407.145211.

[81] D. Cesarsky et al. "Infrared spectrophotometry of M 17 with ISOCAM." In: *A&A* 315 (Nov. 1996), pp. L309–L312.

[82] M. S. Povich et al. "A Multiwavelength Study of M17: The Spectral Energy Distribution and PAH Emission Morphology of a Massive Star Formation Region". In: *ApJ* 660 (May 2007), pp. 346–362. DOI: 10.1086/513073.

[83] T. Allain, S. Leach, and E. Sedlmayr. "Photodestruction of PAHs in the interstellar medium. II. Influence of the states of ionization and hydrogenation." In: *A&A* 305 (Jan. 1996), p. 616.

[84] P. R. Roelfsema et al. "ISO spectroscopy of (ultra) compact galactic HII regions". In: *Star Formation with the Infrared Space Observatory*. Ed. by J. Yun and L. Liseau. Vol. 132. Astronomical Society of the Pacific Conference Series. 1998, p. 76.

[85] M. Compiègne et al. "Dust processing in photodissociation regions. Mid-IR emission modelling". In: *A&A* 491 (Dec. 2008), pp. 797–807. DOI: 10.1051/0004-6361:200809850. arXiv: 0809.5026.

[86] D. Cesarsky et al. "Silicate emission in Orion". In: *A&A* 358 (June 2000), pp. 708–716. eprint: astro-ph/0002282.

[87] C. Watson et al. "Infrared Dust Bubbles: Probing the Detailed Structure and Young Massive Stellar Populations of Galactic H II Regions". In: *ApJ* 681, 1341-1355 (July 2008), pp. 1341–1355. DOI: 10.1086/588005. arXiv: 0806.0609.

[88] F. Schuller et al. "ATLASGAL - The APEX telescope large area survey of the galaxy at 870 μm". In: *A&A* 504 (Sept. 2009), pp. 415–427. DOI: 10.1051/0004-6361/200811568. arXiv: 0903.1369.

[89] N. M. McClure-Griffiths et al. "The Galactic Distribution of Large H I Shells". In: *ApJ* 578 (Oct. 2002), pp. 176–193. DOI: 10.1086/342470. eprint: astro-ph/0206358.

[90] N. M. McClure-Griffiths et al. "The Southern Galactic Plane Survey: The Test Region". In: *ApJ* 551 (Apr. 2001), pp. 394–412. DOI: 10.1086/320095. eprint: astro-ph/0012302.

[91] S. Ehlerová and J. Palouš. "H I shells in the outer Milky Way". In: *A&A* 437 (July 2005), pp. 101–112. DOI: 10.1051/0004-6361:20034389. eprint: astro-ph/0503443.

[92] L. A. Suad et al. "A new catalog of H i supershell candidates in the outer part of the Galaxy". In: *A&A* 564, A116 (Apr. 2014), A116. DOI: 10.1051/0004-6361/201323147. arXiv: 1403.4141.

[93] F. Walter and E. Brinks. "Holes and Shells in the Interstellar Medium of the Nearby Dwarf Galaxy IC 2574". In: *AJ* 118 (July 1999), pp. 273–301. DOI: 10.1086/300906. eprint: astro-ph/9904002.

[94] P. M. W. Kalberla et al. "The Leiden/Argentine/Bonn (LAB) Survey of Galactic HI. Final data release of the combined LDS and IAR surveys with improved stray-radiation corrections". In: *A&A* 440 (Sept. 2005), pp. 775–782. DOI: 10.1051/0004-6361:20041864. eprint: astro-ph/0504140.

[95] S. Kim et al. "H I Shells in the Large Magellanic Cloud". In: *AJ* 118 (Dec. 1999), pp. 2797–2823. DOI: 10.1086/301116.

[96] G. L. Pilbratt et al. "Herschel Space Observatory. An ESA facility for far-infrared and submillimetre astronomy". In: *A&A* 518, L1 (July 2010), p. L1. DOI: 10.1051/0004-6361/201014759. arXiv: 1005.5331 [astro-ph.IM].

[97] R. A. Benjamin et al. "GLIMPSE. I. An SIRTF Legacy Project to Map the Inner Galaxy". In: *PASP* 115 (Aug. 2003), pp. 953–964. DOI: 10.1086/376696. eprint: astro-ph/0306274.

[98] G. Tenorio-Tagle and J. Palouš. "Giant-scale supernova remnants - The role of differential galactic rotation and the formation of molecular clouds". In: *A&A* 186 (Nov. 1987), pp. 287–294.

[99] J. Palouš, J. Franco, and G. Tenorio-Tagle. "The evolution of superstructures expanding in differentially rotating disks". In: *A&A* 227 (Jan. 1990), pp. 175–182.

[100] E. Brinks. "NGC 206, a hole in M31". In: *A&A* 95 (Feb. 1981), pp. L1–L4.

[101] E. Brinks and E. Bajaja. "A high resolution hydrogen-line survey of Messier 31. III - H I holes in the interstellar medium". In: *A&A* 169 (Nov. 1986), pp. 14–42.

[102] E. R. Deul and R. H. den Hartog. "Small-scale structures in the H I distribution of M33". In: *A&A* 229 (Mar. 1990), pp. 362–377.

[103] D. Puche et al. "Holmberg II - A laboratory for studying the violent interstellar medium". In: *AJ* 103 (June 1992), pp. 1841–1858. DOI: 10.1086/116199.

[104] I. Bagetakos et al. "The Fine-scale Structure of the Neutral Interstellar Medium in Nearby Galaxies". In: *AJ* 141, 23 (Jan. 2011), p. 23. DOI: 10.1088/0004-6256/141/1/23. arXiv: 1008.1845.

[105] J. Kamphuis, R. Sancisi, and T. van der Hulst. "An H I superbubble in the spiral galaxy M 101". In: *A&A* 244 (Apr. 1991), pp. L29–L32.

[106] B. Chaboyer and J. P. Vader. "Peculiar morphologies of four IRAS galaxies". In: *PASP* 103 (Jan. 1991), pp. 35–48. DOI: 10.1086/132793.

[107] J. A. Irwin and E. R. Seaquist. "Heiles shells in NGC 3079". In: *ApJ* 353 (Apr. 1990), pp. 469–475. DOI: 10.1086/168635.

[108] S. Ehlerová and J. Palouš. "Correlation of HI shells and CO clumps in the outer Milky Way". In: *A&A* 587, A5 (Mar. 2016), A5. DOI: 10.1051/0004-6361/201526870. arXiv: 1512.07047.

[109] J. R. Dawson et al. "Supergiant Shells and Molecular Cloud Formation in the Large Magellanic Cloud". In: *ApJ* 763, 56 (Jan. 2013), p. 56. DOI: 10.1088/0004-637X/763/1/56. arXiv: 1211.7119 [astro-ph.GA].

[110] L. G. Hou and X. Y. Gao. "A statistical study of gaseous environment of Spitzer interstellar bubbles". In: *MNRAS* 438 (Feb. 2014), pp. 426–437. DOI: 10.1093/mnras/stt2212. arXiv: 1311.4943.

[111] J. M. Stil et al. "The VLA Galactic Plane Survey". In: *AJ* 132 (Sept. 2006), pp. 1158–1176. DOI: 10.1086/505940. eprint: astro-ph/0605422.

[112] J. M. Jackson et al. "The Boston University-Five College Radio Astronomy Observatory Galactic Ring Survey". In: *ApJS* 163 (Mar. 2006), pp. 145–159. DOI: 10.1086/500091. eprint: astro-ph/0602160.

[113] M. K. Dunham et al. "The Bolocam Galactic Plane Survey. VII. Characterizing the Properties of Massive Star-forming Regions". In: *ApJ* 741, 110 (Nov. 2011), p. 110. DOI: 10.1088/0004-637X/741/2/110. arXiv: 1108.1812.

[114] Smithsonian Astrophysical Observatory. *SAOImage DS9: A utility for displaying astronomical images in the X11 window environment*. Astrophysics Source Code Library. Mar. 2000. ascl: 0003.002.

[115] K. Rohlfs and T. L. Wilson. *Tools of Radio Astronomy*. 1996.

[116] R. A. Chevalier. "Supernovae and the interstellar medium". In: *Supernovae*. Ed. by S. A. Bludman, R. Mochkovitch, and J. Zinn-Justin. Jan. 1994, p. 743.

[117] V. Sidorin et al. "Exploring GLIMPSE bubble N107. Multiwavelength observations and simulations". In: *A&A* 565, A6 (May 2014), A6. DOI: 10.1051/0004-6361/201322687. arXiv: 1402.5614.

[118] N. Junkes, E. Fuerst, and W. Reich. "G54.4-0.3: CO shell and star formation region surrounding a shell-type supernova remnant. I - Properties of the CO shell". In: *A&AS* 96 (Nov. 1992), pp. 1–21.

[119] D. A. Leahy, W. Tian, and Q. D. Wang. "Distance Determination to the Crab-Like Pulsar Wind Nebula G54.1+0.3 and the Search for its Supernova Remnant Shell". In: *AJ* 136 (Oct. 2008), pp. 1477–1481. DOI: 10.1088/0004-6256/136/4/1477. arXiv: 0807.1298.

[120] D. A. Green. "A catalogue of 294 Galactic supernova remnants". In: *Bulletin of the Astronomical Society of India* 42 (June 2014), pp. 47–58. arXiv: 1409.0637 [astro-ph.HE].

[121] J.-L. Xu and B.-G. Ju. "Star formation associated with a large-scale infrared bubble". In: *A&A* 569, A36 (Sept. 2014), A36. DOI: 10.1051/0004-6361/201423952. arXiv: 1407.6819 [astro-ph.SR].

[122] C. Watson, U. Hanspal, and A. Mengistu. "Triggered Star Formation and Dust Around Mid-infrared-identified Bubbles". In: *ApJ* 716 (June 2010), pp. 1478–1492. DOI: 10.1088/0004-637X/716/2/1478. arXiv: 1006.0206.

[123] G. Park et al. "H I Shells and Supershells in the I-GALFA H I 21 cm Line Survey. I. Fast-expanding H I Shells Associated with Supernova Remnants". In: *ApJ* 777, 14 (Nov. 2013), p. 14. DOI: 10.1088/0004-637X/777/1/14. arXiv: 1306.6699.

[124] N. Junkes, E. Fuerst, and W. Reich. "G54.4-0.3: CO shell and star formation region surrounding a shell-type supernova remnant. II - Compact CO clouds and the star formation scenario". In: *A&A* 261 (July 1992), pp. 289–300.

[125] L. Bronfman, L.-A. Nyman, and J. May. "A CS(2-1) survey of IRAS point sources with color characteristics of ultra-compact HII regions." In: *A&AS* 115 (Jan. 1996), p. 81.

[126] L. D. Anderson et al. "The Molecular Properties of Galactic H II Regions". In: *ApJS* 181 (Mar. 2009), pp. 255–271. DOI: 10.1088/0067-0049/181/1/255. arXiv: 0810.3685.

[127] F. J. Lockman. "A survey of radio H II regions in the northern sky". In: *ApJS* 71 (Nov. 1989), pp. 469–479. DOI: 10.1086/191383.

[128] E. Rosolowsky et al. "The Bolocam Galactic Plane Survey. II. Catalog of the Image Data". In: *ApJS* 188, 123-138 (May 2010), pp. 123–138. DOI: 10.1088/0067-0049/188/1/123. arXiv: 0909.2871.

[129] E. F. E. Morales et al. "Stellar clusters in the inner Galaxy and their correlation with cold dust emission". In: *A&A* 560, A76 (Dec. 2013), A76. DOI: 10.1051/0004-6361/201321626. arXiv: 1310.2612.

[130] M. Kronberger et al. "New galactic open cluster candidates from DSS and 2MASS imagery". In: *A&A* 447 (Mar. 2006), pp. 921–928. DOI: 10.1051/0004-6361:20054057. eprint: gr-qc/0511021.

[131] M. M. Hanson et al. "Obscured clusters. III. Follow-up observations of Mercer 23". In: *A&A* 516, A35 (June 2010), A35. DOI: 10.1051/0004-6361/200913122.

[132] N. V. Kharchenko et al. "Global survey of star clusters in the Milky Way. II. The catalogue of basic parameters". In: *A&A* 558, A53 (Oct. 2013), A53. DOI: 10.1051/0004-6361/201322302. arXiv: 1308.5822.

[133] D. R. Lorimer, F. Camilo, and K. M. Xilouris. "Arecibo Timing Observations of 17 Pulsars along the Galactic Plane". In: *AJ* 123 (Mar. 2002), pp. 1750–1756. DOI: 10.1086/339026. eprint: astro-ph/0112106.

[134] J. L. Caswell and R. F. Haynes. "Southern H II regions - an extensive study of radio recombination line emission". In: *A&A* 171 (Jan. 1987), pp. 261–276.

[135] N. M. McClure-Griffiths et al. "The Southern Galactic Plane Survey: H I Observations and Analysis". In: *ApJS* 158 (June 2005), pp. 178–187. DOI: 10.1086/430114. eprint: astro-ph/0503134.

[136] J. E. Gaustad et al. "A Robotic Wide-Angle Hα Survey of the Southern Sky". In: *PASP* 113 (Nov. 2001), pp. 1326–1348. DOI: 10.1086/323969. eprint: astro-ph/0108518.

[137] M. C. Pinheiro, M. V. F. Copetti, and V. A. Oliveira. "Spectral classification and distance determination of stars in nine southern Galactic H II regions". In: *A&A* 521, A26 (Oct. 2010), A26. DOI: 10.1051/0004-6361/200912937.

[138] Q. A. Parker et al. "The AAO/UKST SuperCOSMOS Hα survey". In: *MNRAS* 362 (Sept. 2005), pp. 689–710. DOI: 10.1111/j.1365-2966.2005.09350.x. eprint: astro-ph/0506599.

[139] K. Sugitani and K. Ogura. "A catalog of bright-rimmed clouds with IRAS point sources: Candidates for star formation by radiation-driven implosion. 2: The southern hemisphere". In: *ApJS* 92 (May 1994), pp. 163–172. DOI: 10.1086/191964.

[140] J. S. Urquhart et al. "A tale of two cores: triggered massive star formation in the bright-rimmed cloud SFO 75". In: *A&A* 467 (June 2007), pp. 1125–1137. DOI: 10.1051/0004-6361:20077236. eprint: astro-ph/0703252.

[141] E. D. Skillman. "Chemical Evolution of the ISM in Nearby Galaxies". In: *Stellar astrophysics for the local group: VIII Canary Islands Winter School of Astrophysics*. Ed. by A. Aparicio, A. Herrero, and F. Sánchez. 1998, p. 457.

[142] M. Pettini and B. E. J. Pagel. "[OIII]/[NII] as an abundance indicator at high redshift". In: *MNRAS* 348 (Mar. 2004), pp. L59–L63. DOI: 10.1111/j.1365-2966.2004.07591.x. eprint: astro-ph/0401128.